

Vol. 38



No. 3



2017

Chemical and Process Engineering

Inżynieria Chemiczna i Procesowa

Polish Academy of Sciences
Committee of Chemical and Process Engineering

The Journal is supported by the Ministry of Science and Higher Education

Editorial Board

Andrzej Burghardt (Chairman), Polish Academy of Sciences, Gliwice, Poland
Jerzy Bałdyga, Warsaw University of Technology, Poland
Andrzej Górak, T.U. Dortmund, Germany
Leon Gradoń, Warsaw University of Technology, Poland
Andrzej Jarzębski, Silesian University of Technology, Poland
Zdzisław Jaworski, West Pomeranian University of Technology, Szczecin, Poland
Władysław Kamiński, Technical University of Łódź, Poland
Stefan Kowalski, Poznań University of Technology, Poland
Andrzej Krasławski, Lappeenranta University of Technology, Finland
Stanisław Ledakowicz, Technical University of Łódź, Poland
Eugeniusz Molga, Warsaw University of Technology, Poland
Alvin W. Nienow, University of Birmingham, United Kingdom
Andrzej Noworyta, Wrocław University of Technology, Poland
Ryszard Pohorecki, Warsaw University of Technology, Poland
Andrzej Stankiewicz, Delft University of Technology, The Netherlands
Czesław Strumiłło, Technical University of Łódź, Poland
Stanisław Sieniutycz, Warsaw University of Technology, Poland
Krzysztof Warmuziński, Polish Academy of Sciences, Gliwice, Poland
Laurence R. Weatherley, University of Kansas Lawrence, United States
Günter Wozny, T.U. Berlin, Germany
Ireneusz Zbiciński, Technical University of Łódź, Poland

Editorial Office

Andrzej K. Biń (Editor-in-Chief)
Barbara Zakrzewska (Technical Editor)
Marek Stelmaszczyk (Language Editor)

Address

ul. Waryńskiego 1
00-645 Warszawa
cpe.czasopisma.pan.pl; degruyter.com/view/j/cpe

Printed in Poland
Print run: 100 copies

Printing/binding:
Centrum Poligrafii Sp. z o.o.
ul. Łopuszańska 53
02-232 Warszawa

THERMAL TREATMENT OF STARCH SLURRY IN COUETTE-TAYLOR FLOW APPARATUS

Robert Hubacz^{*1}, Hayato Masuda^{2,3}, Takafumi Horie³, Naoto Ohmura³

¹Warsaw University of Technology, Faculty of Chemical and Process Engineering, ul. Waryńskiego 1, 00-645 Warszawa, Poland

²University of Shizuoka, School of Food and Nutritional Science, 52-1 Yada, Suruga, Shizuoka 422-8526, Japan

³Kobe University, Graduate School of Engineering, Department of Chemical Science and Engineering, 1-1 Rokkodai, Nada, Kobe 657-8501, Japan

In this paper, thermal processing of starch slurry in a Couette-Taylor flow (CTF) apparatus was investigated. Gelatinized starch dispersion, after treatment in the CTF apparatus, was characterized using such parameters like starch granule diameters (or average diameter), starch granule swelling degree (quantifying the amount of water absorbed by starch granules) and concentration of dissolved starch. These parameters were affected mostly by the process temperature, although the impact of the axial flow or rotor rotation on them was also observed. Moreover, the analysis of results showed a relatively good correlation between these parameters, as well as, between those parameter and apparent viscosity of gelatinized starch dispersion. Meanwhile, the increase in the value of the apparent viscosity and in shear-thinning behaviour of dispersion was associated with the progress of starch processing in the CTF apparatus. Finally, the CTF apparatuses of different geometries were compared using numerical simulation of the process. The results of the simulation indicated that the apparatus scaling-up without increasing the width of the gap between cylinders results in higher mechanical energy consumption per unit of processed starch slurry.

Keywords: starch gelatinization, starch granule swelling, rheological properties, Couette-Taylor flow

1. INTRODUCTION

Starch gelatinization, that occurs when starch slurry is heated, is a complex phase transition, during which starch partly dissolves in water (mostly amylose) and its granules (composed mostly of amylopectine) swell. One of the problems encountered during starch processing is a significant and rapid growth in the apparent viscosity of starch slurry. Additionally, in order to ensure good heat transfer conditions and to avoid separation of the starch from the water phase, an agitation of the slurry is needed (Sakonidou et al., 2003). In such a context, Couette-Taylor flow (CTF) apparatus was proposed for wheat starch processing (Hubacz and Buczyńska, 2011; Hubacz et al., 2013; Masuda et al., 2013). This type of apparatus consists of two cylinders with the inner one (rotor) rotating, while the fluid flows in the gap between these cylinders. When the angular velocity of the rotor exceeds a certain critical value the characteristic secondary fluid flow (Taylor vortices) arises, which intensifies fluid mixing and heat transfer conditions. Moreover, in the case of some non-Newtonian (shear-thinning) fluids the reduction in their apparent viscosity can be expected when rotor rotation increases. Additionally, it is worth pointing out that a CTF apparatus provides good environment for the

*Corresponding authors, e-mail: Robert.Hubacz@pw.edu.pl

intensification of various processes, e.g., multiple emulsion preparation (Dłuska and Markowska-Radomska, 2010), processes involving gas–liquid flows (Dłuska and Hubacz, 2000), mass transfer in bioreactors (Ramezani et al., 2015), crystallization (Mayra and Kim, 2015).

During our previous studies on wheat starch gelatinization in a CTF apparatus (Hubacz and Buczyńska, 2011, Hubacz et al., 2013) the degree of starch gelatinization (*DSG*), starch granule swelling degree (*SGSD*) and apparent viscosity of gelatinized starch were measured experimentally. The *DSG*, which is one of gelatinization indicators, was evaluated using the method of amylose-iodine complex formation proposed by Baks et al. (2007). Meanwhile, in order to measure the value of *SGSD*, a sample of gelatinized starch dispersion was centrifuged and the supernatant was separated from the swollen starch granules. The *SGSD* was defined as the weight of the granules before freeze-drying to their weight after freeze-drying (Hubacz et al., 2013). It can be seen that *SGSD* quantifies the amount of water absorbed by starch granules, and because of that, *SGSD* can be also related to the size increase of these granules during starch slurry thermal treatments.

The linear relationship between *SDSG* and *DSG* was found during starch processing in CTF apparatuses (Hubacz et al., 2013). However, the experiments (Hubacz et al., 2013) showed as well that, even if the gelatinization was completed ($DSG = 1$), starch granule swelling degree continued to change if the heating in a CTF apparatus was prolonged. This was connected to the starch pasting, which follows the gelatinization process (see e.g. Singh et al., 2009). Therefore, it can be said that the monitoring of starch granule swelling allows the monitoring of the progress of starch slurry thermal processing in a CTF apparatus for a wider range of the values of operating parameters than the monitoring of *DSG*. Nevertheless, the increase in the value of *SGSD*, which is not directly connected with the increase in starch granule diameter, may not be a perfect indicator of starch swelling. Moreover, the measurement of *SGSD* can be affected e.g. by the interstitial water in between starch granules, which could be difficult to remove from the sample using a centrifuge (Lagarrigue et al., 2008). Therefore, in order to estimate starch granule swelling during the heating, a starch granule size should be measured directly. Such an approach can be also supported by the fact that starch granule size distribution is one of the important parameters which affect the properties of starch dispersion after its thermal treatment. For example, the rheological properties of the gelatinized starch dispersion depend on that size distribution (Rao et al., 1997). However, gelatinized starch dispersion is a two-phase system, therefore, its properties depend also on the concentration of dissolved starch in the liquid continuous phase in which the starch granules are suspended. It can be said that this dissolved starch is mostly in the form of amylose, because this polymer dissolves readily in water during the heating. Nevertheless, some shorter or less branched molecules of amylopectine can also be possibly found dissolved in the liquid phase after thermal treatment of starch slurry.

In this work, we studied changes in starch granule diameter distribution after the thermal treatment of starch slurry in a CTF apparatus. This was supplemented by the measurement of the concentration of starch dissolved in water during the process. This concentration was expressed by light absorbance (*ABS*) in the liquid phase separated from the gelatinized starch dispersion. Additionally, such properties of starch dispersion like *SGSD* and its apparent viscosity were estimated.

The first objective of this work was the study how size distribution of starch granules and the values of *ABS* or *SGSD* are affected by experimental conditions in the CTF apparatus. The second objective was to find the relation between different parameters (i.e. average starch granule diameter, *ABS*, *SGSD* and apparent viscosity) characterizing the properties of gelatinized starch dispersion. The third objective was to compare (using computer simulation of the process) the performance of the CTF apparatus used for this work with the performance of CTF apparatuses studied in the previous work (Hubacz et al., 2013).

2. MATERIALS AND METHODS

2.1. Starch origin and its properties

During the experiments starch from wheat provided by Wako Pure Chemical Industries, Ltd. (193-13215) was used (12% of moisture contents and 0.2-0.3% of protein). An average concentration of amylose and amylopectine in wheat starch was 25% and 75%, respectively. The starch slurry was prepared in such a way that 1 dm³ of the slurry contained 50g of wheat starch. Therefore, when the moisture content was taken into account mass percentage of starch and water within the slurry was 4.4% and 95.6%, respectively.

The motivations for this work were the problems encountered during cereal malt enzymatic hydrolysis, like high apparent viscosity of the fluid. Wheat starch represents just a simplification of such a system.

2.2. Experimental conditions

Starch was gelatinized in a Couette-Taylor flow (CTF) apparatus used by Masuda et al. (2013) for starch enzymatic hydrolysis (see Fig. 1). The apparatus was equipped with an outer water heat jacket, which was divided into two chambers in order to improve the control of temperature (important in the case of starch hydrolysis). However, during the present study water of the same temperature was pumped into both chambers of the heat jacket. The length of the CTF apparatus used by us was 0.3m, while the radii of the inner and outer cylinder were 0.0125 and 0.0175 m, respectively.

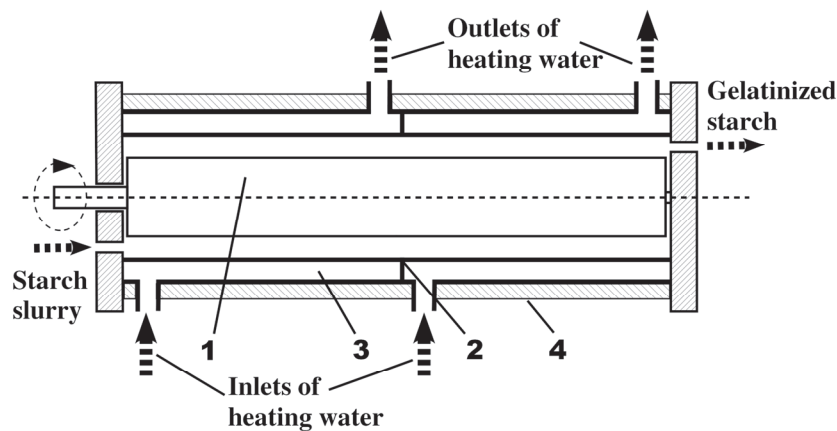


Fig. 1. Sketch of Couette-Taylor flow apparatus;
 1-rotor, 2-outer cylinder, 3-heat jacket, 4- isolation

The conditions of thermal treatment in the CTF apparatus were specified by the rotor angular velocity ω (10.04, 20.09 or 30.13 rad/s), the temperature of water in the heat jacket T_{hj} (65, 70, 85 or 90 °C) and the starch slurry axial velocity u (0.000531 or 0.000743 m/s). The starch slurry axial velocity was defined as:

$$u = Q / \pi(R_2^2 - R_1^2) \quad (1)$$

where Q is the volumetric flow rate of the starch slurry measured at the inlet conditions. Each experiment, specified by the same experimental conditions, was repeated 3 times.

The applied values of the temperature of water in the heat jacket roughly correspond to the gelatinization (about 56 – 65 °C) and pasting temperatures (about 82 °C) of wheat starch (see Sigh et al,

2009). It is also worth underlining that during our study we were interested in the investigation how operating parameters influence starch thermal treatment in a CTF apparatus. Meanwhile, the production of gelatinized starch, which may require even higher temperature from the technological point of view, was less important for us. Moreover, because Patel and Seetharaman (2006) reported problems during the analysis of the pictures of wheat starch granules after their treatment at the temperature above 70 °C, the measurements of starch granule diameter were limited to the experiments carried out at $T_{hj} \leq 70$ °C. A similar approach was applied by other researchers (Malumba et al., 2013 or Patel and Seetharaman, 2006).

2.3. Sample handling

In order to obtain an averaged representation of the starch dispersion after treatment in the CTF apparatus a sample of at least a few ml was taken at the outlet of the apparatus. For this purpose an aluminium vessel (with a thin wall) was used. The outside of the vessel was covered with a layer of ice (1 cm thick), whose temperature was about -5 °C (Hubacz and Buczyńska 2011). The sample taking procedure was a continuous process, during which starch dispersion gathered in the vessel was gently stirred and mixed with a new portion of the dispersion of high temperature. This allowed reduction of the temperature of the sample below the temperature of gelatinization, while keeping this temperature well above 0 °C (around 20 – 25 °C). Subsequently, the sample was analysed within a few minutes.

2.4. Starch granule size measurement

The sample was examined using a digital microscope (VHX-100, Keyence Co., Ltd.), with which the software for image analysis was provided (Particle Analysis Ver. 3.5, Nippon Steel and Sumitomo Metal Technology Co., Ltd.). The microscope observation and picture registration was carried out at ambient temperature (about 25 °C). During the picture analysis, the area occupied by each granule was measured and the diameter of each granule was calculated assuming that the images of the granules can be approximated by circles. The measurement of the area occupied by granule images and the counting of granule numbers were done using a manual mode. This tedious procedure was chosen because some problems with a correct recognition of the granule borders were noticed during automatic working mode of the software. For each experimental condition, the size of 8500 (about 25 pictures) starch granules was measured on average. As a result the granule diameter distribution, mean diameter and standard deviation of granule population were calculated for the given experimental condition.

2.5. Starch solubility and SGSD measurements

To evaluate how much starch dissolved in water during the starch slurry thermal treatment in the CTF apparatus a sample of gelatinized starch was centrifuged at 2000 g for 30 min (to separate solid from liquid phase). The supernatant was 20 times diluted and 1.33 ml of it was mixed with 5 ml of aqueous solution of 0.20% I and 0.66% KI. Subsequently, distilled water was added up to the volume of 20 ml. Finally, the absorbance of the light (wavelength 630 nm) in the sample was measured with a UV-vis spectrophotometer (Shimadzu Co. Ltd.). It was assumed that the value of the light absorbance (ABS) was proportional to the dissolved starch concentration in the supernatant. Although it was believed that dissolved starch was mostly in the form of amylose, some shorter or less branched molecules of amylopectine can be also possibly detected using this method. It is worth remembering that this procedure should not be confused with procedure of DSG measurement (Baks et al. 2007; Hubacz and Buczyńska, 2011), which was also based on the amylose-iodine complex formation. The concentration of amylose (or dissolved starch) in the supernatant was the result of amylose leaching from the starch granules and the water absorption by the granules (i.e. granule swelling). Meanwhile, the DSG

procedure was related only to amylose leaching during gelatinization but did not take into account how much water was absorbed by starch granules during gelatinization.

The value of SGSD was evaluated using the sediment separated from starch dispersion during centrifugation. The wet sediment was weighed, dried in a freeze-dryer (using Eyela Freeze Dryer FD-1000) and once again weighed. The value of SGSD was defined as the weight of the sediment before freeze-drying to its weight after freeze-drying.

2.6. Measurements of starch paste apparent viscosity

The rheological properties of gelatinized starch were measured using a concentric cylinder viscometer (Haake Viscotester 550, Thermo Fisher Scientific Inc.). The sketch of the viscometer was shown in Fig.2. The width of the gaps between cylinders was 350 and 400 μm , which was a few times bigger than the diameter of starch granules in the dispersion (at least in the cases for which the measurement of starch granule diameter was carried out). The measurement of viscosity was conducted at $T = 25\text{ }^\circ\text{C}$, which was approximately the temperature of starch sample after its cooling using the aforementioned procedure. The volume of the sample needed for the measurement was 9 ml. During the measurement the shear rate was changed from 110 to 1999 1/s and subsequently, from 1999 to 100 1/s, while the total duration of the measurement was 406 s.

According to the manual the viscosity range which can be detected using this viscometer was 2 - 2000 Pas. The apparent viscosity of starch dispersion examined in the present study was inside this range. Moreover, the calculation of the rotational Reynolds number for the lowest measured value of apparent viscosity at the highest value of applied shear rate confirmed that the flow in viscometer was laminar without Taylor vortices. However, in the case of gelatinized starch dispersion obtained during the experiments carried out at $T_{hj} \leq 70\text{ }^\circ\text{C}$ the points of the flow curve were rather scattered at low values of shear rate (below approximately 1000 1/s), which suggested high experimental uncertainties at that range of shear rate. Therefore, in the case of such starch dispersion the parameters of the power-law model were estimated only based on the measurement obtained at the values of shear rate higher than about 1000 1/s. On the contrary, in the case of gelatinized starch dispersion obtained during the experiments carried out at $T_{hj} \geq 85\text{ }^\circ\text{C}$ the apparent viscosity was high enough, so that a smooth flow curve could be obtained for the whole range of the shear rate values. Therefore, in the case of such starch dispersion no point forming this flow curve was rejected during the estimation of the parameters of the power-law model.

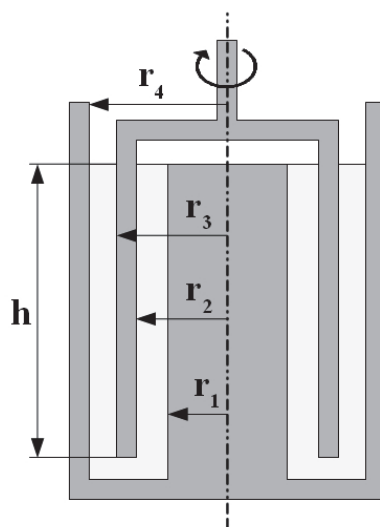


Fig. 2. Sketch of the viscometer geometry;
 $r_4 = 20.5\text{mm}$; $r_3 = 20.1\text{mm}$; $r_2 = 17.85\text{mm}$; $r_1 = 17.5\text{mm}$; $h = 60\text{mm}$

2.7. CFD Simulation

CFD simulation was used in order to compare gelatinization in the studied CTF apparatus with the other two apparatuses studied by Hubacz et al. (2013). The size of the latter apparatuses was defined by the radius of outer cylinder $R_2 = 0.026\text{m}$, the radius of rotor $R_1 = 0.016\text{ m}$ or 0.021 m , and the length $L = 0.3\text{ m}$. This comparison can provide interesting information how to scale-up or intensify the process by changing the geometry of a CTF apparatus. On the other hand, such a comparison through only experimental results could be difficult because numerical simulations provide additional information difficult to obtain through experiments like hydrodynamics of the flow in a CTF apparatus or mechanical power demand for the process. This information is, however, important for the comparison of the apparatus performance.

The hydrodynamics of the flow during starch gelatinization was calculated using steady state Navier-Stokes equations adapted for a 2D axisymmetric swirl model (see Hubacz and Buczyńska, 2011). The 2D axisymmetric swirl model is based on the assumption that there is no circumferential gradient in the flow, although, there may be non-zero circumferential or swirl velocity. In addition to this, energy and species transport equations were solved (see Hubacz and Buczyńska, 2011). These equations were included into the model in order to calculate rheological properties of starch slurry, which was modelled using a power-law equation (see Hubacz et al., 2013):

$$\mu = (0.016DSG + 0.0383)\dot{\gamma}^{-0.35} \quad (2)$$

where, μ is the fluid apparent viscosity and $\dot{\gamma}$ is the shear rate. Nevertheless, it should be remember that Eq. 2 represents rather a simplified approach to the problem, which enables only rough prediction of apparent viscosity of the fluid during the investigated problem.

During the simulation the degree of starch gelatinization was defined using the following equation:

$$DSG = \frac{X_{sg}}{X_{s0}} \quad (3)$$

where X_{sg} is the mass fraction of gelatinized starch, and X_{s0} is the total mass fraction of starch in the slurry. The other fluid properties (density, heat capacity, thermal conductivity, diffusion (dispersion) coefficient were assumed to be constant ($\rho = 998.2\text{ kg/m}^3$, $C_p = 4.182\text{ J/(kg}\cdot\text{K)}$, $\lambda = 0.6\text{ W/(m}\cdot\text{K)}$, $D_j = 10^{-13}\text{ m}^2/\text{s}$). Finally, the kinetics of starch gelatinization was modelled using the first order equation proposed in Brandam et al. (2003).

During the simulation it was assumed, that the temperature of the outer cylinder was between $60\text{ }^\circ\text{C}$ and $85\text{ }^\circ\text{C}$, while the inlet temperature of starch slurry was $20\text{ }^\circ\text{C}$. The axial velocity of starch slurry inside the apparatus was assumed to be between 0.00033 and 0.00099 m/s . Finally, it was assumed that the surface of the rotor was an adiabatic wall (no heat transfer through it) which rotated with the angular velocity ω (between 5.78 and 19.27 rad/s). However, because of a possibility of “back flows” at the outlet from the apparatus, the calculations were carried out for the length of the apparatus which equalled 0.6m . At the location between 0.4 and 0.6 m from the inlet to the apparatus no rotor rotation was imposed. The calculations were conducted assuming that the axial gradients of variables at the outlet plane are zero. No significant influence of the outlet boundary conditions on the results was observed at the distance of 0.3 m from the inlet of the apparatus (it corresponds to the length of the experimental apparatus).

Calculations were carried out using Ansys 14.5 (Fluent) computer code assuming laminar flow due to high apparent viscosity of gelatinized starch. The second order upwind scheme was used to discretize the equations. The pressure-velocity coupling was performed using the SIMPLE scheme. Grids with a cell number 24000 and 96000 were used during the simulations, with no significant deference in the obtained results.

Because the applied rheological model of the fluid is a rather rough approximation of starch slurry properties during its thermal treatments, the model of starch gelatinization described in this chapter represents a rather simplistic approximation of the process. Nevertheless, it enabled judgment how the non-Newtonian properties of the fluid could influence starch gelatinization (Hubacz et al., 2013). Moreover, this model was used for the numerical simulations of starch gelatinization in two concentric CTF apparatuses of different gap width between cylinders (Hubacz et al., 2013). Good agreement between these simulations and the experimental results was achieved. Therefore, it was assumed that this model is good enough for the comparison of CTF apparatuses of different geometries and the preliminary flow hydrodynamics prediction inside of such an apparatus during starch gelatinization.

3. RESULTS

3.1. Starch granule size distribution after treatment in CTF apparatus

The granules of native starch are shown in Fig. 3a, while their size distribution can be seen in Fig. 4. This size distribution was used to calculate the average granule diameter ($D_0 = 20.63 \mu\text{m}$) and standard deviation ($SD_0 = 8.11 \mu\text{m}$) for the native starch granule population.

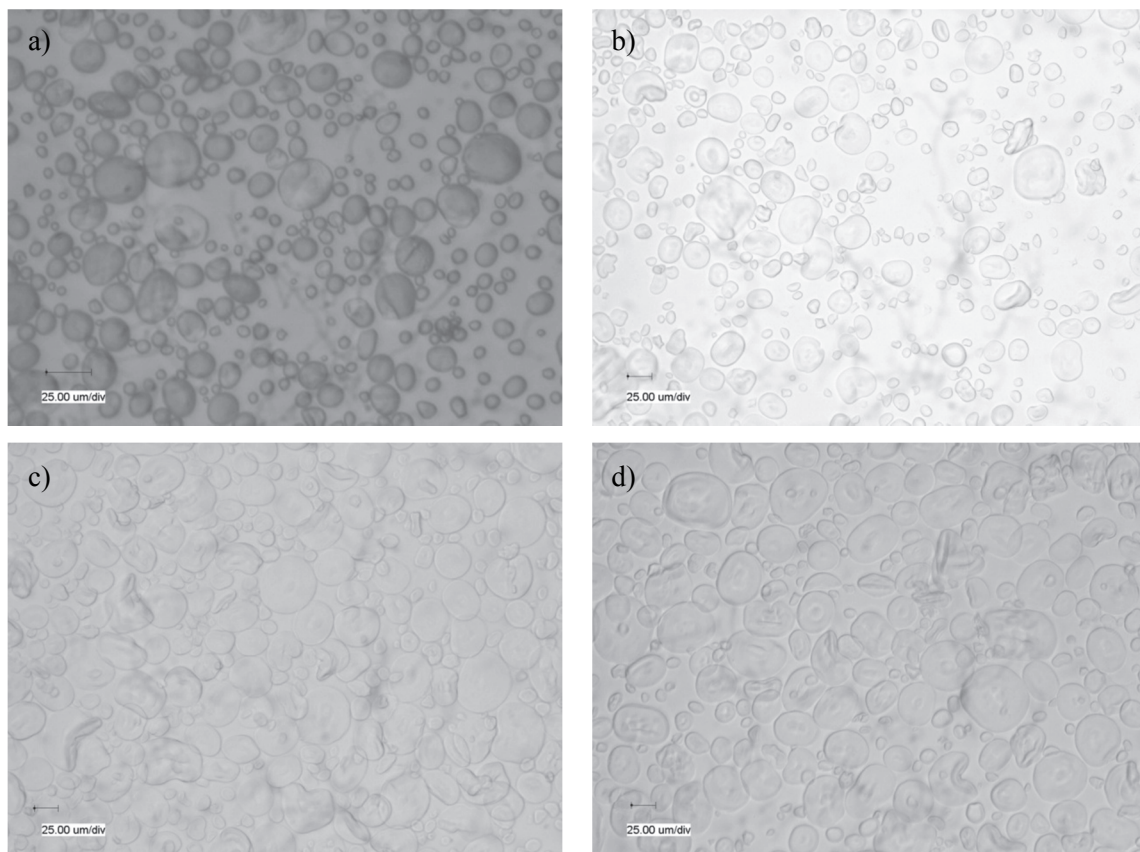


Fig. 3. Native starch (the picture is about 2 times bigger scale than the other pictures); starch granules after treatment in the following conditions: b) $u = 0.000743 \text{ m/s}$, $\omega = 10.04 \text{ rad/s}$, $T_{hj} = 65 \text{ }^\circ\text{C}$, c) $u = 0.000743 \text{ m/s}$, $\omega = 10.04 \text{ rad/s}$, $T_{hj} = 70 \text{ }^\circ\text{C}$, d) $u = 0.000531 \text{ m/s}$, $\omega = 20.09 \text{ rad/s}$, $T_{hj} = 70 \text{ }^\circ\text{C}$ (from Hubacz et al. 2016)

The examples of starch granule appearance after their treatment in the CTF apparatus at different conditions are shown in Figs. 3b-d (the scale of these pictures is about 2 times smaller than the scale of the picture in Fig. 3a), while the examples of granule size distributions of gelatinized starch are

presented in Fig.4. In addition to this, the values of the average granule diameters of gelatinized starch (D) and corresponding standard deviations (SD) are given in Table 1. Both the pictures in Fig. 3 and the data from Table 1 indicate a significant increase in starch granule diameters after its thermal treatment. Similarly, the value of standard deviation of granule population increased after the processing in the CTF apparatus. This agreed with other authors' observation, that gelatinization causes an increase in granule diameter and standard deviation (see e.g. Rao et al., 1997).

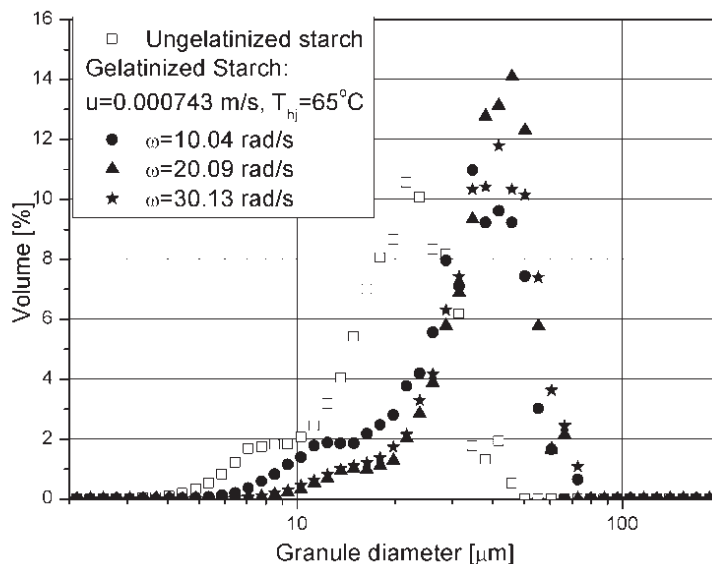


Fig. 4. Distribution of starch granule diameter after treatment in CTF apparatus (from Hubacz et al. 20016)

Table 1. Average starch granule diameter (D) and standard deviation of granule size distribution (SD) after treatment in CTF apparatus (for ungelatinized starch $D_0 = 20.63\mu\text{m}$ and $SD_0 = 8.11\mu\text{m}$) (from Hubacz et al., 2016)

ω rad/s	u m/s	T_{hj} °C	D μm	SD μm
10.04	0.000743	65.0	32.94	13.08
20.09	0.000743	65.0	38.86	11.64
30.13	0.000743	65.0	38.82	13.11
10.04	0.000743	70.0	42.18	15.32
20.09	0.000743	70.0	43.57	14.93
30.13	0.000743	70.0	45.36	14.97
10.04	0.000531	70.0	42.26	14.77
20.09	0.000531	70.0	45.61	14.44

The impact of the operating parameters on D and SD during the treatment in the CTF apparatus is illustrated in Table 1. The values of D and SD were significantly affected only by T_{hj} : higher gelatinization temperature results in higher values of both parameters. On the other hand, the influence of u and ω on D or SD was significantly less pronounced. Therefore, in order to verify whether or not the impact of u and ω on starch granule size distribution can be neglected the Kolmogorov-Smirnov test was done. This test relies on finding the biggest difference between cumulative distribution functions of two compared populations. In this case there are just two populations of starch granule diameters (D_i) obtained at different experimental conditions. Those populations are characterized by cumulative distribution functions (respectively $F_{n_1}(D_i)$ and $F_{n_2}(D_i)$) and by the number of granules in each population (respectively n_1 and n_2). The results of the test are shown in Table 2.

In the last column of Table 2 there are shown values of a parameter which is a product of two other parameters defined by the equations:

$$n = \sqrt{\frac{n_1 n_2}{n_1 + n_2}} \quad (4)$$

$$\delta_{n_1, n_2} = \sup_{D_i} |F_{n_1}(D_i) - F_{n_2}(D_i)| \quad (5)$$

where, δ_{n_1, n_2} is the biggest difference between the cumulative distribution functions of two compared populations of starch granule diameters. In the first five rows of Table 2 there are shown comparisons of granule diameter distributions obtained at different values of ω but with the same values of other operating parameters. Meanwhile, rows 6 and 7 are the comparisons of granule diameter distributions obtained at different values of u but with the same values of other operating parameters. When assuming the value of statistical significance at the level of 0.05, two population of granules are characterized by the same diameter distribution if $n \cdot \delta_{n_1, n_2} < 1.36$ (see e.g. Hellwig, 1998). Nevertheless, in all the cases presented in Table 2 this condition is not fulfilled. Therefore, it can be stated that the impact of the values of ω and u on the distribution of starch granule diameter after a treatment in the CTF apparatus cannot be neglected: the average diameter of gelatinized starch granules increased when the axial velocity decreased and when the rotor angular velocity increased.

Table 2. The results of Kolmogorov-Smirnov Test

No.	Granule population 1			Granule population 2			$n \cdot \delta_{n_1, n_2}$
	ω rad/s	u m/s	T_{hj} °C	ω rad/s	u m/s	T_{hj} °C	
1	10.04	0.000743	65.0	20.09	0.000743	65.0	16.31
2	30.13	0.000743	65.0	20.09	0.000743	65.0	3.06
3	10.04	0.000743	70.0	20.09	0.000743	70.0	2.23
4	30.13	0.000743	70.0	20.09	0.000743	70.0	2.61
5	10.04	0.000531	70.0	20.09	0.000531	70.0	7.92
6	10.04	0.000743	70.0	10.04	0.000531	70.0	2.53
7	20.09	0.000743	70.0	20.09	0.000531	70.0	4.8

The significant increase in D (it can be seen especially in the case of $T_{hj} = 65$ °C) when the value of ω was changed from 10.04 to 20.09 rad/s may suggest that the transition to the Taylor vortex flow in the CTF apparatus (in the investigated system) occurs at a value of ω lower than 20.09 rad/s but higher than 10.04 rad/s. This hypothesis stems from the fact that the transition to the vortex flow pattern denotes the intensification of heat transfer in the apparatus. This statement was verified using computer simulations of starch gelatinization in the CTF apparatus, which revealed that the Taylor vortex flow pattern had been gradually developed with increasing value of ω . At $\omega = 10.04$ rad/s the computations indicated laminar flow without vortices along the whole length of the apparatus. At $\omega = 12.04$ rad/s, only a vortex pair occurred close to the apparatus inlet, but in the farther part of the apparatus it disappeared due to the increase in the fluid apparent viscosity. At $\omega = 15$ rad/s the vortex pattern could be seen along the significant part of the apparatus. However, only when $u = 0.000743$ m/s and $T_{hj} = 65$ °C the increasing viscosity did not suppress the Taylor vortices up to the distance of about 0.3 m from the inlet (corresponding to the length of the experimental apparatus). Finally, when the calculations were conducted at $\omega = 17.5$ rad/s the vortex flow pattern was developed along the whole length of the apparatus independently of the values of u and T_{hj} . To summarize, the results of the simulations seem to support the hypothesis that the transition to the Taylor vortex flow could occur for the value of ω between 10.04 and 20.09 rad/s. Nevertheless, the results of the computer simulations

should be considered with caution, because the model of the process used for the simulations was rather simplified.

3.2. Properties of gelatinized paste

In Table 3 there are shown the values of starch granule swelling degree of gelatinized starch dispersion after treatment in the CTF apparatus. For the same experimental conditions the concentrations of starch dissolved in water were also estimated. The starch concentration was expressed by the value of light absorbance (*ABS* – see also Table 3) in a sample prepared using the water separated from the granules of the gelatinized starch (procedure described above): a higher value of *ABS* denoted higher concentration of dissolved amylose.

Table 3. Starch granule swelling degree and light absorbance by the continuous phase of starch dispersion

u m/s	ω rad/s	T_{hj} °C	SGSD	ABS
0.000743	10.04	65	5.27	0.064
0.000743	20.09	65	5.16	0.082
0.000743	30.13	65	5.18	0.086
0.000743	10.04	70	6.00	0.110
0.000743	20.09	70	6.03	0.127
0.000743	30.13	70	6.10	0.134
0.000531	10.04	70	6.13	0.139
0.000531	20.09	70	6.07	0.156
0.000531	30.13	70	6.14	0.152
0.000531	10.04	85	8.02	0.336
0.000531	20.09	85	8.06	0.339
0.000531	30.13	85	8.23	0.346
0.000531	10.04	90	9.04	0.485
0.000531	20.09	90	9.40	0.529
0.000531	30.13	90	9.63	0.565

The value of *ABS* depended on the values of operating parameters in the same manner like in the case of *D* (Tables 1 and 3). Temperature in the heat jacket affected light absorbance in the most significant way: the increase in temperature caused the growth in the value of *ABS*. The value of *ABS* also grew when angular velocity of rotor increased and axial velocity decreased. This observation suggested that the correlation between *ABS* and *D* can be found. Moreover, similarly like in the case of *D* a significant increase in the value of *ABS* was observed when the value of ω was changed from 10.04 to 20.09 rad/s. This seems to confirm the suggestion that the transition to the Taylor vortex flow in the CTF apparatus (in the investigated system) occurs at a value of ω lower than 20.09 rad/s but higher than 10.04 rad/s.

On the contrary, a similar impact of operating parameters on *SDSG* like in the case of *ABS* and *D* could be seen only for experiments carried out at $T_{hj} \geq 85^\circ\text{C}$ (see Table 3). When the heat jacket temperature was smaller the impact of this temperature on *SGSD* was still significant, but the changes in ω or u seemed to have little influence on *SGSD* (Table 3). One of the possible explanations of those observations could be the fact that different phenomena dominate the process at $T_{hj} \leq 70^\circ\text{C}$ and at $T_{hj} \geq 85^\circ\text{C}$. When the experiments were carried out at $T_{hj} \leq 70^\circ\text{C}$ the early stage of starch slurry processing probably preponderated during the treatment in the CTF apparatus. Such an early stage of starch processing denoted that gelatinization of starch was not completed and water absorption by

starch granules was accompanied by e.g. amylose leaching. Therefore, the weight gain of starch granules caused by water absorption, which can be measured by *SGSD*, could be reduced to some extent by amylose leaching from the granules. Meanwhile, both amylose leaching and water absorption favored the increase in dissolved starch concentration (represented by *ABS*) in the continuous water phase in which starch granules were suspended. On the contrary, at $T_{hj} \geq 85$ °C gelatinization can be completed ($DSG = 1$) even for higher values of starch slurry axial flow and values of ω lower than those investigated here (see Hubacz et al., 2013 and Masuda et al., 2013). When gelatinization is completed a pasting process starts and water absorption by starch granules (i.e. granule swelling) dominates that process. Under such conditions starch granule swelling, water absorption and the increase in the concentration of dissolved starch should be related with each other.

Nevertheless, in the case of experiments conducted at $T_{hj} \leq 70$ °C D increased when ω increased, while the value of *SGSD* did not seem to depend very significantly on the rotor angular velocity. This suggested that starch granule swelling (represented by the changes in D) was independent from water absorption by these granules (represented by *SGSD*) at that range of process temperature. This in turn is difficult to understand. Therefore, the weak impact of u and ω on *SGSD* at $T_{hj} \leq 70$ °C could just result from the *SGSD* measurement procedure. For example the impact of the interstitial water in between starch granules (which could be difficult to remove from the sample using a centrifuge) on the value of *SGSD* could be more significant when $T_{hj} \leq 70$ °C than when $T_{hj} \geq 85$ °C. This stemmed from the fact that the amount of water absorbed by the granules was lower at the lower value of temperature.

Furthermore, the impact of ω on *SGSD* seemed to be different than that observed in the case of our previous studies (Hubacz et al., 2013). The results from Hubacz et al. (2013) revealed an increase in *SGSD* with increasing ω for $\omega < 11.56$ rad/s and a reversed tendency for $\omega > 11.56$ rad/s. Meanwhile, in the present experiments the impact of ω on *SGSD* was difficult to evaluate for $T_{hj} \leq 70$ °C, while for $T_{hj} \geq 85$ °C the increase in *SGSD* with the increasing ω (without changing the tendency) was observed. The reason of this discrepancy cannot be easily found using the available experimental data, because the CTF apparatuses used by Hubacz et al. (2013) were bigger than that the one used in our experiment. This means that the transitions between flow regimes occur at the higher ω in the case of the apparatus used for the present study than in the case of the apparatuses used previously (Hubacz et al., 2013). Therefore, a similar impact of ω on granule swelling could be observed if the present experiments were carried out for the wider range of ω than it was done so far.

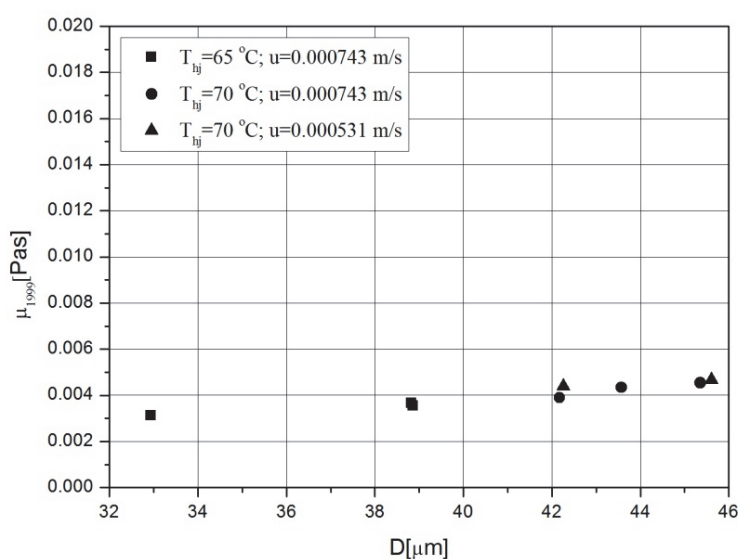


Fig. 5. Dependence of μ_{1999} on average starch granule diameter, μ_{1999} apparent viscosity of gelatinized starch paste at the maximum shear rate (1999 1/s)

The dependences of starch dispersion apparent viscosity measured at the highest value of shear rate (1999 1/s) on D , $SDSG$ and ABS are shown in Figs. 5 - 7. The correlations between these parameters and μ_{1999} are relatively good. This agreed with the results presented in Hubacz et al. (2013), in which good correlation of gelatinized starch apparent viscosity with $SGSD$ was observed. Moreover, this seems to confirm that the values of D , $SDSG$ or ABS convey similar information on the state of gelatinized starch paste. Nevertheless, when only experimental results obtained at $T_{hj} \leq 70^\circ\text{C}$ were analysed the correlation between μ_{1999} and $SGSD$ was a little worse. This (as aforementioned) is probably connected with the fact that $SGSD$ did not depend significantly on the rotor angular velocity when the experiments were conducted at $T_{hj} \leq 70^\circ\text{C}$.

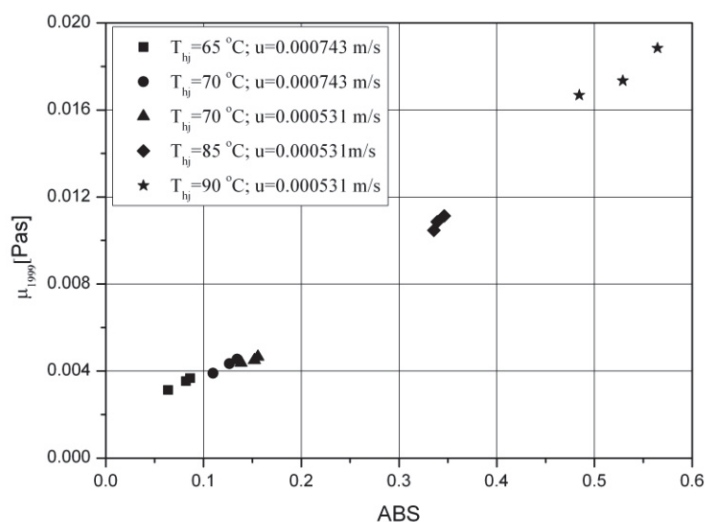


Fig. 6. Dependence of μ_{1999} on ABS - μ_{1999} apparent viscosity of gelatinized starch paste at the maximum shear rate (1999 1/s)

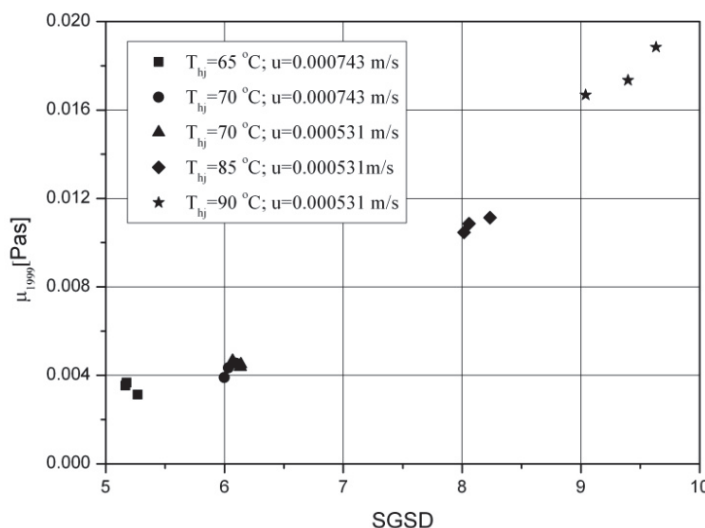


Fig. 7. Dependence of μ_{1999} on $SGSD$ - μ_{1999} apparent viscosity of gelatinized starch paste at the maximum shear rate 1999 1/s)

In Fig. 8 there are shown the examples how apparent viscosity of gelatinized starch dispersion depends on the value of shear rate. The results of viscosity measurement suggested that gelatinized starch dispersions obtained during our experiments were shear-thinning fluid of thixotropic properties.

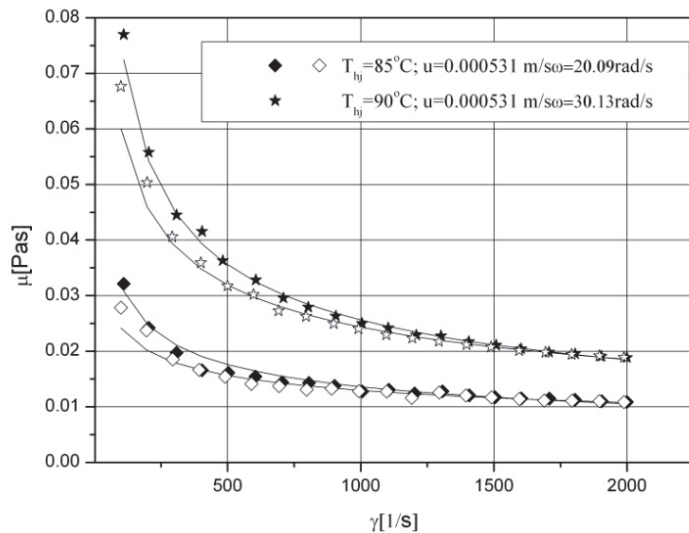


Fig. 8. Apparent viscosity of gelatinized starch as a function of shear rate: black points denote ascending segment of shear cycle, while white points denote descending segment of shear cycle, while lines are the approximation of the results using the power law model

Additionally, the rheological properties of gelatinized starch were approximated using a power law equation. The consistency coefficient (k) and flow behaviour index (n) were calculated for the ascending and descending segments of shear cycle. A relatively good correlation of these parameters with the values of ABS is shown in Figs. 9 and 10.

It confirms the results from our previous work (Hubacz et al. 2016), where a good correlation of the power law parameters with ABS was obtained for starch dispersions after their processing in the CTF apparatus at $T_{hj} \geq 85 \text{ }^\circ\text{C}$, but at the different than now values of u and ω . The data in Fig. 10 also confirmed the literature observation (Rao et al., 1997) that the shear-tinning properties of starch dispersion increase with the progress of starch thermal processing.

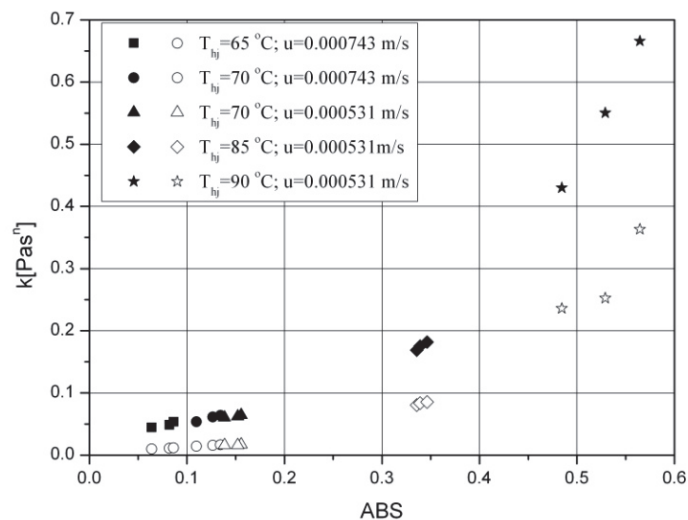


Fig. 9. Consistency coefficient as a function of ABS : black points denote ascending segment of shear cycle, while white points denote descending segment of shear cycle

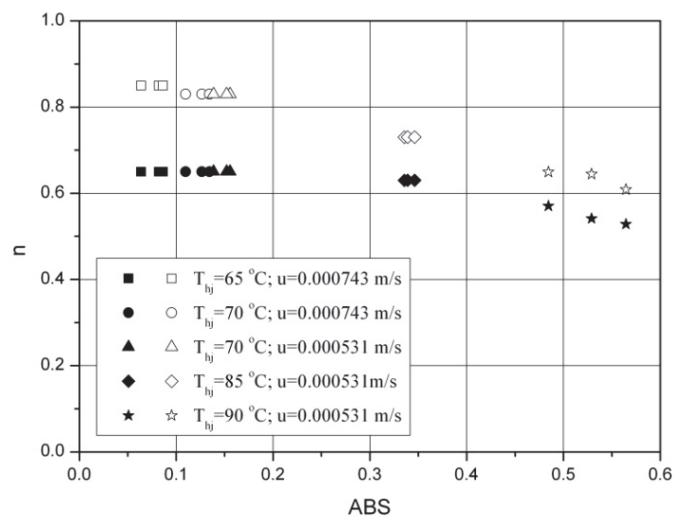


Fig. 10. Flow behaviour index as a function of *ABS*: black points denote ascending segment of shear cycle, while white points denote descending segment of shear cycle

3.3. Comparison of CTF apparatuses of different geometries

The reason for the computer simulation of starch gelatinization in the CTF apparatus investigated in this work (apparatus I) was the comparison with other two CTF apparatuses (apparatus II and apparatus III) investigated by Hubacz et al. (2013). Because, the volumes of apparatuses II and III were bigger than the volume of apparatus I this comparison should provide interesting information concerning scaling-up of the process.

In Table 4, there are shown the values of degree of starch gelatinization (DSG) calculated during numerical simulation of the process in CTF apparatuses at different values of operating parameters. Additionally, the amount of the mechanical energy connected with the rotor rotation was provided in Table 4. In order to compare the results obtained for three different geometries of the apparatus this energy was calculated using the following equation (Hubacz et al., 2013):

$$E = \frac{\omega R_1 \iint \tau_{r,\theta} dA}{u\pi(R_2^2 - R_1^2)} \quad (6)$$

where E denotes the amount of the mechanical energy (connected with the rotor rotation) needed for the production of a volume unit of the gelatinized starch, $\tau_{r,\theta}$ is the angular component of shear stress tensor at the rotor surface calculated from the numerical simulations, dA is the differential surface of the rotor. In order to correctly understand the obtained results it should be also mentioned that the applied model of the process predicted Taylor vortex flow for $\omega \leq 11.56$ rad/s in the case of apparatus II and III (Hubacz et al., 2013). Meanwhile, in the cases of apparatus I the model predicted Taylor vortex flow only for $\omega = 19.27$ rad/s. This arises from the fact that the CTF apparatus used in this work was the smallest one (see Table 4). According to the results in Table 4 the degree of starch gelatinization obtained in the case of apparatus I and apparatus II were similar. However, the energy needed for the process was significantly bigger in apparatus II. This means that the increase in the apparatus size while keeping the same value of gap width is not really profitable. On the contrary, the significant reduction in the value of E was obtained when apparatus III with the bigger gap width was used. Although most of the values of DSG was smallest in the case of apparatus III, the additional profit of this apparatus could be the occurrence of Taylor vortices at the lower value of ω than in the case of apparatus I (see the value of DSG for $\omega = 11.56$ rad/s, $u = 0.00099$ m/s and $T_{hj} = 65^\circ\text{C}$ in Table 4).

Table 4. Results of computer simulation of starch gelatinization in a CTF apparatus

ω rad/s	u m/s	T_{hj} °C	Apparatus I $R_1 = 0.0125\text{m}; d = 0.005\text{m}$		Apparatus II* $R_1 = 0.021\text{m}; d = 0.005\text{m}$		Apparatus III* $R_1 = 0.016\text{m}; d = 0.01\text{m}$	
			DSG	E [J/m ³]	DSG	E [J/m ³]	DSG	E [J/m ³]
5.78	0.00099	65	0.55	1373.48	0.55	3007.5	0.19	640.98
11.56	0.00099	65	0.56	4330.62	0.76	11543.54	0.65	3135.3
19.27	0.00099	65	0.70	13615.52	0.72	42446.3	0.66	9483.98
19.27	0.00099	60	0.40	13154.69	0.46	40834.57	0.35	9028.39
5.78	0.00099	85	0.99	1556.66	0.99	3392.72	0.44	675.36
11.56	0.00099	85	0.99	4904.24	1	11611.91	0.99	3397.07
19.27	0.00099	85	1.00	14226.22	1	44845.26	0.99	10143.86

* results from Hubacz et al. (2013)

4. CONCLUSIONS

The granule size distribution in gelatinized starch dispersion was more strongly influenced by the processing temperature than by other operating parameters. An increase in the heat jacket temperature caused an increase in the values of D and SD . However, the average granule diameter of gelatinized starch also increased when the axial flow was reduced or the rotor rotation velocity increased. The concentration of dissolved starch and starch granule swelling degree depended on the operating parameters in a similar way. However, the changes in ω or u seemed to have little influence on $SGSD$ when the starch processing was conducted at $T_{hj} \leq 70^\circ\text{C}$. This was attributed to different phenomena, which may dominate the process at the lower and at the higher temperature. Nevertheless, the problems with the separation of water, which was not absorbed by starch granules during the processing, from these granule could also affect the value of $SGSD$ especially in the case of the low value of the processing temperature. This can be the second reason why the changes in ω or u did not affect the value of $SGSD$ significantly at $T_{hj} \leq 70^\circ\text{C}$.

The significant increase in the value of D and ABS when ω was changed from 10.04 to 20.09 could be related to the transition from laminar to Taylor vortex flow pattern inside the apparatus. This conclusion was also supported by numerical simulation of the process.

The gelatinized starch dispersion obtained after treatment in the CTF apparatus consisted of shear-thinning fluids of thixotropic properties. Moreover, a good correlation of starch dispersion apparent viscosity with ABS , $SGSD$ or D was observed. Meanwhile, the increase in the value of the apparent viscosity and in shear-thinning behaviour of dispersion was associated with the progress of starch processing in the CTF apparatus.

Finally, simulation results of starch processing in CTF apparatuses indicated that the apparatus scaling-up without increasing the width of the gap between cylinders results in higher mechanical energy consumption per unit of processed starch slurry.

SYMBOLS

ABS	light absorbance
C_p	specific heat capacity, J/(kg·K)
D	average starch granule diameter, μm

D_i	starch granule diameter associated with i -range of this diameter values, μm
D_j	diffusion (dispersion) coefficient of species j , m^2/s
DSG	degree of starch gelatinization
$F_{nk}(D_i)$	cumulative distribution function of granule number in k th granule population
h	height of the zone in viscometer where a sample was sheared, mm
k	consistency coefficient, Pas^n
n	flow behavior index
n_k	number of starch granules in k th granule population, respectively
Q	volumetric flow rate of the starch slurry measured at the inlet conditions, m^3/s
r_1, r_2, r_3, r_4	radii of viscometer cylinders, mm
R_1, R_2	radii of rotor and outer cylinder, respectively, m
SD	standard deviation of granule size distribution, μm
$SGSD$	starch grain swelling degree
T	temperature, $^\circ\text{C}$
u	superficial velocity of starch slurry inside the apparatus, m/s
X	mass fraction
X_{s0}	the total mass fraction of starch in the slurry
X_{sg}	the mass fraction of gelatinized starch

Greek symbols

$\delta_{n1,n2}$	the biggest difference between the cumulative distribution functions of two compared populations of starch granule diameters
μ	the fluid apparent viscosity, Pas
ω	rotor angular velocity, rad/s

Subscripts

hj	heat jacket
i	range of granule diameter values
j	species
k	population of starch granules
sg	starch gelatinized
$s0$ or 0	starch before gelatinization

REFERENCES

- Baks T., Ngene I.S., Van Soest J.J.G., Janssen A.E.M., Boom R.M., 2007. Comparison of methods to determine the degree of gelatinisation for both high and low starch concentrations. *Carbohydr. Polym.*, 67, 481–490. DOI: 10.1016/j.carbpol.2006.06.016.
- Brandam C., Meyer X. M., Proth J., Strehaiano P., Pinguad H., 2003. A original kinetic model for the enzymatic hydrolysis of starch during mashing. *Biochem. Eng. J.*, 13, 43-52. DOI: 10.1016/S1369-703X(02)00100-6.
- Dłuska E., Markowska-Radomska A., 2010. Regimes of multiple emulsions of W-1/O/W-2 and O-1/W/O-2 type in the continuous Couette-Taylor flow contactor. *Chem. Eng. Technol.*, 33, 113-120. DOI: 10.1002/ceat.200900278.
- Dłuska E., Hubacz R., 2000. Mass transfer in the two-phase helicoidal contactor. *Inż. Chem. Proces.*, 21, 1, 103-113.
- Hellwig Z., 1998. *Elementy rachunku prawdopodobieństwa i statystyki matematycznej*. 13th edition, WNT, Warszawa.
- Hubacz R., Buczyńska M., 2011. Starch gelatinisation in Couette-Taylor flow apparatus. *Chem. Process Eng.*, 32, 267-279. DOI: 10.2478/v10176-011-0021-7.
- Hubacz R., Ohmura N., Dłuska E., 2013. Intensification of starch processing using apparatus with Couette–Taylor flow. *J. Food Process Eng.*, 36, 6, 774-785. DOI: 10.1111/jfpe.12046.

- Hubacz R., Masuda H., Horie T., Ohmura N., 2016. Starch granules swelling during gelatinization in Couette-Taylor flow apparatus. *Proceedings of the 22nd of Chemical and Process Engineering*. Spółka, Poland, 5-9 September 2016, 435-444.
- Lagarrigue S., Alvarez G., Cuvelier G., Flick D., 2008. Swelling kinetics of waxy maize and maize starches at high temperatures and heating rates. *Carbohydr. Polym.*, 73, 148-155. DOI: 10.1016/j.carbpol.2007.11.018.
- Malumba P., Jacquet N., Delimme G., Lefebvre F., Bera F., 2013. The swelling behaviour of wheat starch granules during isothermal and non-isothermal treatments. *J. Food Eng.*, 114, 199-206. DOI: 10.1016/j.jfoodeng.2012.08.010.
- Mayra Q.-P., Kim W.-S., 2015. Agglomeration of Ni-Rich hydroxide in reaction crystallization: Effect of Taylor vortex dimension and intensity. *Cryst. Growth Des.*, 15, 1726-1734. DOI: 10.1021/cg501727v.
- Masuda H., Horie T., Hubacz R., Ohmura N., 2013. Process intensification of continuous starch hydrolysis with a Taylor-Couette flow reactor. *Chem. Eng. Res. Des.*, 91, 11, 2259-2264. DOI: 10.1016/j.cherd.2013.08.026.
- Patel B. K., Seetharaman K., 2006. Effect of heating rate on starch granule morphology and size. *Carbohydr. Polym.*, 65, 381-385. DOI: 10.1016/j.carbpol.2006.01.028.
- Ramezani M., Kong B., Gao X., Olsen M.G., Vigil R.D., 2015. Experimental measurement of oxygen mass transfer and bubble size distribution in an air-water multiphase Taylor-Couette vortex bioreactor. *Chem. Eng. J.*, 279, 286-296. DOI: 10.1016/j.cej.2015.05.007.
- Rao M.A., Okechukwu P.E., Da Silva P.M.S., Oliveira J.C., 1997. Rheological behaviour of heated starch dispersions in excess water: role of starch granule. *Carbohydr. Polym.*, 33, 273-283. DOI: 10.1016/S0144-8617(97)00025-8.
- Sakonidou E.P., Karapantsios T.D., Raphaelides S.N., 2003. Mass transfer limitations during starch gelatinization. *Carbohydr. Polym.*, 53, 53-61. DOI: 10.1016/S0144-8617(03)00010-9.
- Singh N., Singh S., Isono, N., Noda T., Singh A. M., 2009. Diversity in amylopectin structure, thermal and pasting properties of starches from wheat varieties/lines. *Int. J. Bio Macromol.* 45, 298-304. DOI: 10.1016/j.ijbiomac.2009.06.005.

Received 19 October 2016

Received in revised form 22 May 2017

Accepted 25 June 2017

PYROLYSIS OF WASTE TYRES – THE EFFECT OF REACTION KINETICS ON THE RESULTS OF THERMOGRAVIMETRIC ANALYSIS

Robert Cherbański^{*1}, Krzysztof Wróblewski², Eugeniusz Molga¹

¹Warsaw University of Technology, Faculty of Chemical and Process Engineering, ul. Waryńskiego 1, Warsaw, Poland

²CONTEC Ltd., ul. Książęca 17/1B, Warsaw, Poland

This paper presents a systematic thermogravimetric (TG) study on the kinetics of end-of-life tyre (ELT) pyrolysis. In the experimental part of this work, TG results are compared for tyre samples of different mass and size. This shows that the conduction resistance in the milligram scale (up to ~100 mg) tyre sample can be neglected. A comparison of experimental results demonstrates that the characteristic maxima on the DTG curve (the first derivative of TG signal) shift towards higher temperatures for higher heating rates. This phenomenon is explained to have kinetic origin and it is not caused by the internal heat transfer resistance. In the modelling part of this work, the kinetic parameters of the Three-Component Simulation Model (TCSM) are calculated and compared to the literature values. Testing of the kinetic model is carried out using experiments with a varying heating rate. This shows the limitation of the simplified kinetic approach and the appropriate selection method of the kinetic parameters.

Keywords: TGA, pyrolysis, end-of-life tyres, kinetics, TCSM

1. INTRODUCTION

Approximately 3.6 million tonnes of used tyres were generated in Europe in 2013 (ETRMA, 2015). In general, used tyres can be divided into two groups: part-worn tyres and end-of-life tyres (ELTs). While part-worn tyres can be reused after retreading, end-of-life tyres can not be used on vehicles any more.

ELTs are classified as non-hazardous waste (Council Directive 91/156/EEC). However, potential hazards were identified for ELTs when landfilled. They mainly include landfill fires with emissions of toxic gases and leaching into water. Therefore, the direct disposal of ELTs in landfills is banned in Europe (Council Directive 1999/31/EC). Instead, the two following recovery routes of ELTs exist: material recovery and energy recovery.

Since ELTs have a similar calorific value as a high quality coal, they are used as a substitute to fossil fuels. The cement sector is the main application for energy recovery where ELTs are co-incinerated in cement kilns. Concerning material recovery ELTs are used in different civil engineering applications (e.g.: a foundation for roads and railways, coastal protection, insulation) and product applications (e.g.: children's playgrounds, sport fields, artificial turf). Tyre pyrolysis is an alternative to the above mentioned methods but for some technical and economic reasons it is applied at a limited scale in Europe. Pyrolysis is the thermal degradation of organic compounds which is carried out in the absence of oxygen. Therefore, the emissions of NO_x and SO_x are lower for pyrolysis of tyres when compared to incineration. Three fractions of the product are obtained from pyrolysis: solid (char), liquid (oil) and gaseous (gas). Typical yield of the char is in the range of 38 - 40 wt.% (Williams, 2013). Selling prices

*Corresponding authors, e-mail: Robert.Cherbanski@pw.edu.pl

of such a primary product are rather low and subsequent physical or chemical activation of the char is needed to obtain the secondary product of relatively high market value. The non-condensable gas and pyrolysis oil can be directly used to heat the pyrolysis reactor. On the other hand, improvement of the economics is possible when you consider separation of the oil into valuable chemical compounds. It follows from different analyses that pyrolysis oil contains significant concentrations of chemical compounds such as benzene, toluene, xylenes, styrene and limonene. Separation of these species can give the secondary products of relatively high market value (Williams, 2013).

Thermogravimetric analysis (TGA) is a well established method of thermal analysis. The measuring principle is based on an accurate measurement of sample weight as a function of temperature or time in a strictly defined and controlled environment. Analysis results are usually presented as a TG curve representing the relative sample mass and a DTG curve (the corresponding first derivative of the TG signal) representing the process rate. TGA is widely used in research of all types of organic and inorganic solids and liquids, especially to determine their thermal stability, thermal degradation kinetics or catalysts activity.

TGA is also used to investigate the kinetics of ELT pyrolysis. Frequently, kinetic modeling relies on deconvolution of the DTG curve and determination of kinetic parameters for individual components. This approach was applied in two different kinetic models proposed by Leung and Wang (Leung and Wang, 1999): Three-Component Simulation Model (TCSM) and Three-Elastomer Simulation Model (TESM). The TCSM assumes that the kinetics of ELT pyrolysis can be modeled using three major components which decompose independently. Such compounds as oil, plasticizer, moisture and other specific additives are treated as the first component. The other two components are natural rubber (NR) and styrene-butadiene rubber (SBR) or polybutadiene rubber (BR) depending on the mixture used for the tyre production. The TESM assumes that the kinetics of ELTs pyrolysis can be modeled using the three elastomers NR, SBR and BR together with their respective oil components (six components in total). Many researchers (Al-Salem et al., 2009; Galvagno et al., 2007; González et al., 2001; Lah et al., 2013; Mui et al., 2010; Seidelt et al., 2006; Quek and Balasubramanian, 2009) have dealt with the kinetic modeling of ELTs pyrolysis after Leung and Wang (1999). The details can be found in an excellent review by Quek and Balasubramanian (2012).

A lot of effort has been taken to better understand the complex reaction mechanism for ELTs pyrolysis (Al-Salem et al., 2009; Chen et al., 2001; Islam et al., 2009). However, most of the papers have been devoted to simplified kinetic models (Quek and Balasubramanian, 2012). Indeed, they are frequently used for practical reasons. For instance, the CFD modelling of pyrolysis reactors requires reliable and computationally cheap kinetic models (Rudniak and Machniewski, 2016). This gap can be filled by simplified approaches which assume three, four or five major components. Mui et al. performed calculations for three, four and five components showing the best fit for the five-component model (Mui et al., 2008). More recently, Lah et al. developed a model acknowledging reaction kinetics and the internal heat transfer resistance during ELTs pyrolysis (Lah et al., 2013). The model was based on the individual consideration of four major compounds: volatiles, NR, BR and SBR. Moreover, influence of three different fabrics and wire on the reaction kinetics was considered.

This paper presents a systematic TGA study on the kinetics of ELTs pyrolysis. The original contribution of this work is that it explains the origin of the observed phenomenon of shifting the local maxima on DTG curves in the direction of higher temperatures for higher heating rates. The phenomenon is explained on the basis of reaction kinetics rather than the internal heat transfer resistance. Moreover, the kinetic model is verified with experiments of varying heating rates. The testing shows the limitation of the simplified kinetic approach and the appropriate selection method of the kinetic parameters.

2. EXPERIMENTAL

All experiments were performed in a thermobalance TG 209 F1 Libra (Netzsch, Germany) equipped with a micro furnace and a precise ultra-microbalance. The micro furnace is made of high-performance ceramics. Its maximum temperature is 1100 K and heating rates are in the range of 0.001 - 200 K/min. The ultra-microbalance under thermostatic control provides resolution of 0.1 μg .

The conditions of all performed measurements are shown in Table 1.

Table 1. Conditions of the performed measurements

No.	m (mg)	Stage	T_0 (K)	β (K/min)	T_f (K)	$t_{isotherm.}$ (min)	\dot{V} (ml/min)
1	24.17	I	300	50	1073	20	40
2	92.66	I		50			
3	35.15	I		20			
4	25.89	I		10			
5	86.84	I		10			
6	23.45	I		1			
7	25.47	I		1			
8	50.91	I	300	12.7	672	-	40
		II	672	3.33	773	4	
9	14.9	I	300	21.24	659	-	40
		II	659	5.63	873	4	
10	18.75	I	300	200	573	-	40
		II	573	50	653	60	

The samples for measurements No. 1-7 were cut from the same piece of car tyre tread with a size of 5 cm \times 3 cm using a punch having an internal diameter of 2.5 mm for smaller samples (measurements No. 1, 3-4, 6-7) or 5.0 mm for larger samples (measurements No. 2 and 5). Such standardization provided similar masses and sizes of the samples within each of the two groups. Minor differences between the samples followed from the deformation of the rubber at the moment of cutting. The samples for the measurements No. 8-10 were not standardized and had an irregular shape.

The measurements No. 1-7 were carried out at a constant heating rate β up to the final temperature $T_f=1073$ K at which the samples were held for 20 minutes. In the measurements No. 8-10 heating of the samples was conducted in two stages at two different heating rates. At the end of the measurements the samples were held at a constant temperature for a specified time (for details see Table 1). The measurements No. 8-10 were used for validation of the kinetic model.

Figure 1 shows a typical course of ELT pyrolysis in a form of the TG and DTG curves. While the TG curve represents the relative sample mass during pyrolysis, the DTG curve (the corresponding first derivative of the TG curve) displays the pyrolysis rate. There are two measurements shown in Fig. 1 (No. 6 and 7). They were carried out at the same heating rate, $\beta=1$ K/min. A comparison of the DTG curves demonstrates very high accuracy and repeatability of the measurements. From the modeling point of view, there are also three characteristic maxima indicated on the DTG curves. They correspond to three stages of the process.

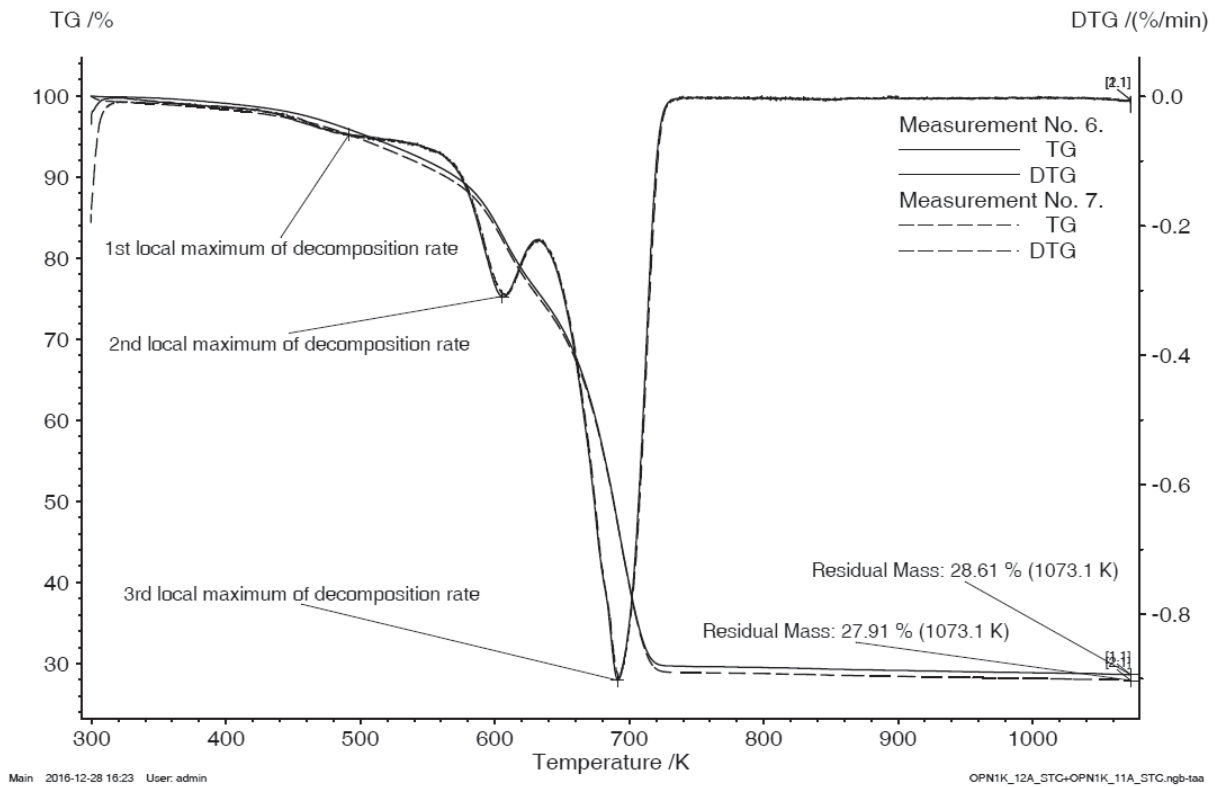


Fig. 1. Comparison of the measurements for heating rate $\beta = 1$ K/min: TG - relative sample mass, DTG - rate of relative mass loss

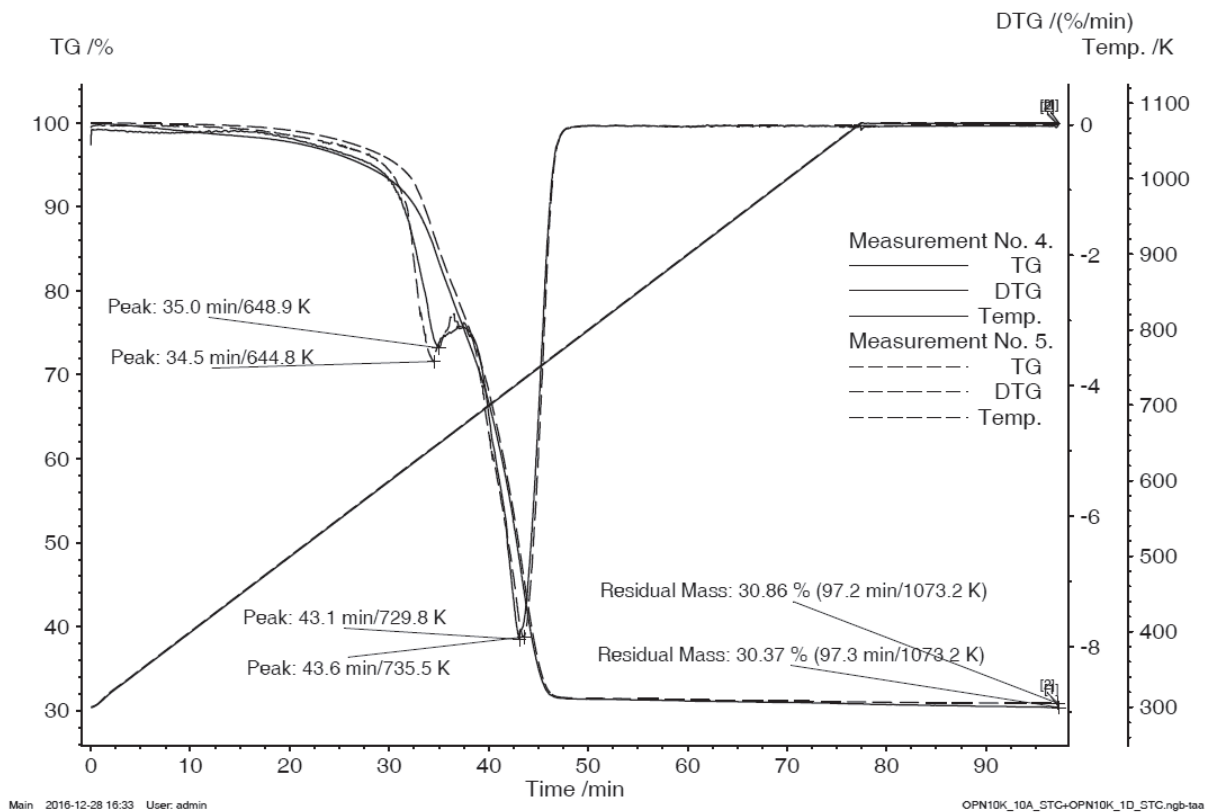


Fig. 2. Comparison of the measurements for heating rate $\beta = 10$ K/min: TG – relative sample mass, DTG - rate of relative mass loss, Temp. – temperature

The results of two samples with different mass and size (No. 4 and 5) are presented in Fig. 2. The measurements were carried out at the same constant heating rate, $\beta = 10$ K/min. A comparison of the DTG curves reveals that the differences in the thermal decomposition rates are quite small and consist in a slight shift of maxima on the curves. For the larger of the tested samples (No. 5), the first maximum appears 30 seconds before the corresponding maximum for the smaller sample (No. 4) (34.5 min. / 644.8 K compared to 35.0 min. / 648.9 K). On the other hand, the second maximum appears 30 seconds later than the corresponding maximum for the smaller sample (43.6 min. / 735.5 K compared to 43.1 min. / 729.8 K). These shifts have the opposite direction, which is probably related to small differences in compositions of the tested samples. This is reflected in the final masses of these samples at the end of pyrolysis (30.86 % compared to 30.37 %).

Similar conclusions can be drawn from a comparison of the DTG curves obtained at the higher heating rate $\beta = 50$ K/min (Fig. 3). Although both of the compared samples differ significantly in mass and size (No. 1 and 2), the maxima appear at almost identical temperatures. Finally, based on the results shown in Figs. 2 and 3, it can be stated that the conduction resistance did not play a significant role in the milligram scale pyrolysis and it may be omitted from further analysis. Leung and Wang concluded the same on the basis of their experimental results with a granular scrap tyre in four sizes: 1.18 - 2.36 (8 - 16 mesh), 1.0 - 1.18 (16 mesh), 0.5 - 0.6 (30 mesh) and 0.355 - 0.425 mm (40 mesh) (Leung and Wang, 1999). Note that their biggest tyre samples had similar dimensions to our samples from measurements No. 1, 3 - 4, 6 - 7. Similarly, Gonzalez et al. demonstrated that the pyrolysis rate was not affected by the intraparticle and interparticle heat transfer resistances for the particle sizes up to 1.6 mm and the tyre sample masses in the range of 10 - 100 mg, respectively (González et al., 2001). In contradiction with the above findings Lah et al. stated that the internal heat transfer resistance was significant in the tested rubber samples with masses of 7 - 21 mg (Lah et al., 2013). This was deduced from the dynamic TG and DSC runs which present the characteristic shift of the mass loss rate and the generated heat of reaction towards higher temperatures for higher heating rates. Also, Olazar et al. (2005) stated that the heat and mass transfer limitations were significant for tyre particle size between 1.0 and 4.0 mm. This was deduced from the comparison of the kinetic parameters calculated for two particle size ranges (between 0.1 and 0.8 mm and between 0.8 and 4.0 mm) in the range of temperatures between 450 and 600 °C. The kinetic parameters were determined by fitting a first-order rate equation to the experimental results which were obtained from experiments in the conical spouted bed reactor. As follows from the above quoted findings they are clearly contradictory. However, supporting our results, it can be noted that the first two conclusions were drawn directly from the TG measurements with varying sample masses and dimensions while the other findings were deduced indirectly.

Figure 4 shows a comparison of the results obtained for heating rates, β , in the range of $\beta = 1 - 50$ K/min. It can be observed from the DTG curves that the process is more rapid when the heating rate increases. Moreover, it is clearly visible that the characteristic maxima of thermal degradation shift towards higher temperatures. This phenomenon has kinetic origin taking into account that the internal heat transfer resistance can be neglected. This aspect will be discussed in the further part of this work.

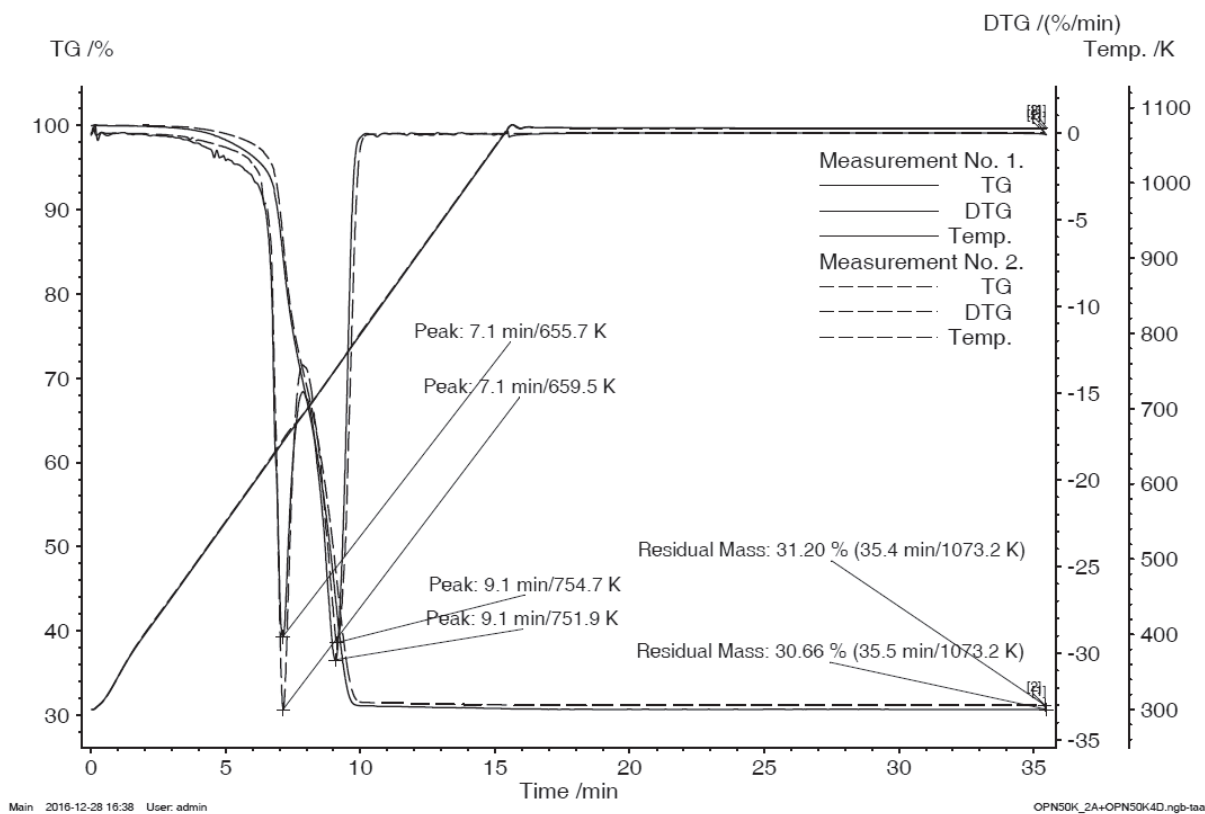


Fig. 3. Comparison of the measurements for heating rate $\beta = 50$ K/min: TG – relative sample mass, DTG - rate of relative mass loss, Temp. – temperature

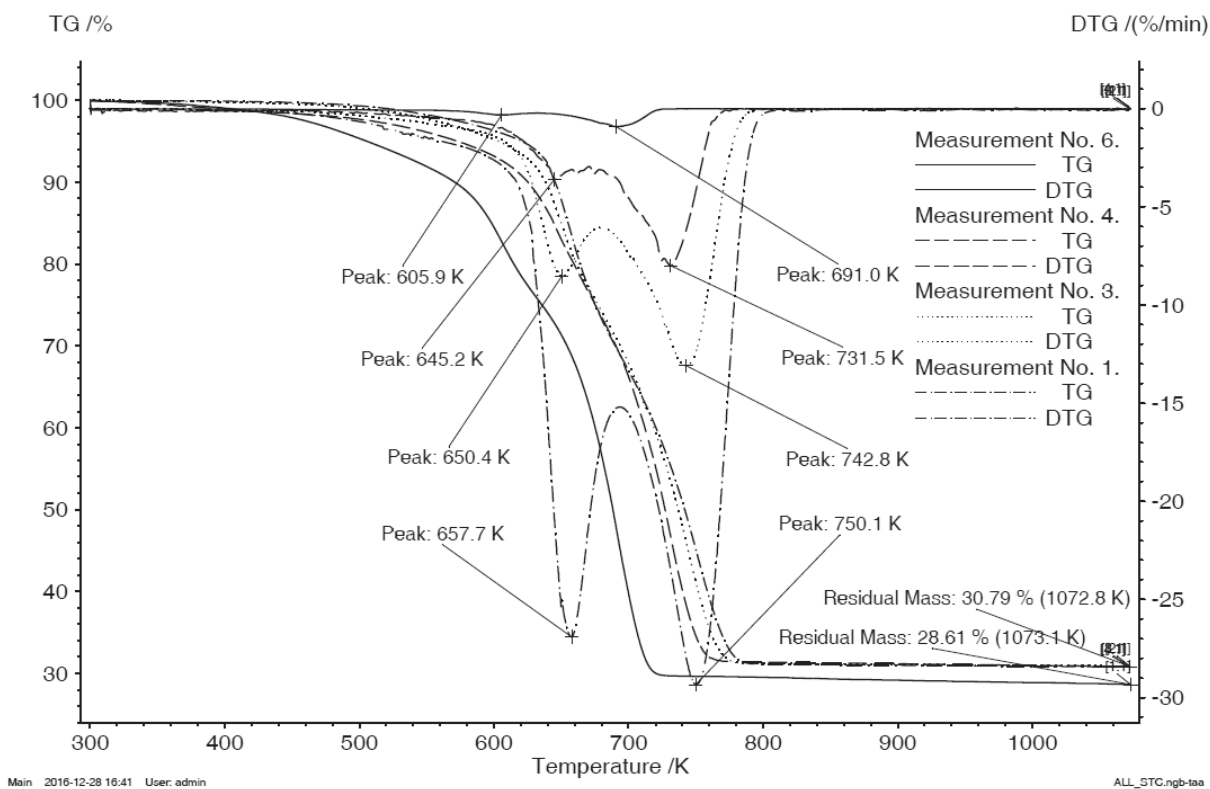


Fig. 4. Comparison of the measurements for different heating rates: TG – relative sample mass, DTG - rate of relative mass loss

3. CALCULATIONS

In kinetic modeling of ELT pyrolysis the TCSM was used (Galvagno et al., 2007; Leung and Wang, 1999). This model is based on two key assumptions: (1) car tyres consist of three major components, (2) thermal decomposition of each component takes place independently. Kinetics of the thermal decomposition of the major components is usually modeled as a first- or n -order reaction. In this work first-order kinetics was assumed. Therefore, the rate of reaction can be described by the following set of equations:

$$\frac{d\alpha}{dt} = \sum_{i=1}^3 z_i \frac{d\alpha_i}{dt} \quad (1)$$

and

$$\frac{d\alpha_i}{dt} = A_i e^{-E_i/RT} (1 - \alpha_i) \quad (2)$$

where the conversion of the tyre sample, α is calculated as follows

$$\alpha = \frac{(m_0 - m)}{(m_0 - m_\infty)} \quad (3)$$

Because the heating rate was constant in the performed experiments, $\beta = dT / dt = \text{const.}$, e.q. (1) can be transformed into an equivalent form (4)

$$\frac{d\alpha}{dT} = \frac{1}{\beta} \sum_{i=1}^3 z_i \frac{d\alpha_i}{dt} = \sum_{i=1}^3 z_i \frac{d\alpha_i}{dT} \quad (4)$$

Firstly, to calculate the kinetic parameters the composite function, $d\alpha / dT$ was deconvoluted into three individual thermal decomposition functions describing each of the modeled compounds (Fig. 5). This calculation step was necessary to determine the temperature ranges for the conversions of the three major components. In general, many different peak functions can be used, i.e.: various versions of Gaussian, asymmetric double sigmoidal or log-normal. In this work each thermal decomposition step was modeled using the particular case of extreme function (the Gumbel probability density function distribution) shown below (Galvagno et al., 2007).

$$\frac{d\alpha}{dT} = \sum_{i=1}^3 (\varepsilon_i \exp(-\exp(-\delta_i) - \delta_i + 1)) \quad (5)$$

where $\delta_i = (T - T_{c,i}) / \omega_{c,i}$ (since the function offset is 0 for the considered case, it is ruled out from this equation).

The Levenberg-Marquardt algorithm was used to compute the following 9 parameters ($i = 1, 2, 3$): ε_i , $T_{c,i}$ and $\omega_{c,i}$. The calculations consisted in minimizing the sum of squared deviations between the experimental and calculated reaction rates (with Eq. 5), $d\alpha / dT$. Figure 5 shows a comparison of the calculated curve to the experimental one. There are also the thermal decomposition curves for the three major components shown in Figure 5.

The values of z_i , denoting the contribution of the i -th reaction to the total mass loss, were obtained after integration of the individual decomposition rates giving: $z_1 = 0.0528$, $z_2 = 0.294$ and $z_3 = 0.653$ (see Fig. 6).

Finally, the pre-exponential factor, A_i , and the activation energy, E_i , were calculated for each major component. The calculations were carried out using the Levenberg-Marquardt algorithm. The aim of the calculations was to minimize the sum of squared deviations between the individual decomposition

rates obtained from deconvolution of the composite function and that calculated from the kinetic model (see Fig. 7).

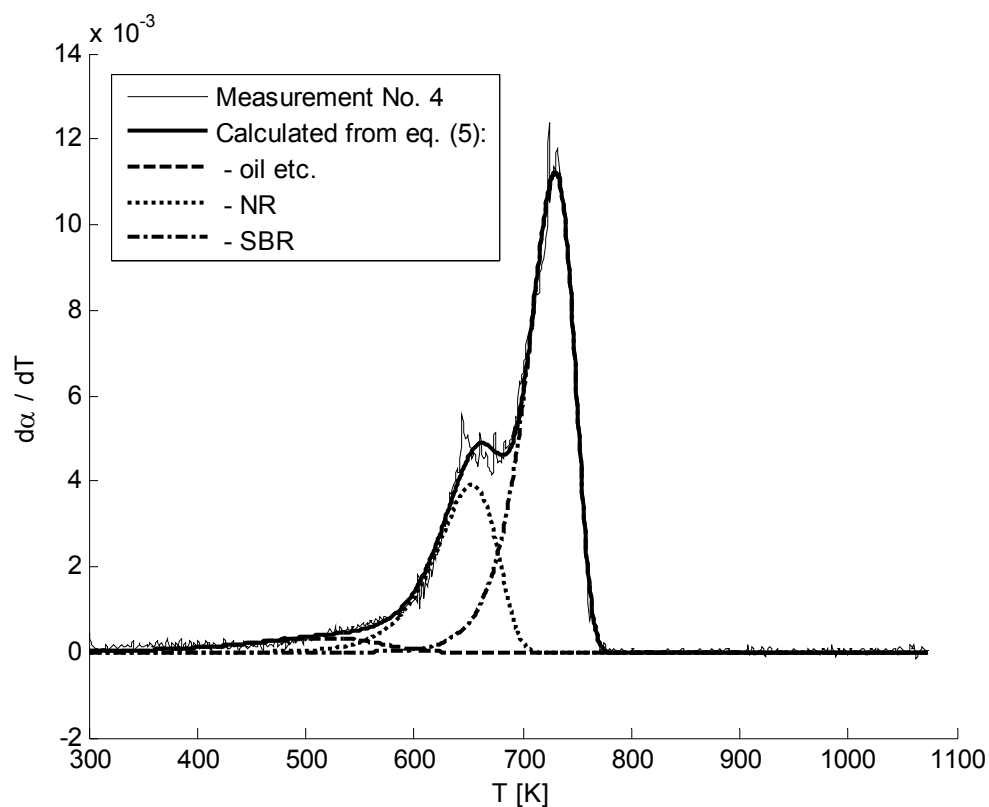


Fig. 5. Comparison of the pyrolysis rate curves: calculated from Eq. (5) and experimental (measurement No. 4), and the decomposition rate curves for three major components (oil etc., NR, SBR)

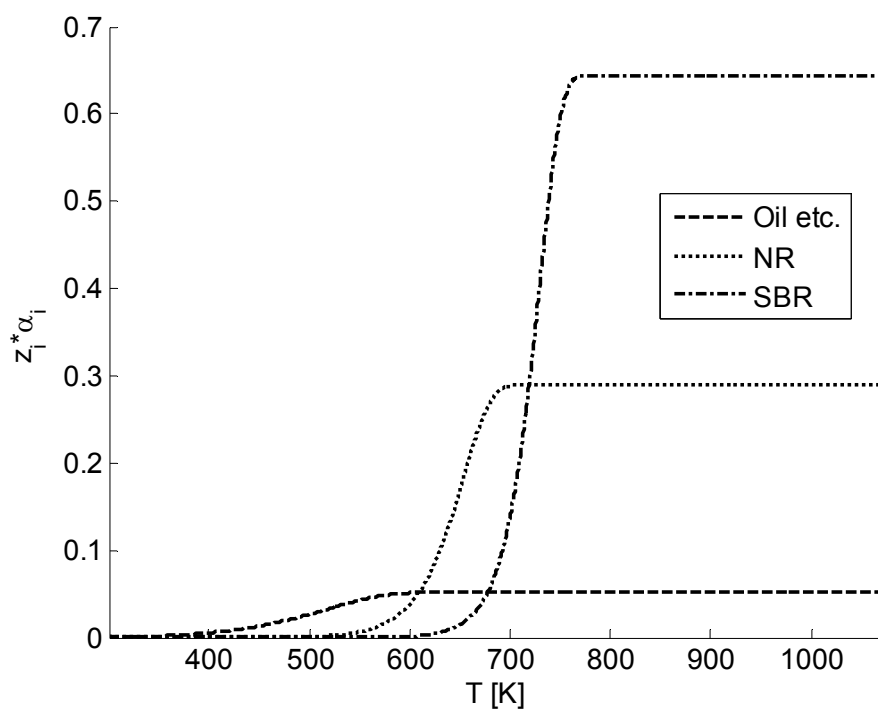


Fig. 6. The integral curves of the decomposition rates for the three major components (oil etc., NR, SBR)

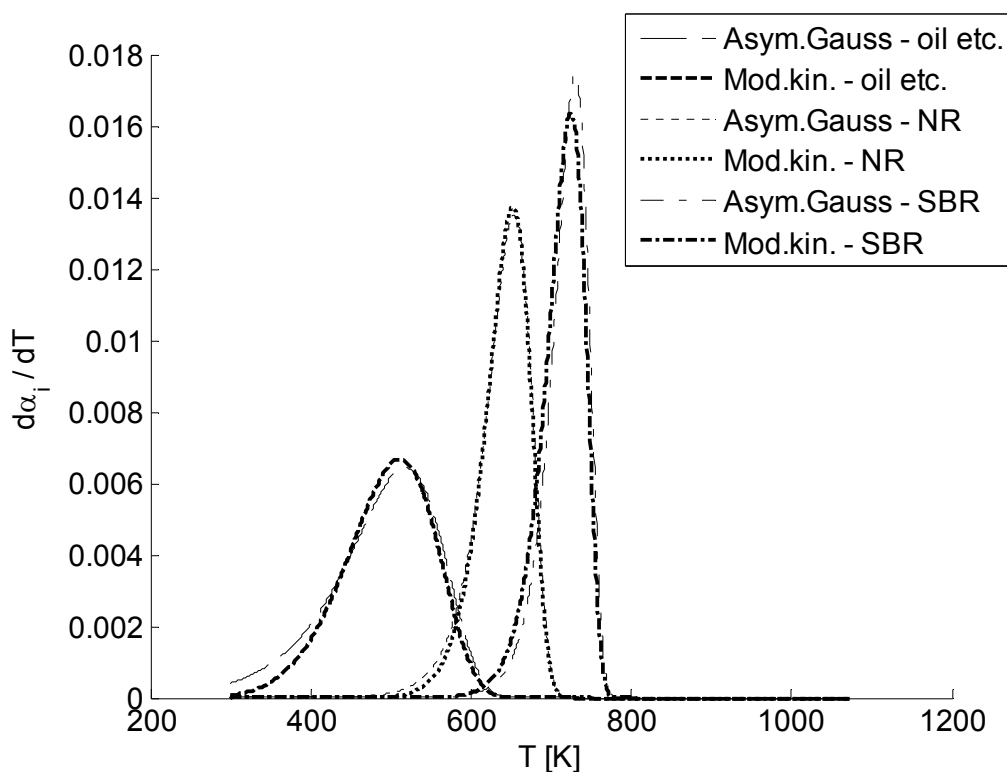


Fig. 7. Comparison of the individual decomposition rates obtained from deconvolution of the composite function and the calculated from the kinetic model

The values of the calculated kinetic parameters are shown in Table 2.

Table 2. Comparison of calculated and literature values of the kinetic parameters

Component	Heating rate	Kinetic parameters		Ref.
	β (K/min)	A (1/min)	E (kJ/mol)	
1. Oil etc.	10	3.8×10^2	33.1	This work
		2.0×10^4	52.5	(Leung and Wang, 1999)
		5.0×10^2	50.3	(Mui et al., 2010)
		9.34×10^2	38.7	(Kim et al., 1995)
		1.00×10^5	66.8	(González et al., 2001)
2. NR		3.1×10^9	124.1	This work
		6.3×10^{13}	164.5	(Leung and Wang, 1999)
		1.9×10^7	102.8	(Mui et al., 2010)
		3.78×10^{16}	209.0	(Kim et al., 1995)
		3.00×10^4	44.8	(González et al., 2001)
3. SBR/BR	1.6×10^{11}	161.6	This work	
	2.3×10^9	136.1	(Leung and Wang, 1999)	
	1.13×10^{17}	237.1	(Mui et al., 2010)	
	8.75×10^8	127.3	(Kim et al., 1995)	
	7.56×10^2	32.9	(González et al., 2001)	

Note that there is no relationship between the parameters of the auxiliary model presented in Eq. (5) and the kinetic parameters presented in Table 2. As noted earlier, the auxiliary model (5) was only needed to deconvolute the composite function $d\alpha/dT$ obtained from TGA. Significant differences in the values of kinetic parameters can be seen in Table 2. This possibly results from different composition of the tyres used in these individual experiments. To some extent, this effect was also visible in our measurements. This is indicated by the residual mass after pyrolysis which varies in successive experiments (see Fig. 4). Although the reported differences are not very pronounced, one should note that the samples for the analysis were taken from the same piece of tyre with a size of 5 cm \times 3 cm. In the case of different brands and/or pieces of tyres this effect can be naturally enhanced. The kinetic parameters calculated in this work for NR and SBR/BR are in the range of reported values by other authors. On the other hand, the parameters obtained for the first component (oil etc.) are beyond the range. However, given that this modeling component comprises not only the processing oil but also plasticizer, moisture and other specific additives, the values of its kinetic parameters depend on the composition of the tyre and the initial moisture content, which can vary for different tyre samples.

The conversion vs. temperature curve was obtained by integration of the kinetic model. Figure 8 shows a comparison of the calculated and experimental profiles for measurement no. 4. A quite accurate prediction is observed. This is because the kinetic parameters were determined from the same measurement. More validation cases are presented in Figs. 10 - 13.

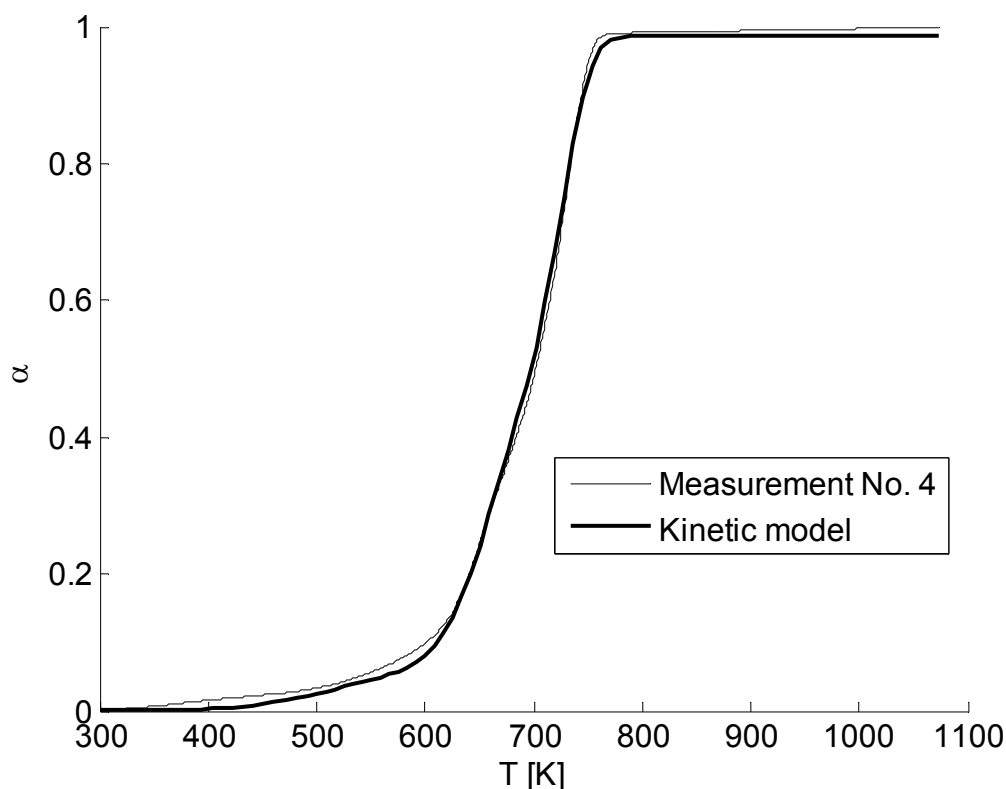


Fig. 8. Comparison of the conversion curves: calculated from the kinetic model and experimental (measurement No. 4)

Figure 9 shows the results of integration of the kinetic model for different heating rates in the range of 1 - 50 K/min. The temperatures corresponding to the conversion of 0.5 are also indicated in Figure 9 for each of the calculated curves.

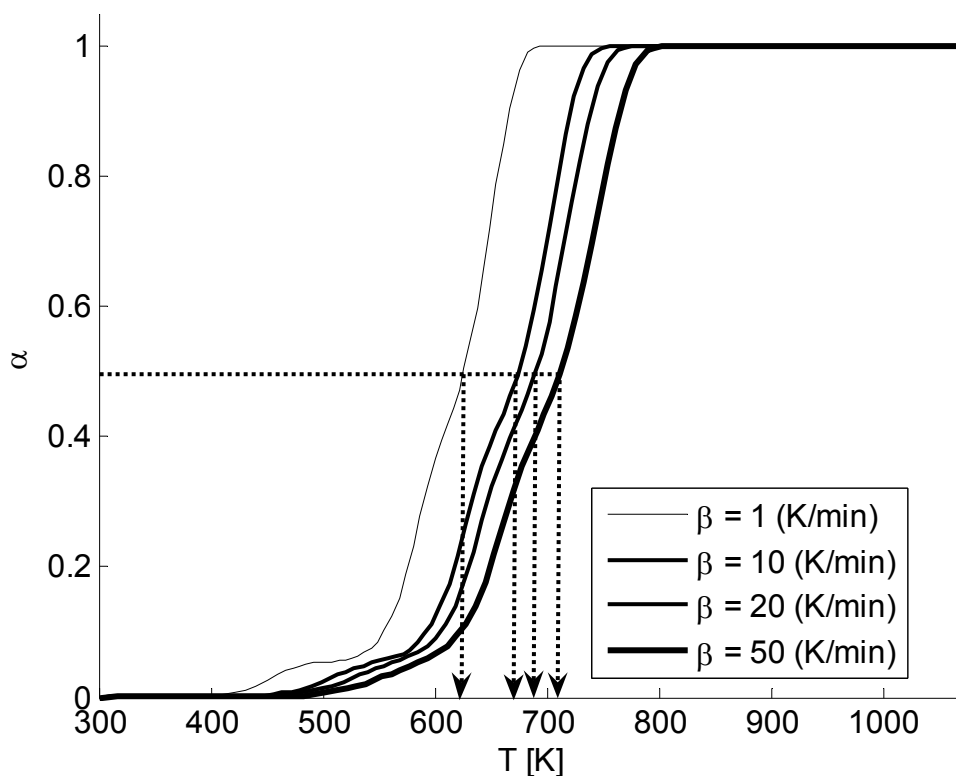


Fig. 9. Effect of heating rate, β , on the conversion curves, α , as predicted by the kinetic model

The most remarkable result to emerge from the data is that the calculated results explain the phenomenon of shifting the characteristic maxima on the DTG curve in the direction of higher temperatures for higher heating rates. The phenomenon is observed in this work (see Fig. 4) and many previous publications (Galvano et al., 2007; González et al., 2001; Lah et al., 2013; Leung and Wang, 1999; Mui et al., 2010; Seidelt et al., 2006). Intuitively, this can be related to the internal heat transfer resistance. But given that the conduction resistance is negligible in the tested milligram samples, as shown in the previous part of this work, it is evident that the phenomenon is caused by the kinetics itself. Thus, this effect is caused by the different residence times of the samples in the varying temperature (sample history). As can be seen from the experimental results in Fig. 4 and from the modeling results in Fig. 9, the tested milligram tyre sample needs longer time when the heating rate is higher to reach a certain level of conversion.

Testing of the kinetic model was carried out using the experiments No. 8 - 10 (see Table 1). As mentioned earlier these experiments were performed for variable heating rates. A comparison of the experimental and calculated results is shown in Figs. 10 - 12.

The kinetic model predicts the first two experiments correctly (Figs. 10 and 11). On the other hand, the quality of prediction for the third experiment is worse with a maximum error of 20% (Fig. 12). A comparison of the conditions under which these experiments were conducted showed that the experiment No. 10 was performed at the highest heating rates (1st stage $\beta = 200$ K/min / 2nd stage $\beta = 50$ K/min). Therefore, another test was conducted, in which the same kinetic model was used. However, this time, the kinetic parameters were determined from the measurement No. 1 in which the heating rate was $\beta = 50$ K/min. Then, the kinetic model was tested again by comparison of the calculated results to the experimental results. This time, it turned out that the model predicted the experiment very well (Fig. 13).

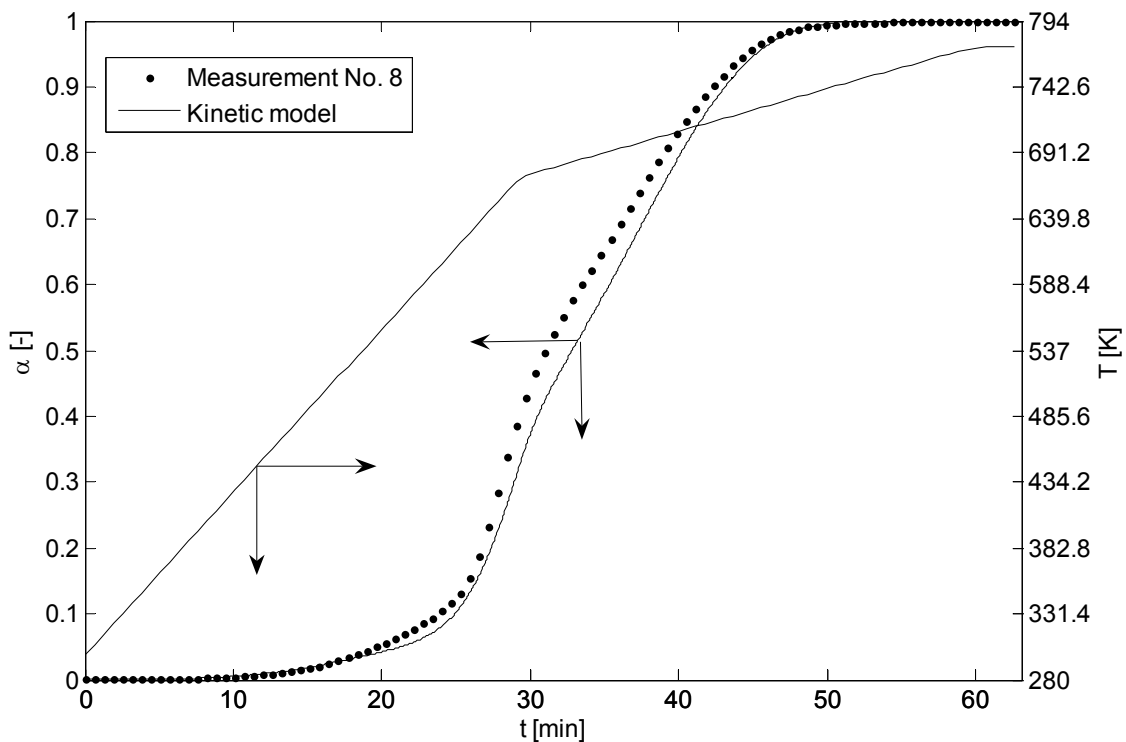


Fig. 10. Testing of the kinetic model based on measurement No. 8

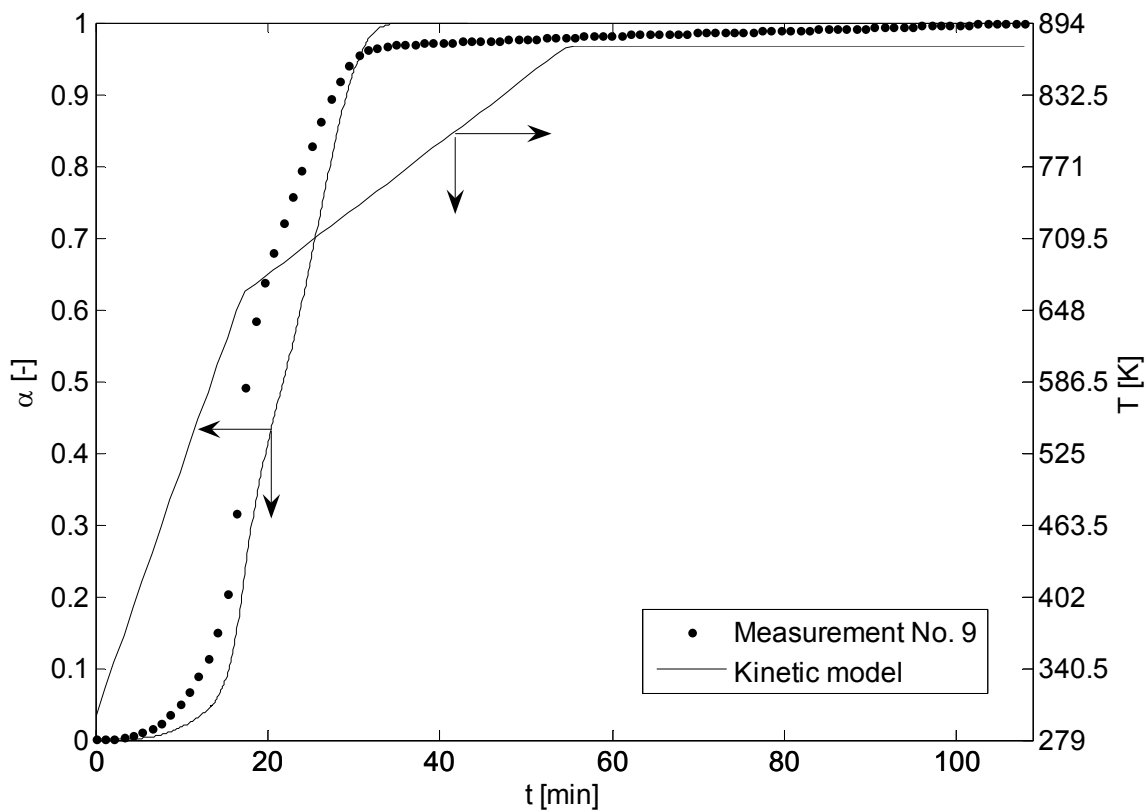


Fig. 11. Testing of the kinetic model based on measurement No. 9

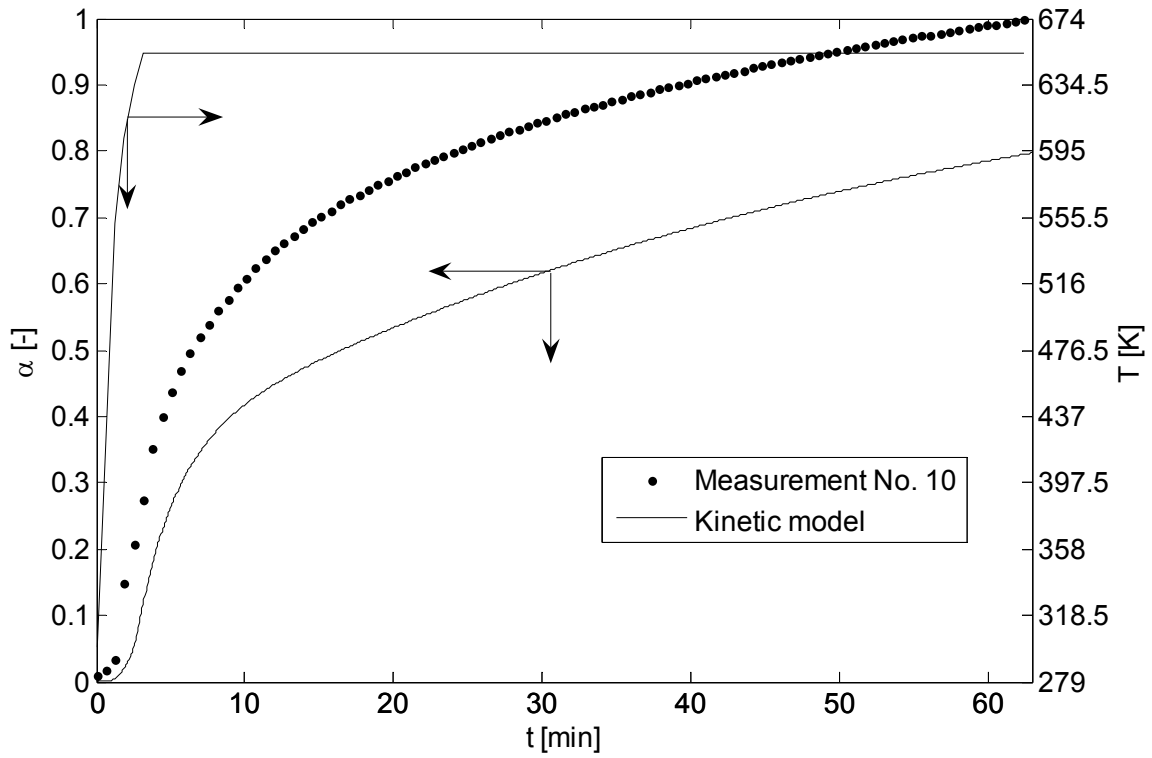


Fig. 12. Testing of the kinetic model based on measurement No. 10

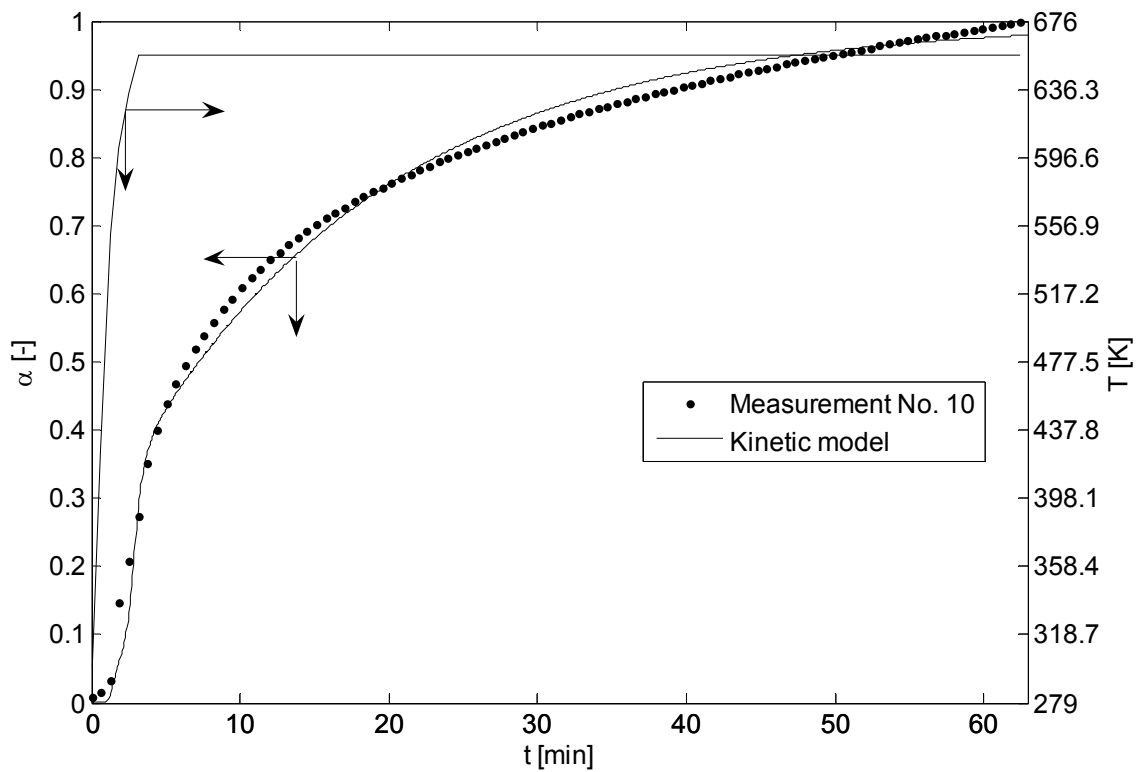


Fig. 13. Testing of the kinetic model based on measurement No. 10. The kinetic parameters were calculated from the measurement No. 1 conducted at heating rate $\beta = 50$ K/min

4. CONCLUSIONS

- The measurements showed that three characteristic steps can be distinguished in ELT pyrolysis. These steps correspond to the evaporation and thermal decomposition of: 1) oil, plasticizer, additives and moisture in the first step, 2) natural rubber in the second step, and 3) styrene-butadiene rubber in the third step.
- The Three-Component Simulation Model was able to correctly describe the kinetics of ELT pyrolysis. However, the accuracy of predictions was enhanced if the parameters of the kinetic model were determined from the measurement carried out at a similar heating rate.
- Comparison of DTG curves for samples of different sizes showed that the conduction resistance in the samples was negligible. This enabled detailed kinetic analysis of ELT pyrolysis by TG analysis.
- The calculation results obtained for different heating rates explain the cause of the observed shifting of the local maxima on the DTG curves in the direction of higher temperatures for higher heating rates. This work shows that the phenomenon has kinetic origin and follows directly from different residence times of samples at varying temperatures (history of the sample).
- CFD modeling of pyrolysis reactors requires a reliable and computationally cheap kinetic model. The Three-Component Simulation Model due to its relative simplicity seems to be an appropriate candidate for this.

The project funded by the National Centre for Research and Development and the European Union under the European Regional Development Fund under the agreement UOD-DEM-1-217 / 001.

SYMBOLS

A	pre-exponential factor, 1/min
c_p	heat capacity, J/(kg·K)
DTG	rate of relative mass loss, %/min
E	activation energy, kJ/mol
m	sample mass, mg
T	temperature, K
T_c	parameter of the extreme function
$t_{isotherm.}$	length of the isothermal stage, min
$Temp$	temperature, K
TG	relative sample mass, %
\dot{V}	flow rate, ml/min
z_i	contribution of the i -th reaction to the total mass loss

Greek symbols

α	conversion
β	heating rate, K/min
$\delta_i = (T - T_{c,i}) / \omega_{c,i}$	parameter of the extreme function for the i -th component
ε_i	parameter of the extreme function for the i -th component
$\omega_{c,i}$	parameter of the extreme function for the i -th component

Subscripts

0	initial
-----	---------

f, ∞	final
i	i -th component
N_2	nitrogen

REFERENCES

- Al-Salem S.M., Lettieri P., Baeyens J., 2009. Kinetics and product distribution of end of life tires (ELTs) pyrolysis: a novel approach in polyisoprene and SBR thermal cracking. *J. Hazard. Mater.*, 172, 1690–1694. DOI: 10.1016/j.jhazmat.2009.07.127.
- Chen J.H., Chen K.S., Tong L.Y., 2001. On the pyrolysis kinetics of scrap automotive tires. *J. Hazard. Mater.*, 84, 43-55. DOI: 10.1016/S0304-3894(01)00180-7.
- Council Directive 1999/31/EC of 26 April 1999 on the Landfill of Waste. 1999. Office for Official Publications of the European Communities Luxembourg.
- Council Directive 91/156/EEC of 18 March 1991 Amending Directive 75/442/EEC on Waste. 1991. Council of European Communities. European Commission: Brussels.
- ETRMA's End-of-life Tyres Management report, 2015. Available at: <http://www.etrma.org/tyres/ELTs>.
- Galvagno S., Casu S., Martino M., Di Palma E., Portofino S., 2007. Thermal and kinetic study of tyre waste pyrolysis via TG-FTIR-MS analysis. *J. Therm. Anal. Calorim.*, 88, 507-514. DOI: 10.1007/s10973-006-8409-1.
- González J.F., Encinar J.M., Canito J.L., Rodríguez J.J., 2001. Pyrolysis of automobile tyre waste. Influence of operating variables and kinetics study. *J. Anal. Appl. Pyrolysis*, 58, 667-683. DOI: 10.1016/S0165-2370(00)00201-1.
- Islam M.R., Haniu H., Fardoushi J., 2009. Pyrolysis kinetics behavior of solid tire wastes available in Bangladesh. *Waste Manage.*, 29, 668-677. DOI: 10.1016/j.wasman.2008.04.009.
- Kim S., Park J., Chun H., 1995. Pyrolysis kinetics of scrap tire rubbers. I: Using DTG and TGA. *J. Environ. Eng.*, 121, 507-514. DOI: 10.1061/(ASCE)0733-9372(1995)121:7(507).
- Lah B., Klinar D., Likozar B., 2013. Pyrolysis of natural, butadiene, styrene-butadiene rubber and tyre components: Modelling kinetics and transport phenomena at different heating rates and formulations. *Chem. Eng. Sci.*, 87, 1-13. DOI: 10.1016/j.ces.2012.10.003.
- Leung D.Y.C., Wang C.L., 1999. Kinetic modeling of scrap tire pyrolysis. *Energy Fuels*, 13, 421-427. DOI: 10.1021/ef980124l.
- Mui E.L.K., Cheung W.H., Lee V.K. C., McKay G., 2010. Compensation effect during the pyrolysis of tyres and bamboo. *Waste Manage.*, 30, 821-830. DOI: 10.1016/j.wasman.2010.01.014.
- Mui E.L.K., Lee V.K.C., Cheung W.H., McKay G., 2008. Kinetic modeling of waste tire carbonization. *Energy Fuels*, 22, 1650-1657. DOI: 10.1021/ef700601g.
- Quek A., Balasubramanian R., 2009. An algorithm for the kinetics of tire pyrolysis under different heating rates. *J. Hazard. Mater.*, 166, 126-132. DOI: 10.1016/j.jhazmat.2008.11.034.
- Quek A., Balasubramanian R., 2012. Mathematical modeling of rubber tire pyrolysis. *J. Anal. Appl. Pyrolysis*, 95, 1-13. DOI: 10.1016/j.jaap.2012.01.012.
- Rudniak L., Machniewski P., 2017. Modelling and experimental investigation of waste tyre pyrolysis process in a laboratory reactor. *Chem. Process Eng.*, 38, 445-454. DOI: 10.1515/cpe-2017-0034.
- Seidelt S., Müller-Hagedorn M., Bockhorn H., 2006. Description of tire pyrolysis by thermal degradation behaviour of main components. *J. Anal. Appl. Pyrolysis*, 75(1), 11-18. DOI: 10.1016/j.jaap.2005.03.002.
- Williams P.T., 2013. Pyrolysis of waste tyres: A review. *Waste Manage.*, 33, 1714-1728. DOI: 10.1016/j.wasman.2013.05.003.

Received 26 October 2016

Received in revised form 12 June 2017

Accepted 17 June 2017

FLOCCULATION OF FLOTATION TAILINGS USING THERMOSENSITIVE POLYMERS

Wojciech Bogacz^{*1}, Marcin Lemanowicz¹, Andrzej Gierczycki¹, Anna Mielańczyk²

¹Silesian University of Technology, Faculty of Chemistry, Department of Chemical Engineering and Process Design, ul. ks. M. Strzody 7, 44-100 Gliwice, Poland

²Silesian University of Technology, Faculty of Chemistry, Department of Physical Chemistry and Technology of Polymers, ul. ks. M. Strzody 9, 44-100 Gliwice, Poland

The key feature of thermosensitive polymers is the reversible transition between the hydrophilic and hydrophobic forms depending on the temperature. Although the main research efforts are focused on their application in different kinds of drug delivery systems, this phenomenon also allows one to precisely control the stability of solid-liquid dispersions. In this paper research on the application of poly(N-isopropylacrylamide) copolymers in processing of minerals is presented. In the experiments tailings from flotation plant of one of the coal mines of Jastrzębska Spółka Węglowa S.A. (Poland) were used. A laser particle sizer Fritsch Analysette 22 was used in order to determine the Particle Size Distribution (PSD). It was proved that there are some substantial issues associated with the application of thermosensitive polymers in industrial practice which may exclude them from the common application. High salinity of suspension altered the value of Lower Critical Solution Temperature (LCST). Moreover, the co-polymers used in research proved to be efficient flocculating agents without any temperature rise. Finally, the dosage needed to achieve steric stabilization of suspension was greatly beyond economic justification.

Keywords: aggregation, flocculation, thermosensitive polymers, PNIPAM

1. INTRODUCTION

The key feature of thermosensitive polymers is the reversible transition between the hydrophilic and hydrophobic forms depending on the temperature (Cheng et al., 2006; Kuźnik et al., 2010; Sakohara et al., 2008; Xing et al., 2014). The phenomenon occurs after passing the Lower Critical Solution Temperature (LCST) as a result of shape change of polymer chains from extended coils into collapsed globules. Poly(N-isopropylacrylamide) (PNIPAM), as the most common example of thermosensitive polymer, is a non-toxic polymer which can be used as environmentally friendly substitute to industrial agents (Burdukova et al., 2010a; Ghimici and Constantin, 2011; Seidi and Heshmati, 2015; Yan et al., 2010). Moreover, Forbes (2011) indicated that PNIPAM may be more efficient than conventional flotation agents. Its copolymers can be used for selective removal of desired mineral (Burdukova et al., 2010b). At the present moment, one may find papers where thermosensitive polymers were used for suspension flocculation (Burdukova et al., 2011; Deng et al., 1996; Forbes, 2011; Ghimici and Constantin, 20011; Kuźnik et al., 2010; Lemanowicz et al., 2012; Mori et al., 2013; Sakohara et al., 2008; Sakohara et al., 2013), nanoparticles stabilization (Budgin et al., 2012; Gong et al., 2012) or heavy metal ion removal (Tokuyama et al., 2010). Franks proved that cooling of sediment leads to enhanced consolidation (Franks, 2005). He used zircon suspension and methylcellulose as the thermosensitive agent. Identical conclusions were made in other papers (Franks et al., 2009; Li et al.,

*Corresponding authors, e-mail: Wojciech.Bogacz@polsl.pl

2009). Thus, research of new materials and phenomena associated with thermoresponsive polymers is of great interest in the areas of selective separation, process control, flotation, dewatering and generally speaking environmentally sustainable technology.

The behavior of thermosensitive polymers and associated particulate processes depend on many factors. The most important are: molecular weight, molecular structure, pH and temperature (Budgin et al., 2012; Burdukova et al., 2010; Burdukova et al., 2011; Deng et al. 1996; Liu et al., 2001; Qin et al., 2014; Yue et al., 2012, Zhang et al., 2013). Moreover, in the case of flocculation three additional factors come into play; polymer dose, addition method and heating method (Lemanowicz et al., 2012). Any change of these parameters may influence the aggregation mechanism significantly.

The aggregation via standard flocculation runs in four steps (Gregory, 1993). In the first step a polymer is added to the solution and they are mixed. In the second step polymer chains are adsorbed on the surface of particles and then, in the third step, they undergo reformation. At this point the suspension is destabilized and particles may aggregate with each other as a result of following three mechanisms: charge neutralization, charge patching or bridging. In the first case the electrostatic charge between particles and solution is reduced which allows them to aggregate via Van der Waals forces. In the second case polymer chains adsorbed on particles create charge patches in the electrostatic barrier through which particles can connect with each other. Finally, in the third case polymer chains create bridges between solid particles. What is important in this process is irreversible (Šulc et al., 2012; Tadros, 2013).

In the case of thermosensitive aggregation, aggregates are formed due to hydrophobic interactions between particles (Lemanowicz et al., 2016a). However, the transformation of macromolecules as a result of temperature change is hampered due to their adsorption onto the surface of particles (Kuźnik et al., 2010). Generally, in this case the higher the temperature of suspension the more complete the polymer transition is. Particles covered with a hydrophobic polymer tend to aggregate in order to reduce their free energy and, as a result, they create large aggregates. When the suspension is cooled down the breakage phenomenon occurs because the surface of particles becomes hydrophilic (Burdukova et al., 2011; Kuźnik et al., 2010; Lemanowicz et al., 2016b; Sakohara et al., 2008).

So far, studies on thermoresponsive flocculants were mainly focused on model suspensions. However, additional factors have to be taken into consideration if such systems are to be used in practical applications. In the case of typical industrial slurries the thermoresponsive flocculation process can be expected to be affected by the presence of salt, acidity/alkalinity and possibly other substances. In the presented research the flocculation of suspension of industrial origin was investigated. The aim of this study was to verify the possibility of practical application of thermosensitive polymers, especially in the mineral processing technology. The results concerning flocculation of a coal mine flotation tailings with a thermoresponsive polymer based on poly(N-isopropylacrylamide) are presented. The research was focused on PSDs and their change during destabilization of the system.

2. EXPERIMENTAL

Samples of flotation tailings were taken from one of the mines of Jastrzębska Spółka Węglowa S.A (Poland). In order to receive representative samples the suspension was collected during normal work of flotation plant into two 50 dm³ barrels. In the industrial practice, in the next step, it would be mixed with a flocculant and transferred to a Dorr settler.

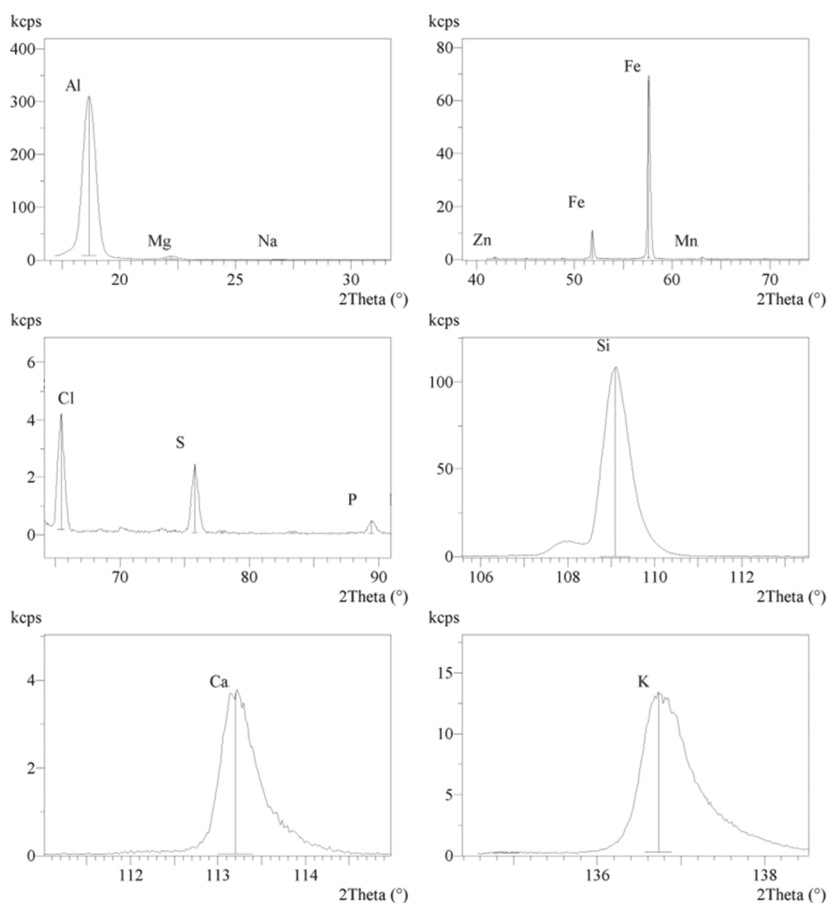


Fig. 1. Chemical composition of flotation tailing solid matter

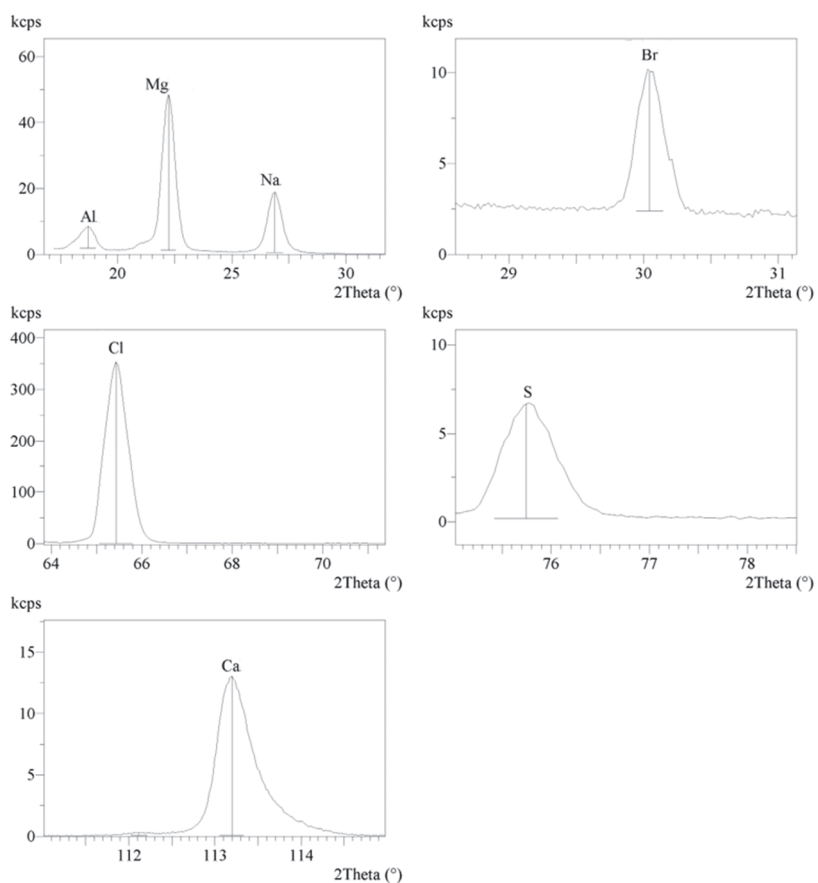


Fig. 2. Chemical composition of flotation tailing filtrate

The samples had a form of diluted, gray suspensions. The chemical composition of the samples was determined using a Philips PW2400 spectrometer (Fig. 1 and 2). As expected, the solid matter was mainly composed of aluminum, silicon and iron compounds with some trace amounts of other elements. In the case of filtrate it contained dissolved salts of magnesium chloride, sodium chloride, calcium chloride and smaller amounts of other elements. The size of particles was determined based on the laser light scattering method using Fritsch Analysette 22. The minimum size of particles was equal to 0.15 μm (measurement limit), the maximum size was equal to 40 μm whereas the dominant value was equal to 5 μm . Finally, the Sauter mean diameter d_{32} was equal to 2.65 μm . The zeta potential of the suspension was measured using Malvern Nano Z equipment. Due to the limitations of particle size that can be analyzed, a 100 ml of suspension was taken and subjected to settling in a measuring cylinder. Next the fraction of the smallest particles which were present at the top of suspension was collected and their zeta potential was measured. It was equal to (-20.1) mV. The mass of suspended solids as well as salinity were determined on the basis of the weight method. For that purpose a small portion of suspension was placed in a beaker and dried in a laboratory dryer at the temperature of 378 K as long as its mass was constant. Simultaneously, another sample of suspension was filtrated using the Büchner funnel. The filtrate was collected and evaporated in the laboratory dryer in the same conditions as the suspension. The desired parameters were calculated using difference in mass of the samples before and after drying/evaporating. Concluding, the mass fraction of suspended solids was equal to 1.57% w/w and the salinity was equal to 1.62% w/w.

In the experiments two different polymers were used as the flocculants. The intentions of the authors were to synthesize two destabilization agents, one of cationic nature and one of anionic nature, with similar weight average molecular weight and transition temperature. Such samples would allow one to research the flocculation process in a qualitative way without interference on the physicochemical properties of industrial samples. Unfortunately, the incorporation of the ionic element into the polymeric chain alters the LCST significantly (Sakohara et al., 2008; Sakohara et al., 2013). Therefore considering economical aspects of the investigated process the molar ratio of ionic repeating units to nonionic ones had to be very low in order to keep LCST at a reasonable level. The synthesis procedure was identical to that presented in (Kuźnik et al., 2010). The only difference was the type and amount of the second comonomer. The polymer samples were synthesized in free radical polymerization with redox initiating system – ammonium persulfate (98% purity, Acros Organics, Avantor Performance Materials), and tetramethylethylenediamine (TEMED) (99% purity, Sigma-Aldrich) (Fig. 3). The comonomers were used as received: N-isopropylacrylamide (NIPAM, Acros Organics, Avantor Performance Materials) and methacrylic acid (MAA, Sigma Aldrich) or diallyldimethylammonium chloride (DADAMAC, Sigma-Aldrich) in 99:1 molar ratio (Fig. 4). The reaction mixture was purged with an inert gas for one hour before the addition of TEMED. Reaction products were separated by thermoprecipitation – the reaction mixture was heated to induce polymer separation from low molecular weight reagents and water. The thermoprecipitation was repeated twice, and the polymers were then dried to constant mass at 378.15 K, weighed and dissolved in Reverse Osmosis (RO) purified water. The weight average molecular weights (M_w) of the polymers were determined on the basis of the Static Light Scattering (SLS) measurements using Malvern Nano S90 applying the Rayleigh equation which describes the intensity of light scattered from a particle in a solution. The Debye plot for each polymer was obtained from several individual measurements: a zero concentration measurement (water) and samples of various polymer concentrations which allowed to determine M_w . In both cases the average weight molecular weights were comparable and were approximately 1200 kDa. Attempts have also been made to perform a molecular weight measurement using the size exclusion chromatography (SEC). Unfortunately, the high viscosity of polymer solutions, probably caused by relatively high M_w , disabled the preparation of samples with appropriate concentration for analysis.

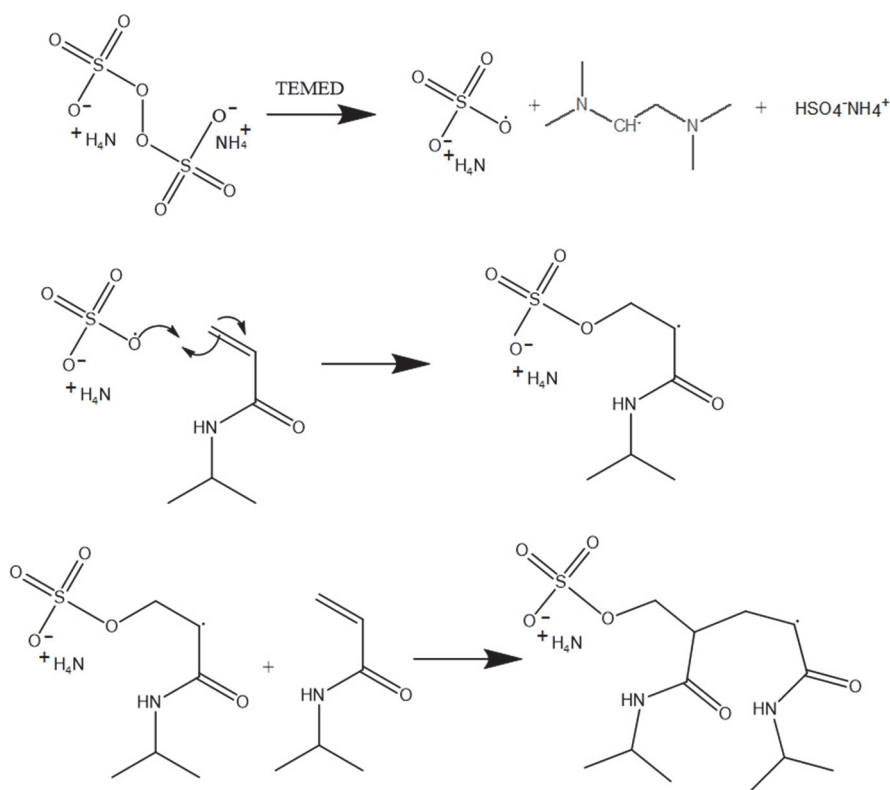


Fig. 3. Initiation of copolymerization scheme

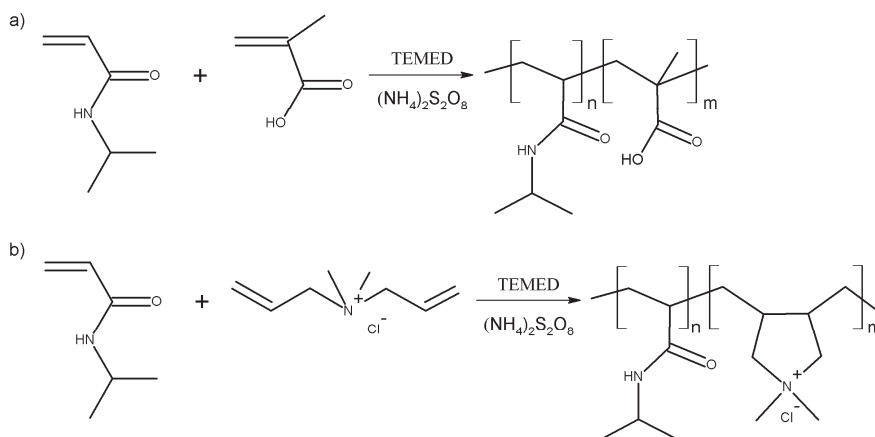


Fig. 4. Schematic representation for the synthesis of MAA-ended P1 (a) and DADMAC-ended P2

Due to the salinity of the suspension one should expect that the LCST value will be altered compared to the pure polymer solution. For that reason, appropriate solutions of polymers were prepared using flotation tailing filtrate as a base liquid and the transmittance was measured using Hitachi U-2800 A spectrophotometer at a wavelength of 500 nm. The flocculation experiments were performed in a thermostated mixing tank equipped with 4 baffles and a mechanical marine propeller. This kind of stirrer was chosen in order to limit shear stress which would be generated e.g. by the Rushton turbine. The stirrer worked with 6.67 s^{-1} rotational speed. The key dimensions of the laboratory setup are presented in Fig. 5. During experiments the temperature of the thermostatic jacket as well as the temperature within the tank were monitored. Moreover a special electrode for continuous pH measurements of suspensions was installed. The measurement procedure was as follows. When the suspension was transferred to the mixing tank its temperature was set to 298 K. Then, a blank sample (without the polymer) was measured with the laser sizer. Next, an appropriate dose of the polymer was injected to the suspension and the process time measurement began using a stopwatch. After that,

samples were taken at different stages of the flocculation process. Before each PSD measurement, the background measurement was done using RO purified water. After 20 minutes of mixing the heating of suspension started. In this case also the measurements were made at different points of time as long as the steady state was achieved. In the case of both polymers the final temperature of the system was equal to 318 K. The samples were transferred from the mixing tank to the laser sizer using a preheated plastic pipette. Moreover, the temperature of suspension within the sizer was controlled.

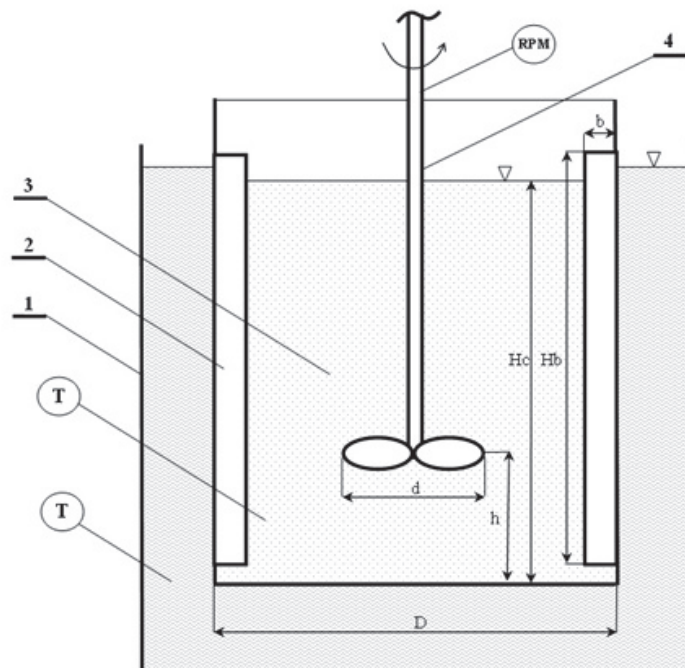


Fig. 5. Mixing tank scheme: 1) thermostatic jacket, 2) baffle, 3) mixing tank, 4) propeller.

Dimensions: $D = 0.098$ m, $d = 0.038$ m, $b = 0.01$ m, $H_c = D$, $H_b = D$, $h = \frac{1}{3}H_c$

3. RESULTS AND DISCUSSION

3.1. Salinity and pH

Due to the salinity of samples the LCST point of polymers was determined using the filtrate solution and compared with the results for RO water solutions. The transmittance change with temperature is presented in Figs. 6 and 7. In the case of DADMAC1 sample the transition in RO water was sharp and occurred at 306 K. This phenomenon could be observed with a naked eye because the solution became milky white. However, in the case of filtrate solution the LCST value decreased to 303 K. Simultaneously, the sharp transition from hydrophilic to hydrophobic form was preserved. Such results should be expected as the presence of salts in the solution generally decreases the LCST (Eeckman et al., 2001). Surprisingly, in the case of P1 sample the transition behavior for the filtrate solution changed significantly. The phenomenon occurred at higher temperature compared to the RO water sample and it was more gentle. The zero transmittance was achieved above 315 K. This fact results from the changed pH compared to the pure polymer solution. The P1 as well as P2 samples were pH sensitive because their chains possessed incorporated ionic repeating units at the end of the polymeric chain. As a result higher pH values increased substantially the location of the LCST point. The pH of suspension was equal to 7.6. This parameter was also monitored during the flocculation process. However, it did not change significantly after polymer injection also for P2 sample nor P1 sample compared to the fluctuations resulting from turbulent mixing.

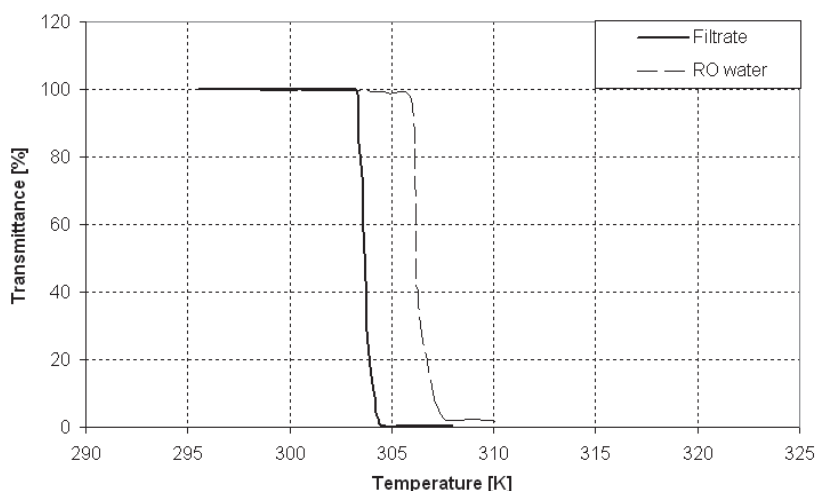


Fig. 6. The LCST determination of DADMAC1 polymer in RO water and flotation filtrate

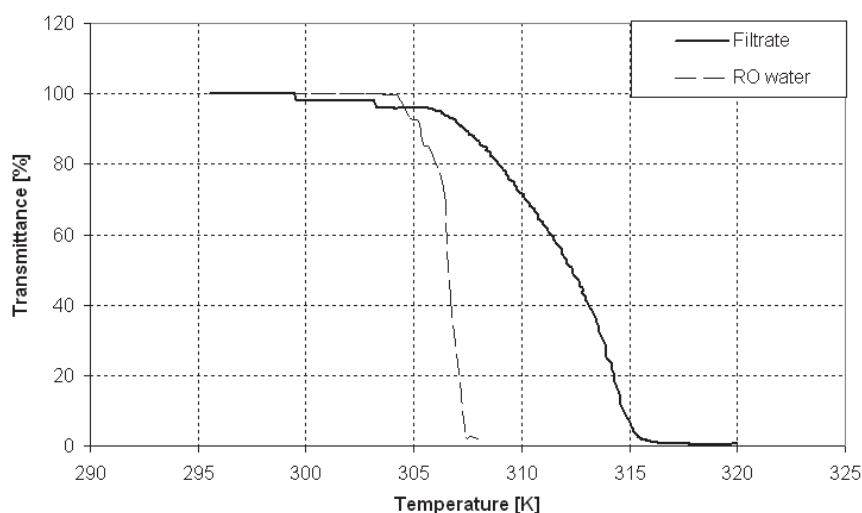


Fig. 7. The LCST determination of P1 polymer in RO water and flotation filtrate

These results reveal the first important issue of the practical application of thermosensitive polymers as flocculants, especially in the processing of minerals. The problem is that the chemical and physical properties of raw materials differ significantly, especially in the case of mineral processing. One may expect that the salinity of the feed will vary depending on acquisition site. It is probable that the change of pH and salt concentration will change the LCST value of a thermosensitive polymer above the range of operation of the production plant. As a result the polymer that was effective in the case of one sample may be totally ineffective for another one. On the other hand, there is a possibility that the LCST value will decrease below the feed temperature. In such a case the polymer will take the hydrophobic form immediately after its addition to the suspension, which of course, makes its application pointless. This is a significant disadvantage compared to standard flocculants used in mineral processing. In the standard process the effectiveness of flocculation can be controlled via polymer dosage. Moreover, such flocculating agents are less sensitive to the process conditions.

3.2. Flocculation

The flocculation process course was investigated by the analysis of particle size distribution. The data presented in Figs. 8 to 14 are summarized in the table attached as supplementary materials. P2 polymer was added to the suspension at 298 K. Unfortunately, this flocculant proved to be efficient below LCST

point (Fig. 8). After injection, very large aggregates were created rapidly. After 5 minutes of the process the Sauter mean diameter was equal to $9.19 \mu\text{m}$ and the largest aggregates had the size of $170 \mu\text{m}$. Ten minutes later, at the steady state of the process, a part of the biggest aggregates underwent breakage thus the mean diameter decreased to $8.93 \mu\text{m}$. When the suspension was heated, the PSD moved insignificantly toward larger sizes (Fig. 9). The mean diameter rose to $10.85 \mu\text{m}$. However, no bigger aggregates were created. It has to be emphasized that the change in the PSD was very small compared to the initial process below LCST.

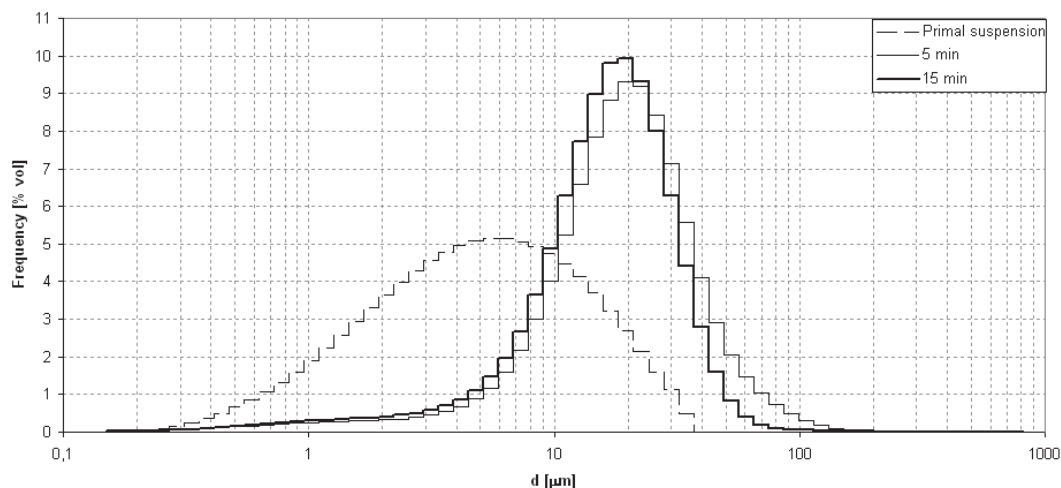


Fig. 8. PSDs for the thermosensitive flocculation using 1.0 mg/g of P2

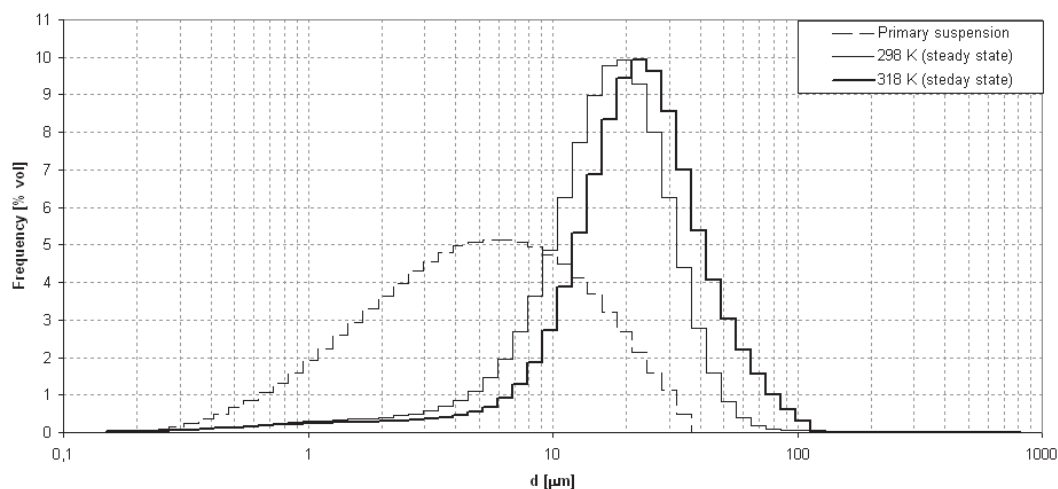


Fig. 9. PSDs for the thermosensitive flocculation using 1.0 mg/g of P2

When the polymer dose was decreased tenfold, i.e. it was more similar to the polymer doses used in the existing flotation plants, once again flocculation occurred (Fig. 10). However, the effect was very weak. Practically, no larger aggregates were created. The PSD moved toward larger dimensions. When the suspension was heated, no change in the PSD was noticed. These facts are in agreement with the mechanism of thermosensitive flocculation. If polymer chains successfully bridge solid particles it will be very difficult for them to undergo the hydrophilic-hydrophobic transition. Therefore, at temperatures above LCST almost no aggregation effect was visible. As expected the results for P1 polymer were very similar (Figs. 11 and 12). After injection of the polymer solution a rapid growth of aggregates occurred. The change of the system was visible with a naked eye. At 5th minute of the process the largest aggregates had the size above $50 \mu\text{m}$, whereas the Sauter mean diameter was equal to $7.74 \mu\text{m}$.

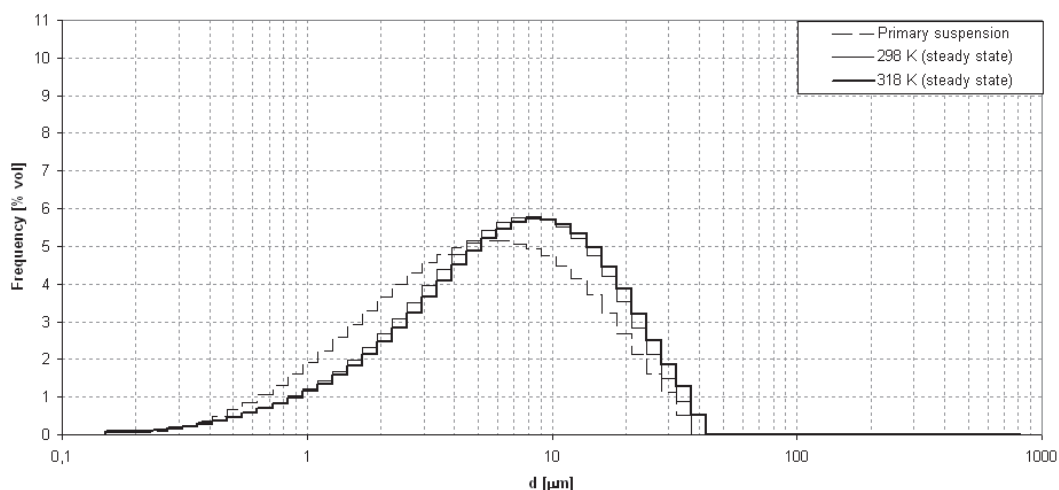


Fig. 10. PSDs for the thermosensitive flocculation using 0.1 mg/g of P2

The dominant value of particle diameter was approximately the same as in the case of DADMAC1 polymer. The lack of particles larger than 100 μm and resulting smaller mean diameter can be easily explained by the electrostatic interactions between polymer ionic groups and the surface charge of particles. The zeta potential of the particles was negative, thus the macromolecule possessing cationic groups proved to be more efficient than the polymer which possessed negatively charge groups. Due to the fact that the bridging mechanism of flocculation was dominating the differences are not very large, yet they are visible.

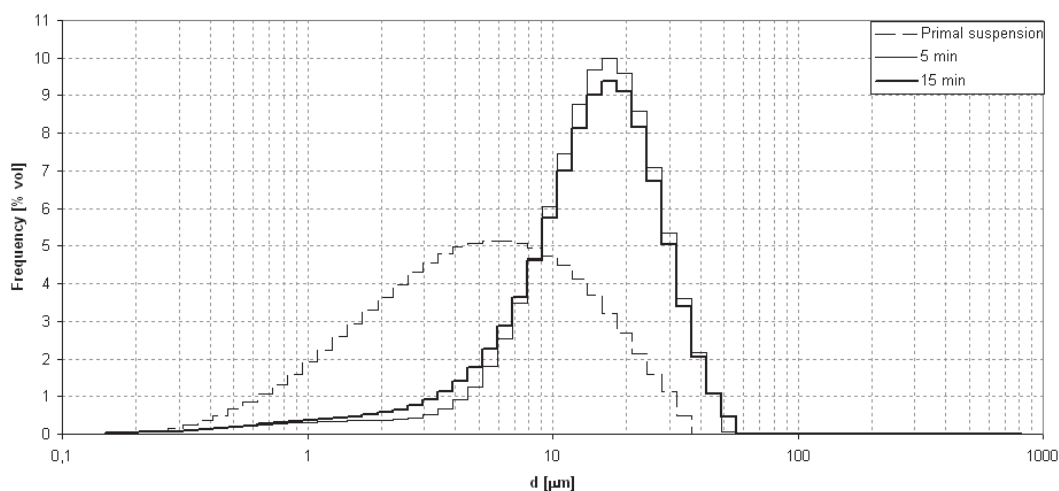


Fig. 11. PSDs for the thermosensitive flocculation using 1.0 mg/g of P1

When a smaller polymer dose was used (Fig. 13) practically no change of the PSD was noticed. Unfortunately, when the system was heated also no larger aggregates were created. Therefore, it was decided to use a high, economically unjustified overdose of P1 polymer which would guarantee the steric stabilization of solid particles and as a result strong thermosensitive behavior of the polymer. A dose equal to 10 mg/g was chosen (Fig. 14). One may notice that for the temperature below LCST significant larger aggregates were created (larger than 100 μm). This means that the range of flocculating window for this system of suspension-polymer is extremely wide. In result, one should expect that full stabilization effect will occur for significantly higher polymer dosages. On the other hand, the impact of temperature on the PSD was clearly visible in this case. Although no larger aggregates were created after heating (inhibition due to bridging) still the mean particle diameter increased from 6.38 to 15.85 μm .

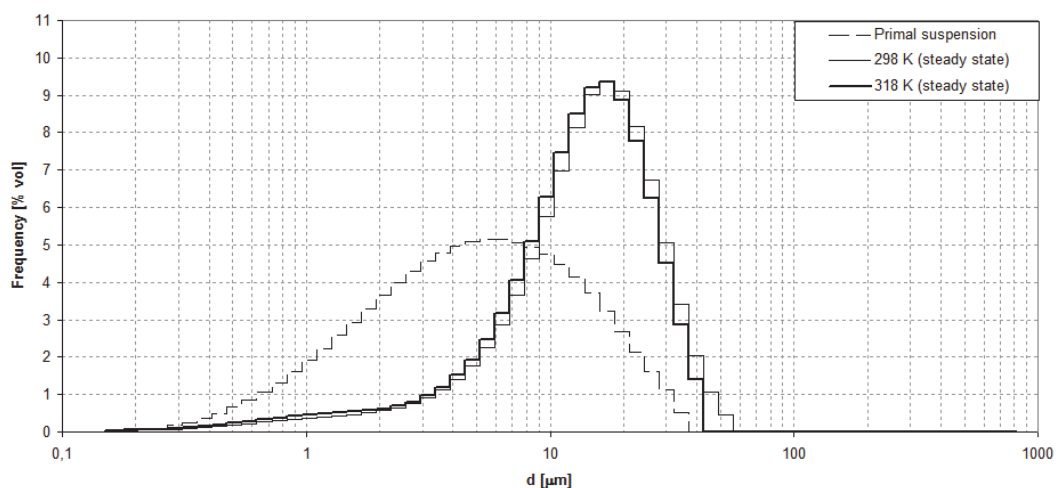


Fig. 12. PSDs for the thermosensitive flocculation using 1.0 mg/g of P1

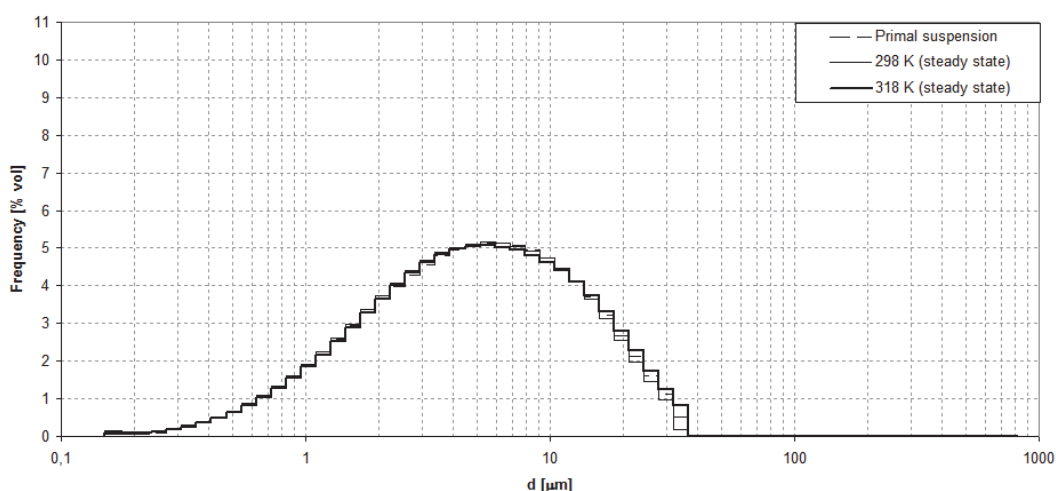


Fig. 13. PSDs for the thermosensitive flocculation using 0.1 mg/g of P1

In all experiments described above the molar fraction of ionic groups in the polymer chains was approximately equal to 1%. In general, the reactivity of DADMAC is much lower than that of NIPAM. Although direct kinetic data for copolymerization of NIPAM/DADMAC are not available, according to the literature the reactivity ratios of DADMAC and acrylamide (AM), which exhibit similar reactivity to NIPAM, are respectively: $r_{DADMAC} = 0.06$ $r_{AM} = 6.4$, $r_{DADMAC} = 0.58$ $r_{AM} = 6.7$ (Deng and Pelton, 1995). Deng and Pelton performed copolymerization of NIPAM and DADMAC. Unfortunately, they did not determine reactivity ratios of NIPAM/DADMAC. However, from their work it can be concluded that in case of molar ratio of comonomers equal to NIPAM/DADMAC = 99:1, the resulting fraction of repeating units in copolymer is 99.3:0.7 mol%.

In case of NIPAM/MAA copolymerization, reactivity ratios of $r_{NIPAM} = 10.2$ and $r_{MAA} = 0.01$ are reported (Xue et al., 2000). Consequently, since in both cases $r_{NIPAM} \gg 1 \gg r_{DADMAC/MAA}$, the compositional homogeneity up to quite a high conversion of NIPAM for those copolymers is presumed. Simultaneously DADMAC or MAA was incorporated at the end of the polymeric chain and PNIPAM enriched with DADMAC-end or PNIPAM enriched with MAA-end were obtained.

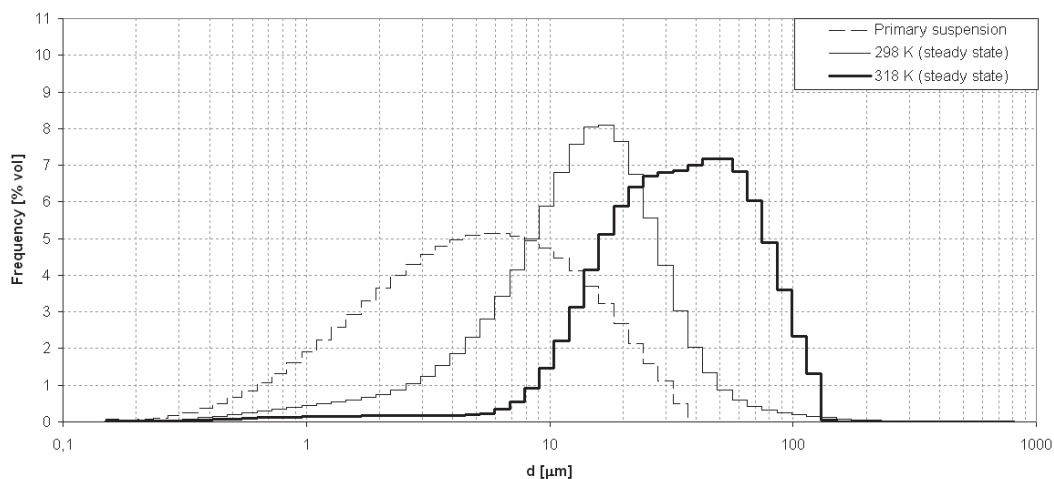


Fig. 14. PSDs for the thermosensitive flocculation using 10 mg/g of P1

Unfortunately, in the examined cases the interaction between polymers and solid particles was very strong resulting in fast flocculation via the bridging mechanism. This in turn, practically disabled thermosensitivity of the macromolecules. Of course, the structure of thermosensitive flocculants may be modified. However, one has to remember that the higher molar fraction of ionic groups, the higher the LCST point. As a result, the application of the thermosensitive polymer may be unprofitable due to high heating costs.

As was mentioned before the majority of papers concerning thermosensitive flocculation is focused on model suspensions. Therefore, it is hard to compare received experimental results. According to the authors' knowledge only the team of prof. Sakohara performed research using thermosensitive polymers in flocculation of industrial origin suspensions (Sakohara et al., 2007; Sakohara et al., 2011). As in the presented case, these authors had to overcome two substantial issues, namely the reasonable level of LCST and the amount of polymer used in the process. The incorporation of ionic groups into the polymeric chain resulted in an elevated value of transition temperature. Therefore, a method based on dual ionic thermosensitive polymers was proposed. Firstly, a cationic thermosensitive polymer was introduced to the suspension. After 5 minutes of mixing at room temperature an anionic thermosensitive polymer was added. This procedure allowed the authors to enhance dewatering process at relatively low temperatures. However, in both cases, i.e. dewatering of inorganic sludge as well as activated sludge, the dosages of polymers used in experiments were extremely high. Sakohara et al. stated that in the case of activated sludge the effective dosage was more than 3% w/w which is three times more than that of commercial flocculants. In the presented research the dosage of commercial flocculant varied between 0,01% to 0,02% whereas the dosage of thermosensitive polymer equal to 1% w/w was not enough to achieve desirable results.

The last issue associated with the practical application of thermosensitive polymers in mineral processing is the economy. First of all, the cost of standard flocculants is significantly lower compared to thermosensitive polymers. Of course, this situation would change if the mass production of such macromolecules would start. Still, at the present moment such polymer substitution would be expensive. Moreover, in order to fully take advantage of thermosensitive transition steric stabilization should be achieved which in consequence results in significantly higher polymer dosages compared to standard flocculants. Combined with a higher polymer price, the application of such flocculants would be even more expensive. Finally, the application of standard flocculants does not require any additional feed processing. In turn, in the case of thermosensitive polymers a large amount of suspension should be heated above the LCST.

4. CONCLUSIONS

In this paper the idea of thermosensitive polymer application in industry is discussed. Experimental results concerning flotation flocculation are presented. In experiments an industrial suspension was investigated. It was proved that there are some key issues concerning the application of thermosensitive polymers like the salinity or strong interactions between particle surface and polymer chains. Yet, thermosensitive polymers may be very efficient in some applications where the selectivity and hydrophobicity are of key importance. In the authors' opinion, thermosensitive polymers should be rather employed in processes where the reversibility of the aggregation process is fully utilized and the same polymer could be used many times in cyclic operations.

This research was supported by the Ministry of Science and Higher Education (Poland) under grant IUVENTUS PLUS no. IP2012019972.

REFERENCES

- Budgin A.M., Kabachii Y.A., Shifrina Z.B., Valetsky P.M., Kochev S.S., Stein B.D., Malyutin A., Bronstein L.M., 2012. Functionalization of magnetic nanoparticles with amphiphilic block copolymers: Self-assembled thermoresponsive submicrometer particles. *Langmuir*, 28, 4142-4151. DOI: 10.1021/la205056k.
- Burdukova E., Ishida N., Shaddick T., Franks G.V., 2011. The size of particle aggregates produced by flocculation with PNIPAM, as a function of temperature. *J. Colloid. Interf. Sci.*, 354, 82-88. DOI: 10.1016/j.jcis.2010.10.016.
- Burdukova E., Li H., Bradshaw D.J., Franks G.V., 2010a. Poly (N-isopropylacrylamide) (PNIPAM) as a flotation collector: Effect of temperature and molecular weight. *Miner. Eng.*, 23, 921-927. DOI: 10.1016/j.mineng.2010.03.003.
- Burdukova E., Li H., Ishida N., O'Shea J.P., Franks G.V., 2010b. Temperature controlled surface hydrophobicity and interaction forces induced by poly (N-isopropylacrylamide). *J. Colloid. Interf. Sci.*, 342, 586-592. DOI: 10.1016/j.jcis.2009.10.049.
- Cheng H., Shen L., Wu C., 2006. LLS and FTIR studies on the hysteresis in association and dissociation of poly(N-isopropylacrylamide) chains in water. *Macromolecules*, 39, 2325-2329. DOI: 10.1021/ma052561m.
- Deng Y., Pelton R., 1995. Synthesis and solution properties of poly(N-isopropylacrylamide-co-diallyldimethylammonium chloride). *Macromolecules*, 28, 4617-4621. DOI: 10.1021/ma00117a036.
- Deng Y., Xiao H., Pelton R., 1996. Temperature-sensitive flocculants based on poly(N-isopropylacrylamide-co-diallyldimethylammonium chloride). *J. Colloid. Interf. Sci.*, 179, 188-193. DOI: 10.1006/jcis.1996.0201.
- Eeckman F., Amighi K., Moës A.J., 2001. Effect of some physiological and non-physiological compounds on the phase transition temperature of thermoresponsive polymers intended for oral controlled-drug delivery. *Int. J. Pharm.*, 222, 259-270. DOI: 10.1016/S0378-5173(01)00716-5.
- Forbes E., 2011. Shear, selective and temperature responsive flocculation: A comparison of fine particle flotation techniques. *Int. J. Miner. Process.*, 99, 1-10. DOI: 10.1016/j.minpro.2011.02.001.
- Franks G.V., 2005. Stimulant sensitive flocculation and consolidation for improved solid/liquid separation. *J. Colloid Interf. Sci.*, 292, 598-603. DOI: 10.1016/j.jcis.2005.06.010.
- Franks G.V., Li H., O'Shea J.P., Qiao G.G., 2009. Temperature responsive polymers as multiple function reagents in mineral processing. *Adv. Powder Technol.*, 20, 273-279. DOI: 10.1016/j.apt.2009.02.002.
- Ghimici L., Constantin M., 2011. Novel thermosensitive flocculating agent based on pullulan. *J. Hazard. Mater.*, 192, 1009-1016. DOI: 10.1016/j.jhazmat.2011.06.002.
- Gong Z., Tang D., Guo Y., 2012. The fabrication and self-flocculation effect of hybrid TiO₂ nanoparticles grafted with poly(N-isopropylacrylamide) at ambient temperature via surface-initiated atom transfer radical polymerization. *J. Mater. Chem.*, 22, 16872-16879. DOI: 10.1039/C2JM32168H.
- Gregory J., Shamlou P.A. (Eds.), 1993. *Processing of solid-liquid suspensions*. Butterworth-Heinemann, Oxford, UK, 59-92.

- Kuźnik W., Lemanowicz M., Kuś A., Gibas M., Gierczycki A., 2010. Temperature-controlled particle size distribution of chalk suspension utilizing a thermosensitive polymer. *Powder Technol.*, 201, 1-6. DOI: 10.1016/j.powtec.2010.02.026.
- Lemanowicz M., Gierczycki A., Kuźnik W., 2016a. Review of stimuli-responsive polymers application as stabilization agents in solid-liquid dispersion systems. *Polimery*, 61, 92-97. DOI: 10.14314/polimery.2016.092.
- Lemanowicz M., Gierczycki A., Kuźnik W., Milczyńska J., Bulanda P., 2016b. Application of thermosensitive polymers in stabilization of colloids. *Adv. Powder Technol.*, 27, 471-480. DOI: 10.1016/j.appt.2016.01.026.
- Lemanowicz M., Kuźnik W., Gibas M., Dzido G., Gierczycki A., 2012. Impact of heating method on the flocculation process using thermosensitive polymer. *Water Res.*, 46, 4091-4098. DOI: 10.1016/j.watres.2012.05.014.
- Li H., O'Shea J.P., Franks G.V., 2009. Effect of molecular weight of poly(N-isopropyl acrylamide) temperature-sensitive flocculants on dewatering. *AIChE J.*, 55, 2070-2080. DOI: 10.1002/aic.11859.
- Liu J., Yan Y., Yao P., 2011. Binding of thermo-sensitive and pH-sensitive butylated poly(allylamine)s with lysozyme. *Chinese J. Polym. Sci.*, 29, 397-406. DOI: 10.1007/s10118-011-1054-6.
- Mori T., Tsubaki J., O'Shea J.P., Franks G.V., 2013. Hydrostatic pressure measurement for evaluation of particle dispersion and flocculation in slurries containing temperature responsive polymers. *Chem. Eng. Sci.*, 85, 38-45. DOI: 10.1016/j.ces.2012.02.014.
- Qin H., Liu H., Chen Y., 2014. Influence of aliphatic amide terminals on the thermoresponsive properties of hyperbranched polyethylenimines. *Chinese J. Polym. Sci.*, 32, 1338-1347. DOI: 10.1007/s10118-014-1509-7.
- Sakohara S., Hinago R., Ueda H., 2008. Compaction of TiO₂ suspension by using dual ionic thermosensitive polymers. *Sep. Purif. Technol.*, 63, 319-323. DOI: 10.1016/j.seppur.2008.05.014.
- Sakohara S., Kawachi T., Gotoh T., Lizawa T., 2013. Consolidation of suspended particles by using dual ionic thermosensitive polymers with incorporated a hydrophobic component. *Sep. Purif. Technol.*, 106, 90-96. DOI: 10.1016/j.seppur.2012.12.030.
- Sakohara S., Ochiai E., Kusaka T., 2007. Dewatering of activated sludge by thermosensitive polymers. *Sep. Purif. Technol.*, 56, 296-302. DOI: 10.1016/j.seppur.2007.02.004.
- Sakohara S., Yagi S., Iizawa T., 2011. Dewatering of inorganic sludge using dual ionic thermosensitive polymers. *Sep. Purif. Technol.*, 80, 148-154. DOI: 10.1016/j.seppur.2011.04.022.
- Seidi F., Heshmati P., 2015. Synthesis of a PEG-PNIPAm Thermosensitive dendritic copolymer and investigation of its self-association. *Chinese J. Polym. Sci.*, 33, 192-202. DOI: 10.1007/s10118-015-1561-y.
- Šulc R., Lemanowicz M., Gierczycki A.T., Effect of flocculant sonication on floc growth kinetics occurring in an agitated vessel. *Chem. Eng. Proc.*, 60, 49-54. DOI: 10.1016/j.cep.2012.05.008.
- Tadros T. (Ed.), 2013. *Encyclopedia of colloid and interface science*. Springer-Verlag Berlin Heidelberg, New York, Dordrecht, London. DOI: 10.1007/978-3-642-20665-8.
- Tokuyama H., Hisaeda J., Nii S., Sakohara S., 2010. Removal of heavy metal ions and humic acid from aqueous solutions by co-adsorption onto thermosensitive polymers. *Sep. Purif. Technol.*, 71, 83-88. DOI: 10.1016/j.seppur.2009.11.005.
- Xing X., Liu G., Ding Y., Zhang G., 2014. Revisiting the thermosensitivity of poly(acrylamide-co-diacetone acrylamide). *Chinese J. Polym. Sci.*, 32, 531-539. DOI: 10.1007/s10118-014-1440-y.
- Xue W., Champ S., Huglin M.B., 2000. Observations on some copolymerisations involving N-isopropylacrylamide. *Polymer*, 41, 7575-7581. DOI: 10.1016/S0032-3861(00)00171-3.
- Yan J., Ji W., Chen E., Li Z., Liang D., 2010. Effect of heating rate on thermo-induced aggregation of poly(ethylene oxide)-b-poly(N-isopropylacrylamide) in aqueous solutions. *Chinese J. Polym. Sci.*, 28, 437-447. DOI: 10.1007/s10118-010-9085-y.
- Yue G., Cui Q., Zhang Y., Wang E., Wu F., 2012. Thermo-responsive block copolymers based on linear-type poly(ethylene glycol): Tunable LCST within the physiological range. *Chinese J. Polym. Sci.*, 30, 770-776. DOI: 10.1007/s10118-012-1179-2.
- Zhang, S., Chen, C., Li, Z., 2013. Effects of molecular weight on thermal responsive property of pegylated poly-l-glutamates. *Chinese J. Polym. Sci.*, 31, 201-210. DOI: 10.1007/s10118-013-1218-7.

Received 19 April 2016

Received in revised form 17 May 2017

Accepted 27 June 2017

APPENDIX

Table A. Volume fractions of PSDs presented in Figs. 8-14

		1.0 mg/g of P2				0.1 mg/g of P2		1.0 mg/g of P1				0.1 mg/g of P1		10 mg/g of P1	
d, μm	Primal	5, min	15, min	298, K	318, K	298, K	318, K	5, min	15, min	298, K	318, K	298, K	318, K	298, K	318, K
0.16	0.07	0.04	0.04	0.04	0.03	0.07	0.10	0.05	0.04	0.04	0.04	0.14	0.10	0.03	0.02
0.19	0.05	0.04	0.04	0.04	0.04	0.07	0.10	0.05	0.04	0.04	0.05	0.11	0.07	0.03	0.02
0.22	0.07	0.04	0.04	0.04	0.04	0.08	0.11	0.05	0.05	0.05	0.05	0.12	0.08	0.04	0.02
0.25	0.11	0.05	0.05	0.05	0.04	0.11	0.13	0.06	0.05	0.05	0.07	0.16	0.12	0.05	0.03
0.29	0.17	0.06	0.06	0.06	0.06	0.15	0.17	0.07	0.07	0.07	0.09	0.22	0.17	0.06	0.03
0.33	0.25	0.07	0.08	0.08	0.07	0.21	0.22	0.09	0.09	0.09	0.12	0.30	0.25	0.09	0.04
0.38	0.36	0.09	0.10	0.10	0.09	0.28	0.29	0.11	0.11	0.11	0.16	0.40	0.35	0.12	0.06
0.44	0.50	0.11	0.12	0.12	0.11	0.36	0.37	0.14	0.15	0.15	0.20	0.53	0.48	0.15	0.07
0.51	0.66	0.14	0.15	0.15	0.14	0.46	0.46	0.17	0.18	0.18	0.24	0.68	0.63	0.20	0.09
0.59	0.85	0.16	0.19	0.19	0.16	0.57	0.57	0.21	0.22	0.22	0.29	0.87	0.81	0.25	0.10
0.67	1.07	0.19	0.22	0.22	0.18	0.70	0.69	0.24	0.26	0.26	0.33	1.08	1.02	0.30	0.11
0.78	1.32	0.21	0.25	0.25	0.21	0.85	0.82	0.27	0.30	0.30	0.38	1.33	1.26	0.35	0.13
0.89	1.60	0.24	0.27	0.27	0.22	1.02	0.98	0.30	0.34	0.34	0.42	1.61	1.54	0.40	0.14
1.03	1.91	0.25	0.30	0.30	0.24	1.21	1.15	0.32	0.37	0.37	0.45	1.91	1.84	0.45	0.14
1.18	2.24	0.27	0.32	0.32	0.25	1.43	1.34	0.34	0.40	0.40	0.48	2.25	2.17	0.50	0.15
1.36	2.58	0.28	0.34	0.34	0.26	1.69	1.57	0.35	0.43	0.43	0.51	2.61	2.53	0.54	0.16
1.57	2.94	0.29	0.36	0.36	0.27	1.98	1.83	0.35	0.47	0.47	0.54	2.98	2.90	0.60	0.16
1.80	3.30	0.30	0.38	0.38	0.28	2.31	2.13	0.36	0.51	0.51	0.57	3.36	3.28	0.67	0.16
2.08	3.65	0.32	0.41	0.41	0.30	2.67	2.47	0.36	0.57	0.57	0.62	3.73	3.65	0.75	0.17
2.39	3.99	0.35	0.45	0.45	0.31	3.08	2.84	0.38	0.65	0.65	0.69	4.08	4.01	0.87	0.17
2.75	4.29	0.39	0.50	0.50	0.34	3.51	3.24	0.43	0.76	0.76	0.81	4.40	4.33	1.04	0.17
3.17	4.57	0.45	0.58	0.58	0.37	3.95	3.67	0.51	0.92	0.92	0.97	4.67	4.61	1.25	0.17
3.64	4.79	0.54	0.70	0.70	0.41	4.39	4.10	0.66	1.13	1.13	1.20	4.88	4.83	1.53	0.17
4.19	4.97	0.68	0.87	0.87	0.46	4.79	4.51	0.90	1.41	1.41	1.51	5.03	4.97	1.87	0.17
4.83	5.08	0.88	1.11	1.11	0.54	5.15	4.89	1.27	1.77	1.77	1.93	5.12	5.05	2.30	0.19
5.56	5.14	1.17	1.46	1.46	0.68	5.43	5.21	1.80	2.25	2.25	2.47	5.15	5.07	2.81	0.23
6.39	5.13	1.59	1.97	1.97	0.90	5.64	5.47	2.53	2.87	2.87	3.18	5.13	5.03	3.43	0.34
7.36	5.07	2.18	2.68	2.68	1.28	5.76	5.64	3.49	3.65	3.65	4.05	5.06	4.94	4.15	0.55
8.47	4.94	2.99	3.64	3.64	1.86	5.78	5.71	4.68	4.62	4.62	5.10	4.93	4.81	4.98	0.91
9.75	4.74	4.02	4.86	4.86	2.72	5.70	5.69	6.04	5.76	5.76	6.27	4.73	4.63	5.89	1.46
11.22	4.48	5.25	6.27	6.27	3.89	5.51	5.57	7.47	6.98	6.98	7.46	4.45	4.40	6.79	2.21
12.91	4.13	6.59	7.72	7.72	5.32	5.20	5.32	8.77	8.14	8.14	8.50	4.09	4.11	7.56	3.13
14.86	3.71	7.84	8.99	8.99	6.88	4.76	4.95	9.68	9.02	9.02	9.19	3.64	3.74	8.04	4.14
17.10	3.22	8.82	9.79	9.79	8.35	4.20	4.46	9.99	9.39	9.39	9.34	3.12	3.31	8.09	5.10
19.68	2.68	9.31	9.92	9.92	9.45	3.55	3.87	9.60	9.11	9.11	8.86	2.55	2.81	7.65	5.89
22.65	2.13	9.19	9.30	9.30	9.92	2.84	3.20	8.57	8.17	8.17	7.78	1.98	2.27	6.76	6.41
26.07	1.60	8.42	8.01	8.01	9.62	2.14	2.51	7.09	6.74	6.74	6.25	1.44	1.74	5.57	6.69
30.00	1.12	7.14	6.27	6.27	8.55	1.50	1.85	5.35	5.05	5.05	4.52	0.98	1.25	4.26	6.80
34.53	0.50	5.58	4.41	4.41	6.98	0.88	1.27	3.62	3.40	3.40	2.87	0.18	0.83	3.04	6.87
39.74	0.00	4.10	2.79	2.79	5.38	0.00	0.52	2.16	2.04	2.04	1.42	0.00	0.01	2.04	7.01
45.74	0.00	2.92	1.60	1.60	4.05	0.00	0.00	1.10	1.07	1.07	0.00	0.00	0.00	1.33	7.18
52.64	0.00	2.06	0.84	0.84	3.02	0.00	0.00	0.05	0.46	0.46	0.00	0.00	0.00	0.87	7.18
60.59	0.00	1.47	0.40	0.40	2.21	0.00	0.00	0.00	0.01	0.01	0.00	0.00	0.00	0.59	6.83
69.73	0.00	1.04	0.19	0.19	1.55	0.00	0.00	0.00	0.00	0.00	0.00	0.00	0.00	0.42	6.04
80.25	0.00	0.73	0.09	0.09	1.01	0.00	0.00	0.00	0.00	0.00	0.00	0.00	0.00	0.32	4.90
92.37	0.00	0.50	0.06	0.06	0.60	0.00	0.00	0.00	0.00	0.00	0.00	0.00	0.00	0.25	3.59
106.31	0.00	0.32	0.05	0.05	0.31	0.00	0.00	0.00	0.00	0.00	0.00	0.00	0.00	0.20	2.34
122.35	0.00	0.19	0.04	0.04	0.04	0.00	0.00	0.00	0.00	0.00	0.00	0.00	0.00	0.16	1.31
140.81	0.00	0.10	0.04	0.04	0.00	0.00	0.00	0.00	0.00	0.00	0.00	0.00	0.00	0.12	0.06
162.06	0.00	0.03	0.04	0.04	0.00	0.00	0.00	0.00	0.00	0.00	0.00	0.00	0.00	0.09	0.00
186.52	0.00	0.00	0.03	0.03	0.00	0.00	0.00	0.00	0.00	0.00	0.00	0.00	0.00	0.06	0.00
214.66	0.00	0.00	0.00	0.00	0.00	0.00	0.00	0.00	0.00	0.00	0.00	0.00	0.00	0.04	0.00
247.06	0.00	0.00	0.00	0.00	0.00	0.00	0.00	0.00	0.00	0.00	0.00	0.00	0.00	0.02	0.00
284.34	0.00	0.00	0.00	0.00	0.00	0.00	0.00	0.00	0.00	0.00	0.00	0.00	0.00	0.02	0.00
327.25	0.00	0.00	0.00	0.00	0.00	0.00	0.00	0.00	0.00	0.00	0.00	0.00	0.00	0.02	0.00
376.64	0.00	0.00	0.00	0.00	0.00	0.00	0.00	0.00	0.00	0.00	0.00	0.00	0.00	0.00	0.00

APPLICATION OF GAUSSIAN CUBATURE TO MODEL TWO-DIMENSIONAL POPULATION BALANCES

Jerzy Bałdyga¹, Grzegorz Tyl^{*1}, Mounir Bouaifi²

¹Warsaw University of Technology, Department of Chemical and Process Engineering, Waryńskiego 1, 00-645 Warsaw, Poland

²Centre de Recherche et d'Innovation de Lyon, Solvay, 85 Avenue des Frères Perret, BP 62, 69192 Saint-Fons Cedex, France

In many systems of engineering interest the moment transformation of population balance is applied. One of the methods to solve the transformed population balance equations is the quadrature method of moments. It is based on the approximation of the density function in the source term by the Gaussian quadrature so that it preserves the moments of the original distribution. In this work we propose another method to be applied to the multivariate population problem in chemical engineering, namely a Gaussian cubature (GC) technique that applies linear programming for the approximation of the multivariate distribution. Examples of the application of the Gaussian cubature (GC) are presented for four processes typical for chemical engineering applications. The first and second ones are devoted to crystallization modeling with direction-dependent two-dimensional and three-dimensional growth rates, the third one represents drop dispersion accompanied by mass transfer in liquid-liquid dispersions and finally the fourth case regards the aggregation and sintering of particle populations.

Keywords: crystallization, drop breakage, extraction, Gaussian cubature, population balance, QMOM

1. INTRODUCTION

Multiphase reactors are very common in chemical industry and the population balance framework is considered as a pragmatic approach for modeling particulate, bubble or droplet dynamics in multiphase processes including polymerization, crystallization and precipitation systems. The last two processes i.e. crystallization and precipitation are used for more than 70% of solid materials produced by the chemical industry (Silva, 2007). Concerning industrial requirements it is preferred to have particles with high purity, desired size distribution, satisfactory stability and good shape. Producing a material with the desired quality often requires knowledge of the elementary steps involved in the process: creation of supersaturation, nucleation, particle growth, aggregation and other secondary processes. The product quality is mainly determined by operating conditions. However, these processes are still not well predictable because their course is strongly affected by complex interactions between fluid flow, mixing, particle aggregation and particle breakage subprocesses. Simple models are often used to interpret these effects but they do not account well for such complex interactions. To achieve real progress in an efficient process control and scale-up, a wide range of problems needs to be addressed by multidisciplinary, multiphysics and multiscale approaches – starting from the modeling of molecular level phenomena, to the crystal and, subsequently, the product design, including advanced measurement techniques coupled to advanced modeling tools. In order to properly model such complex

*Corresponding authors, e-mail: g.tyl@ichip.pw.edu.pl

phenomena, population balance equations supplemented with fast and efficient solution algorithms can be coupled with Computational Fluid Dynamics (CFD) modeling to correctly predict the particle size distribution (PSD).

One of the commonly used approaches for solving population balance equations in chemical engineering applications is the quadrature method of moments (QMOM), which has been introduced by McGraw (1997) to simulate the course of particulate processes. It is based on the approximation of the density function in the source term by the Gaussian quadrature so that it preserves the moments of the original distribution. In this method one determines weights and abscissas that are used in the quadrature approximation using inversion algorithms. McGraw (1997) applied the product-difference algorithm by Gordon (1968), although more such algorithms are available in the literature. One can mention the long quotient-modified difference algorithm from Sack and Donovan (1972) and the Golub-Welsch (1969) algorithm.

The Gaussian quadrature (GQ) approach generates the moment-preserving approximations for one-dimensional distributions. However, this feature does not generalize to multivariate probability distributions, with the exception of independent random variables.

Wright et al. (2001) extended the QMOM method to the multivariate population problem. As mentioned above, in this case no exact algorithms are available. Several attempts have been made to apply approximate algorithms also for the multidimensional case, which resulted for example in a multiple 3-point quadrature technique and a 12-point quadrature technique (Wright et al., 2001). The DQMOM equations (Marchisio and Fox, 2005) are derived via the moment transfer method, in a similar way to QMOM.

Currently there are no numerical techniques allowing to solve the closure problem generated by the moment transformation of population balance equations for the number of internal dimensions higher than two. In this work another method is proposed to be applied to the multivariate population problem in chemical engineering, namely a Gaussian cubature (GC) technique which applies linear programming for the approximation of the multivariate distribution. It can be applied to systems of an arbitrary number of internal dimensions without reformulation. This leads to simplicity of the solution method and shows universality of this approach. Gaussian cubatures are feasible for joint, but independent distributions. In spite of the fact that this method is heuristic for joint, dependent distributions, it appears to be reliable and to accurately approximate expectations of many functions. This approach has been used by DeVuyst and Preckel (2007) for the modeling of economic processes. Linear program returns weights (restricted to be positive) for each of the created lattice points. The maximum number of points with strictly positive weights is equal to the number of constraints used.

Examples of the application of the Gaussian cubature (GC) are presented in this paper for four processes typical for chemical engineering applications. The first and second cases are devoted to crystallization modeling with direction-dependent growth rates. The third one represents drop dispersion accompanied by mass transfer in liquid-liquid dispersions, and in the fourth case the aggregation and sintering of particle populations is considered. In the first, third and fourth cases, two-dimensional population balance equations (PBE) are used. In the second case a 3-dimensional crystal growth in the MSMPR crystallizer is simulated to show the possibility of the proposed numerical scheme to address the cases with more internal dimensions.

2. THE METHOD OF MOMENTS APPROACH FOR SOLVING POPULATION BALANCE EQUATIONS

The population balance equations are powerful tools that are used to predict the behavior of dispersed systems. For the first time they were introduced by Hulburt and Katz (1964) and emerged from the

dynamic description of a dispersed system treated as a statistical ensemble moving through the phase space. This statistical mechanical approach resulted in the system of integro-differential equations (Eq. (1)) governing the evolution of the distribution f , of dispersed phase properties in a way similar to the Liouville theorem of classical statistical mechanics (Sorgato, 1981; Hulburt and Katz, 1964).

$$\frac{\partial f}{\partial t} + \sum_{i=1}^3 \frac{\partial \{v_i(\mathbf{x}, t) f\}}{\partial x_i} + \sum_j^N \frac{\partial \{G_j f\}}{\partial r_j} = B(\mathbf{x}, \mathbf{r}, t) - D(\mathbf{x}, \mathbf{r}, t) \quad (1)$$

The phase space consists of external coordinates, \mathbf{x} , describing the position of particles in the physical space and internal coordinates, \mathbf{r} , that characterize properties of the dispersed phase, i.e. the size of particles or droplets, species concentration within droplets, fractal dimension of aggregates and many other. The convective flow of points through the phase space is described by the velocities v_i in the physical space, and G_j in the space of internal coordinates, which can be physically interpreted as the growth rate of crystals or dissolution of liquid droplets depending on the system under consideration. Also new points can appear or disappear in the phase space corresponding to effects of breakage or coalescence of droplets, as well as aggregation and breakage of solid crystals. Those effects are defined by the birth and death functions, $B(\mathbf{x}, \mathbf{r}, t)$ and $D(\mathbf{x}, \mathbf{r}, t)$. Although the population balance equations are well defined, they are difficult to solve due to high dimensionality of the system, especially when nonlinear source terms are present. For linear cases, Hulburt and Katz (1964) introduced the method of moments which allowed to transform the set of partial differential equations into the set of ordinary differential equations and reduce the dimensionality of the system. The transformed set of population balance equations is easier to solve. However, instead of the full distribution of the dispersed phase properties one gets only average values defined by the moments of distribution:

$$m_{k_1, k_2, \dots, k_N} = \int_0^\infty \dots \int_0^\infty r_1^{k_1} r_2^{k_2} \dots r_N^{k_N} f(\mathbf{r}, t) dr_1 dr_2 \dots dr_N \quad (2)$$

The expected values of distribution can describe many physical properties of the dispersed phase like the number of particles, average size, area or volume. The set of the ordinary differential equations for the moments is generated by the moment transformation as given below:

$$\begin{aligned} \int_0^\infty \dots \int_0^\infty r_1^{k_1} r_2^{k_2} \dots r_N^{k_N} \left(\frac{\partial f}{\partial t} + \sum_{i=1}^3 \frac{\partial \{v_i(\mathbf{x}, t) f\}}{\partial x_i} + \sum_j^N \frac{\partial \{G_j f\}}{\partial r_j} \right) dr_1 dr_2 \dots dr_N = \\ = \int_0^\infty \dots \int_0^\infty r_1^{k_1} r_2^{k_2} \dots r_N^{k_N} (B(\mathbf{x}, \mathbf{r}, t) - D(\mathbf{x}, \mathbf{r}, t)) dr_1 dr_2 \dots dr_N \end{aligned} \quad (3)$$

In many cases the birth and death functions consist of nonlinear terms, a good example here is aggregation. In such cases the moment transformation creates the closure problem, i.e. the set of equations becomes unclosed as there are more unknowns than equations. The closure problem can be solved by introducing some additional information. For systems with one internal dimension this can be done by using the quadrature method of moments (QMOM) introduced by McGraw (1997). It applies a quadrature approximation of the source term integrals using so called inversion algorithms such as a product-difference (PD) algorithm (Gordon, 1968). QMOM has been further generalized to bivariate cases (Wright et al., 2001) i.e. where two internal coordinates are used to describe the dispersed phase system. In the current state of the art there are no numerical techniques allowing to solve without approximation the closure problem generated by the moment transformation of population balance equations for the number of internal dimensions higher than two. Therefore another efficient approximate method, the Gaussian Cubature (GC) numerical scheme, has been developed to approach the closure problem in multidimensional cases for an arbitrary number of internal coordinates.

3. GAUSSIAN CUBATURE TECHNIQUE

The introduced technique is based on the approximation of the source term integrals in the moment - transformed PBEs by a Gaussian cubature, such that:

$$E[g(\mathbf{X})] = \int g(\mathbf{X}) f(\mathbf{X}) d\mathbf{X} \approx \sum_{i=1}^N g(\mathbf{X}_i) w_i \quad (4)$$

where \mathbf{X} is an s -dimensional vector of random variables having density $f(\mathbf{X})$, and $g(\mathbf{X})$ denotes the integrand function i.e. function whose expected value is to be computed.

To apply this approximation it is necessary to determine weights w_i , and abscissas \mathbf{X}_i of the cubature points. GC technique chooses points and weights for the cubature approximation so as to preserve the lower-order moments of the original distribution. A d -degree GC approximation can be defined by the following system of linear equations:

$$\sum_{i=1}^N w_i \prod_{j=1}^s (x_{ij})^{k_j} = E \left[\prod_{j=1}^s (X_j)^{k_j} \right] \quad (5)$$

with

$$\sum_{j=1}^s k_j \leq d, k_j \geq 0, w_i \geq 0 \quad (6)$$

By E the expectation value is denoted, hence the right-hand sides of Equation (5) are the raw moments of order at most d of the approximated distribution.

To determine weights and abscissas of the cubature points it is necessary to set up a lattice in s -dimensional domain. It is done by following the algorithm presented by DeVuyst and Preckel (2007). First an equally spaced grid over each variable is set up. The range of each variable has to be chosen based on the knowledge of the process conditions. The number of created grid points is an important parameter that determines the convergence of the algorithm (more points to choose from) but also sufficiently influences calculation time, so it has to be chosen as low as possible but large enough to ensure determination of the cubature points. The lattice in s -dimensional phase space is formed by a Cartesian product of the previously created grids over each axis.

The second step is to set up a linear program (LP) over the lattice points using the system expressed by Eq. (5) as the equality constraints. Because one is interested in obtaining any set of points having positive weights that satisfy Eq. (5), the objective function vector is set to zero. The LP can be solved via Simplex method, which results in a set of weights associated to vectors of the feasible basis. Each of those vectors corresponds to the specific point in the phase space resulting in a complete set of points with associated weights for the cubature approximation.

During iterative solving of population balance equations the GC is calculated in each time step and then used to determine integrals in the source term. It occurred that during the time evolution of the initial distribution, the above presented algorithm could not find a feasible solution even for a dense lattice. Therefore some changes have been introduced to the algorithm to assure better convergence. The most important modification is the exchange of the set of equality constraints, Eq. (5), for the set of inequality constraints defined as follows:

$$\sum_{i=1}^N w_i \prod_{j=1}^s (x_{ij})^{k_j} \leq E \left[\prod_{j=1}^s (X_j)^{k_j} \right] \cdot (1 + Tol) \quad (7)$$

$$\sum_{i=1}^N w_i \prod_{j=1}^s (x_{ij})^{k_j} \geq E \left[\prod_{j=1}^s (X_j)^{k_j} \right] \cdot (1 - Tol) \quad (8)$$

In the above set, Tol denotes the tolerance of moments determination by the linear program. Introducing this parameter enables one to control the desired accuracy but also for some cases allows the LP to find a feasible solution. This modification also makes it easy to find the initial feasible basis for the linear programming solver. The initial basis consisting of vectors corresponding to the slack variables is in this case dual-feasible, hence the dual-simplex algorithm is further used to solve the LP.

To demonstrate the possibilities of the above introduced algorithm, four test cases are presented in the following sections. The first one regards the seeded crystallization process including the nucleation and growth of crystals in two directions (2D growth). Then a 3-dimensional population balance model of crystal growth and nucleation will be presented, showing the possibility of applying the above presented numerical scheme. The third test case is the extraction process in a water-acetone-toluene system. Bivariate population balance is used to simulate the simultaneous drop breakage and mass transfer in the system. In the last test case the aggregation and sintering of the population of particles is considered, which has been also approached by Wright et al. (2001) when introducing the bivariate extension of the QMOM technique. PBEs are solved using MATLAB programming language and the dual-simplex algorithm implemented in the software.

4. APPLICATION OF GC TO CRYSTALLIZATION PROCESS

4.1. 2D case

As the first test case for the presented method the two-dimensional population balance model of the pharmaceutical crystallization process (Sen et al., 2014) has been chosen. Sen et al. (2014) developed a model for the growth of crystals in two dimensions. Model constants for the kinetics of the process have been also determined. The population balance equation describing this process takes the form:

$$\frac{\partial f(L_1, L_2, t)}{\partial t} + \frac{\partial (G_1(L_1, t) f(L_1, L_2, t))}{\partial L_1} + \frac{\partial (G_2(L_2, t) f(L_1, L_2, t))}{\partial L_2} = B_0(C, t) \delta(L_1) \delta(L_2) \quad (9)$$

Where G_1 and G_2 denote the rate of crystal growth in directions L_1 and L_2 respectively and B_0 stands for the rate of nucleation. The growth rates can be written as follows (Gunawan et al., 2004):

$$G_1 = k_{g1} \left(\frac{C - C_{sat}}{C_{sat}} \right)^{g_1} \quad (10)$$

$$G_2 = k_{g2} \left(\frac{C - C_{sat}}{C_{sat}} \right)^{g_2} \quad (11)$$

In this model only secondary nucleation is taken into account and its rate is given by:

$$B_0 = k_b S(L_1, L_2, t) \left(\frac{C - C_{sat}}{C_{sat}} \right)^{bs} \quad (12)$$

Kinetic constants: k_{g1} , k_{g2} , k_b , g_1 , g_2 , have been determined by Sen et al. (2014) by fitting them to experimental data. In the above equation C stands for the concentration of the solute and C_{sat} denotes the solubility of the solute. Since it is assumed that the shape of crystals is cuboid with two

characteristic dimensions L_1 and L_2 , the surface area of the single crystal is $2L_1^2 + 4L_1L_2$, which after integration over the whole population results in the total surface area of the crystals $S(L_1, L_2, t)$:

$$S(L_1, L_2, t) = \int_0^\infty \int_0^\infty F(L_1, L_2, t) (2L_1^2 + 4L_1L_2) dL_1 dL_2 \quad (13)$$

The above presented model has to be solved simultaneously with the mass balance in the form:

$$\frac{dC}{dt} = -\rho_c \int_0^\infty \int_0^\infty F(L_1, L_2, t) (2G_1(L_1L_2 - L_1^2) + G_2L_1^2) dL_1 dL_2 \quad (14)$$

where ρ_c stands for the density of crystals.

The described crystallization process is a cooling process so the nucleation and growth of crystals are caused by the decrease in solute solubility with decreasing temperature. For the test case of our GC technique, linear solubility change in time has been used (data set 1.1 from Sen et al. (2014)). The density of crystals has been assumed by us to be $\rho_c = 1500 \text{ kg/m}^3$. Moment transformation of (9) results in the system of ordinary differential equations for the lower-order moments of crystal size distribution. There is no closure needed in the model, hence it can be solved explicitly and therefore is the perfect base for comparison to the introduced GC technique. The parameters chosen to be compared for this process are the characteristic length and aspect ratio defined as follows:

$$D_{avg} = \left(\overline{L_1 L_2^2} \right)^{1/3} \quad (15)$$

$$AR = \frac{\overline{L_1}}{\overline{L_2}} \quad (16)$$

Calculations were made using cubature of degrees 3 and 5. In this case they both gave exactly the same results because only moments of order equal of less than 3 were needed to calculate D_{avg} and AR .

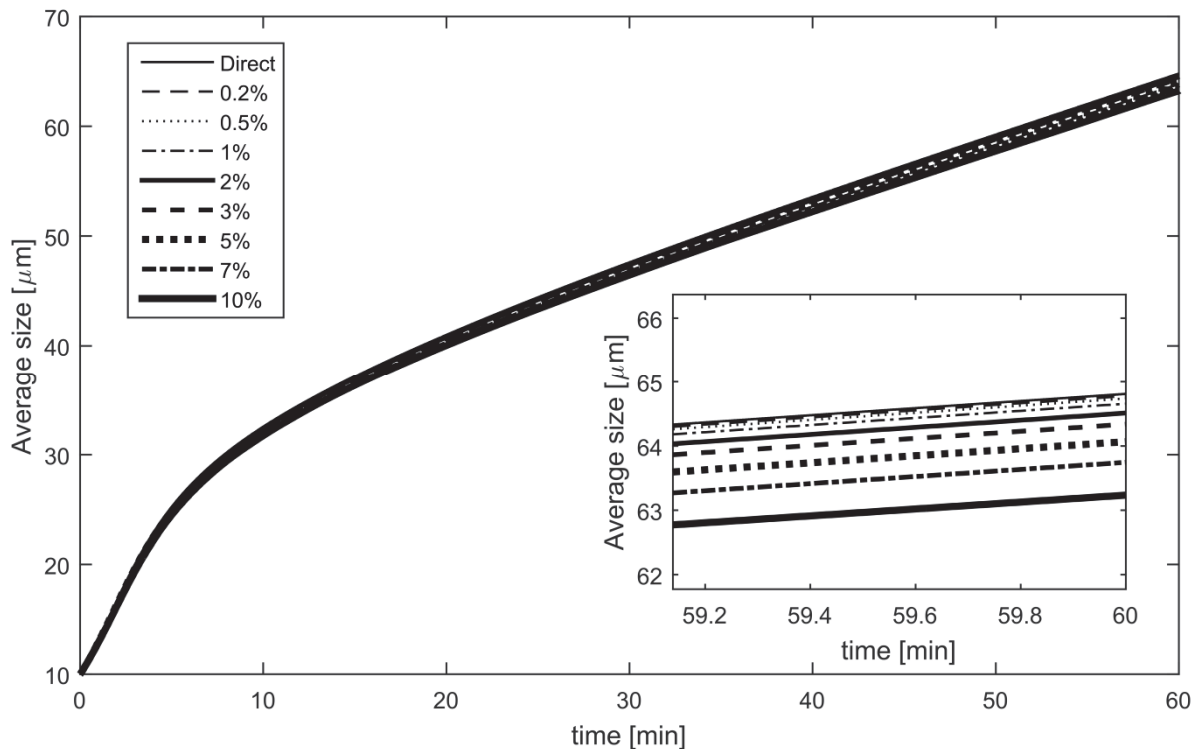


Fig. 1. Comparison of calculated crystal average size for different cubature tolerance with results of direct solution

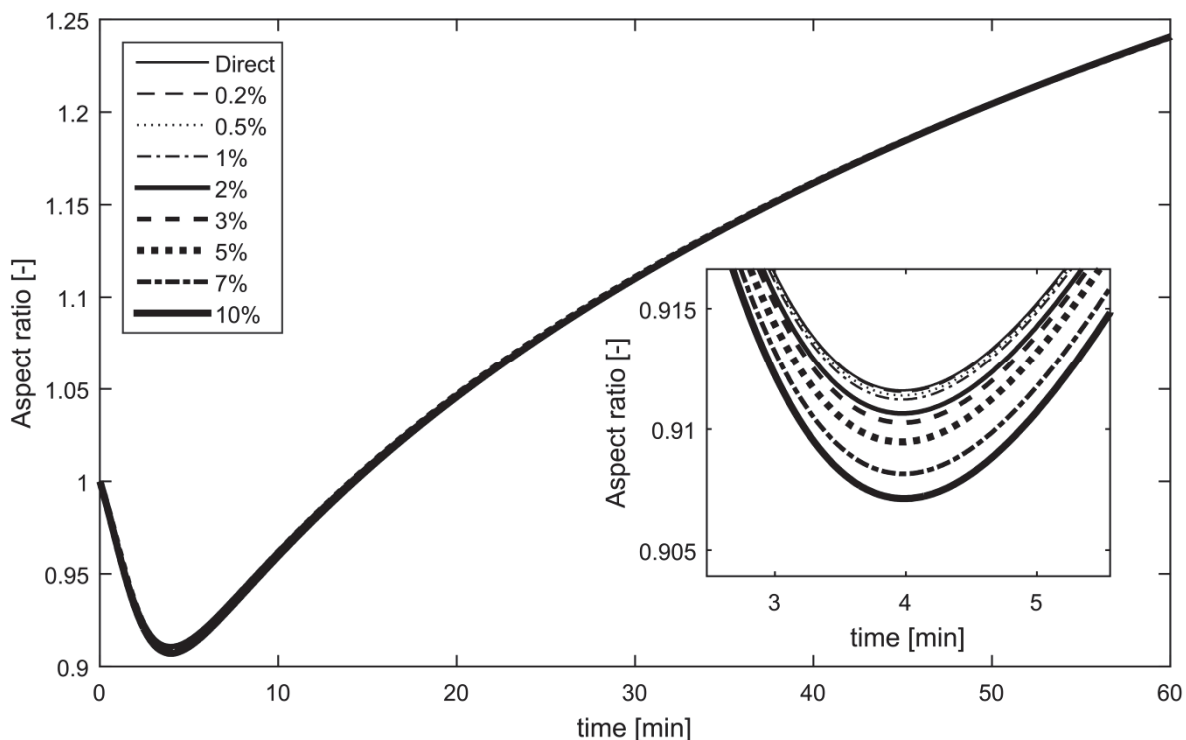


Fig. 2. Comparison of aspect ratio for different cubature tolerances with results of direct solution

Table 1. Percent error of characteristic size and aspect ratio determination

Tolerance	Final average size [μm]	Error [%]	Final Aspect Ratio	Error [%]
Direct	64.810	0.000	1.2399	0.000
0.20%	64.776	-0.052	1.2399	0.000
0.5%	64.737	-0.113	1.2399	0.000
1%	64.657	-0.236	1.2401	0.016
2%	64.511	-0.461	1.2401	0.016
3%	64.337	-0.730	1.2401	0.016
5%	64.067	-1.146	1.2405	0.048
7%	63.746	-1.642	1.2401	0.016
10%	63.235	-2.430	1.2407	0.065

In Figs. 1 and 2 time dependencies of those parameters are presented. It can be noticed that increasing the cubature tolerance only slightly influences the calculated final crystal size but has almost no influence on the final aspect ratio. The relative error of average size and aspect ratio determination is presented in Table 1.

An important factor influencing the calculation time and the minimum possible tolerance is the number of divisions of each axis. Increasing the number of points along each axis enables to decrease the cubature tolerance but also sufficiently influences calculation time due to the significant rise in the number of lattice points. Calculation time of 6000 time steps is presented in Table 2. It can be noticed that for a certain number of domain divisions there exists a minimum achievable tolerance where the linear program solver can still find a feasible solution in each time step. Execution time generally does not depend on the cubature tolerance but for some reason for 20 axis divisions and 7% tolerance it calculates two times faster. A similar minimum seems to exist for 50 axis divisions and 1% tolerance.

The tolerance of 0.2% can be achieved with 80 axis divisions but it also results in the increase in execution time of up to around 1200s.

Table 2. Calculation time in seconds of 6000 time steps depending on cubature tolerance and number of axis divisions (Intel Core i7-2630QM 2GHz, 8GB DDR3)

Tolerance	Number of axis divisions		
	10	20	50
10%	589	581	787
7%	-	296	818
5%	-	598	807
3%	-	561	817
2%	-	-	833
1%	-	-	659
0.5%	-	-	872

4.2. 3D case

The crystal growth case can be extended to the 3D model if one needs to consider the independent growth of each crystal face. The natural extension is the growth model of 3D cuboid shaped crystals. As an example a process taking place in the MSMMPR continuous crystallizer is considered. The process kinetics has been taken from Borchert et al. (2009). In this paper the authors considered a system in the steady state and checked the influence of the mean residence time on crystal dimensions. In the present work a dynamic model has been developed and solved using GC to check if it converges to the steady state results presented in the paper by Borchert et al. (2009). Similarly as in the previous test case the model equations were solved directly to have the dynamic results for comparison. A cuboid shape of crystals has been assumed with crystal dimensions, h_1, h_2, h_3 , measured from the center. For the simulation the following set of moments of crystal size distribution: $m_{0,0,0}, m_{1,0,0}, m_{0,1,0}, m_{0,0,1}, m_{1,1,1}, m_{2,0,0}, m_{0,2,0}, m_{0,0,2}, m_{1,1,0}, m_{1,0,1}, m_{0,1,1}$ was used. This is equivalent to the GC of degree 2 with the additional moment $m_{1,1,1}$ that is present in the mass balance and therefore has to be accurately determined to minimize the error. After performing the moment transformation of the population balance equations one gets the following set of governing equations for the moments of crystal size distribution in the crystallizer having mean residence time θ :

$$\frac{dm_{0,0,0}}{dt} = B_0 - \frac{m_{0,0,0}}{\theta} \quad (17)$$

$$\frac{dm_{k,l,n}}{dt} = kG_1 m_{k-1,l,n} + lG_2 m_{k,l-1,n} + nG_3 m_{k,l,n-1} - \frac{1}{\theta} m_{k,l,n} \quad (18)$$

where G_1, G_2, G_3 are the face specific growth rates given by:

$$G_i = k_{g,i} \sigma^{g_i} \quad (19)$$

Kinetic constants $k_{g,i}$ and g_i are taken directly from the paper by Borchert et al. (2009) and the supersaturation is defined as follows:

$$\sigma = \frac{C - C_{sat}}{C_{sat}} \quad (20)$$

where C is the mass concentration of the solute and C_{sat} denotes the saturation concentration.

The rate of nucleation, B_0 , is assumed to be a power law dependency:

$$B_0 = k_b \sigma^b \quad (21)$$

It should be noted that the system parameters in the paper by Borchert et al. (2009) do not refer to a specific physical system.

Simultaneously to the population balance equations, the mass balance given by Eq. (22) has been solved.

$$\frac{dC}{dt} = \frac{1}{\theta} (C_{in} - C) - 8\rho_s \left(\frac{dm_{1,1,1}}{dt} \right)_{kin} \quad (22)$$

Where ρ_s denotes the solid density. The first term on the right-hand side of Eq. (22) describes the net flux of the solute to the system. The second term represents the decrease of solute concentration due to crystallization. Subscript *kin* denotes the first three terms on the right-hand side of Eq. (18) that describe the concentration drop described by the crystal growth kinetics. These three terms of Eq. (18) are substituted to Eq. (22) for $k, l, m = 1$.

The considered system has been simulated for two mean residence time values, $\theta = 0.36$ s and $\theta = 1$ s, which correspond to the characteristic points predicted by the steady state model. As the initial condition a supersaturated state was assumed with the inlet and outlet solutions having equal supersaturation, $\sigma_0 = \sigma_{in} = 2$. In Fig. 3. the evolutions of the characteristic crystal dimensions obtained using GC and by direct calculation are presented depending on the mean residence time in the crystallizer. In the first case (Fig. 3a)) the needle-like shape of the crystals is observed, which also corresponds to the result presented by Borchert et al. (2009). In the second case (Fig. 3b)) the cubic crystal shape is predicted, which also was obtained by the steady state model. The cubature tolerances used in those cases were 0.01 and 0.02 respectively. For both accuracy levels the results do not differ much from results of the direct solution of the PB. The comparison of relative error obtained using GC approximation is presented in Table. 3. One can see that while for the crystal dimensions the relative error is of the order of a few percent, for supersaturation it is actually negligible even for the higher tolerance. The evolution of supersaturation in time is virtually identical for both numerical methods (see Fig. 4.).

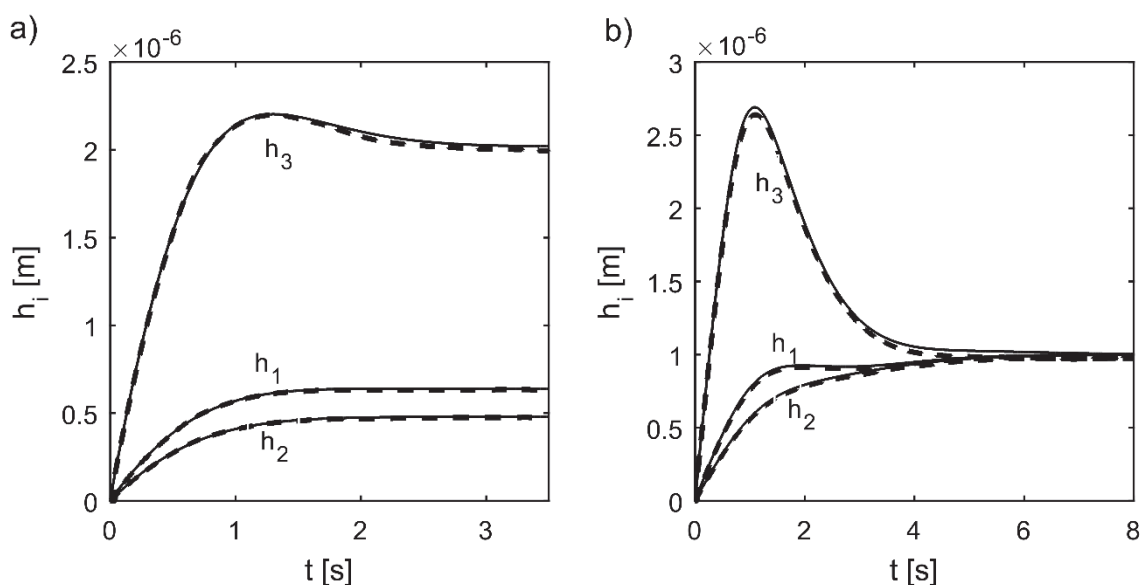


Fig. 3. Time evolution of the characteristic crystal dimensions for different mean residence times (direct solution - solid line, GC - dashed line); a) $\theta = 0.36$ s, b) $\theta = 1$ s

Table 3. Relative error of determining the steady state values using GC approximation for the considered cases

	$\theta = 0.36$ s			$\theta = 1$ s		
	Direct	Cubature	Error [%]	Direct	Cubature	Error [%]
h_1 [m]	6.40E-07	6.31E-07	1.41	1.00E-06	9.63E-07	3.73
h_2 [m]	4.80E-07	4.73E-07	1.42	1.00E-06	9.63E-07	3.68
h_3 [m]	2.02E-06	1.99E-06	1.35	1.00E-06	9.60E-07	4.01
σ [-]	1.7768	1.7765	0.02	1.0000	0.9989	0.11

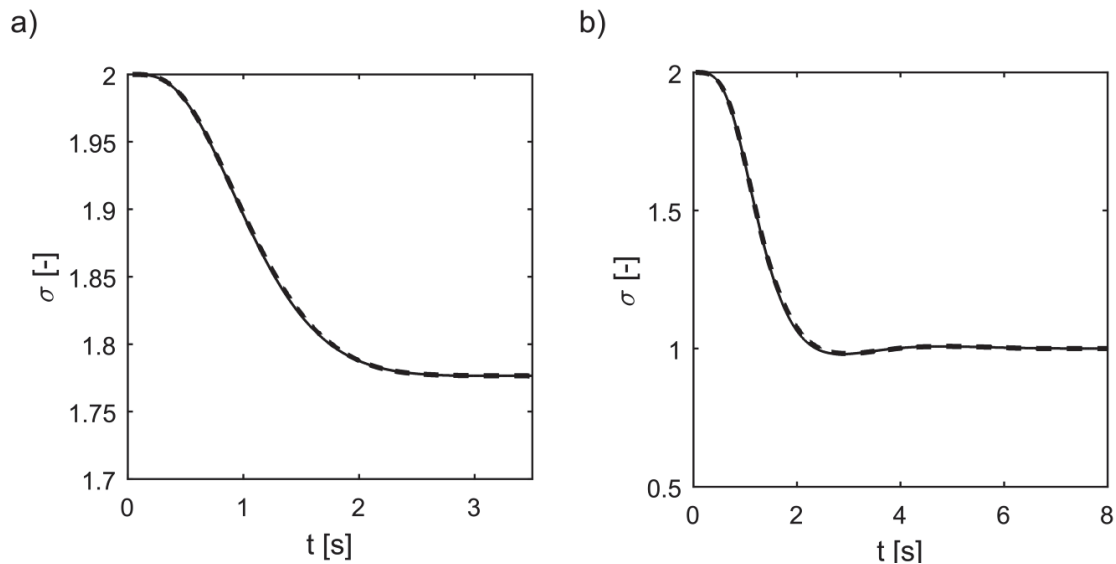


Fig. 4. Evolution of the supersaturation in the crystallizer predicted using GC and direct method for a) $\theta = 0.36$ s, b) $\theta = 1$ s (direct method - solid line, GC - dashed line)

5. APPLICATION OF GC TO MODELING OF MASS TRANSFER IN LIQUID - LIQUID SYSTEMS

For the full description of some processes like extraction or absorption it is necessary to follow not only the dispersed phase size distribution but also concentration of the extracted/absorbed component in both phases. The system under investigation is water-benzoic acid-toluene with water as the continuous phase, toluene as the dispersed phase and benzoic acid as the component transferred between phases. The dispersion is mixed in a 10 dm³ stirred tank (diameter, $T = 0.23$ m, height, $H = 0.24$ m) equipped with a 0.133 m diameter Rushton turbine.

For the modeling the two-cell model introduced by Okamoto (1981) is applied. Population balance equations are solved using GC technique and compared with results obtained using bivariate quadrature method of moments with a 3-point quadrature technique for the approximation of weights and abscissas. In QMOM diameter is chosen to be the main coordinate on which the process depends, therefore abscissas on the size axis are first calculated from the moments of distribution with respect to diameter using product-difference algorithm and then concentrations are calculated from the mixed moments $m_{3,1}$, $m_{4,1}$, $m_{5,1}$ which define a linear system of equations.

The partition coefficient of the benzoic acid has been calculated from the formulas proposed by Brändström (1966):

$$\frac{C_{BT}}{C_{HBW}} = 1.09 + 1.009C_{HBW} \quad (23)$$

where C_{BT} is the total concentration of benzoic acid in toluene and C_{HBW} is the concentration of not dissociated benzoic acid in water. The mass transfer coefficient introduced by Batchelor (1980) has been used with diffusion coefficient of the benzoic acid in water in 20 °C equal to $D = 0.91 \times 10^{-9} \text{ m}^2 \text{ s}^{-1}$. Driving force of the mass transfer process is:

$$\Delta C = \langle C_{bulk} \rangle - C_{HBW} \quad (24)$$

Where C_{HBW} is the concentration of the benzoic acid in water which would be in the equilibrium state with C_{BT} concentration in the dispersed phase so it directly depends on the droplet composition. The mean concentration of acid in the bulk $\langle C_{bulk} \rangle$ is calculated from the mass balance of the transferred component in the form:

$$V \cdot \phi \cdot (\langle C_d \rangle_0 - \langle C_d \rangle) = V \cdot (1 - \phi) \cdot (\langle C_{bulk} \rangle - \langle C_{bulk} \rangle_0) \quad (25)$$

which gives:

$$\langle C_{bulk} \rangle = \langle C_{bulk} \rangle_0 + \frac{\phi}{1 - \phi} (\langle C_d \rangle_0 - \langle C_d \rangle) \quad (26)$$

It should be noted that in this case there are no direct solutions and the methods based on approximation have to be used. In the comparison of QMOM and GC model predictions, toluene is assumed to be the dispersed phase. Benzoic acid is initially present only in the droplets and transfers to the bulk during the process. In the calculations dispersed phase concentration $\phi = 10\%$ is used. Average energy dissipation rate in the tank is assumed to be $\varepsilon = 5 \text{ W/kg}$.

The applied model consists of breakage kernel developed by Bałdyga and Podgórska (1998) based on the multifractal model of intermittency described in detail by Bałdyga and Bourne (1993, 1995). The continuous parabolic daughter size distribution introduced by Hill (1995) has been used.

In Figs. 5 and 6 predicted mean drop diameters are presented. Results obtained using the introduced GC technique are in agreement with QMOM predictions for d_{10} as well as for Sauter diameter d_{32} . Time dependence of the mean concentration of benzoic acid in the dispersed phase is presented in Fig. 7. In this case GC technique gives the same prediction as the QMOM. Details regarding the application of GC algorithm to modeling of mass transfer in liquid-liquid dispersions are presented in Appendix.

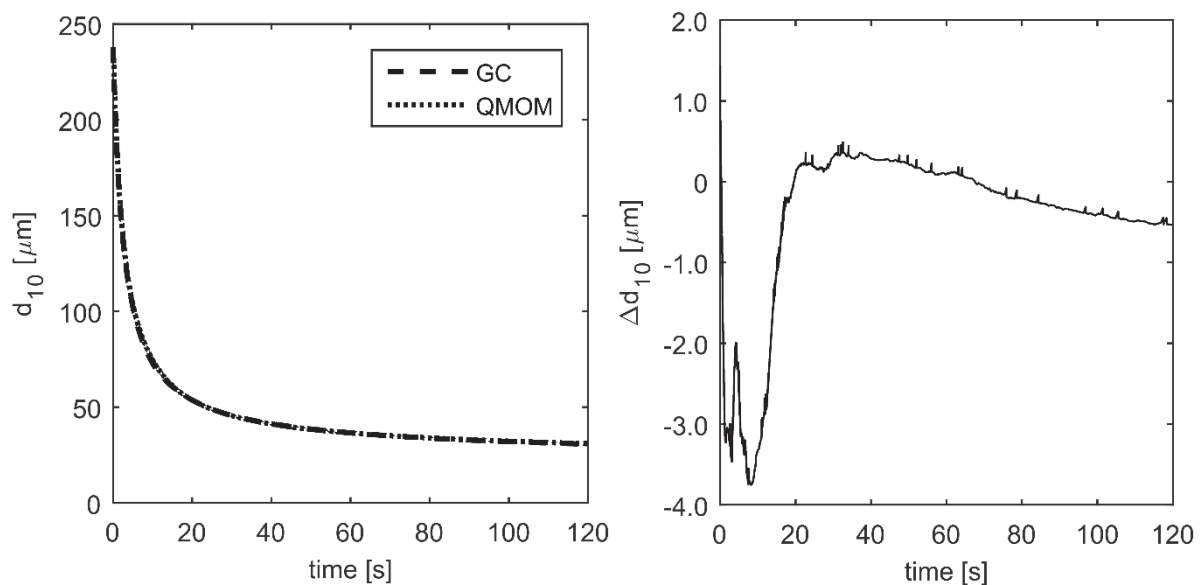


Fig. 5. Comparison of mean drop size d_{10} calculated using GC and QMOM. Δd_{10} denotes the difference between the results obtained using GC and QMOM techniques

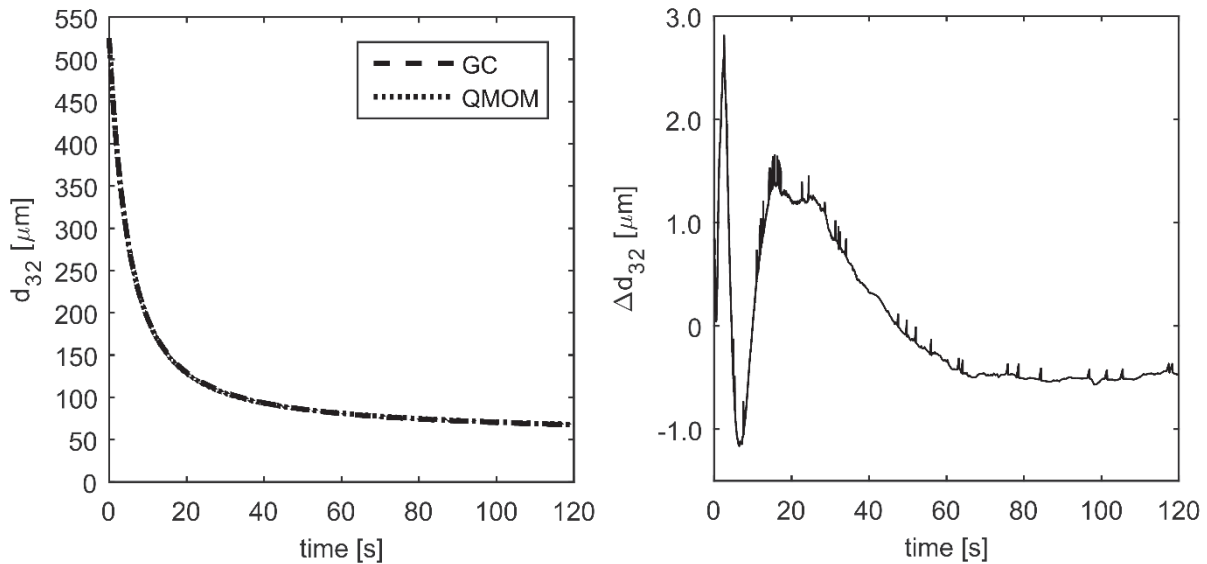


Fig. 6. Comparison of droplet Sauter diameter d_{32} calculated using GC and QMOM. Δd_{32} denotes the difference between the results obtained using GC and QMOM techniques

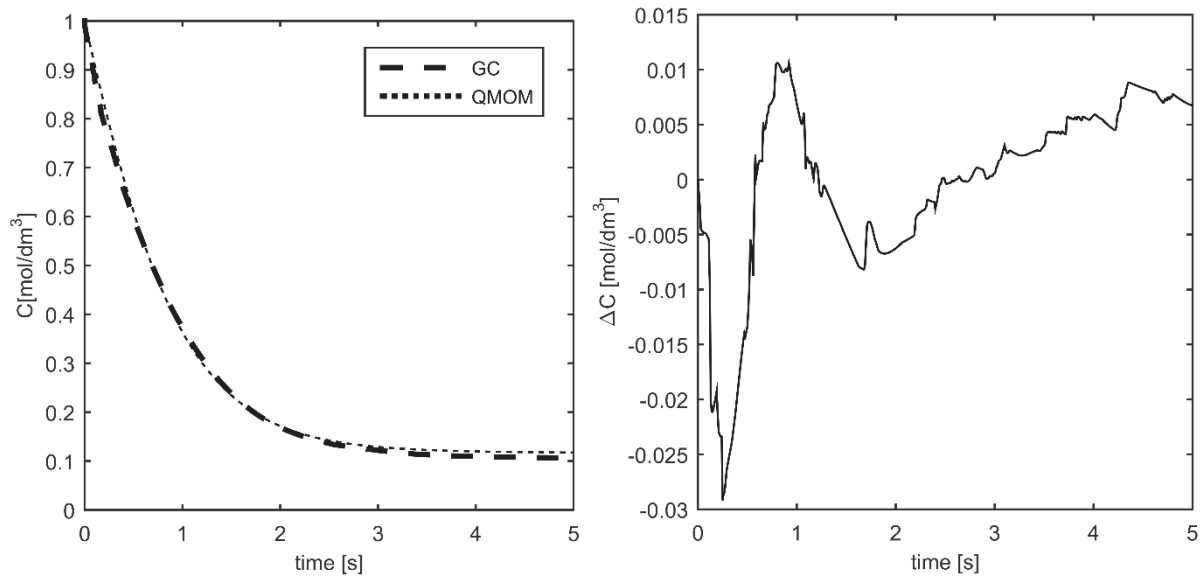


Fig. 7. Evolution of the mean concentration of benzoic acid in the dispersed phase. ΔC denotes the difference between the results obtained using GC and QMOM techniques

6. APPLICATION OF GC TO MODELING OF AGGREGATION AND SINTERING OF SOLID PARTICLES

The last test case regards the 2-dimensional model of aggregation and sintering of particle populations considered earlier by Wright et al. (2001). Aggregation is modeled by the Brownian coagulation kernel (Eq. 27) and the sintering by the convection in the phase space using relaxation term (Eq. 28).

$$\beta(V_1, V_2) = K \cdot (V_1^{-1/D_f} + V_2^{-1/D_f}) (V_1^{1/D_f} + V_2^{1/D_f}) \quad (27)$$

$$\left[\frac{\partial f(V_p, a)}{\partial t} \right]_{sint} = - \frac{\partial}{\partial a} [\dot{a} f(V_p, a)] \quad (28)$$

with

$$\dot{a} = - \frac{1}{t_f} (a - a_{min}) \quad (29)$$

where a_{min} is the area of a fully compacted (spherical) particle and t_f is the characteristic time of sintering. In this case we have assumed $t_f = 10$ s, $K = 1$ m³/s, and $D_f = 3$ after McGraw et al. (2001). The initial distribution was lognormal over each axis with the initial moments taken directly from the paper.

Due to the presence of nonlinear terms in the PB equations the closure problem is generated by the moment transformation. The model has been solved using GC and two variants of bivariate QMOM for comparison. Both of them are 3 point bivariate quadrature techniques. QMOM(v) has volume chosen to be the primary variable. It means that first the monovariate quadrature is calculated from pure volume moments and then the corresponding specific areas are recalculated from moments of order 1/3 over the area. QMOM(a) is constructed similarly using the area as the primary variable. They are less exact than the complete 12p QMOM but much faster.

In GC the moments of the order up to 2 were followed, plus the 1/3 and -1/3 moments over the volume coordinate due to their presence in the aggregation kernel. 50 axis divisions and 0.1% tolerance have been used. The calculation time was 12.15 s/1000 time steps for the QMOM techniques and 79.6 s/1000 time steps for GC. We can see that the QMOM is faster but the more accurate techniques like 12p QMOM are about 100 times slower than QMOM as stated by the authors. For 12p QMOM we would also need to follow 36 moments of the distribution compared to 7 moments needed for the GC.

In Fig. 8 the time changes of average volume and average surface area of the particles are presented. We can see that the GC can predict accurately the effect of aggregation as well as sintering. QMOM(v) results for the area differ from the others when predicting surface area and QMOM(a) predicts aggregation effect less accurately.

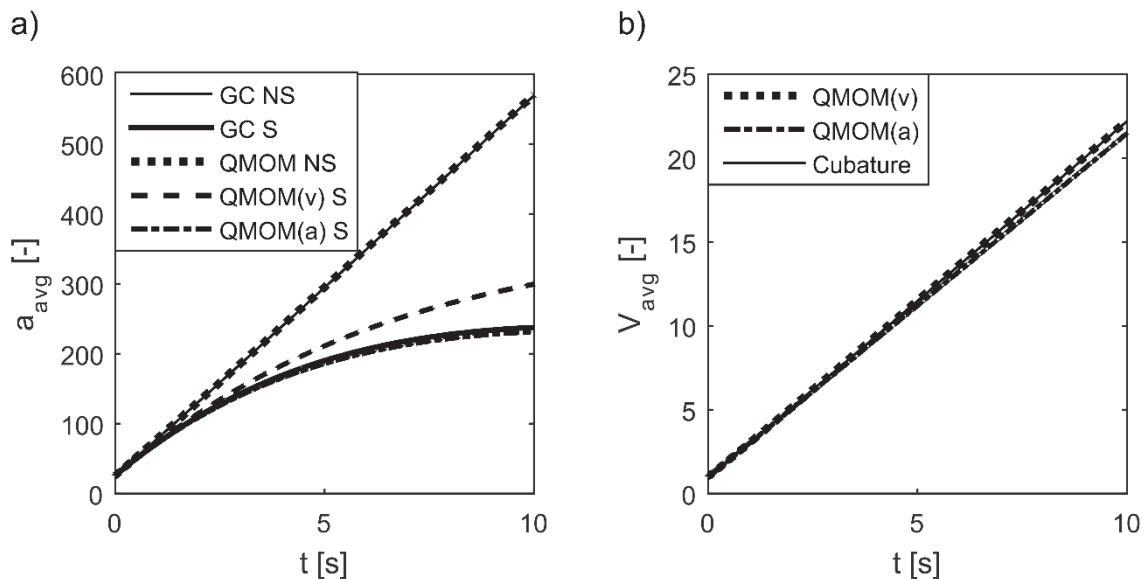


Fig. 8. Time evolution of a) average surface area, b) average volume of the particle population (NS - without sintering, S - with sintering)

7. CONCLUSIONS

A new moment based method for solving multidimensional population balance has been applied to chemical engineering processes. This new approach uses linear programming algorithms to develop a Gaussian cubature approximation of multivariate distributions which is further used to solve PBEs. The method has been applied to bivariate and 3-dimensional population balances, and proved to accurately describe the evolution of systems under investigation. Therefore it can be considered as a promising technique for the future implementation in CFD codes. Compared to other methods like QMOM the presented algorithm has no limitations in the number of internal dimensions and therefore it can be used to precisely determine the evolution of many independent parameters of the system under consideration. Also, the algorithm itself does not require any reformulation before being applied to higher dimensional systems, which makes it convenient to use. However, there are two parameters to be adjusted by the user, which severely influences the performance of this numerical scheme. From those two i.e. the grid resolution and cubature tolerance the latter seems to be more important for the overall performance while keeping the grid density in reasonable range (between 20 and 50 divisions of each axis). The tolerance influences the convergence of the algorithm and its precision. To overcome the problem of lack of convergence at some points in simulations, which would cause the crash of the program, the authors suggest using a loop, which in each time step starts the cubature with low tolerance. In the case of no convergence the tolerance should be subsequently increased to the level which allows for convergence. For simulations of higher dimensional systems another problem may arise, namely a significant increase in the number of lattice points with the rising number of axis divisions. In those cases it would be necessary to decrease the number of axis divisions at the cost of increasing the tolerance to keep the execution time reasonable. Those issues will have to be addressed before implementing the GC algorithm in the CFD code to ensure the stability and convergence of the simulation.

The authors gratefully acknowledge the financial support from Solvay, France.

SYMBOLS

a	dimensionless surface area of the particle
a_{avg}	dimensionless average surface area of the population of particles
a_{min}	dimensionless area of the fully compacted particle
AR	aspect ratio
$B(\mathbf{x}, \mathbf{r}, t)$	birth function
B_0	nucleation rate, $\text{m}^{-3}\text{s}^{-1}$
C	concentration of solute, kg/m^3
C_{bulk}	concentration of benzoic acid in water phase, mol/dm^3
C_{BT}	equilibrium concentration of benzoic acid in toluene, mol/dm^3
C_d	concentration of benzoic acid in toluene phase, mol/dm^3
C_{HBW}	equilibrium concentration of benzoic acid in water, mol/dm^3
C_{sat}	saturation concentration, kg/m^3
d	degree of GC approximation
d_d	droplet diameter, μm
d_{10}	average droplet size, μm
d_{32}	droplet Sauter diameter, μm
D	diffusion coefficient of benzoic acid in water, m^2s^{-1}
$D(\mathbf{x}, \mathbf{r}, t)$	death function
D_{avg}	average crystal size, m

D_f	fractal dimension
E	expectation value
f	number density function
$g(d')$	breakage kernel, s^{-1}
$g(\mathbf{X})$	arbitrary function of vector \mathbf{X}
G_i	growth rate in i -th dimension
h_1, h_2, h_3	characteristic dimensions of cuboid crystal, m
k_b	kinetic constant, $m^{-3}min^{-1}$
$k_{g,1}, k_{g,2}$	kinetic constants, m/min
K	constant in the aggregation kernel
L_i	length of crystal in i -th dimension, m
m_i	raw moment of the distribution of order i
N	number of cubature points
$\mathbf{r}=[r_1, r_2, \dots, r_N]$	vector of internal coordinates
s	number of phase space dimensions
t	time, s
Tol	cubature tolerance
V_1, V_2	dimensionless volumes of the aggregating particles
V	volume of stirred tank, dm^3
V_{avg}	dimensionless average volume of the population of particles
V_p	dimensionless volume of the particle
v_i	i -th component of the velocity vector in physical space, m/s
w_i	weight of the i -th cubature point
$\mathbf{x}=[x_1, x_2, x_3]$	position in the physical space
x_{ij}	j -th coordinate of the i -th abscissa of GC approximation
\mathbf{X}	s -dimensional vector of random variables

Greek symbols

β	aggregation kernel, m^3/s
$\beta_d(d, d')$	daughter size distribution, m^{-1}
ε	average energy dissipation rate, W/kg
$\nu(d', \varepsilon)$	number of daughter droplets
ϕ	concentration of the dispersed phase
ρ_c	density of crystal phase, kg/m^3
ρ_s	density of solid phase, kg/m^3
σ	supersaturation
σ_0	initial supersaturation
σ_{in}	supersaturation of the inlet solution
θ	mean residence time, s

Subscripts

k_1, k_2, \dots, k_N	order of moment over i -th coordinate
------------------------	---

Superscript

bs	kinetic exponent
g_1, g_2	kinetic exponent

Abbreviations

DQMOM	direct quadrature method of moment
GC	Gaussian cubature
GQ	Gaussian quadrature
LP	linear program

PB	population balance
PBE	population balance equation
QMOM	quadrature method of moments

REFERENCES

- Baldyga J., Bourne J.R., 1993. Drop breakup and intermittent turbulence. *J. Chem. Eng. Jpn.*, 26, 738-741. DOI: 10.1252/jcej.26.738.
- Baldyga J., Bourne J.R., 1995. Interpretation of turbulent mixing using fractals and multifractals. *Chem. Eng. Sci.*, 50, 381-400. DOI: 10.1016/0009-2509(94)00217-F.
- Baldyga J., Podgórska W., 1998. Drop break-up in intermittent turbulence: maximum stable and transient sizes of drops. *Can. J. Chem. Eng.*, 76, 456-470. DOI: 10.1002/cjce.5450760316.
- Batchelor G.K., 1980. Mass transfer from small particles suspended in turbulent fluid. *J. Fluid Mech.*, 98, 609-623. DOI: 10.1017/S0022112080000304.
- Borchert C., Nere N., Ramkrishna D., Voigt A., Sundmacher K., 2009. On the prediction of crystal shape distributions in a steady-state continuous crystallizer. *Chem. Eng. Sci.*, 64, 686-696. DOI: 10.1016/j.ces.2008.05.009.
- Brändström A., 1966. On the existence of acid salts of monocarboxylic acids in water solutions. *Acta Chem. Scand.*, 20, 1335-1343. DOI: 10.3891/acta.chem.scand.20-1335.
- DeVuyst E.A., Preckel P.V., 2007. Gaussian cubature: A practitioner's guide. *Math. Comput. Modell.*, 45, 787-794. DOI: 10.1016/j.mcm.2006.07.021.
- Golub G.H., Welsch J.H., 1969. Calculation of Gauss quadrature rules. *Math. Comput.* 23, 221-230. DOI: 10.1090/S0025-5718-69-99647-1.
- Gordon R.G., 1968. Error bounds in equilibrium statistical mechanics. *J. Math. Phys.* 9, 655-663. DOI: 10.1063/1.1664624.
- Gunawan R., Fusman I., Braatz R.D., 2004. High resolution algorithms for multidimensional population balance equations. *AIChE J.*, 50, 2738-2749. DOI: 10.1002/aic.10228.
- Hill P.J., Ng, K.M., 1995. New discretization procedure for the breakage equation. *AIChE J.*, 41, 1204-1216. DOI: 10.1002/aic.690410516.
- Hulburt H.M., Katz S., 1964. Some problems in particle technology. A statistical mechanical formulation. *Chem. Eng. Sci.*, 19, 555-574. DOI: 10.1016/0009-2509(64)85047-8.
- Marchisio D.L., Fox R.O., 2005. Solution of population balance equations using direct quadrature method of moments. *J. Aerosol Sci.*, 36, 43-73. DOI: 10.1016/j.jaerosci.2004.07.009.
- McGraw R., 1997. Description of aerosol dynamics by the quadrature method of moments. *Aerosol Sci. Technol.*, 27, 255-265. DOI: 10.1080/02786829708965471.
- Okamoto Y., Nishikawa M., Hashimoto K., 1981. Energy dissipation rate distribution in mixing vessels and its effects on liquid-liquid dispersion and solid-liquid mass transfer. *International Chemical Engineering*, 21, 88-94.
- Sack R.A., Donovan A.F., 1972. An algorithm for Gaussian quadrature given modified moments. *Numer. Math.* 18, 465-478. DOI: 10.1007/BF01406683.
- Sen M., Chaudhury A., Singh R., Ramachandran R., 2014. Two-dimensional population balance model development and validation of a pharmaceutical crystallization process. *Am. J. Mod. Chem. Eng.*, 1, 13-29.
- Silva J.E., Paiva A.P., Soares D., Labrincha A., Castro F., 2007. Crystallization from solution, In *Trends in Hazardous Materials Research*. Nova Science Publishers, New York.
- Sorgato, I., 1983. *Statistical approach to kinetics*. Università Degli Studi di Padova- Istituto di Impianti Chimici, Antoniana S.p.A, Padova, Italy .
- Wright D.L., McGraw R., Rosner D.E., 2001. Bivariate extension of the quadrature method of moments for modeling simultaneous coagulation and sintering of particle populations. *J. Colloid Interface Sci.*, 236, 242-251. DOI: 10.1006/jcis.2000.7409.

Received 11 October 2016

Received in revised form 11 July 2017

Accepted 12 July 2017

APPENDIX

The details of application of the GC algorithm to modeling of drop break up with simultaneous mass transfer, as considered in Section 4, are presented in what follows. One starts with choosing internal coordinates, which in this case are the droplet diameter, d_d , and the concentration of the benzoic acid in the dispersed phase, C_d . The bivariate moments of the distribution of order k over droplet diameter and l over the concentration are obtained by transforming Eq. (2):

$$m_{k,l} = \int_0^\infty \int_0^\infty d_d^k C_d^l f(d_d, C_d, t) dC_d dd_d \quad (30)$$

After performing a moment transformation of the population balance equations, Eq. (3), one gets a set of integro-differential equations governing the time evolution of the system:

$$\begin{aligned} \frac{dm_{k,l}(t)}{dt} = & l \int_0^\infty \int_0^\infty d_d^k C_d^{l-1} \dot{C}_d f(d_d, C_d, t) dC_d dd_d + \\ & + \int_0^\infty \int_0^\infty d_d^k C_d^l \nu(d'_d, \varepsilon) \beta_d(d_d, d'_d) g(d') f(d'_d, C_d, t) dd'_d dC_d dd_d - \\ & - \int_0^\infty \int_0^\infty d_d^k C_d^l g(d_d) f(d_d, C_d, t) dC_d dd_d \end{aligned} \quad (31)$$

where \dot{C}_d denotes the mass flux, $\nu(d'_d, \varepsilon)$ the number of daughter droplets created in the breakage event, $\beta_d(d_d, d'_d)$ the daughter size distribution, and $g(d'_d)$ is a breakage kernel. The right hand side terms refer to mass transfer (convection in a phase space), appearing and disappearing of droplets due to breakage (birth and death terms), respectively. The source term integrals are now approximated using the Gaussian Cubature (Eq. (4)) leading to the set of differential equations:

$$\frac{dm_{k,l}(t)}{dt} = l \sum_{i=1}^N d_{di}^k C_{di}^{l-1} \dot{C}_{di} w_i + \sum_{i=1}^N C_{di}^l \left(\nu(d_{di}, \varepsilon) \int_0^{d_{di}} L^k \beta_d(L, d_{di}) dL - d_{di}^k \right) g(d_{di}) w_i \quad (32)$$

To obtain weights, w_i , and abscissas, d_{di} and C_{di} , of the cubature, the GC algorithm is used following Eqs. (5) to (8). One of the output parameters in this case is the Sauter diameter, d_{32} , which requires the second and the third moment of distribution. Hence, the Gaussian cubature of order 3 is used. This order of approximation should ensure sufficient accuracy. Therefore one gets a set of 10 moments of distribution to be followed during the simulation. The linear program (LP) resulting from the GC procedure is then solved in each time step using the dual-simplex method implemented in the MATLAB software libraries giving weights for each point of the previously set up lattice. Points having strictly positive weights are then used for the GC approximation.

DYNAMICAL AND TECHNOLOGICAL CONSEQUENCES OF MULTIPLE ISOLAS OF STEADY STATES IN A CATALYTIC FLUIDISED-BED REACTOR

Katarzyna Bizon*

Cracow University of Technology, Department of Chemical and Process Engineering, 30-155
Kraków, ul. Warszawska 24, Poland

Steady-state characteristics of a catalytic fluidised bed reactor and its dynamical consequences are analyzed. The occurrence of an untypical steady-state structure manifesting in a form of multiple isolas is described. A two-phase bubbling bed model is used for a quantitative description of the bed of catalyst. The influence of heat exchange intensity and a fluidisation ratio onto the generation of isolated solution branches is presented for two kinetic schemes. Dynamical consequences of the coexistence of such untypical branches of steady states are presented. The impact of linear growth of the fluidisation ratio and step change of the cooling medium temperature onto the desired product yield is analyzed. The results presented in this study confirm that the identification of a region of the occurrence of multiple isolas is important due to their strong impact both on the process start-up and its control.

Keywords: catalytic fluidised-bed reactor, steady states, non-linear analysis, multiplicity, multiple isolas

1. INTRODUCTION

A phenomenon of generation of single isolas, i.e. isolated closed branches of steady states has been demonstrated a number of times in chemical engineering systems, both in theoretical and experimental works. Their occurrence has been observed in very simple systems such as non-adiabatic continuously stirred tank reactors (Berezowski, 2002; Uppal et al., 1976), tubular heterogeneous reactors (Berezowski, 2000) as well as in more complex catalytic processes carried out in fluidised-bed reactors (Ajbar et al., 2001). Several works, e.g. (Pinto and Ray, 1995), report on the possibility of the occurrence of so-called multiple isolas of steady states. In such a case several closed branches of steady states co-existing with open steady-state branches are observed in a bifurcation diagram. In the work cited above the authors also described scenarios of generation and disappearance of the isolas. Pinto and Ray (1995) demonstrated the possibility of occurrence of two isolas of steady states in the bifurcation diagram of the process of copolymerization of vinyl acetate and methyl methacrylate in tert-butanol. The isolas are located next to each other, that is in different ranges of the selected bifurcation parameter, in this case a residence time. In this study such isolas will be referred to as the first type isolas. Despite an extensive body of literature concerning the steady-state analysis of chemically reactive systems, the possibility of co-existence of two isolas in the same range of the bifurcation parameter, i.e. one isola above the other, and an open branch of steady states was demonstrated only in a couple of works. The possibility of such a phenomenon was mentioned in (Zahn, 2012) and in the earlier study of the author of this work (Bizon, 2016). These isolas will be referred to as the second type isolas.

*Corresponding authors, e-mail: kbizon@chemia.pk.edu.pl

This study demonstrates that such an untypical structure of steady-states can develop in catalytic fluidised-bed reactors. A single chemical reaction and a system of two consecutive reactions were used to exemplify the occurrence of multiple isolas. The impact of a heat exchange intensity and a fluidisation ratio onto the generation of isolated solution branches was evaluated. Dynamical and technological consequences of the existence of multiple isolas of steady states were analysed.

2. MATHEMATICAL MODEL OF A CATALYTIC FLUIDISED-BED REACTOR

Let us consider the chemical processes taking place in a catalytic fluidised-bed reactor, namely:

- a single irreversible first order chemical reaction proceeding according to a scheme $A \xrightarrow{k_1} P$;
- a system of consecutive irreversible first order chemical reactions: $A \xrightarrow{k_1} P \xrightarrow{k_2} R$, where P is a desired product, whereas R is an undesired product.

For the process (a) the reaction rate with respect to the component A is $r_A = r_1$, whereas for the system of reactions in series the rates with respect to A and P are, respectively, $r_A = r_1$ and $r_P = r_1 - r_2$, where

$$r_i = C_j \cdot k_{0i} \exp\left(-\frac{E_i}{RT}\right), \quad i = 1, 2; \quad j = A, P \quad (1)$$

A two-phase bubbling bed model, modified by Tabiś (Tabiś, 2001) was employed to describe hydrodynamics of a fluidised bed. The main assumption of the model is that the bed consists of an emulsion phase and a bubble phase with the mass and heat transfer coefficients between the phases determined as resultant quantities according to the three-phase model of Kunii and Levenspiel (1991). The other assumptions are:

- perfect mixing and negligible mass and heat transfer resistance between the gas and the catalyst particles in the emulsion phase;
- plug flow of the gas and quasi-steady state character of the bubble phase.

According to these assumptions the dynamic mass and heat balance equations in the emulsion phase can be written as:

$$\frac{d\eta_A^e}{dt} = a_2(\eta_{Af} - \eta_A^e) + \varphi_1(\eta_A^e) - a_3 \cdot \tilde{r}_A(\eta_A^e, T^e) = f_1(\eta_A^e, T^e) \quad (2)$$

$$\frac{d\eta_P^e}{dt} = a_2(\eta_{Pf} - \eta_P^e) + \varphi_2(\eta_P^e) + a_3 \cdot \tilde{r}_P(\eta_A^e, \eta_P^e, T^e) = f_2(\eta_A^e, \eta_P^e, T^e) \quad (3)$$

$$\frac{dT^e}{dt} = a_5(T_f - T^e) - \varphi_3(T^e) + a_4 \sum_{i=1}^2 (-\Delta h_i) \cdot \tilde{r}_i(\eta_A^e, \eta_P^e, T^e) - Q_1(T^e - T_q) = f_3(\eta_A^e, \eta_P^e, T^e) \quad (4)$$

where a dimensionless concentration of a j^{th} reactant η_j is defined as

$$\eta_j = \frac{C_j}{C_{Aref}}, \quad j = A, P \quad \text{where} \quad C_{Aref} = \frac{P \cdot y_{Af}}{R \cdot T_f} \quad (5)$$

whereas expressions defining the reaction rates in a function of dimensionless concentration η_j^e and temperature T^e in the emulsion are given by

$$\tilde{r}_i = k_i \eta_j^e = k_{0i} \exp\left(-\frac{E_i}{RT^e}\right) \cdot \eta_j^e, \quad i = 1, 2; \quad j = A, P \quad (6a)$$

$$\tilde{r}_A = \tilde{r}_1; \quad \tilde{r}_P = \tilde{r}_1 - \tilde{r}_2 \quad (6b)$$

The functions $\varphi_1(\eta_A^e)$, $\varphi_2(\eta_P^e)$ and $\varphi_3(T^e)$ in Equations (2) - (4) are defined as

$$\varphi_1(\eta_A^e) = \frac{B_{1A}}{B_{3A}} (\eta_A^e - \eta_{Af}) \cdot [\exp(-B_{3A}) - 1] \quad (7)$$

$$\varphi_2(\eta_P^e) = \frac{B_{1P}}{B_{3P}} (\eta_P^e - \eta_{Pf}) \cdot [\exp(-B_{3P}) - 1] \quad (8)$$

$$\varphi_3(T^e) = \frac{B_2}{B_4 + Q_2} \left[Q_2 (T^e - T_q) + \left(T_f - \frac{B_4 T^e + Q_2 T_q}{B_4 + Q_2} \right) (\exp(-(B_4 + Q_2)) - 1) \right] \quad (9)$$

The parameters in Equations (2) - (4) and in expressions (7) - (9) are calculated as follows

$$a_1 = \frac{\rho_z c_z}{\rho_g c_g}; \quad a_2 = \frac{u_e}{H}; \quad a_3 = \frac{1 - \varepsilon_{mf}}{\varepsilon_{mf}}; \quad a_4 = \frac{(1 - \varepsilon_{mf}) C_{Aref}}{(1 - \varepsilon_{mf} + \varepsilon_{mf}/a_1) \rho_z c_z} \quad (10a)$$

$$a_5 = \frac{\varepsilon_{mf} u_e}{H[(1 - \varepsilon_{mf})a_1 + \varepsilon_{mf}]}; \quad B_2 = \frac{\delta}{(1 - \delta)(1 - \varepsilon_{mf} + \varepsilon_{mf}/a_1)} \left(\frac{\alpha_q^{be}}{\rho_z c_z} + \beta_z^{be} \right) \quad (10b)$$

$$B_{1j} = \frac{\delta \beta_{gj}^{be}}{(1 - \delta) \varepsilon_{mf}}; \quad B_{3j} = \frac{H}{u_b} \beta_{gj}^{be}, \quad j = A, P \quad (10c)$$

$$Q_1 = \frac{a_q k_q}{(1 - \varepsilon_{mf} + \varepsilon_{mf}/a_1) \rho_z c_z}; \quad Q_2 = \frac{H a_q k_q}{u_b \rho_z c_z} \quad (10d)$$

Additional details concerning determination of the hydrodynamic parameters of the bed and mass and heat transfer coefficients between the emulsion phase and bubble phase can be found in (Bizon, 2016).

In case of the single chemical reaction it can be assumed that $k_{02} = 0$, then the dynamics of the reactor is described by the system of two differential equations, i.e. Eqs. (2) and (4).

Table 1. Values of the model parameters used in numerical simulations

No	Parameter	Value	Dimension
1	$a_q k_q$	0.04 – 0.16	kW/m ³ ·K
2	c_g	1.0	kJ/kg·K
3	c_z	0.8	kJ/kg·K
4	d_z	2.0×10^{-4}	m
5	E_l	7.0×10^4	kJ/kmol
6	Δh_1	-4.0×10^5	kJ/kmol
7	H_{mf}	1.0 - 1.2	m
8	k_{01}	4.0×10^5 or 1.0×10^7	1/s
9	T_f	450	K
10	T_q	300 or 320	K
11	$x_E, x_{\Delta h}$	1.5	x_E
12	x_k	1.0	x_k
13	y_{Af}	0.1	-
14	ρ_g	0.7	kg/m ³
15	ρ_z	2300	kg/m ³

3. RESULTS AND DISCUSSION

Values of the parameters used in numerical simulations both for the single chemical reaction and for the system of consecutive reactions are reported in Table 1. The values were selected based on the analysis of typical catalytic processes (Balakotaiah and West, 2014; Westerink and Westertrep, 1992). Symbols x_E , $x_{\Delta h}$, and x_k refer, respectively, to a ratio of activation energies, enthalpies and frequency coefficients in Arrhenius equation for the consecutive reaction, namely

$$x_E = \frac{E_2}{E_1}, \quad x_{\Delta h} = \frac{\Delta h_2}{\Delta h_1}, \quad x_k = \frac{k_{02}}{k_{01}} \quad (11)$$

A home-made code for continuation of the solution branches based on a local parameterisation (Seydel, 1994) was developed and used to determine the parametric dependency of the state variables and to characterize the structure of steady states of the fluidised-bed reactor. This is permitted to avoid application of complex continuation software, as recommended also in the reference (Berezowski, 2010).

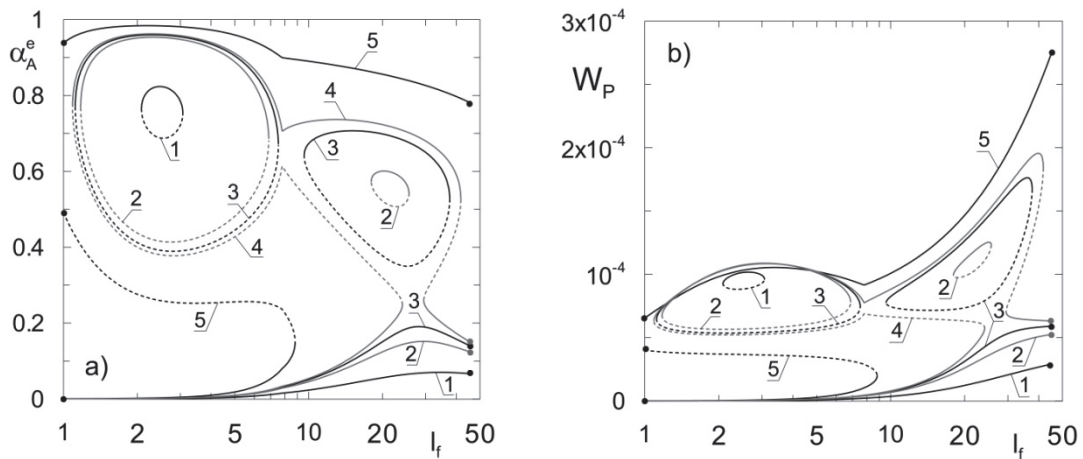


Fig. 1. Steady-state branches (a) and process yield W_P (b) for a single chemical reaction with respect to l_f and $a_q k_q$; $a_q k_q = \{1- 0.16; 2- 0.129; 3- 0.125; 4- 0.123; 5- 0.1\}$ kW/m³·K; $H_{mf} = 1.2$ m, $T_f = 450$ K; $T_q = 300$ K (• - boundaries of the fluidised-bed existence)

Figure 1 shows steady-state characteristics of a catalytic fluidised-bed reactor for a single irreversible exothermic reaction with respect to a fluidisation ratio l_f and for different values of a parameter $a_q k_q$. The parameter $a_q k_q$ is associated with the heat transfer between the fluidised-bed and a cooling medium. When $a_q k_q = 0$, then the reactor is adiabatic. Solid lines indicate stable steady states, while dashed lines indicate unstable steady states. Values of a conversion degree of the reactant A, i.e. α_A , (Fig. 1a) are determined as follows

$$\alpha_A = \frac{C_{Af} - C_A}{C_{Af}} = 1 - \eta_A \frac{T^e}{T_f} \quad (12)$$

whereas the process yield W_P (Fig. 1b) for the single chemical reaction is defined as

$$W_P = \frac{V_P}{|V_A|} u_0 C_{Af} \cdot \bar{\alpha}_A(l) \quad (13)$$

where $\bar{\alpha}_A(l)$ is an average conversion degree of A leaving the fluidised-bed.

Two first type isolas arising above the lower stable steady state were detected at relatively high values of the parameter $a_q k_q$. The complexity of the steady-state structure of the reactor is a result of a

coupling of chemical reaction with mass and heat transfer processes between the bubbles and the emulsion phase. It can be observed that stable fragments (branches 2 and 3 in Fig. 1b) of the right isola located in the region of high values of the fluidisation l_f are characterized by higher yield of the process W_P .

The location of the isolas in the bifurcation diagram depends on the type of a chemical process carried out in the fluidised-bed. The steady-state structure of the fluidised-bed corresponding to the process described by two consecutive chemical reactions is shown in Fig. 2. In such a case the process yield with respect to the product P, W_P is calculated as

$$W_P = \frac{V_P}{|V_A|} u_0 C_{Af} \cdot \bar{\alpha}_P \quad (14)$$

where a dimensionless concentration of the product P defined with respect to the feed temperature is as follows

$$\alpha_P = \frac{C_P - C_{Pf}}{C_{Af}} = 1 - \eta_P \frac{T^e}{T_f} \quad (15)$$

In case of the system of two reactions in series, fivefold steady states can occur. For the catalytic process analysed in this study for a certain set of the model parameters the branches of steady states may take a form of multiple isolas. This is confirmed by the results presented in Fig. 2. Unlike the single chemical reaction, the isolas are located in the same range of the parameter, i.e. one isola is located above the other. Therefore, for such isolas the concept of co-existence was introduced.

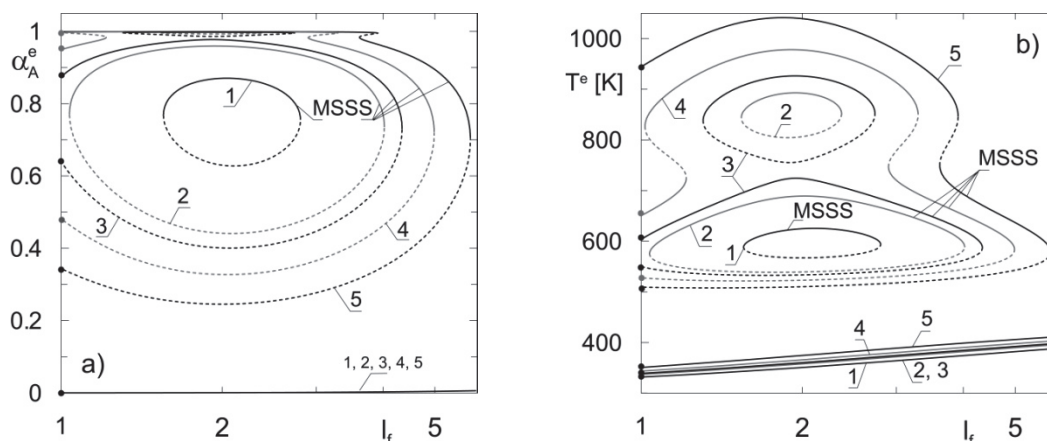


Fig. 2. Steady-state branches for a system of consecutive reactions with respect to l_f and $a_q k_q$; $a_q k_q = \{1- 0.076; 2- 0.062; 3- 0.058; 4- 0.05; 5- 0.04\}$ kW/m³·K; $H_{mf} = 1$ m, $T_f = 450$ K; $T_q = 300$ K (• - boundaries of the fluidised-bed existence)

To evaluate the influence of the bed hydrodynamics and the intensity of heat exchange on the steady-state structure globally, catastrophic sets in the plane $(l_f, a_q k_q)$ were then determined. The diagrams presented in Fig. 3 are the result of a two-parameter continuation (Seydel, 1994) of the turning points from Fig. 1 and Fig. 2. For a better understanding of the phenomenon of generation and disappearance of multiple isolas, the ranges of the parameter $a_q k_q$ in which they emerge are delimited with dashed lines.

In case of the single chemical reaction (Fig. 3a) and relatively high values of $a_q k_q$ the system has a unique stable solution branch. It is characterized by a low conversion degree and thus by a low yield of the reactor W_P . Maxima of the upper curve marked with letters A and B (Fig. 3a) are referred to as the isola centres. They correspond to the values of the parameters $a_q k_q$ and l_f at which the isolas are

generated being an origin of a region of the triple steady states. Diminution of the heat exchange intensity represented by the product $a_q k_q$ leads to enlargement of the isolas and thus extension of the region of the triple steady states. At the value of $a_q k_q$ corresponding to the point C (Fig. 3a) the two isolas merge, then further diminution of $a_q k_q$ leads to their coalescence with the lower stable branch of steady states.

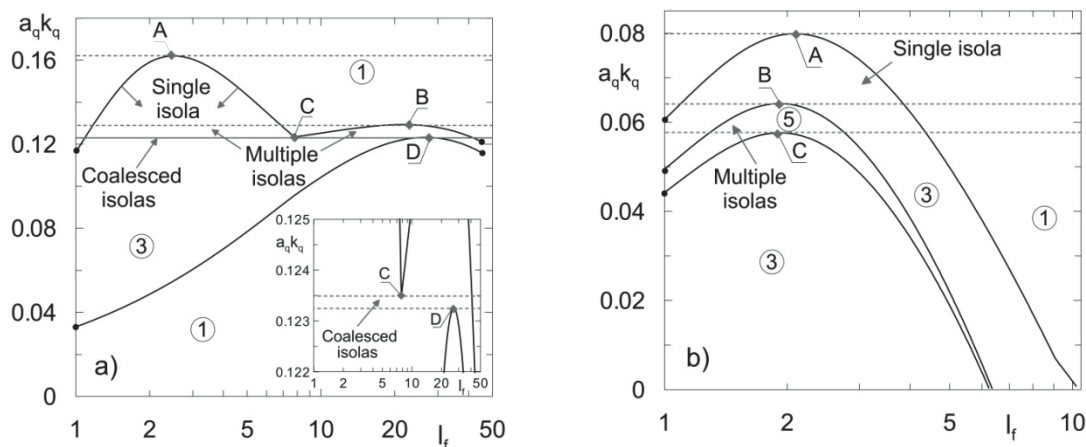


Fig. 3. Catastrophic sets in the plane $(l_f, a_q k_q)$ for a single chemical reaction (a) and for a system of consecutive reactions (b); $T_f=450$ K, $T_q=300$ K (numbers indicate the number of steady states)

Figure 3b shows a steady-state structure in the plane $(l_f, a_q k_q)$ determined for the reactor in which a system of two consecutive chemical reactions takes place. Extrema of the curves marked with A and B (Fig. 3b) correspond, respectively, to the parameters for which isolas occur in the system. The point C (Fig. 3b) corresponds to the process conditions at which the isolas coalesce. The region of the triple steady states resulting from the coalescence of the isolas, i.e. the area located under the lower curve, corresponds to solutions disadvantageous from the technical point of view. In this region the system only has the lower steady state that does not guarantee the autothermicity of the process and the upper steady state corresponding to a very high conversion but also to an extremely high temperature, thus it characterised by a very low yield of the process W_P .

Taking into account that the model of the reactor depends on some parameters whose values can change dynamically during the process, both intentionally and due to the external disturbances, the appearance both of a single and multiple isolas may strongly influence the process dynamics. Due to the observed strong impact of the fluidisation ratio l_f onto the steady-state structure, the influence of its variation onto the reactor dynamics was evaluated. The variation of l_f may be intentional, i.e. it can take place during the reactor start-up, when the fluidisation ratio is dynamically increased to reach a given target value. It can also be induced by the process kinetics, which is the case for non-equimolar processes (Abba et al., 2002) characterized by a variable volumetric flow rate of a fluidising medium.

Figure 4 shows various scenarios of the variation of the fluidization ratio l_f (Fig. 4a) with corresponding dynamical responses of the reactor (Fig. 4b and Fig. 4c) in which a single irreversible reaction takes place. Two starting values of the fluidization ratio corresponding to the time instant $t = 0$ were used in the simulations, i.e. $l_{f0} = 2$ and $l_{f0} = 5.5$. For all the evaluated cases the initial conditions of the dynamic model of the reactor were set to $\alpha_{A0}^e = 0$ that corresponds to $\eta_{A0}^e = 1$ and $T_0^e = 450$ K. A target value of the fluidization ratio was set to $l_f = 25$. Trajectories $l_f(t)$, $T^e(t)$ and $W_P(t)$ corresponding to $l_{f0} = 2$ labelled with numbers 1 and 2 in Fig. 4 correspond, respectively, to fast and slow variations of the fluidisation ratio (Fig. 4a). In both cases the reactor eventually reaches the upper steady state. Yet, in case of a low rate of increase (curves marked with 2 in Fig. 4) the trajectory $T^e(t)$ exhibits a substantial maximum. This phenomenon can be dangerous from the technological point of view as it can lead, for

instance, to the thermal deactivation of the catalyst. Moreover, it also causes a significant decrease in the instantaneous yield of the process (Fig. 4c).

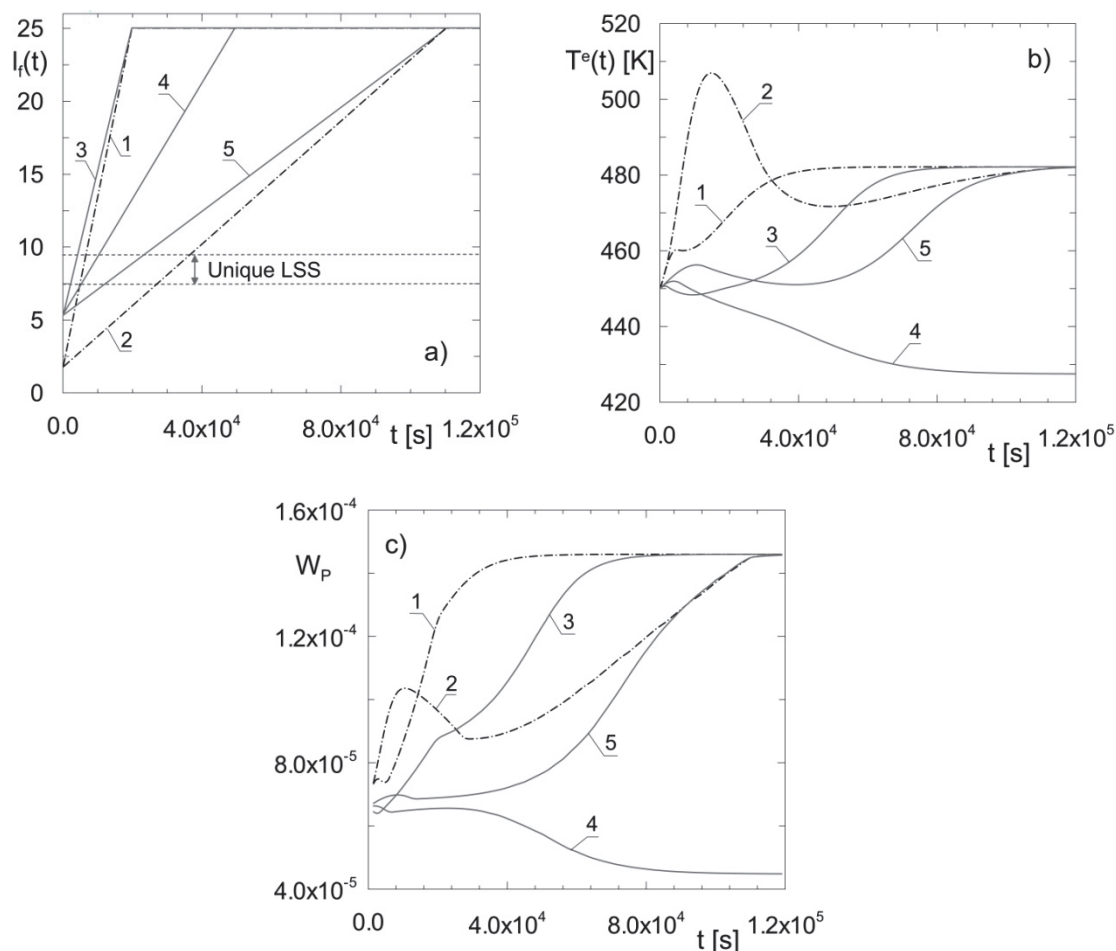


Fig. 4. Dynamic variation of l_f (a) and corresponding responses of the reactor (b-c) for a single chemical reaction for $a_q k_q = 0.125 \text{ kW/m}^3 \cdot \text{K}$; $H_{mf} = 1.2 \text{ m}$; $T_f = 450 \text{ K}$; $T_q = 300 \text{ K}$

The dynamical response of the reactor to the variation of fluidization ratio changes when $l_{f0} = 5.5$. In such a case the fast increase of the fluidization ratio value leads to the convergence of the trajectory at the upper steady state (curves labelled with 3 in Fig. 4). For a lower rate of the variation of $l_f(t)$ the trajectory converges at the lower steady state as shown by curves marked with 4 in Fig. 4. However, further prolongation of the time interval in which the process conditions change (curves labelled with 5 in Fig. 4) again results in the convergence at the upper steady state. Such a phenomenon is associated with the fact that if the rate of increase of the fluidization ratio is low then in the initial stage of the process the bed heats up enough to maintain a sufficient level of the temperature, even when operating transitorily in the interval of l_f for which the reactor has only the lower steady state.

Three scenarios of the increase of the fluidization ratio were considered for a system of reactions in series, starting at the minimal value $l_f = 1.01$, and ending at the target value coinciding with a high yield of the reactor, that is at $l_{f0} = 3.5$ (Fig. 5a). A dangerous rise of the bed temperature is observed at a low rate of the variation of l_f (curve labelled with 3 in Fig 5b). This is due to the fact that for the assumed value of the parameter $a_q k_q = 0.05$ two merged isolas of the second type were detected in the reactor and only two stable steady states exist in the interval $l_f = [1.214, 2.899]$ (branches marked with 4 in Fig. 2), with the upper one being disadvantageous from the process point of view. Thus, exceeding the value $l_f = 1.214$ corresponding to the first turning point, results in the temporary attraction of the trajectories by the upper steady state. At the higher cooling intensity of the reactor, i.e. for $a_q k_q = 0.058$ at which the

multiple isolas were detected (branches denoted with number 3 in Fig. 2) this risk does not exist. In such a case the trajectories converge directly at the middle steady state (Fig. 5c). If the initial conditions belong to the basins of attraction of the middle steady state then in the region of the occurrence of multiple isolas the dynamical variation of l_f always leads to the convergence at this steady state.

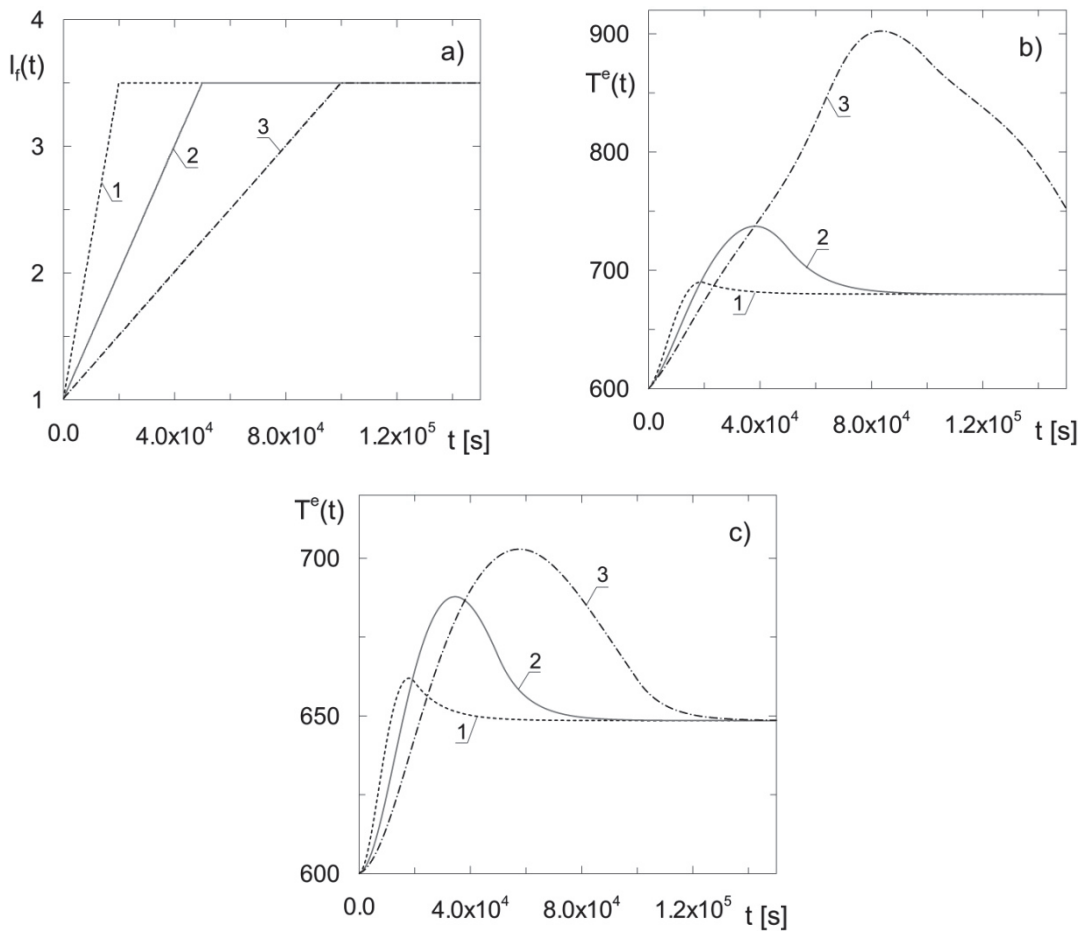


Fig. 5. Dynamic variation of l_f (a) and corresponding responses of the reactor of a system of consecutive chemical reactions for $a_qk_q = 0.05 \text{ kW/m}^3\cdot\text{K}$ (b) and for $a_qk_q = 0.058 \text{ kW/m}^3\cdot\text{K}$ (c); $H_{mf} = 1.2 \text{ m}$; $T_f = 450 \text{ K}$; $T_q = 300 \text{ K}$

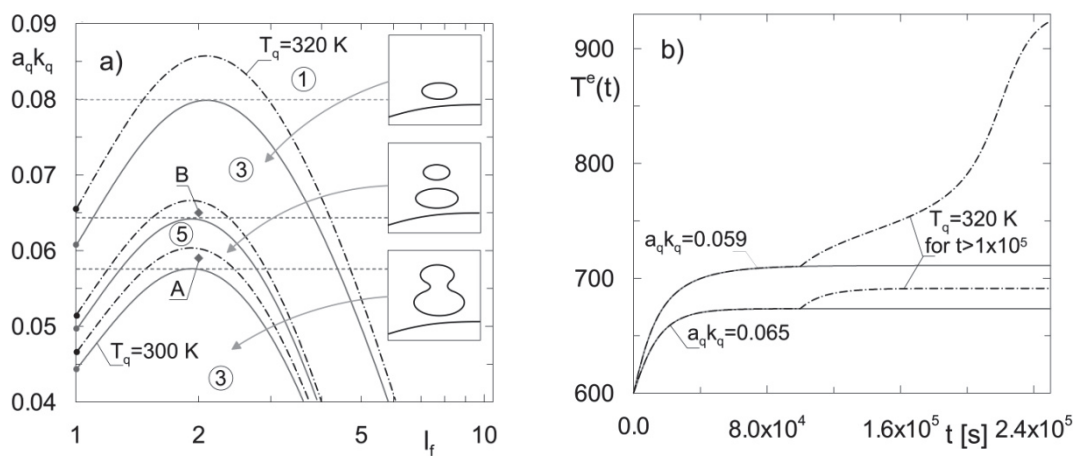


Fig. 6. Catastrophic sets in the plane (l_f, a_qk_q) for a system of consecutive reactions for $T_q = 300 \text{ K}$ (solid line) and for $T_q = 320 \text{ K}$ (dashed line) (a) and the reactor response to a step disturbance of a cooling medium temperature T_q (b); ($T_f = 450 \text{ K}$, $l_f = 2$; numbers indicate the number of steady states)

All the above analysis is focused on the influence of variation of the fluidisation ratio onto the reactor dynamics. However, other parameters of the model may also vary during the process, both intentionally and uncontrollably. Figure 6 shows the impact of the cooling medium temperature T_q onto the stationary and dynamical properties of the reactor for a system of reactions in series. It can be observed (Fig. 6a) that the increase of the temperature T_q from 300 to 320 K does not change the steady-state structure fundamentally. There is only a quantitative shift of the regions of a given multiplicity in the plane $(l_f, a_q k_q)$. However, it appears that the shift of the regions may have a strong impact on the reactor dynamics in case of step disturbances of the temperature T_q .

Let us assume that the process is carried out at a fixed intensity of a heat exchange and at a constant value of the fluidization ratio. In particular, a pair of parameter values $a_q k_q = 0.059$ and $l_f = 2$ corresponding to point A in Fig. 6a is considered. In such a case, at the temperature $T_q = 300$ K fivefold steady states occur in the reactor, with the middle and upper steady states located on the second type isolas. The dynamic properties of the reactor in the neighbourhood of point A can be learnt by the analysis of the trajectories of the reactor subject at some time instant t_0 to a step disturbance of the cooling medium temperature T_q . The trajectories of the temperature of emulsion $T^e(t)$ are shown in Fig. 6b. It can be observed that the dynamic response of the reactor and its performance at a new steady state depends on the choice of the parameter characterizing the intensity of the heat exchange, i.e. $a_q k_q$. Let us consider the first case in which $a_q k_q = 0.059$ corresponds to the point A in Fig. 6a. If a step disturbance of the cooling medium temperature up to $T_q = 320$ K takes place at a certain time instant t_0 then a substantial rise of the temperature in the reactor is detected (dashed line in Fig. 6b). This is due to the fact that for this value of T_q the point A belongs to the triple steady-state region arisen from the coalescence of two isolas (Fig. 6a), therefore the trajectories are attracted by the upper steady state that is disadvantageous from the technological point of view.

The situation changes at $a_q k_q = 0.065$ and $l_f = 2$ corresponding to the point B in Fig. 6a. Then, at $T_q = 300$ K the reactor has three steady states resulting from the first isola above the lower steady state. Stable fragments of the isola correspond to moderate temperatures and thus satisfactory values of the process yield W_p . The trajectories shown in Fig. 6b confirm the convergence at the technologically advantageous stable steady state. There is no qualitative change of the solution in the event of step increase of the cooling medium temperature at a certain t_0 , that is after stabilization of the process in the apparatus, to the value $T_q = 320$ K. As a result of the shift of the boundaries of the multiplicity regions mentioned before, the point B belongs then to the fivefold steady-state area. Despite a relatively large magnitude of the disturbance the trajectories are not attracted by the other steady state, i.e. the lower or upper one.

4. CONCLUSIONS

An influence of the selected operating parameters onto steady-state characteristics and dynamics of a catalytic fluidized bed reactor was presented. The relationship between the steady-state characteristics of the reactor, in particular of the region of multiple isolas, and its dynamics was evaluated.

For a single chemical reaction and for a system of two consecutive reactions the model was shown to exhibit an untypical steady-structure having a form of multiple isolas. Depending on the process kinetics, a relative location of the isolas in the bifurcation diagram can be different, both from a mathematical and technological point of view.

It was demonstrated that for the single exothermic reaction two isolas of steady states can coexist in different intervals of the bifurcation parameter. They can be classified as the first type isolas. Quite distinct steady-state characteristics was observed for the system of two consecutive reactions. Due to the higher complexity of the process a region of fivefold steady states may occur. Hence, there is a

possibility of the generation of two isolas located one above the other. They were called the second type isolas.

The analysis performed in the paper shows that the occurrence of multiple isolas of steady states can have serious dynamical and technological consequences. It is particularly important in the case of variation of a process parameter that influences the bed hydrodynamics, in this case the fluidization ratio l_f . For the single chemical reaction, in order to maintain the performance of the reactor at a high level, a dynamical change of l_f has to be done fast enough or slow enough, depending on the initial conditions in the apparatus. Therefore the choice of the strategy of variation of this parameter requires prior knowledge of the reactor dynamics. As demonstrated in this work, running the process in the region of the isolas detected for the system of consecutive reactions can also have serious technological consequences.

It was demonstrated that in the region of the second type multiple isolas the reactor's response to a step disturbance of the cooling medium temperature depends on the heat exchanger size. For the mismatched size of the heat exchanger the disturbance of the cooling medium temperature may lead the reactor to the disadvantageous steady state characterized by high temperature and low performance.

The results presented in this work confirm that the knowledge of steady-state and dynamic properties of the reactor is indispensable to design and to run exothermal processes in systems characterized by such a complex steady-state structure.

SYMBOLS

a_i	model parameter
a_q	heat transfer area per unit volume of a bed, m^{-1}
B_i, B_{ij}	model parameter determining the interphase mass and heat transfer
c_g, c_z	specific heat of gas and solid particles, $\text{kJ}\cdot\text{kg}^{-1}\cdot\text{K}^{-1}$
C_j	concentration of j^{th} reactant, $\text{kmol}\cdot\text{m}^{-3}$
d_z	catalyst pellet diameter, m
E_i	activation energy of i^{th} chemical reaction, $\text{kJ}\cdot\text{kmol}^{-1}$
h	height above the distributor, m
Δh_i	enthalpy of i^{th} chemical reaction, $\text{kJ}\cdot\text{kmol}^{-1}$
H	total height of a fluidized bed, m
k_q	overall heat transfer coefficient, $\text{kJ}\cdot\text{m}^{-2}\cdot\text{s}^{-1}\cdot\text{K}^{-1}$
k_i	rate constant of the i^{th} chemical reaction
k_{0i}	frequency coefficient in Arrhenius equation of i^{th} chemical reaction, s^{-1}
l_f	fluidization ratio
Q_i	model parameters determining intensity of heat transfer
r_i	rate of i^{th} chemical reaction, $\text{kmol}\cdot\text{m}^{-3}\cdot\text{s}^{-1}$
\tilde{r}_i	rate of i^{th} chemical reaction in a function of dimensionless concentration η_j , s^{-1}
R	gas constant, $\text{kJ}\cdot\text{kmol}^{-1}\cdot\text{K}^{-1}$
t	time, t
T	temperature, K
u	velocity, $\text{m}\cdot\text{s}^{-1}$
W_P	yield of a process with respect to product P, $\text{kmol}\cdot\text{m}^{-2}\cdot\text{s}^{-1}$
y_j	molar fraction of j^{th} reactant
z	dimensionless height above distributor

Greek symbols

α_A	conversion degree of reactant A
------------	---------------------------------

α_P	dimensionless concentration of product P defined with respect to the feed temperature
α_q^{ij}	heat exchange coefficient between phase i and j , $\text{kJ}\cdot\text{m}^{-3}\cdot\text{s}^{-1}\cdot\text{K}^{-1}$
β_{gk}^{ij}	gas exchange coefficient of k^{th} reactant between phases i and j , s^{-1}
β_z^{ij}	solid exchange coefficient between phases i and j , s^{-1}
δ	volumetric fraction of bubbles in a bed
ε_{mf}	void fraction at minimum fluidization
ν_j	stoichiometric coefficient of the j^{th} reactant
η_j	dimensionless concentration of j^{th} reactant
ρ_g, ρ_z	gas and solid particles density, $\text{kg}\cdot\text{m}^{-3}$

Subscripts

A, P	refers to reactant A and product P
b	refers to bubbles
e	refers to emulsion
f	refers to feed stream
mf	refers to minimum fluidisation condition
q	refers to cooling medium

Superscript

b, c, e	refers to bubble, clouds and emulsion phase, respectively
-----------	---

REFERENCES

- Abba I.A., Grace J.R., Bi H.T., 2002. Variable-gas-density fluidized bed reactor model for catalytic processes. *Chem. Eng. Sci.*, 57, 4797-4807. DOI: 10.1016/S0009-2509(02)00289-0.
- Ajbar A., Alhumazi K., Elnashaie, S.S.E.H., 2001. Classification of static and dynamic behaviour in a fluidized-bed catalytic reactor. *Chem. Eng. J.*, 84, 503-516. DOI: 10.1016/S1385-8947(00)00373-9.
- Balakotaiah V., West D.H., 2014. Thermal effects and bifurcations in catalytic partial oxidations. *Curr. Opin. Chem. Eng.*, 5, 68-77. DOI: 10.1016/j.coche.2014.05.002.
- Berezowski M., 2000. Method of determination of steady-state diagrams of chemical reactors. *Chem. Eng. Sci.*, 55, 4291-4295. DOI: 10.1016/S0009-2509(00)00058-0.
- Berezowski M., 2002. Złożona struktura stanów stacjonarnych układu równolegle połączonych reaktorów zbiornikowych. *Inż. Chem. Proc.*, 23, 415-423.
- Berezowski M., 2010. The application of the parametric continuation method for determining steady state diagrams in chemical engineering. *Chem. Eng. Sci.*, 65, 5411-5414. DOI: 10.1016/j.ces.2010.07.003.
- Bizon K., 2016. Autothermicity, multiplicity, yield and selectivity of catalytic processes in a polytropic fluidized bed reactor. *Chem. Eng. J.*, 288, 834-844. DOI: 10.1016/j.cej.2015.12.061.
- Pinto J.C., Ray W.H., 1995. The dynamic behavior of continuous solution polymerization reactors – VIII. A full bifurcation analysis of a lab-scale copolymerization reactor. *Chem. Eng. Sci.*, 50, 1041-1056. DOI: 10.1016/j.cej.2015.12.061.
- Seydel R., 1994. *Practical bifurcation and stability analysis. From equilibrium to chaos*. Springer-Verlag, New York.
- Tabiś B., 2001. Methanol synthesis in a fluidized-bed reactor coupled with an external heat exchanger. The effect of feedback deformation. *Chem. Eng. J.*, 83, 191-200. DOI: 10.1016/S1385-8947(00)00254-0.
- Uppal A., Ray W.H., Poore A.B., 1976. The classification of the dynamic behavior of continuous stirred tank reactors - Influence of reactor residence time. *Chem. Eng. Sci.*, 31, 205-214. DOI: 10.1016/0009-2509(76)85058-0.
- Westerink E.J., Westerterp K.R., 1990. Stable design and operation of catalytic fluidized-bed reactors for multiple reactions: Uniqueness and multiplicity. *Chem. Eng. J.*, 45, 317-332. DOI: 10.1016/0009-2509(90)87103-Y.
- Zahn V.M., 2012. *Adiabatic simulated moving bed reactor – principle, nonlinear analysis and experimental demonstration*. Shaker Verlag GmbH, Herzogenrath.

Received 3 October 2016
Received in revised form 10 July 2017
Accepted 13 July 2017

INFLUENCE OF ROTATING MAGNETIC FIELD ON GAS-LIQUID VOLUMETRIC MASS TRANSFER COEFFICIENT

Rafał Rakoczy^{*1}, Maciej Konopacki¹, Marian Kordas¹, Radosław Drozd², Karol Fijałkowski²

¹West Pomeranian University of Technology, Szczecin, Faculty of Chemical Engineering, Institute of Chemical Engineering and Environmental Protection Processes, al. Piastów 42, 71-065 Szczecin, Poland

²West Pomeranian University of Technology, Szczecin, Faculty of Biotechnology and Animal Husbandry, Department of Immunology, Microbiology and Physiological Chemistry, al. Piastów 45, 70-311 Szczecin, Poland

The main objective of these experiments was to study the oxygen mass transfer rate through the volumetric mass transfer coefficient (k_La) for an experimental set-up equipped with a rotating magnetic field (RMF) generator and various liquids. The experimental results indicated that k_La increased along the magnetic strength and the superficial gas velocity. Mathematical correlations defining the influence of the considered factors on k_La were proposed.

Keywords: mass transfer; volumetric mass transfer coefficient; rotating magnetic field

1. INTRODUCTION

In many biotechnological processes oxygen supplied to a liquid is insufficient to meet the demand of microorganisms. The oxygen transfer rate is often the limiting factor in bioprocesses due to the low solubility in the medium (Karimi et al., 2013). The oxygen supply into a liquid constitutes one of the decisive factors for microbial growth and can play an important role in optimization of aeration of microbial culture (Galaction et al., 2004a). It should be noticed that the gas-liquid mass transfer is generally the rate-limiting step in many industrial processes (Mills et al., 1999). Therefore, it is important to ensure an adequate delivery of oxygen to the culturing media.

The oxygen mass transfer, described and analyzed by using the volumetric mass transfer coefficient, k_La , is controlled by oxygen solubility into liquids. This parameter may be affected by a lot of factors, such as geometrical and operational characterization of the mixing system. Generally, mechanically agitated gas-liquid contractors are frequently applied in chemical processes or biochemical industries. Mechanical agitation can promote the mass transfer rate because it increases interfacial area between the liquid and gas phases (Garcia-Ochoa et al., 2009; Torab-Mostaedi et al., 2008).

There have been various strategies to improve the oxygen transfer rate in mixers. The novel approach for a mixing process was based on the application of a rotating magnetic field (RMF). As reported by Rakoczy et al. (2011), the RMF can augment the process intensity instead of mechanical mixing. Magnetic fields can be applied to induce *in vivo* and *in vitro* effects in many biological systems (Rakoczy et al., 2016). Recently, increasing attention is directed towards bio-magnetic stimulation of microorganisms using various types of magnetic fields (El-Gaddar et al., 2013; Gorobets et al., 2013;

*Corresponding authors, e-mail: rrakoczy@zut.edu.pl

Santos et al., 2010). Magnetically assisted bioprocesses are conducted using a non-conventional stimulation of classical bioprocesses by various types of magnetic field (Hristov et al., 2011). It should be noted that RMF can be a versatile option for enhancing molecular transport and diffusion in aqueous culture media (Hajiani et al., 2013b).

Weng et al. (2011) pointed out that the increase of magnetic strength enhanced the volumetric mass transfer coefficient ($k_L a$). Al-Qodah et al. (2000) found that this parameter becomes higher as the gas velocity and the magnetic strength increase. Chen et al. (2001) presented that the $k_L a$ was enhanced by the magnetic strength. A recent study by Hajiani et al. (2013a) involved the influence of RMF on the gas-liquid transfer. These results demonstrated that the mass transfer rate was enhanced due to nanoconvective stirring using magnetic nanoparticles.

The main aim of this work was to study the influence of RMF on the aeration process of distilled water and Herstin-Schramm (HS) medium and to work out some mathematical correlation for oxygen transfer in the presence of the external magnetic field (MF). The proposed equations may be useful for optimization or scaling-up of aeration efficiency under the action of RMF.

2. EXPERIMENTAL DETAILS

A schematic of the experimental set-up used in the presented study is shown in Fig. 1.

A total of 4 dm³ of the working liquid was introduced into a vessel (3). The distilled water and Herstin-Schramm (HS) medium composed of glucose (2 w/v%), yeast extract (0.5 w/v%), bacto-pepton (0.5 w/v%), citric acid (0.115 w/v%), Na₂HPO₄ (0.27 w/v%), MgSO₄·7H₂O (0.05 w/v%) and ethanol (1 v/v%) added after sterilization of the base (Ciechańska et al., 1998) were used as experimental liquids. The HS medium is commonly used as the growth medium in the process production of bacterial cellulose (Fijałkowski et al., 2015). The liquid phase height and temperature was equal to 0.3 mm and 20 °C, respectively.

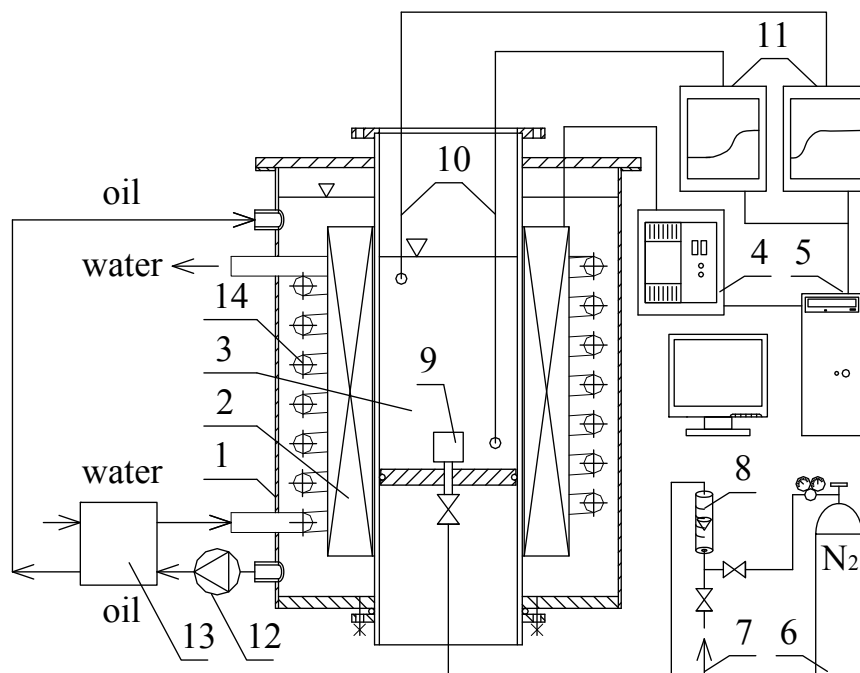


Fig. 1. Schematic diagram of the experimental set-up;

- 1 – housing, 2 – RMF generator, 3 – vessel, 4 – a.c. transistorized inverter, 5 – personal computer, 6 – nitrogen cylinder, 7 – air supply, 8 – rotameter, 9 – membrane sparger, 10 – oxygen probes, 11 – recorders, 12 – circulating pump, 13 – heat exchanger, 14 – internal coil

Nitrogen gas (6) was used for oxygen elimination from the experimental set-up. A rotameter (8) was applied in order to monitor the flow of nitrogen and the average supply air flow rate (7). Gas was injected into the tested liquids by means of a membrane sparger (9). The membrane enabled to obtain fine bubbles with narrow size distribution (in the range between 0.5 and 3 mm). The gas (air) flow rate was varied between 1 and 5 dm³·min⁻¹. The superficial gas velocity was changed in the range between 0.001 - 0.005 m·s⁻¹.

Oxygen probes (10) and recorders (11) were used to measure changes in dissolved oxygen concentration. The solved oxygen concentration in the working liquids was measured using CX-701 multifunction meters with COG-1 probes (Elmetron, Poland). It was assumed that the response of the oxygen electrode to the change in the oxygen concentration is sufficiently fast and does not affect the determination accuracy (Galaction et al., 2004b; Montes et al., 1999; Ozbek and Gayik, 2001).

The temperature of the working liquid during the exposition to RMF was controlled by an additional cooling system based on oil circulation (in a heat exchanger (13) a pump (12)) and water circulation in an internal coil (14).

The active power for the RMF system was calculated by the following relation (Rakoczy, 2013):

$$P = \sqrt{3} U I \cos(\varphi) \Rightarrow P = \sqrt{3} U I 0.85 \Rightarrow P = 1.47 U I \quad (1)$$

The values of current intensity and voltage were recorded by means of the inverter software.

According to the proposed relationship (see Eq. (1)), a plot from calculated data is presented in coordinates (P, f and $P/V_L, f$) in Fig. 2.

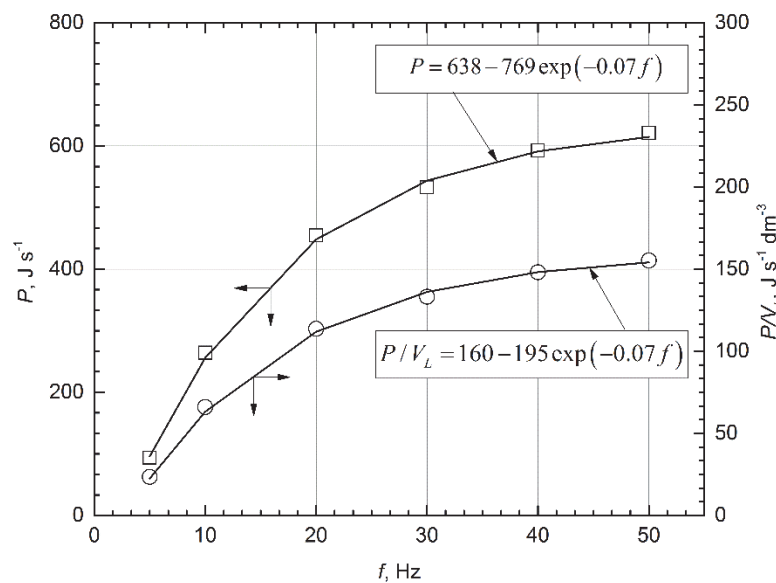


Fig. 2. The graphical presentation of relations between the calculated active power and the specific power input versus the RMF frequency

In the case of the current study, the RMF was identified by means of the magnetic induction B . The values of magnetic induction B at different points inside the vessel were measured using the Hall probe connected and controlled by the frequency of the ac excitation current, f . A typical example of the magnetic field distribution in the cross-section of the RMF generator is given in Fig. 3a. Based on experimental measurements, the relationships of the maximum and the averaged values of the magnetic induction versus the frequency of the excitation current are shown in Fig. 3b.

The volumetric mass transfer coefficient, $k_L a$, was determined using the well-known dynamic gassing-in method (Chistii, 1989). Two independent measurements were made simultaneously by means of two

oxygen probes (localization is given in Fig. 1). The coefficient $k_L a$ was calculated as the averaged value from these measurements. The fluid was deoxygenated with nitrogen until the dissolved oxygen concentration had declined below 2% of air saturation. At that point the nitrogen flow was stopped, the present flow of air established and the dissolved oxygen concentration measured until the liquid became saturated with oxygen to the initial level.

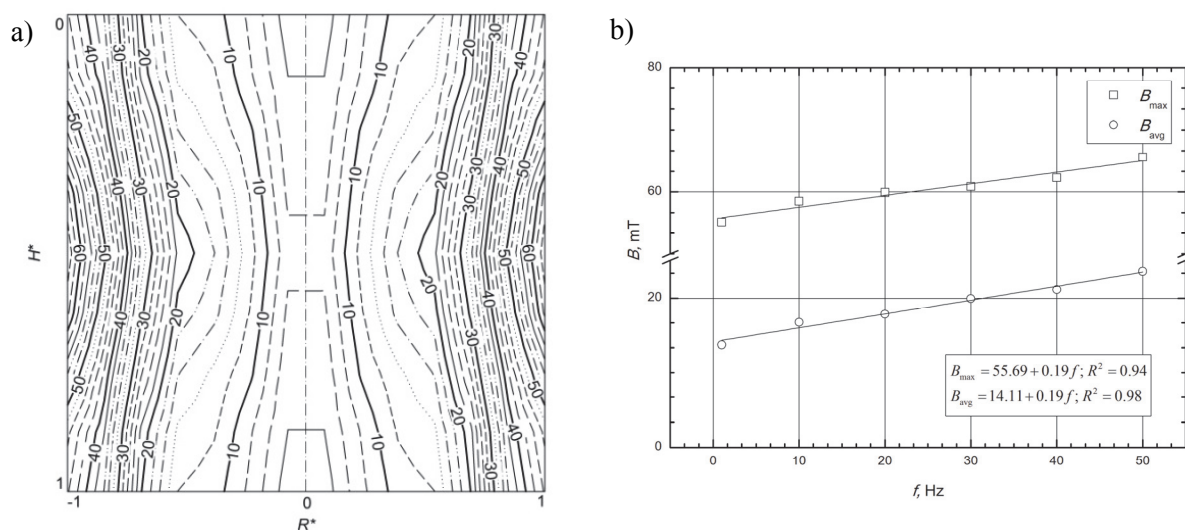


Fig. 3. A typical example of spatial distribution of the magnetic field in the cross-section of the RMF generator for $f = 30$ Hz (a) and the graphical presentation of the relations between the maximal (B_{\max}) and the averaged (B_{avg}) values of magnetic induction versus the frequency of the excitation current f (b)

The volumetric mass transfer coefficient, $k_L a$, was determined on the basis of the following expression (Heim et al., 1995):

$$\frac{dc}{dt} = k_L a (c^* - c) \quad (2)$$

Taking into consideration that the oxygen transfer coefficient was constant throughout the process, the above Eq. (2) was integrated to:

$$k_L a = -\frac{1}{t - t_0} \ln \left(\frac{c^* - c}{c^* - c_0} \right) \quad (3)$$

3. RESULTS AND DISCUSSION

The proposed correlations for the volumetric mass transfer coefficient in mechanically mixers are usually presented in the following form (Galaction et al., 2004b):

$$k_L a = f \left(\frac{P}{V_L}, w_s \right) \Rightarrow k_L a = p_1 \left(\frac{P}{V_L} \right)^{p_2} (w_s)^{p_3} \quad (4)$$

In the case of these experimental results, the total power input P was equal to the active power PR_{MF} as defined by Eq. (1) (Rakoczy, 2013).

In order to provide a comparison of the mass transfer performance of the tested liquids, the experimental volumetric mass transfer coefficients $k_L a$ are plotted in Fig. 4.

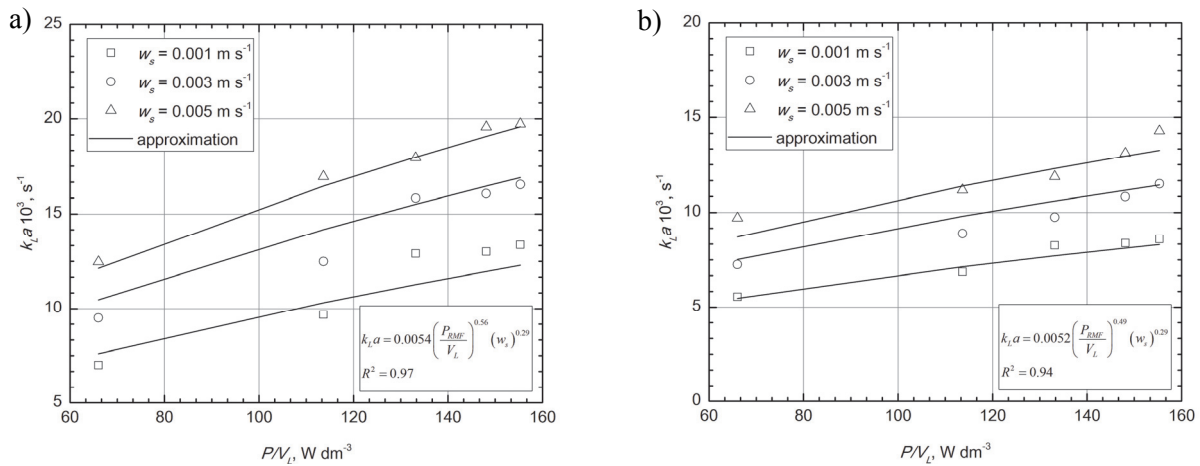


Fig. 4. The volumetric mass transfer coefficient versus the specific power input for distilled water (a) and HS medium (b)

Figure 4 shows that for a particular value of w_s , at equivalent P/V_L , both liquids were characterized by different values of $k_L a$. Figure 4 also shows that the increase of specific power input increased the volumetric mass transfer coefficient for the distilled water (Fig. 4a) and the H-S medium (Fig. 4b). This parameter was enhanced by increasing aeration and specific power. The dependence of the oxygen mass transfer rate on the specific power is more pronounced for the distilled water. As shown in Fig. 4, the increase of the specific power led to the significant intensification of oxygen mass transfer.

The obtained results are compared with available experimental data for the standard mixer (Karimi et al., 2013). Fig. 5 demonstrates that the mixer which produces higher values of $k_L a$ is the Rushton type turbine (single and dual impellers) for the tested aeration rates. The mass transfer data obtained for the mixer with a dual Rushton turbine is consequently higher than the data obtained for a single impeller and magnetically assisted aeration process.

In the present work, the gas-liquid mass transfer under the action of RMF may be correlated by the following relationship (Li et al., 2006)

$$k_L a = f(B_{avg}, w_s) \quad (5)$$

Based on the experimental results, it can be assumed that the volumetric mass transfer coefficient is the function of magnetic induction and the superficial gas velocity.

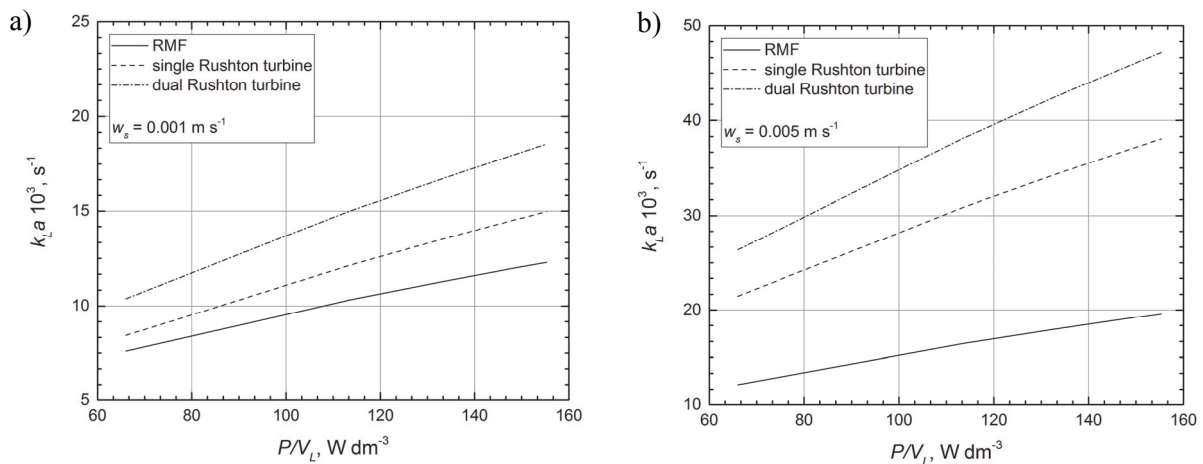


Fig. 5. The performance comparison of the obtained results for distilled water (with RMF application) with literature data from viewpoint of volumetric mass transfer coefficient (two types of impellers – single and dual Rushton turbines)

The following correlation was developed to estimate $k_L a$ for the distilled water and the HS medium, respectively:

$$k_L a|_{water} = 0.0035 (B_{avg})^{1.11} (w_s)^{0.32} \quad (6a)$$

$$k_L a|_{H-S\ medium} = 0.0028 (B_{avg})^{1.03} (w_s)^{0.31} \quad (6b)$$

The $k_L a$ measurement data are presented as a function of the averaged value of the magnetic induction and the superficial gas velocity in Fig. 6. As can be seen, the volumetric mass transfer coefficient did not react very sensitively on the airflow modulation. In contrast it more sensitively responded to changes in magnetic induction. Fig. 6 also shows that over a wide interval of the averaged magnetic induction, the application of distilled water as the working liquid led to significantly higher $k_L a$ values than the HS medium at the same magnetic induction.

The influence of the magnetic field on the volumetric mass transfer coefficient may be described by means of the amplification factor (Galaction et al, 2004b). The effect observed due to the magnetic field can be described using the ratio between the volumetric mass transfer coefficient under the RMF action, $(k_L a)_{B_{avg}=var}$, and for the volumetric mass transfer coefficient without the RMF action, $(k_L a)_{B_{avg}=0}$, obtained for similar experimental conditions.

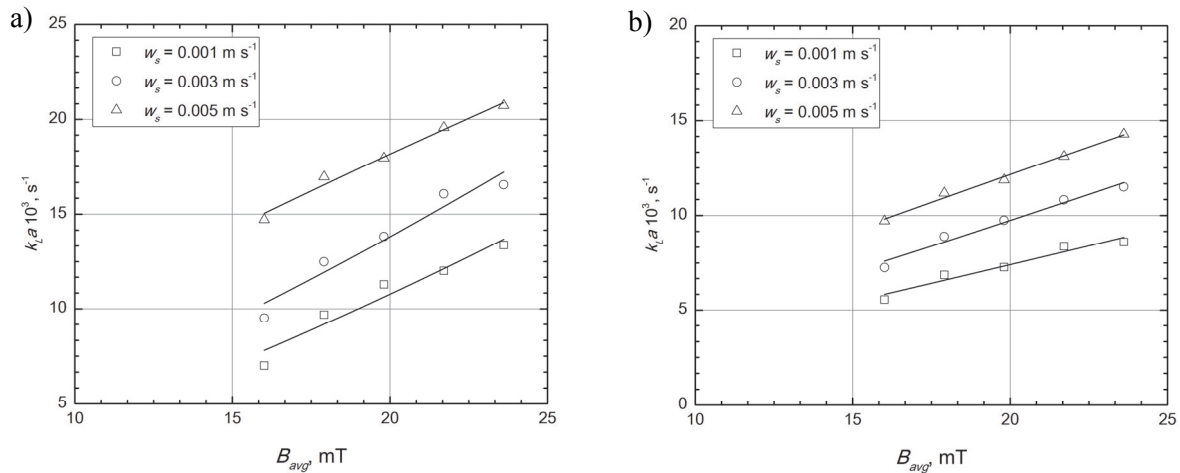


Fig. 6. The volumetric mass transfer coefficient versus the averaged magnetic induction for distilled water (a) and HS medium (b)

The variation in the coefficient $k_L a$ depending on the volumetric flow rate of air is presented in Fig. 7.

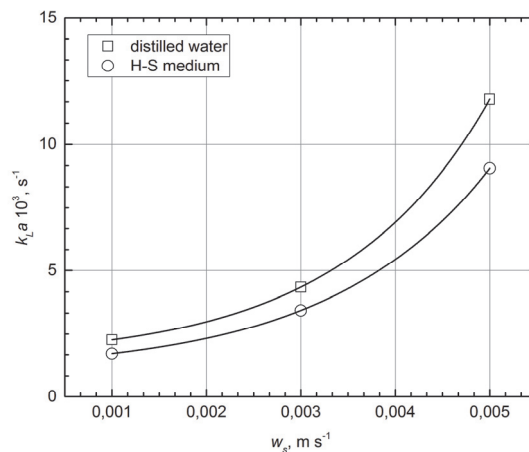


Fig. 7. The volumetric mass transfer coefficient versus the superficial gas velocity

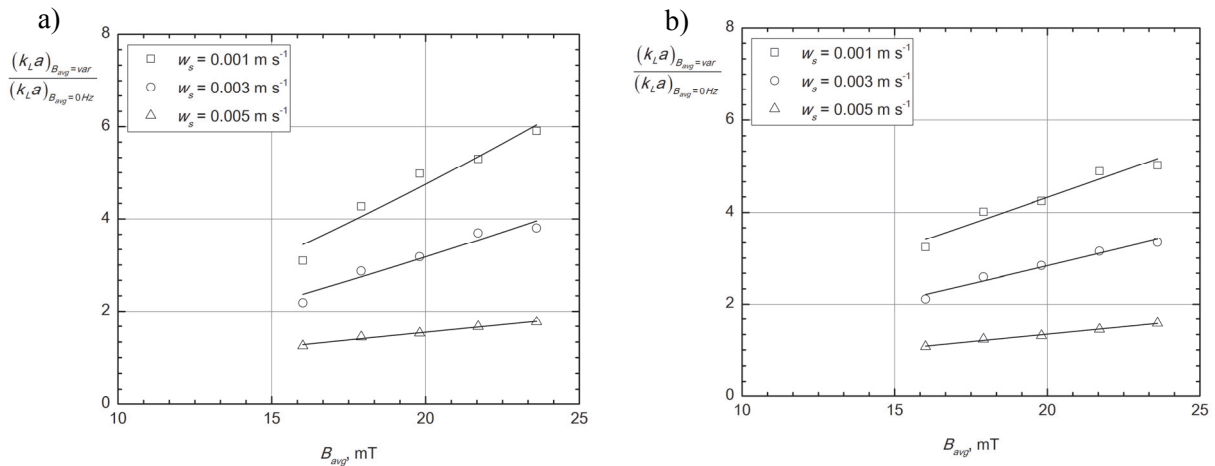


Fig. 8. The effect of the averaged magnetic induction on the amplification factor of the volumetric mass transfer coefficient

Figure 8 shows the ratio $(k_L a)_{B_{avg}=var}/(k_L a)_{B_{avg}=0}$ obtained with aeration and in the presence of RMF. Figure 8 also shows that RMF caused a significant enhancement of the volumetric mass transfer coefficient as compared to the $k_L a$ value for the working liquids without the RMF action.

For a better characterization of the RMF generator according to the oxygen mass transfer, the term of oxygen transfer efficiency, E_{O_2} , may be applied and defined as (Chisti et al., 2002)

$$E_{O_2} = \frac{k_L a}{\left(\frac{P}{V_L}\right)} \quad (7)$$

As can be seen from Figures 9a and 9b, plotted for the two considered liquids, the variation of the oxygen transfer efficiency with the specific power input was contrary to that of $k_L a$ with the specific power input (see Fig. 4). These results suggest that the oxygen mass transfer rate reaches higher values under the action of RMF, but with considerable energy consumption. As shown in Fig. 9 for the air-distilled water and the air-H-S medium systems, the increase of the aeration rate is connected with the increase of the oxygen transfer efficiency due to the enhancement of turbulence and of the extent of the interfacial area needed for oxygen transfer.

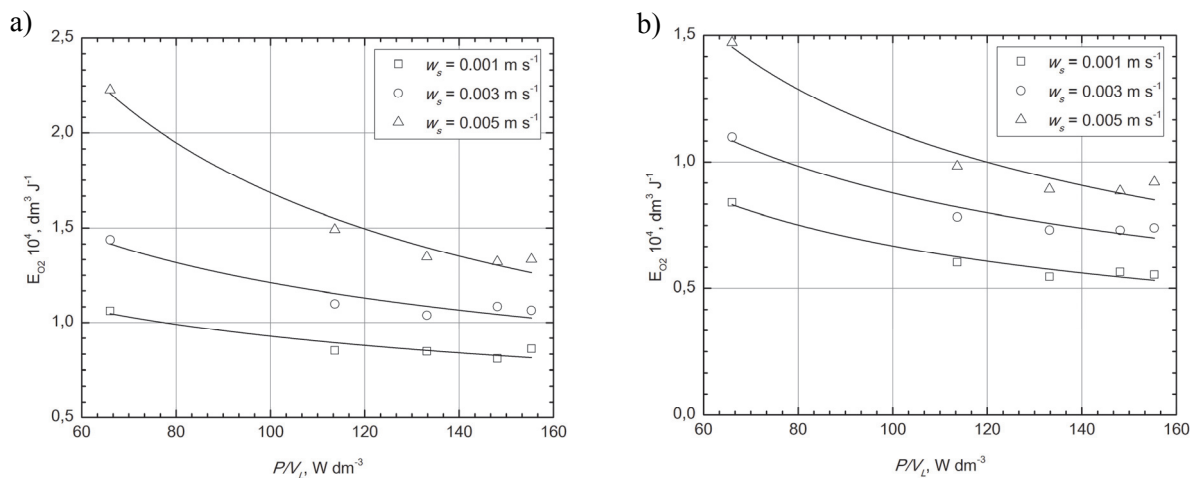


Fig. 9. The influence of specific power input on oxygen transfer efficiency

The obtained results may be explained by the fact that apart from molecular diffusion, fluid vorticity is the only mixing mechanisms of the liquid bulk in gas-liquid contractor (Hajiani et al., 2013a). It should

be noticed that the electrically conductive fluid exposed to alternating MF (including RMF) induce the Lorentz electromagnetic force. This force which is generated perpendicularly to the electric field, acts as the driving force inducing currents inside the liquid and causing liquid rotation (Moffat, 1965; Rakoczy, 2011; Spitzer, 1999; Volz et al., 1999).

The movement of the medium exposed to RMF can be explained on the basis of micro-level dynamo concept (Gaafar, 2008). The RMF associated eddy currents can be induced in the liquid as a consequence of the magnetic field because the liquid contains various charged particles e.g. ions (Anton-Leberre et al., 2010; Hristov 2010). Eddy currents may generate local MFs around ions, which in combination with an externally-applied MF, cause induction of their rotation and thus the movement of the liquid in accordance to the MF vector. As a consequence of this process, rotating ions create “dynamos” which cause the effect of micro-mixing (Anton-Leberre et al., 2010; Mehedintu et al. 1997). This mixing effect of RMF can enhance the mass transfer by reducing the diffusion mass transfer resistance (Hristov, 2010). Hristov (2010) indicated that the hydrodynamic effects on the mass transfer in magnetically assisted bioreactors are of primary importance. It was also suggested that the coefficient k_{La} can be effectively controlled by the magnetic field. Iwasaka et al. (2004) showed that the magnetic field gradient in the horizontal direction causes a convectional flow, which increases oxygen concentration in the liquid. It was suggested that the magnetic field can be applied for the motion control of diamagnetic and paramagnetic elements in the liquid phase (Iwasaka et al., 2004). Kitazawa et al. (2001) clearly indicated that the application of magnetic field significantly enhances oxygen concentration in water dissolved from the gas phase. It has turned out that dissolution kinetics can be enhanced several times by the magnetic field. A possible explanation for the enhancement of k_{La} factor under the RMF action might be that the increase of k_{La} is mainly due to the possibility of keeping bubbles small in size (Al-Qodah et al., 2000). Weng et al. (1992) reported that bubble rise velocity and bubble diameter decrease with the magnetic field strength. It was suggested that the magnetic field retains bubbles in liquid and it might increase the surface tension of bubbles, thereby enhancing the lifetime of bubbles (Fabian, 2002).

4. CONCLUSIONS

Results obtained in the present study indicated that RMF provided higher values of the volumetric mass transfer coefficient k_{La} in the analyzed liquids (distilled water and HS medium). This parameter increased along with the magnetic field strength and the superficial gas velocity. The intensification of aeration led to the increase of turbulence inside the analyzed liquids, thus promoting the acceleration of oxygen transfer rate. Therefore, it can be concluded, that modifying the specific power input between 60 - 160 W·dm⁻³ and the superficial air velocity from 0.001 to 0.005 m·s⁻¹, the maximum k_{La} can be increased by 6 times in the case of distilled water and by 5 times in the case of the HS medium.

This study was supported by the National Centre for Research and Development in Poland (Grant No. LIDER/011/221/L-5/13/NCBR/2014).

The authors would like to thanks firm STAGUM-EKO for co-operation and technical support in the area of the membrane sparger.

SYMBOLS

B_{avg}	vector magnitude of magnetic field, kg·A ⁻¹ ·s ⁻²
c	instantaneous concentration of dissolved oxygen, kmol·m ⁻³

c_0	initial concentration of dissolved oxygen, $\text{kmol}\cdot\text{m}^{-3}$
c^*	saturation concentration of dissolved oxygen, $\text{kmol}\cdot\text{m}^{-3}$
I	current intensity, A
$k_L a$	volumetric mass transfer coefficient, s^{-1}
P	total power input, W
Pa	active power, $\text{J}\cdot\text{s}^{-1}$
p_1, p_2 and p_3	constants for a given combination of the fluid and the RMF generator
t	time, s; t_0 – initial time, s
U	voltage, V
V_L	volume of liquid, m^3
w_s	superficial gas velocity, $\text{m}\cdot\text{s}^{-1}$

Greek symbols

$\cos(\varphi)$	phase shift angle between voltage and current
-----------------	---

REFERENCES

- Al-Qodah Z., Al-Hassan M., 2000. Phase holdup and gas-to-liquid mass transfer coefficient in magneto stabilized G-L-S airlift fermenter. *Chem. Eng. J.*, 79, 41-52. DOI: 10.1016/S1385-8947(00)00142-X.
- Anton-Leberre V., Haanappel E., Marsaud N., Trouilh L., Benbadis L., Boucherie H., 2010. Exposure to high static or pulsed magnetic fields does not affect cellular processes in the yeast *Saccharomyces cerevisiae*. *Bioelectromagnetics*, 31, 28-38. DOI: 10.1002/bem.20523.
- Chen C.M., Leu L.P., 2001. Hydrodynamics and mass transfer in three-phase magnetic fluidized beds. *Powder Technol.*, 117, 198-206. DOI: 10.1016/S0032-5910(00)00370-3.
- Chisti M.Y., 1989. *Airlift Bioreactors*. Elsevier, New York, USA.
- Chisti M.Y., Jauregui-Haza U.J., 2002. Oxygen transfer and mixing in mechanically agitated airlift bioreactors. *Biochem. Eng. J.*, 10, 143-153. DOI: 10.1016/S1369-703X(01)00174-7.
- Ciechańska D., Struszczyk H., Gruzńska K., 1998. Modification of Bacterial Cellulose. *Fibres Text. East. Eur.*, 6, 61-65.
- El-Gaddar A., Frénéa-Robin M., Voyer D., Aka H., Haddour N., Krähenbühl L., 2013. Assessment of 0.5 T static fields exposure effect on yeast and HEK cells using electrorotation. *Biophys. J.* 104, 1805-1811. DOI: 10.1016/j.bpj.2013.01.063.
- Fabian A.C., 2002. Bubbles, flows and fields. *Science*, 296, 1040-1041. DOI: 10.1126/science.1072074.
- Fijałkowski K., Żywicka A., Drozd R., Niemczyk A., Junka A. F., Peitler D., Kordas M., Konopacki M., Szymczyk P., El Fray M., Rakoczy R., 2015. Modification of bacterial cellulose through exposure to the rotating magnetic field. *Carbohydr. Polym.*, 133, 52-60. DOI: 10.1016/j.carbpol.2015.07.011.
- Gaafar E.S.A., Hanafy M.S., Tohamy E.Y., Ibranhim M.H., 2008. The effect of electromagnetic field on protein molecular structure of *E. Coli* and its pathogenesis. *Rom. J. Biophys.*, 18, 145-169.
- Galaction A.-I., Dan C., Comelin O., Marius T., 2004a. Enhancement of oxygen mass transfer in stirred bioreactors using oxygen-vectors: 1. Simulated fermentation broths. *Bioproc. Biosyst. Eng.*, 26, 231-238. DOI: 10.1007/s00449-004-0353-5.
- Galaction A.-I., Cascaval D., Oniscu C., Turnea M., 2004b. Prediction of oxygen mass transfer coefficients in stirred bioreactors for bacteria, yeasts and fungus broths. *Biochem. Eng. J.*, 20, 85-94. DOI: 10.1016/j.bej.2004.02.005.
- Garcia-Ochoa F., Gomez E., 2009. Bioreactor scale-up and oxygen transfer rate in microbial processes: An overview. *Biotechnol. Adv.*, 27, 153-176. DOI: 10.1016/j.biotechadv.2008.10.006.
- Gorobets S.V., Yu G.O., Demianenko I.V., Nikolaenko R.N., 2013. Self-organization of magnetic nanoparticles in providing *Saccharomyces cerevisiae* yeasts with magnetic properties. *J. Magn. Magn. Mater.*, 337-338, 53-57. DOI: 10.1016/j.jmmm.2013.01.004.
- Hajiani P., Larachi F., 2013a. Remotely excited magnetic nanoparticles and gas-liquid mass transfer in Taylor flow regime. *Chem. Eng. Sci.*, 93, 257-265. DOI:10.1016/j.ces.2013.01.052.

- Hajiani P., Larachi F., 2013b. Giant effective liquid-self diffusion in stagnant liquids by magnetic nanomixing. *Chem. Eng. Process.*, 71, 77-82. DOI: 10.1016/j.cep.2013.01.014.
- Heim, A., Kraslawski, A., Rzycki, E., Stelmach, J., 1995. Aeration of bioreactors by self-aspirating impellers. *Chem. Eng. J. Bioch. Eng.*, 58, 59-63. DOI:10.1016/0923-0467(94)06093-2.
- Hristov J., 2010. Magnetic field assisted fluidization - A unified approach. Part 8. Mass Transfer: Magnetically assisted bioprocesses. *Rev. Chem. Eng.*, 26, 55-128. DOI: 10.1515/REVCE.2010.006.
- Hristov J., Perez V.H., 2011. Critical analysis of data concerning *Saccharomyces cerevisiae* free-cell proliferations and fermentations assisted by magnetic and electromagnetic fields. *Int. Rev. Chem. Eng.*, 3, 3-20.
- Iwasaka M., Ikchata M., Miyakoski, Ueno S., 2004. Strong static magnetic field effects on yeast proliferation and distribution. *Bioelectrochemistry*, 65, 59-68. DOI: 10.1016/j.bioelechem.2004.04.002.
- Karimi A., Golbabaee F., Mehrnia M. R., Neghab M., Mohhammad K., Nikpey A., Pourmand M. R., 2013. Oxygen mass transfer in a stirred tank bioreactor using different impeller configurations for environmental purposes. *Iran. J. Environ. Health.*, 10, 6. DOI: 10.1186/1735-2746-10-6.
- Kitazawa K., Ikezoe Y., Uetake H., Hirota N., 2001. Magnetic field effects on water, air and powder. *Physica B*, 294-295, 709-714. DOI: 10.1016/S0921-4526(00)00749-3.
- Li W., Zong B. N., Li X. F., Meng X. K., Zhang J. L., 2006. Interphase mass transfer in G-L-S magnetically stabilized bed with amorphous alloy SRNA-4 catalyst. *Chinese J. Chem. Eng.*, 14, 734-739. DOI: 10.1016/S1004-9541(07)60004-4.
- Mehedintu M., Berg H., 1997. Proliferation response of yeast *Saccharomyces cerevisiae* on electromagnetic field parameters. *Bioelectroch. Bioener.*, 43, 67-70. DOI: 10.1016/S0302-4598(96)05184-7.
- Mills P.L., Chaudhari R.V., 1999. Reaction engineering of emerging oxidation processes. *Catal. Today.*, 48, 17-29. DOI: 10.1016/S0920-5861(98)00354-X.
- Moffat H.K., 1965. On fluid flow induced by a rotating magnetic field. *J. Fluid. Mech.*, 22, 521-528. DOI: 10.1017/S0022112065000940.
- Montes F.Y., Catalan J., Galan M.A., 1999. Prediction of k_{La} in yeast broths. *Proc. Biochem.*, 34, 549-554. DOI: 10.1016/S0032-9592(98)00125-3.
- Ozbek B., Gayik S., 2001. The studies on the oxygen mass transfer coefficient in a bioreactor. *Proc. Biochem.*, 36, 729-741. DOI: 10.1016/S0032-9592(00)00272-7.
- Rakoczy R., 2011. *Theoretical and experimental analysis of the influence of the rotating magnetic field on the selected unit operations and processes of chemical engineering*. Academic Publisher of West Pomeranian University of Technology, Szczecin. ISBN 978-83-7663-074-8.
- Rakoczy R., 2013. Mixing energy investigations in a liquid vessel that is mixed by using a rotating magnetic field. *Chem. Eng. Process. Process Intensif.*, 66, 1-11. DOI: 10.1016/j.cep.2013.01.012.
- Rakoczy R., Konopacki M., Fijałkowski K., 2016. The influence of a ferrofluid in the presence of an external rotating magnetic field on the growth rate and cell metabolic activity of a wine yeast strain. *Biochem. Eng. J.* 109, 43-50. DOI: 10.1016/j.bej.2016.01.002.
- Rakoczy, R., Masiuk, S., 2011. Studies of a mixing process induced by a transverse rotating magnetic field. *Chem. Eng. Sci.*, 66, 2298-2308. DOI: 10.1016/j.ces.2011.02.021.
- Santos L.O., Alegre R.M., Garcia-Diego C., Cuellar J., 2010. Effects of magnetic fields on biomass and glutathione production by the yeast *Saccharomyces cerevisiae*. *Process. Biochem.*, 45, 1362-1367. DOI: 10.1016/j.procbio.2010.05.008.
- Spitzer K.H., 1999. Application of rotating magnetic fields in Czochralski crystal growth. *Prog. Cryst. Growth. Ch.*, 38, 59-71. DOI: 10.1016/S0960-8974(99)00008-X.
- Torab-Mostaedi M., Safdari S.J., Moosavian M.A., Maragheh M.G., 2008. Mass transfer coefficients in a Hanson mixer-settler extraction column. *Braz. J. Chem. Eng.*, 25, 473-481. DOI: 10.1590/S0104-66322008000300005.
- Volz M. P., Mazuruk K., 1999. Thermoconvective instability in a rotating magnetic field. *Int. J. Heat Mass Tran.*, 42, 1037-1045. DOI: 10.1016/S0017-9310(98)00168-9.
- Weng D.C., Cheng L.N., Han Y., Zhu W.X., Xu S.M., Ouyang F., 1992. Continuous ethanol fermentation in a three-phase magnetic fluidized bed bioreactor. *AIChE Symposium Series, Fluidized Processes: Theory and Practice*, 88, 107-115.

Received 28 September 2016

Received in revised form 11 July 2017

Accepted 14 July 2017

ENERGETIC EFFICIENCY OF MASS TRANSFER ACCOMPANIED BY CHEMICAL REACTIONS IN LIQUID-LIQUID SYSTEMS

Magdalena Jasińska*, Jerzy Baldyga

Warsaw University of Technology, Faculty of Chemical and Process Engineering, ul. Waryńskiego 1, Warsaw, Poland

Energetic efficiency depicting the fraction of energy dissipation rate used to perform processes of drop breakup and mass transfer in two-phase, liquid-liquid systems is considered. Results of experiments carried out earlier in two types of high-shear mixers: an in-line rotor-stator mixer and a batch rotor-stator mixer, have been applied to identify and compare the efficiency of drop breakage and mass transfer in both types of mixers. The applied method is based on experimental determination of both: the product distribution of chemical test reactions and the drop size distributions. Experimental data are interpreted using a multifractal model of turbulence for drop breakage and the model by Favelukis and Lavrenteva for mass transfer. Results show that the energetic efficiency of the in-line mixer is higher than that of the batch mixer; two stator geometries were considered in the case of the batch mixer and the energetic efficiency of the device equipped with a standard emulsor screen (SES) was higher than the efficiency of the mixer equipped with a general purpose disintegrating head (GPDH) for drop breakup but smaller for mass transfer.

Keywords: chemical test reactions, energetic efficiency of mixing, mass transfer, liquid-liquid system, rotor-stator mixer

1. INTRODUCTION

In this paper drop breakage and mass transfer accompanied by complex chemical reactions carried out in in-line and batch rotor-stator devices are considered. Rotor-stator devices are used in many technologies in the chemical, pharmaceutical, biochemical, agricultural, cosmetic, health care and food processing industries. They belong to the group of high-shear devices and are characterized by a focused delivery of energy to active high-shear regions that occupy very a small fraction of internal mixer space. High stresses and high shear rates are generated in rotor-stator mixers because the rotor is situated in a close proximity of the stator and very high rotor speeds are applied. Such delivery of energy results in fast breakage of droplets and intensive mass transfer in the small active region of the mixer but the same time there is slow mass transfer and no breakage in larger regions characterized by a low rate of energy dissipation. Creation of high shear requires applying high agitation power and thus it is important to check how efficiently this power is used. This means that development of methods that can be used to predict the agitation power, to estimate both the efficiency of drop breakage and the efficiency of mass transfer is of importance. Moreover, to characterize properly mass transfer one needs to apply reliable models.

The energy dissipation rate in the in-line rotor-stator mixer resulting from agitation and flow can be calculated from the power number equation in the form proposed by Baldyga et al. (2007) and published for considered Silverson 088/150 MS mixer by Hall et al. (2013) as

*Corresponding authors, e-mail: magdalena.jasinska@pw.edu.pl

$$N_p = 6.9 \cdot N_Q + 0.252 \quad (1)$$

where

$$N_Q = Q / (ND_{out}^3) \quad (2)$$

represents dimensionless flow rate or the dimensionless pumping capacity of the rotor-stator device.

In the case of batch mixers instead of Eq. (1) one should use a constant value of the power number, N_p ; for considered in present work batch mixers one has $N_p = 1.7$ for the device equipped with a general purpose disintegrating head (GPDH) and $N_p = 2.3$ when a standard emulsor screen (SES) is used (Utomo, 2009; Padron, 2001).

The average rate of energy dissipation is given by Eq. (3)

$$\varepsilon_T = N_p N^3 D_{out}^5 / V_H \quad (3)$$

One can see that in the case of the in-line mixer the average rate of energy dissipation, ε_T , increases with increasing both the rotor speed and the pumping capacity of the rotor-stator, Q , and in the case of batch mixer it depends on the rotation speed similarly as in the case of batch stirred tanks.

The maximum stable drop size d_d can be estimated including intermittency effects using equation given by Bałdyga and Podgórska (1998):

$$d_d = C_x^{1.54} L \left(\frac{\sigma}{\rho_c \varepsilon^{2/3} L^{5/3}} \right)^{0.93} \quad (4)$$

where L is the integral scale of turbulence and $C_x = 0.23$.

The method to characterize mass transfer is based on identifying effects of mass transfer on the product distribution of complex test reactions, applied as reactive tracers to two-phase, liquid-liquid systems. As a system of test reactions a set of two parallel reactions is used



the first of them being instantaneous and the second one fast relative to mixing and mass transfer. Two reactants, benzoic acid (B) and ethyl chloroacetate (C), initially dissolved in toluene are transferred from a dispersed, organic phase to the continuous aqueous phase, where they react with the third reactant, the same for both of them, sodium hydroxide (A). The product distribution of this set of parallel chemical reactions

$$X_S = \Delta N_C / N_{C0} \quad (6)$$

where ΔN_C represents the number of ester moles reacting with NaOH and N_{C0} is the complete number of ester moles introduced into the system, is a good measure of a competition between reactions, mixing and mass transfer and can be used to identify energetic efficiency of mass transfer (Jasińska et al., 2013a).

Regarding reliable prediction of the mass transfer coefficient to or from spherical particles, starting from works of Levich (1962) and Batchelor (1980) there are two basic methods available in the chemical engineering and fluid mechanics literature that are applied for modeling of mass transfer at small values of the particle Reynolds number resulting from small particle size. The first method considers surface mobility but neglects fluid deformation (so neglects velocity variation in the vicinity of droplet), whereas the second method neglects surface mobility but takes into account deformation of fluid. The first method is applied to describe external mass transfer of bubbles and not very viscous

liquids (Levich, 1962) and predicts $Sh \propto Pe^{1/2}$, the second one predicts $Sh \propto Pe^{1/3}$ and is applied to model mass transfer between ambient fluid and solid particles, very viscous drops or drops with immobilized surface, under assumptions that droplets behave as hard spheres. The spherical particle shape was assumed in both cases. Moreover, mass transfer models do not converge at infinitely high viscosity of dispersed phase; in correlation derived for drop dependence $Sh \propto Pe^{1/2}$ is conserved at infinitely large viscosity of the dispersed phase, μ_d .

Favelukis and Levrenteva (2013) included effects of drop deformation to the shape of prolate ellipsoid by using the Taylor deformation parameter:

$$Sh \cdot A^* = \frac{k_L a_{drop}}{4\pi R_{eq} D_i} = \sqrt{\frac{3}{2\pi(1+K)}} \left[1 - \frac{4(4+31K)Y}{315(1+K)} N_{Ca} \right] Pe^{1/2} \quad (7)$$

where $Y = (19K + 16) / (16K + 16)$, K is the viscosity ratio $K = \eta_d / \eta_c$, $Pe = \dot{\gamma} R_{eq}^2 / D_i$, and the capillary number is defined by $N_{Ca} = \eta_c \dot{\gamma} R_{eq} / \sigma$. R_{eq} represents the equivalent radius, i.e. the radius of a sphere of equal volume to that of the deformed drop and A^* is the ratio of the surface area of deformed drop surface area a_{drop} to the area of equivalent sphere, $4\pi R_{eq}^2$.

Equation (7) describes mass transfer to or from spherical drops. Notice that the exponent on Pe is equal to 0.5 and is independent of the viscosity ratio, and for $K = \eta_d / \eta_c \rightarrow \infty$ the mass transfer coefficient becomes equal to zero!

Problems related to mass transfer modeling with an exponent on the Péclet number varying between 1/2 and 1/3 when the viscosity ratio increases from zero to infinity were considered in our previous publications (Bałdyga and Jasińska, 2011; Jasińska et al., 2013) and some adequate models were developed. Unfortunately, they are too complex for direct use. Based on the results of Bałdyga and Jasińska (2011) the exponent on Pe in Eq.(7) can be approximated by a term $1/2 - \exp(-4/K^2)/6$, yielding:

$$Sh \cdot A^* = \frac{k_L a_{drop}}{4\pi R_{eq} D_i} = \sqrt{\frac{3}{2\pi(1+K)}} \left[1 - \frac{4(4+31K)Y}{315(1+K)} N_{Ca} \right] Pe^{2 - \frac{\exp(-4/K^2)}{6}} \quad (8)$$

Then the model describes relations between fluid deformation rate, drop deformation, surface mobility, molecular diffusion and mass transfer rate.

The aim of this study is to compare energetic efficiency of drop breakage and mass transfer processes carried out in in-line and batch rotor-stator mixers using complex test reactions and the presented above model of mass transfer. Energetic efficiency should illustrate the ratio of the minimum rate of energy dissipation necessary to perform a considered process to the experimentally measured one, and can be expressed by the ratio of time constants using a reliable reference model for mass transfer as presented in Section 3.

2. EXPERIMENTAL INVESTIGATIONS

In the case of in-line experiments (Jasińska et al., 2013a; 2016) the experimental rig consisted of a system for supply of an aqueous solution of NaOH from a constant head tank, the Silverson 088/150 MS mixer and a valve on the outflow to control the flow. The Silverson rotor-stator mixer (Silverson Machines Ltd., Chesham, UK) fitted with double concentric rotors enclosed between concentric double stators was used. The experimental rig and the Silverson mixer are shown in Figs. 1 and 2, while the mixer characteristics are presented in Table 1.

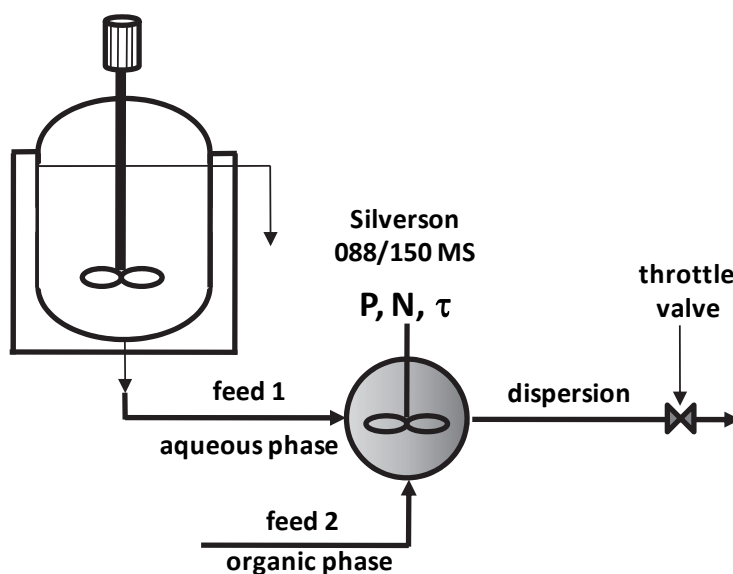


Fig. 1. Silverson 088/150 MS mixer – scheme of experimental system

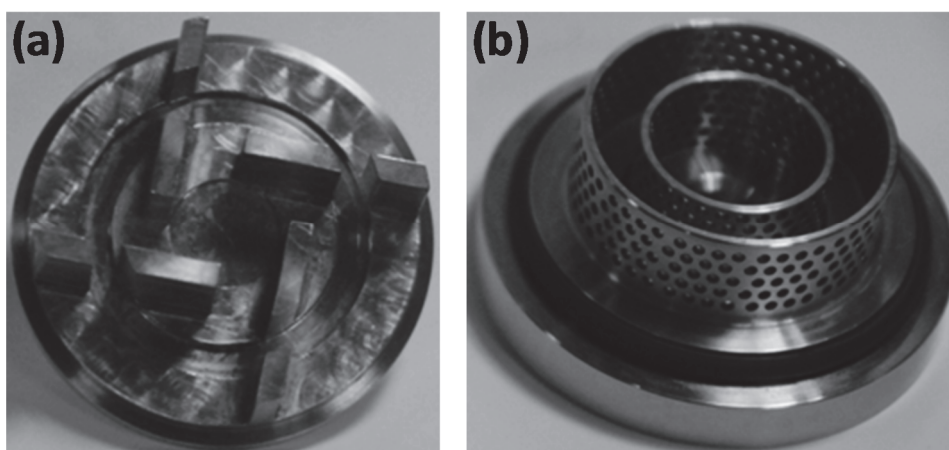


Fig. 2. Double rotors (a) and double emulsor stators (b)

Table 1. Dimensions of the laboratory scale in-line Silverson 088/150 MS mixer

Silverson rotor-stator (088/150 MS) parameters:	Value
D_{out} , mm	38.1
D_{in} , mm	22.4
V_H , mm ³	12655
$N_{r,out}$	4
$N_{r,in}$	4
$H_{r,out}$	240
$H_{r,in}$	180
A_{out} , mm ²	1736
A_P , %	27.4
N , rpm	150 - 11000

The instrumentation included a torque meter. The natural pumping action of the Silverson mixer was used to provide the main flow of the aqueous solution and measured by a Micro Motion Coriolis

R-Series mass flowmeter, whereas the organic solution was introduced using the syringe pump through the separate inlet. Investigations were performed for the rotation speeds ranging from 250 to 10,000 rpm for 3 values of the flow rate: $Q_{aq} = 3.32 \times 10^{-6} \text{ m}^3/\text{s}$, $Q_{org} = 3.33 \times 10^{-8} \text{ m}^3/\text{s}$ (Case 1), $Q_{aq} = 8.26 \times 10^{-6} \text{ m}^3/\text{s}$, $Q_{org} = 8.33 \times 10^{-8} \text{ m}^3/\text{s}$ (Case 2), and $Q_{aq} = 1.65 \times 10^{-5} \text{ kg/s}$, $Q_{org} = 1.67 \times 10^{-7} \text{ m}^3/\text{s}$ (Case 3), respectively.

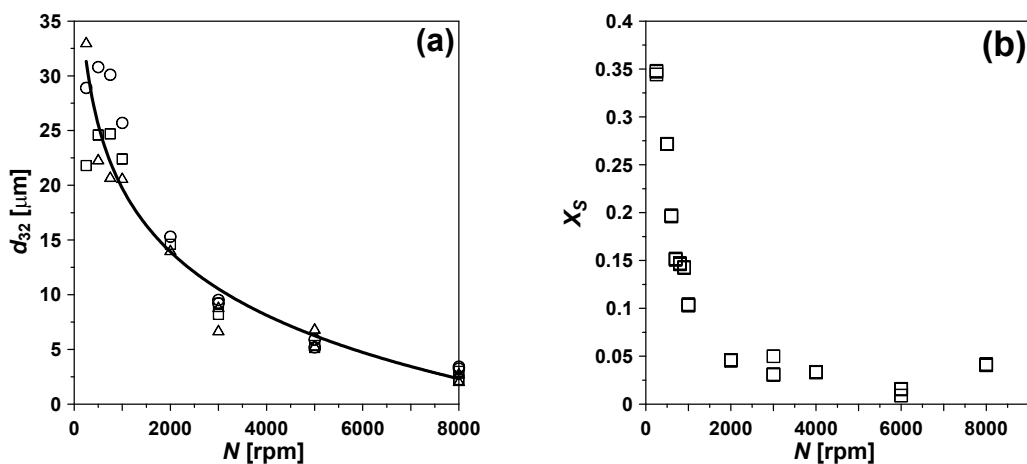


Fig. 3. Examples of experimental results for in-line mixer: (a) effect of the rotor speed on the drop size for Case 1, (b) effect of rotor speed on product distribution X_s for Case 3

In experiments the continuous phase was an aqueous solution of NaOH (A) and the dispersed phase was a solution of benzoic acid (B) and ethyl chloroacetate (C) in toluene. Feed concentrations of reactants used in experiments are presented in Table 2 together with flow rates.

Table 2. Process conditions for Cases 1, 2 and 3

	Q_{aq} [m^3/s]	Q_{org} [m^3/s]	C_{B0} [mol/m^3]	C_{C0} [mol/m^3]	C_{A0} [mol/m^3]
Case 1	3.32×10^{-6}	3.33×10^{-8}	500	500	5
Case 2	8.26×10^{-6}	8.33×10^{-8}	500	500	5
Case 3	1.65×10^{-5}	1.67×10^{-7}	500	500	5

In experiments carried out in a batch system NaOH solution (990 cm^3) was present in the vessel and the organic solution (10 cm^3) was added to start the process (Jasińska et al., 2013). Experiments were carried out in a batch reactor with a diameter of 12 cm, equipped with the Silverson rotor-stator mixer (Fig. 4a). The Silverson mixer was equipped with a four blade rotor with a diameter of 31.2 mm and a height of 12.45 mm, and two stator geometries were investigated: a standard emulsor screen (SES) (Fig. 4b) and a general purpose disintegrating head (GPDH) (Fig. 4c).

An aqueous solution of NaOH (A) of the concentration of $0.005 \text{ mol}/\text{dm}^3$ and a solution of benzoic acid (B) and ethyl chloroacetate (C) in toluene, both of the concentration of $0.5 \text{ mol}/\text{dm}^3$ were applied. The volume fraction of organic phase was 0.01.

In both cases temperature was measured using PT100 probes and all data logged on to an Emersons Delta V system. The product distribution of test reactions was determined based on high-performance liquid chromatography (HPLC) measurements. The drop size distribution was measured with the Malvern MasterSizer 3000. A surfactant Sodium Laureth Sulfate (SLES) was added to samples after carrying out the process of mixing with a chemical reaction to stabilize dispersion and avoid possible effects of droplet coalescence. In the case of droplet dispersion without a chemical reaction, SLES (0.5 wt. %) was added to water before drop dispersion experiment.

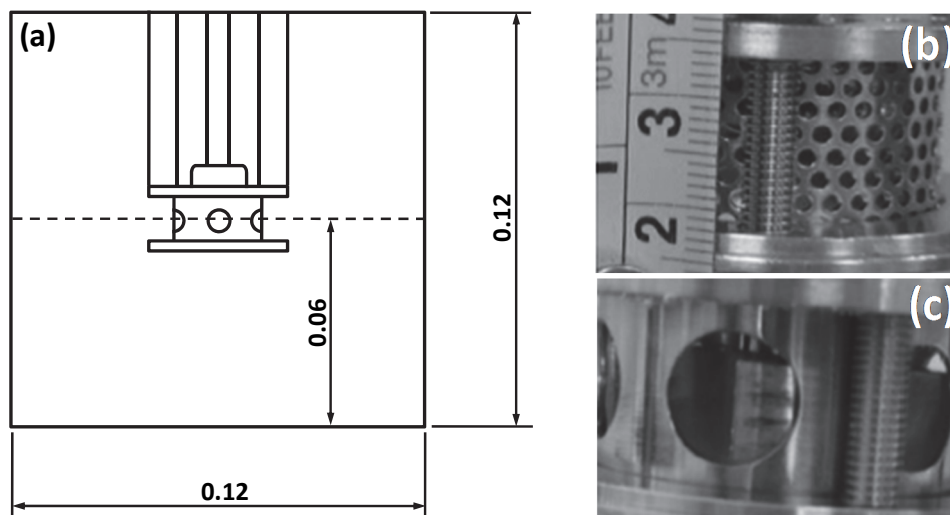


Fig. 4. Batch system, experimental setup: a) rotor-stator in batch system, b) standard emulsor screen (SES), c) general purpose disintegrating head (GPDH)

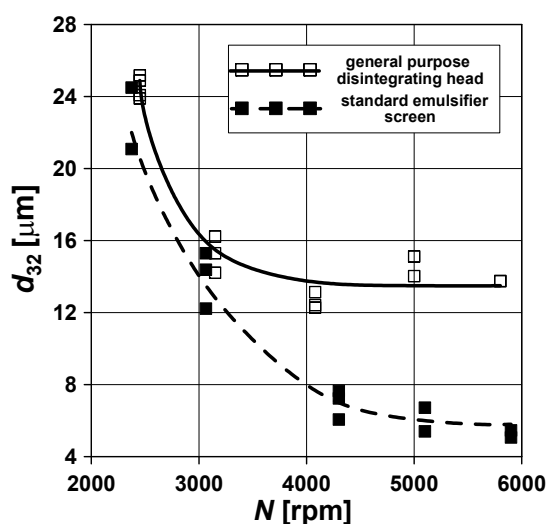


Fig. 5. Effect of rotor speed on the drop size. Silverson batch system. Vessel equipped with rotor-stator homogenizer. Comparison of results obtained with GPDH and SES screens

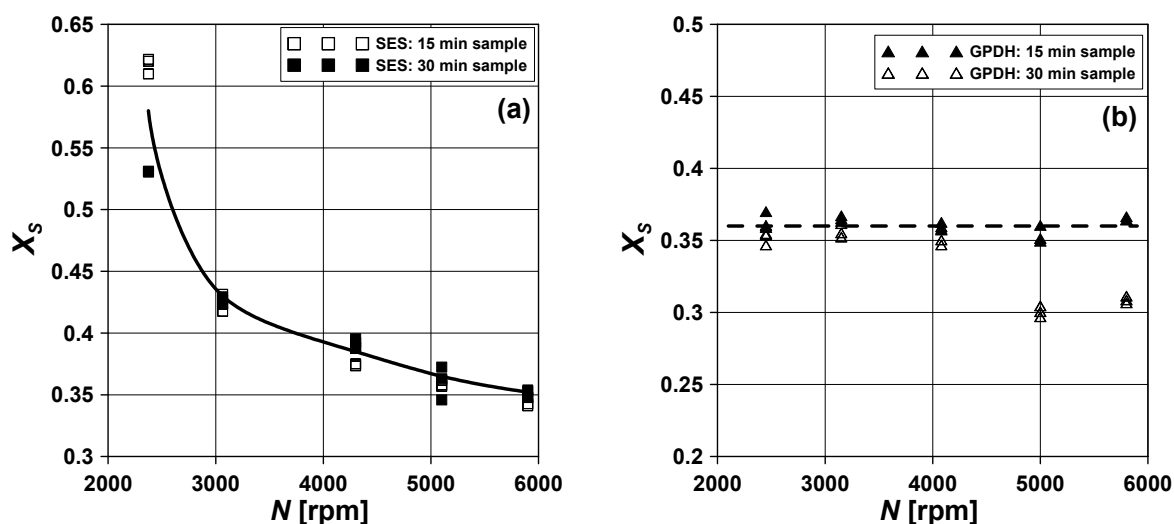


Fig. 6. Effect of rotor speed on variation of product distribution, X_S : Silverson batch system. (a) standard emulsor screen (SES), (b) general purpose disintegrating head (GPDH)

Examples of experimental data are presented in Figs. 5 and 6. The range of drop size variation observed in Fig. 5 is similar to that observed by Rueger and Calabrese (2013) for drop breakup in the Silverson L4R Batch rotor–stator mixer.

3. ENERGETIC EFFICIENCY OF DROP BREAKUP AND MASS TRANSFER IN LIQUID-LIQUID SYSTEMS

Energetic efficiency of the drop breakage process can be defined as a ratio of the rate of energy dissipation, ε_{min} , necessary to break droplets down to the maximum stable drop size assuming that the maximum stable drop size d_d is equal to experimentally measured one d_{32} , and the real power input per unit mass calculated from Eqs.(1) to (3). ε_{min} was calculated from Eq.(4) by substituting the measured d_{32} for d_d .

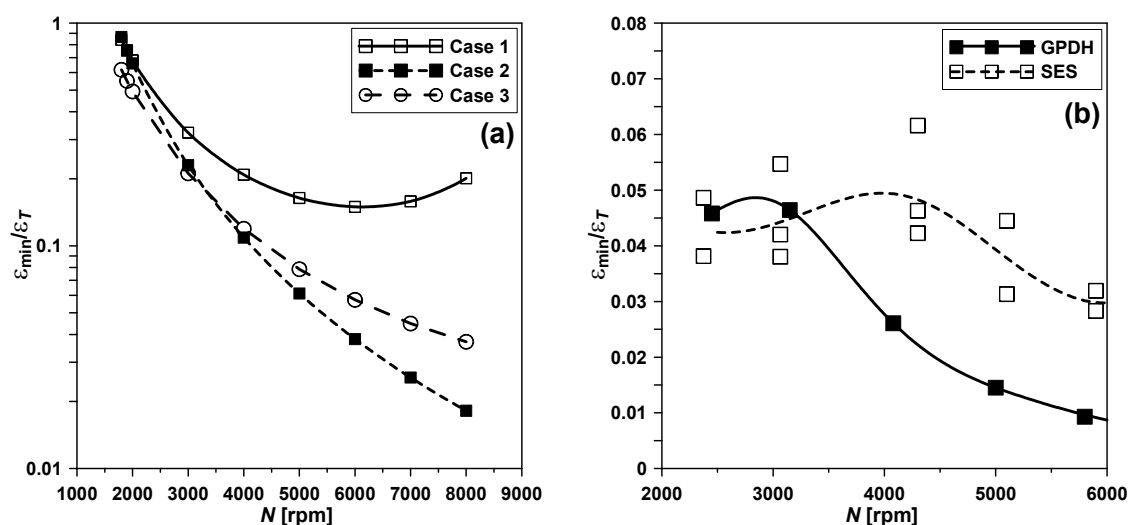


Fig. 7. Effects of rotor speed on asymptotic energetic efficiency of drop breakage (a) in-line rotor-stator mixer; (b) batch rotor-stator mixer

Figure 7 shows that the energetic efficiency is higher in the continuous flow system and decreases with increasing rotor speed and flow rate. In the case of a batch reactor efficiency is smaller and decrease of breakage efficiency with increased rotor speed is observed as well. In this case the standard emulsor screen (SES) is more efficient than the general purpose disintegrating head (GPDH).

Efficiency of mixing and mass transfer can be interpreted as a ratio of time constants for an ideal and real process (Jasińska et al., 2013b). Ideal process or reference process is one based on a reliable reference model and carried out for a constant rate of energy dissipation.

$$\text{eff} = \frac{\tau_{D,min}}{\tau_D} \quad (9)$$

Similarly to E-model having been chosen to be a reference model for mixing in homogeneous systems (Malecha et al., 2009; Jasińska et al., 2013b), one can choose a reliable reference model for mass transfer. In this paper the value of k_{LA} will be calculated using a modified model of Favelukis and Levrenteva (2013), Eq. (7).

Efficiency of drop breakage can be expressed by an effect of drop size on the time constants for mass transfer, τ_D . The time constant $\tau_{D,min}$ in Eq. (9) can be interpreted as the shortest mass transfer time calculated from the model of Favelukis and Levrenteva (2003) using the maximum stable drop size d_d ,

$R_{eq} = d_d/2$. The maximum stable drop size d_d will be estimated including intermittency effects using Eq. (4) as given by Bałdyga and Podgórska (1998).

This results in

$$\tau_{D,min} = \frac{\pi d_d^3}{6\varphi(k_{FL} a_{drop})_{R_{eq}=d_d/2}} \quad (10)$$

where φ represents the mean value of the volume fraction of the organic, dispersed phase. Similar calculations but performed for $R_{eq} = d_{32}/2$ yield the time constant τ_D

$$\tau_D = \frac{\pi d_{32}^3}{6\varphi(k_{FL} a_{drop})_{R_{eq}=d_{32}/2}} \quad (11)$$

Efficiency of development of the interfacial area is presented in Fig. 8 for both mixers: in-line and batch. Analysis of Fig. 8 leads to the same conclusions as in case of Fig. 7.

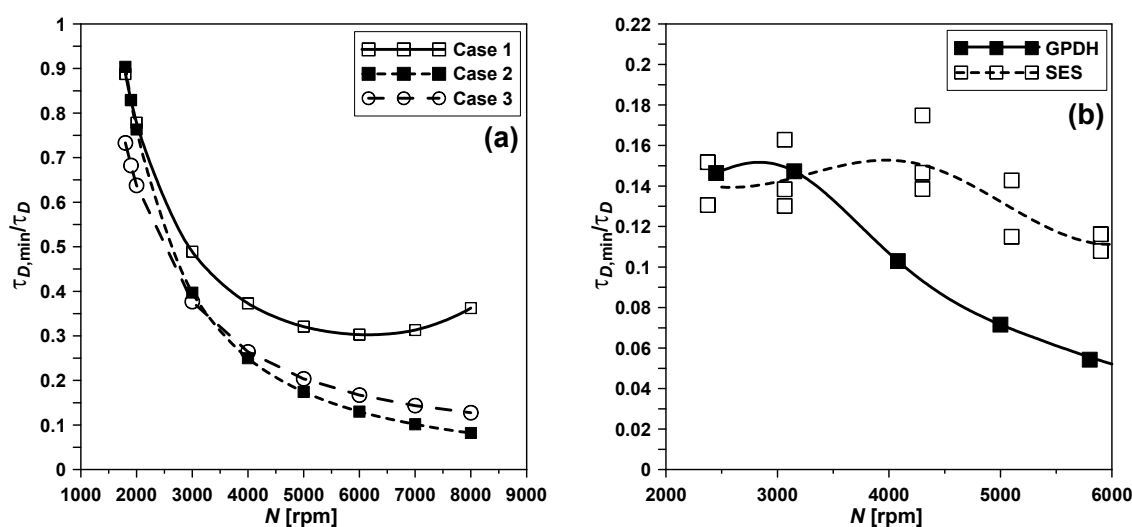


Fig. 8. Effects of rotor speed on asymptotic energetic efficiency of drop breakage based on time constant analysis: (a) in-line rotor-stator mixer; (b) batch rotor-stator mixer

Figures 3 and 6 reveal that the product distribution decreases with increasing rotor speed; in the case of the in-line mixer it increases with increasing flow rate as well, especially at a low rotor speed. Of course, increasing rotor speed gives rise to the mass transfer rate due to decreasing drop size (and so enlarging interfacial area) and increasing mass transfer coefficients. The effect of flow rate on X_S in the case of the in-line mixer results from the fact that increased flow rate decreases the residence time, which is more important at a low rotor speed, as one needs then more time for drop breakage and mass transfer. At higher values of the rotor speed N some increase of X_S with increasing N is observed in this case (Fig. 3b). The reason for this effect is most probably backmixing to the toluene feeding pipe. Faster feeding of organic phase means better protection against backmixing and observed increase of X_S is the smallest for the fastest feeding (Jasińska et al., 2016).

To interpret the observed effects the model of mass transfer with accompanying chemical reaction was applied using film theory as described by Doraiswamy and Sharma (1984). Following Jasińska et al. (2013) it was assumed that the neutralization reaction between benzoic acid (B) and NaOH (A) is instantaneous, and thus the enhancement factor can be expressed by $E = 1 + \frac{D_{CA}C_{A0}}{D_{CB}C_B^*}$, where D_{CA} and

D_{CB} represent diffusion coefficients for sodium hydroxide and benzoic acid respectively, C_{A0} is the bulk concentration of sodium hydroxide, and C_B^* is equilibrium concentration of benzoic acid at the drop surface.

At 20 °C $D_{CA} = 1.47 \times 10^{-9}$ m²/s and $D_{CB} = 0.91 \times 10^{-9}$ m²/s. The rate constant for alkaline ethyl chloroacetate hydrolysis is equal to $k_2 = 23$ dm³/(mol s), so the Hatta number, $Ha = \sqrt{k_2 C_{A0} D_{CB}} / k_L$ takes values between 10^{-6} and 0.1, which means that the regime of the second reaction is between slow and very slow, and there is no reaction in the diffusion film. Other details and properties one can find elsewhere (Jasińska et al., 2013).

The film model was applied to simulate the reaction progress for a constant volume fraction of organic phase and $k_L a$ values calculated from Eq.(8) by Favelukis and Levrenteva (2013) with introducing in the present work a correction of the exponent on Pe. This correction is in fact negligible for the properties of fluids considered in this paper.

Typical results of simulations are presented in Fig. 9 for both $k_L a$ and ε , which shows how the mass transfer coefficient and the rate of energy dissipation affect the formation rate of the secondary product, S, X_S .

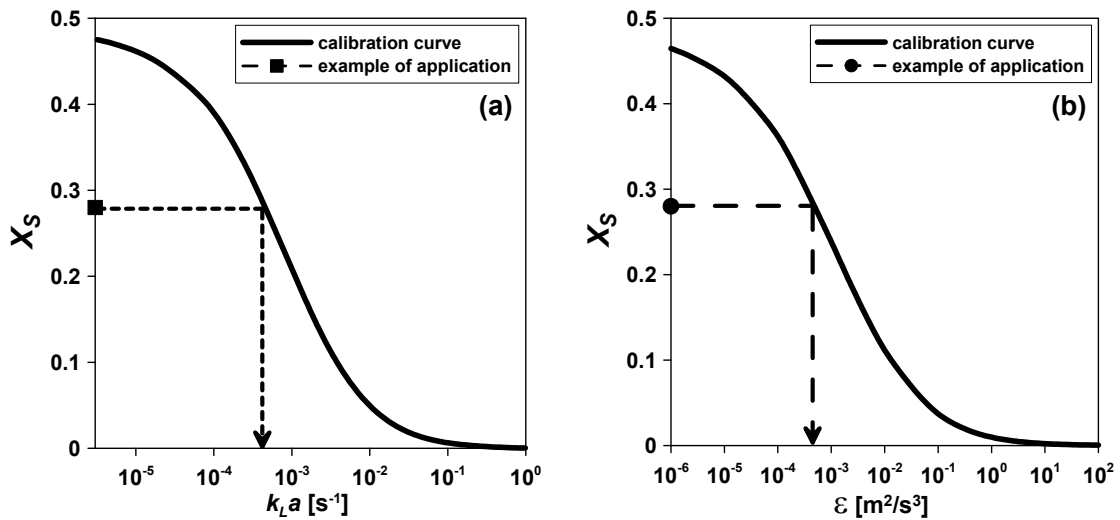


Fig. 9. Predicted effect of the mass transfer coefficient $k_L a$ the energy dissipation rate, ε , on the product distribution X_S for the batch rotor-stator experiment

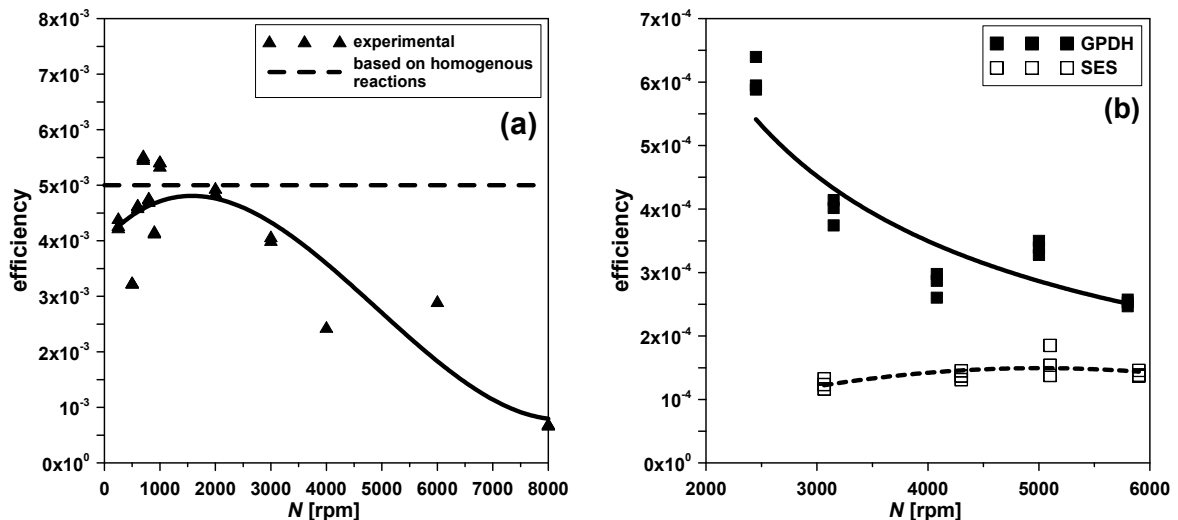


Fig. 10. Efficiency of drop brakeage and mass transfer for (a) in-line mixer system (b) batch mixer system

Figure 9 can be used in what follows as a calibration curve, which based on experimentally determined X_S values provides the smallest, “theoretical” values of the mass transfer coefficient and the rate of energy dissipation necessary to obtain experimental X_S in the batch mixer, which can be compared with the energy ε_T really used in experiment. Because both the mass transfer coefficient $k_L a$ and the energy dissipation rate, ε , depend on the rotor speed N , one can present the energetic efficiency as a function of the rotor speed as shown in Fig. 10.

For the in-line mixer experimental conditions, the calibration curve has a similar shape so it is not presented here.

Resulting efficiency is a combination of efficiencies of both, efficiency of drop breakage and mass transfer, as both of them affect the course of chemical reactions in a liquid-liquid system. A comparison of Figs. 10a and 10b leads to the following conclusions:

- The overall efficiency of drop breakage and mass transfer in the in-line mixer is one order of magnitude higher than that in the batch system. Interestingly, for the range of rotor frequency between 3000 rpm and 6000 rpm the drop size is in the range between 4 μm and 15 μm , and the efficiency of drop breakage is only slightly smaller in the batch experiment. This means that the difference is in the efficiency of mass transfer, and thus it is much smaller in the case of the batch system.
- A rotor-stator mixer equipped with a standard emulsor screen (SES) is more efficient for drop breakage than that equipped with a general purpose disintegrating head (GPDH), which is shown in Figs. 7 and 8. However, as shown in Fig. 10 the overall efficiency of the general purpose disintegrating head (GPDH) mixer is higher than that of the standard emulsor screen (SES) mixer. This means that the efficiency of mass transfer in the SES mixer is very low; the SES mixer can be used for drop breakup but should not be used to carry out mass transfer processes in liquid-liquid systems.

4. CONCLUSIONS

A method based on using complex test reactions to investigate mixing efficiency in a two-phase liquid-liquid system has been applied to compare energetic efficiency of drop breakage and mass transfer processes carried out in in-line and batch rotor-stator mixers. In this method a model of mass transfer rate based on the modified model by Favelukis and Levrenteva (2013) which includes effects of drop deformation, fluid deformation, drop surface mobility and effect of viscosity ratio has been applied to construct calibration curves for identification of mixing efficiency.

It has been shown that the energetic efficiency of the in-line rotor-stator mixer is higher than that of the batch mixer. It has been also shown that a standard emulsor screen (SES) is more efficient for drop breakage than a general purpose disintegrating head (GPDH), whereas the GDPH is more efficient for mass transfer processes. The method presented above enables one a comparison of apparatus and processes based on their energetic efficiency.

The authors acknowledge the financial support from Polish National Science Centre (Grant agreement number: DEC-2013/11/B/ST8/00258).

SYMBOLS

A^*	surface area ratio
A_{out}	outer stator open area, m^2

A_P	fraction of outer stator open area, %
a	interfacial area per unit volume of emulsion, m^{-1}
a_{drop}	drop area, m^2
C	concentration, mol m^{-3}
C_{A0}	bulk concentration for sodium hydroxide, mol m^{-3}
C_B^*	equilibrium concentration for benzoic acid, mol m^{-3}
C_i	concentration of component "i", mol m^{-3}
D_i	molecular diffusivity of component "i", $\text{m}^2 \text{s}^{-1}$
D_{CA}	diffusion coefficient for sodium hydroxide, $\text{m}^2 \text{s}^{-1}$
D_{CB}	diffusion coefficient for benzoic acid, $\text{m}^2 \text{s}^{-1}$
D_{in}	inner rotor diameter, m
D_{out}	outer rotor diameter, m
d	drop diameter, m
d_d	maximum stable drop size, m
d_{32}	Sauter diameter, m
E	enhancement factor
eff	efficiency
Ha	Hatta number, $Ha = \sqrt{k_2 C_{A0} D_{CB}} / k_L$
$H_{r,in}$	number of holes in inner stator
$H_{r,out}$	number of holes in outer stator
K	viscosity ratio, $K = \eta_d / \eta_c$
k_2	rate constant of the 2 nd order chemical reaction, $\text{m}^3 \text{mol}^{-1} \text{s}^{-1}$
k_L	mass transfer coefficient, m s^{-1}
L	integral scale of turbulence, m
N	rotor speed, rpm
N_{Ca}	capillary number, $\mu_c \dot{\gamma} R_{eq} / \sigma$
N_P	power number, $P / (\rho N^3 D_{out}^5)$
$N_{r,in}$	number of inner rotor blades
$N_{r,out}$	number of outer rotor blades
N_Q	dimensionless pumping capacity, $Q / (N D_{out}^3)$
P	power, W
Pe	Péclet number, $Pe = \dot{\gamma} R_{eq}^2 / D_i$
Q	volumetric flow rate, $\text{m}^3 \text{s}^{-1}$
R_{eq}	equivalent radius, m
Sh	Sherwood number, $k_L R_{eq} / D_i$
V_H	rotor swept volume, m^3
X_S	product distributions of complex reactions
Y	deformation parameter in Eqs. (7) and (8)

Greek symbols

ε	rate of energy dissipation, $\text{m}^2 \text{s}^{-3}$
$\dot{\gamma}$	rate of shear, s^{-1}
ν	kinematic viscosity, $\text{m}^2 \text{s}^{-1}$
η_i	viscosity of "i" phase, Pa s
ρ_i	density of "i" phase, kg m^{-3}
σ	interfacial tension, N m^{-1}
τ_D	time constant for mass transfer, s

REFERENCES

- Bałdyga J. and Podgórska W., 1988. Drop break-up in intermittent turbulence. Maximum stable and transient sizes of drops. *Can. J. Chem. Eng.*, 76, 456-470. DOI: 10.1002/cjce.5450760316.
- Bałdyga J., Jasińska M., 2011. Effect of model structure on complex liquid-liquid heterogeneous reactions. *Proceedings of the third European Process Intensification Conference, EPIC2011*, 20-23 June 2011, Manchester, UK, 175-181.
- Bałdyga J., Kowalski A., Cooke M., Jasińska M., 2007. Investigations of micromixing in a rotor-stator mixer. *Chem. Process Eng.*, 28 (4), 867-877.
- Batchelor G.K., 1980. Mass transfer from a particle suspended in turbulent fluid. *J. Fluid Mech.*, 98, 609-623. DOI: 10.1017/S0022112080000304.
- Doraiswamy L.K., Sharma M.M., 1984. *Heterogeneous reactions: Analysis, examples, and reactor design. Vol. 2: Fluid-fluid-solid reactions*. Wiley, New York.
- Favelukis M., Lavrenteva O.M., 2013. Mass transfer around prolate spheroidal drops in an extensional flow. *Can. J. Chem. Eng.*, 91, 1190-1199. DOI: 10.1002/cjce.21727.
- Hall S., Pacek A., Kowalski A.J., Cooke M., Rothman D., 2013. The effect of scale and interfacial tension on liquid-liquid dispersion in in-line Silverson rotor-stator mixers. *Chem. Eng. Res. Des.*, 91, 2156-2168. DOI: 10.1016/j.cherd.2013.04.021.
- Jasińska M., Bałdyga J., Cooke M., Kowalski A., 2016. Mass transfer and chemical test reactions in the continuous-flow rotor-stator mixer. *Theor. Found. Chem. Eng.*, 50, 901-906. DOI: 10.1134/S0040579516060075.
- Jasińska M., Bałdyga J., Cooke M., Kowalski A.J., 2013a. Investigations of mass transfer with chemical reactions in two-phase liquid-liquid systems. *Chem. Eng. Res. Des.*, 91, 2169-2178. DOI: 10.1016/j.cherd.2013.05.010.
- Jasińska M., Bałdyga J., Cooke M., Kowalski A.J., 2013b. Application of test reactions to study micromixing in the rotor-stator mixer (test reactions for rotor-stator mixer). *Appl. Therm. Eng.*, 57, 172-179. DOI: 10.1016/j.applthermaleng.2012.06.036.
- Jasińska M., Lewandowski P., Bałdyga J., 2013. Nowy model wnikania masy z reakcją chemiczną w układach heterofazowych ciecz-ciecz. *Inżynieria i Aparatura Chemiczna*, 52 (4), 325-327.
- Levich V.G., 1962. *Physical hydrodynamics*. Prentice-Hall, Englewood Cliffs, N.J.
- Malecha K., Golonka L.J., Bałdyga J., Jasińska M., Sobieszuk P., 2009. Serpentine microfluidic mixer made in LTCC. *Sens. Actuators B: Chem.*, 143, 400-413. DOI: 10.1016/j.snb.2009.08.010.
- Padron G.A., 2001. *Measurement and comparison of power draw in batch rotor-stator mixers*. M.Sc. Thesis, University of Maryland, College Park, MD, USA.
- Reuger P., Calabrese R.V., 2013. Dispersion of water into oil in a rotor-stator mixer. Part 1: Drop breakup in dilute systems. *Chem. Eng. Res. Des.*, 91, 2122-2133. DOI: 10.1016/j.cherd.2013.05.018
- Utomo A.T., 2009. *Flow patterns and energy dissipation rates in batch rotor-stator mixers*. PhD Thesis, School of Engineering, The University of Birmingham, Edgbaston, UK.

Received 26 November 2016

Received in revised form 12 July 2017

Accepted 15 July 2017

MODELLING AND EXPERIMENTAL INVESTIGATION OF WASTE TYRE PYROLYSIS PROCESS IN A LABORATORY REACTOR

Leszek Rudniak, Piotr M. Machniewski*

Warsaw University of Technology, Faculty of Chemical and Process Engineering, ul. Waryńskiego 1, Warsaw, Poland

A mathematical model of waste tyre pyrolysis process is developed in this work. Tyre material decomposition based on a simplified reaction mechanism leads to main product lumps: non-condensable (gas), condensable (pyrolytic oil) and solid (char). The model takes into account kinetics of heat and mass transfer in the grain of the shredded rubber material as well as surrounding gas phase. The main reaction routes were modelled as the pseudo-first order reactions with a rate constant calculated from the Arrhenius type equation using literature values of activation energy determined for main tyre constituents based on TG/DTG measurements and tuned pre-exponential parameter values obtained by fitting theoretical predictions to the experimental results obtained in our laboratory reactor. The model was implemented within the CFD software (ANSYS Fluent). The results of numerical simulation of the pyrolysis process revealed non-uniformity of sample's porosity and temperature. The simulation predictions were in satisfactory agreement with the experimentally measured mass loss of the tyre sample during pyrolysis process investigated in a laboratory reactor.

Keywords: waste tyres, pyrolysis, kinetics, CFD

1. INTRODUCTION

Rubber wastes such as used car tyres are refractory to quick self-decomposition and biodegradation. It is necessary to process these wastes in order to prevent their accumulation in landfill sites. The common approach is co-incineration of tyre wastes as an alternative fuel in cement or lime kilns, blast furnaces, steam boilers etc. Another possible processing route is pyrolysis, which not only allows for partial recovery of energy but also for utilisation of the by-products (material recycling) and can be carried out in the environment-friendly way. The pyrolysis products include volatile compounds, which can be partly condensed resulting in liquid (oil) and gaseous fractions. The solid remainder (approx. 30 - 40% of tyre mass), mostly composed of char, can be recycled and utilised after purification for manufacture of new tyres. These potential advantages of the pyrolysis process attracted many researchers and their efforts to investigate this process in laboratory, pilot plant and industrial scales. The studies of tyre pyrolysis covered processes carried out in fixed and fluidised bed reactors (Kaminsky et al. 2009), spouted bed (Olazar et al. 2008), moving screw bed (Aylón et al. 2010a; 2010b), and rotary kiln reactors. The process is carried out in the atmosphere of inert gases under normal pressure and in vacuum conditions (Lopez et al. 2010) and temperatures typically between 300 °C and 900 °C. Characteristics and comparison of different reactor types and conditions for the tyre pyrolysis process were broadly and synthetically presented in many review papers (e.g. Wilson, 2013; Antoniou and Zabaniotou, 2013). The published results indicate increase of non-condensable gaseous products typically from 4 - 5% to 25 - 30% if the final temperature in the reactor is increased from 350 - 400 °C to 700 - 900 °C. This is most probably caused by cracking of heavy pyrolysis products

*Corresponding authors, e-mail: p.machniewski@ichip.pw.edu.pl

cpe.czasopisma.pan.pl; degruyter.com/view/j/cpe

into lower molecular mass products (at the higher temperatures). Kinetics of the pyrolysis reaction is in most cases determined based on derivative thermogravimetric (TG/DTG) analysis. The resulting curves of sample mass weight loss rate exhibit usually 2 or 3 peaks, which are said to correspond to main constituents of tyre (elastomers and plasticizers) decomposing at different temperatures. The kinetics of mass loss during TG measurements is usually described by Arrhenius type equation. The paper by Queck and Balasubramanian (2012) extensively reviews many research efforts connected with modelling of tyre pyrolysis and interpretation of DTG measurements. When the size of a tyre sample is above few millimetres additional complications may arise due to possible mass and heat transfer resistances and inhomogeneity of the tyre chip during pyrolysis.

Most publications reporting CFD approach to simulate pyrolysis of solids (mostly biomass) focus on fluidised bed reactors (see e.g. Lam et al., 2012) or conical spouted beds (Niksiar and Sohrabi, 2014) using models where particulate (solid) and gas phases are treated as pseudo-homogeneous continua coupled with interfacial exchange terms in the balance equations for momentum, mass and energy. However, the number of publications dealing with tyre pyrolysis is very low. An example might be the work of Mtui (2013) on CFD modelling of devolatilization and combustion of shredded tires and pine wood in rotary cement kilns, or the work of Bianchi et al. (2014) on CFD modelling of pyrolysis of the whole tyre focused on optimal design of the furnace and gas collector geometry.

This work is focused on applying CFD tools for modelling of pyrolysis process of inhomogeneous tyre chips of 1 cm in size (typical for industrial tyre cutters) with potential application of this methodology to fixed or moving bed pyrolysis reactors.

2. KINETIC MODEL OF TYRE PYROLYSIS

The mechanism of reactions occurring during pyrolysis is very complex. Therefore a simplified approach based on lumped kinetic parameters is proposed by many researchers (cf. e.g. Aylón et al. 2005; Olazar et al. 2008; Miranda et al. 2013). The model used in our previous work (Machniewski et al., 2016) is based on simplified pyrolysis reaction (Eq. 1) where f denotes mass yield of a given product.



The products were segregated into three different lumps depending on their state after cooling: non-condensing gases (G), condensing vapours (L) and solid reminder (S).

The yields of gaseous products (f_G) and liquid (pyrolytic oil) products (f_L) depend on pyrolysis process parameters (temperature, heating rate, pressure etc.) and the composition of the raw material (tyre). The published experimental results of tyre pyrolysis indicate 60%-70% mass loss attributed to volatile products, including 5 - 20% of mass loss due to noncondensable gaseous products (Wilson, 2013; Antoniou and Zabaniotou, 2013). According to the results of Miranda et al. (2013) obtained during experiments carried out in an autoclave heated to 350 °C – 450 °C, the fraction of gaseous (non-condensable) products was 5%. The amount of gaseous products usually increases with the temperature rise. Olazar et al. (2008) investigated pyrolysis of 1 - 2 mm tyre particles in a fluidised bed and observed a drop of liquid (condensable vapours) products fraction from 65% to 63% and a growth of gaseous fraction from 1.5% to 2.7% in the temperature range of 425 °C – 610 °C.

A higher growth of gaseous fraction, from 5% to 12% in the temperature range of 400 °C – 600 °C, was observed by Cherbański et al. (2016). The authors also found that the total mass loss increased from 53% to 63% within this temperature range.

As tyres are usually composed of different kinds of elastomers, plasticizers and fillers (carbon black, silica etc.), the kinetics of pyrolysis can be assumed as a sum of thermal decomposition reaction rates (r_i) for each component according to Arrhenius type equation and the first order kinetics (Eq. 2):

$$r_p = \sum_i r_i = \sum_i A_i \exp\left(-\frac{E_i}{RT}\right) X_i \quad (2)$$

Then the total rate of volatile production can be expressed as:

$$r_V = \sum_i (f_{L,i} + f_{G,i}) r_i = \sum_i f_{G+L,i} r_i \quad (3)$$

It is assumed here that samples of the tyre, used in the experimental part of this work, are composed of one elastomer type (styrene-butadiene rubber) and a plasticizer oil. The initial content of the plasticiser (oils) in the tyre is typically 10% - 20%.

Kinetic parameters in Eq. 2 for these components used in subsequent calculations are shown in Table 1. The parameters based on the TG/DTG measurements by Yang et al. (1995), which are also shown in Table 1, were tuned for the purpose of this work by adjusting the values of A used for calculation of relative mass loss of the sample based on a simplified model fitted to the mass loss measured in the laboratory reactor used in this work. The values of activation energies E were assumed after Yang et al. (1995). The simplified model (cf. Machniewski et al., 2016) was based on an assumption of conductive heat transfer in a spherical particle of variable porosity, being heated in a flow reactor similar to that used in this work and described in the experimental part.

Table 1. Kinetic parameters in Eq. (2) used in this work

Component of tyre	A [1/min] (this work)	A [1/min] (Yang et al. 1995)	E [kJ/mol] (Yang et al. 1995)
plasticiser, oils (A)	2.01×10^3	4.01×10^4	49.1
styrene-butadiene rubber (SBR)	1.08×10^{10}	1.78×10^{10}	152.0

3. CFD MODELLING OF TYRE PYROLYSIS PROCESS

The inert gas (nitrogen) and volatile products of tyre pyrolysis can be modelled as a laminar flow fluid zone. Continuity, momentum and energy balance equations for laminar flow are in the following form in the gas phase:

$$\frac{\partial \rho}{\partial t} + \nabla \cdot (\rho \vec{V}) = S_m \quad (4)$$

$$\frac{\partial (\rho \vec{V})}{\partial t} + \nabla \cdot (\rho \vec{V} \vec{V}) = \mu \nabla^2 \vec{V} - \nabla P + \rho \vec{g} + S_p \quad (5)$$

$$\frac{\partial (\rho C_p T)}{\partial t} + \nabla \cdot [\vec{V} (\rho C_p T)] = \nabla \cdot [k \nabla T] + S_h \quad (6)$$

Additionally species equations for gas species take a form:

$$\frac{\partial (\rho Y_i)}{\partial t} + \nabla \cdot [\vec{V} (\rho Y_i)] = \nabla \cdot [\rho D_i \nabla Y_i] + S_i \quad (7)$$

The above set of equations was solved using the finite volume method (ANSYS ver. 18.0 documentation). In the above equations source terms S_i are due to the pyrolysis reaction. Diffusivity of

the volatile species (treated as a surrogate component) in the gas phase was set as $D = 10^{-5} \text{ m}^2/\text{s}$. The tire can be modelled as porous media, in which the solid phase is in thermal equilibrium with the gas phase during pyrolysis. ANSYS Fluent solver uses the following equation in order to solve heat transfer in the porous zone:

$$(\rho C_p)_{\text{pm}} \left(\frac{\partial T_{\text{pm}}}{\partial t} + \vec{V} \cdot \nabla T_{\text{pm}} \right) = \nabla \cdot (k_{\text{eff}} \nabla T_{\text{pm}}) + S_h \quad (8)$$

$$(\rho C_p)_{\text{pm}} = (\rho C_p)_s (1 - \gamma) + (\rho C_p)_v \gamma \quad (9)$$

$$k_{\text{eff}} = k_v \gamma + k_s (1 - \gamma) \quad (10)$$

The momentum balance (Equation 5) with the appropriate source term S_p based on Ergun model was used within the porous zone (see ANSYS ver. 18.0 Documentation).

Specific heat and heat conductivity used in the calculations are given in Table 2. The values were assumed according to Yang et al. (1995). The porosity of the rubber sample during pyrolysis was adapted by means of user defined functions (UDF) in Fluent solver according to the mass of solid components in the rubber and overall mass balance in the control volume.

Table 2. Thermal properties used in the calculations after Yang et al. (1995)

Parameter	Value
Specific heat of rubber [kJ/(kg·K)]	$1.9 + 3 \times (T - 298)$ for $T > 298\text{K}$
Specific heat of carbon black [kJ/(kg·K)]	1.8
Specific heat of gaseous components [kJ/(kg·K)]	2.4
Heat conductivity of rubber [W/(m·K)]	0.38
Heat conductivity of carbon black [W/(m·K)]	0.2

The density of the gas phase was calculated assuming the ideal gas model. The density of the solid phase (solids, rubber, carbon black) was set as 1100 kg/m^3 . Initial porosity of tyre material was assumed as 5%.

4. EXPERIMENTAL

In order to validate the presented modelling approach a small series of experiments were performed. A schematic of the experimental setup is shown in Fig 1. Samples of car tyre of an approximately cylindrical shape (diameter 8 mm, height 10 mm) were electrically heated in a cylindrical reactor of 20 mm internal diameter and 100 mm in length. The reactor was supplied with nitrogen flow of 100 mL/min (STP). This flow corresponds to inert gas superficial velocity applicable for a moving screw bed reactor. Also the applied temperature program was aimed to mimic conditions in the entrance section of the reactor. Temperature of the gas phase in the vicinity of the sample was measured during each experiment. The mass of the sample was also measured during the experiments with the aid of a laboratory analytical balance (resolution of 0.1 mg). The mass of used tyre samples (taken from the sidewall of a passenger car tyre) was approx. 0.4 - 0.5 g and average moisture of 0.49%. Their average heat of combustion (measured in a calorimetric bomb) was 37871 J/g and average ash remainder was 3%.

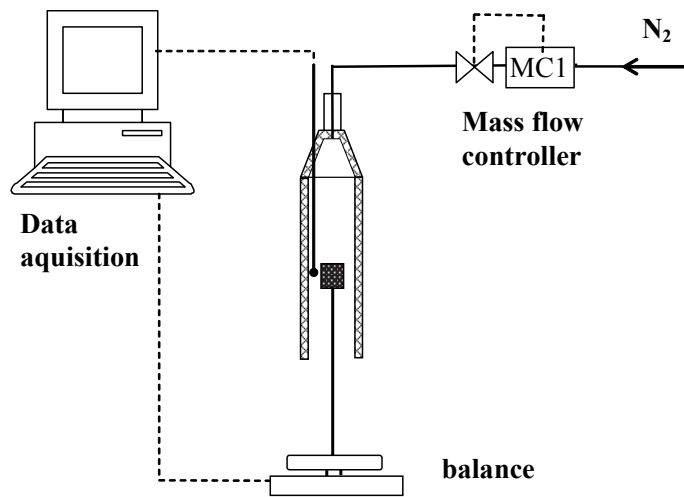


Fig. 1. Scheme of the experimental setup

The following heating programs were performed during experimental runs:

- Heating rate: 13 °C /min, initial temperature 28 °C , final temperature: 360°C,
- Heating rate: 26 °C /min, initial temperature 28 °C , final temperature: 391°C,
- Heating rate: 22 °C /min, initial temperature 21 °C , final temperature: 455°C.

After reaching the final temperature, it was kept at an approximately constant level for approximately 30 minutes.

5. RESULTS

The recorded variation of sample's mass for each of the performed experiments is shown in Fig. 2. It was observed that pyrolysis and the volatilisation of tyre starts at the temperature of approximately 250 °C – 300 °C when the mass loss is mainly connected with vaporisation of plasticisers and oils. Depending on final temperature the relative total mass loss in the experiments varied between 25 and 65% (approximately linearly within the investigated final temperature range of 360 °C – 470 °C).

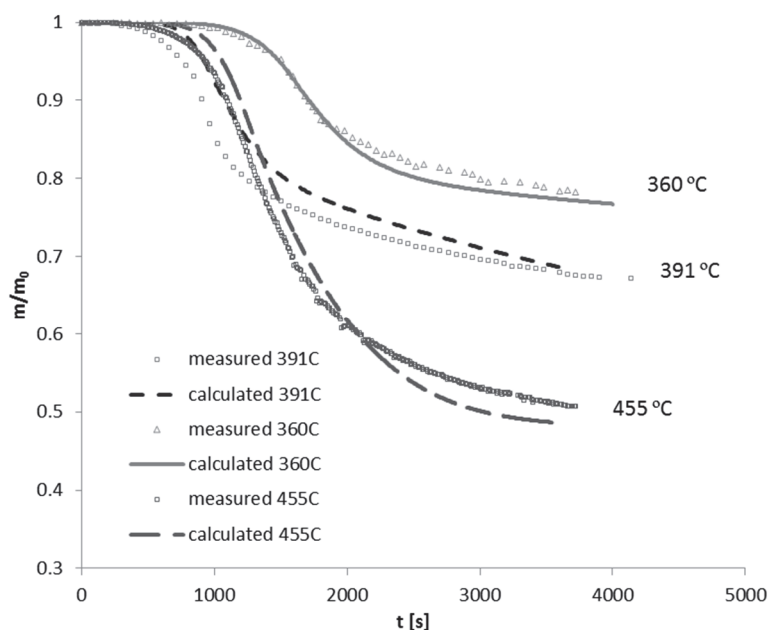


Fig. 2. Variation of relative mass of tyre samples during the pyrolysis experiments (run #1, #2, #3). Comparison of the CFD simulation results with the measurements

The measured variation of relative mass of tyre samples during the pyrolysis process can be compared with the calculated one in the course of CFD simulation also shown in Fig. 2. It can be observed that the results of simulation are in fair agreement with the measured mass loss of tyre sample for all the test runs. Nevertheless the best agreement of calculated and measured sample mass variation can be observed in the run with the slowest heating rate (run #1, 360 °C) when the sample (i.e. temperature and porosity profiles) was more homogeneous during pyrolysis. CFD predictions for the runs corresponding to higher heating rates (run #2 and run#3) are somehow delayed compared to the measurements. The run with the highest heating rate (run #2, 391 °C) exhibits the worst agreement. This is most probably connected with more pronounced non-uniformity (inhomogeneity) of temperature and porosity fields in this case.

CFD calculations which were performed for conditions reflecting the pyrolysis process investigated in the experiments were based on the assumption that the size of the sample remains constant during pyrolysis process simulation. Thus porosity of the tyre sample varied as a result of local volatilisation reaction. Also, it was assumed that non-volatile mineral fillers and carbon black used during tyre manufacture process are treated as part of non-volatile products (solids) produced during pyrolysis. The simulation was performed for tyre samples containing initially 20% of volatile additives (oil, plasticisers), which was responsible for initial mass loss of the sample. It was assumed that a fraction of the volatile products of the plasticiser (oils) volatilisation/decomposition in the course of pyrolysis is approximately equal to $f_{G+L,A} = 1$, and a fraction of volatile pyrolysis products originating from the of styrene-butadiene rubber decomposition as $f_{G+L,SBR} = 0.4$.

The calculated temperature contours in the reactor and tyre sample for run #3 (final temperature = 445 °C) at the time instants $t = 800$ s and $t = 1500$ s are shown in Fig. 3. The chosen times correspond to the initial stage of the pyrolysis process ($t = 800$ s) and the stage when its rate is approximately at its maximum ($t = 1500$ s) when half of the sample's mass was volatilised. At the applied heating rate (22 °C/min) a significant temperature difference can be observed, reaching approx. 40 °C between the gas phase in the vicinity of the sample's surface and the core of the sample.

The calculated porosity contours in the tyre sample and the streamlines in the reactor at the same time instants are shown in Figs. 4 and 5, respectively.

Simulation results indicate that spatial variation of porosity in the sample is not very significant (up to 10 %) during the whole process. Pyrolysis starts at the edges of the sample where the temperature is higher and the front of reaction forms, which is more or less smeared depending on the heating rate and stage of the process. The conversion front corresponds to porosity profile contours (isolines) moving towards the centre of the sample in the course of the pyrolysis process. The reaction zone extends throughout the whole sample and its porosity grows, while maintaining mild variation of the spatial profile.

Comparison of the gas phase stream lines shown in Fig. 5 for the two chosen times may illustrate increase of gas flow rate due to the production of volatiles, which is clearly visible in Fig. 5b ($t=1500$ s) for fully developed pyrolysis process, where some of the streamlines originate from the sample's region.

The calculated contours of mass fraction of the volatile products of tyre pyrolysis in the gas phase for the same run #3, at the same time instants ($t = 800$ s) and ($t = 1500$ s) are shown in Figs. 6 a) and b), respectively. As the flow direction of nitrogen is from right (narrow inlet) to left (outlet) in Fig. 6, the mass fraction of volatile products at the outlet reaches approximately 1.5% at the beginning of the pyrolysis process ($t = 800$ s) and 8% at $t = 1500$ s, when the rate of the process is much higher in the considered case of run #3 (see Fig. 2, final temperature = 455 °C). This also involves a proportional increase of the total mass flow rate of the gaseous products through the reactor. The total mass flow rate

at the outlet increased by 6.6% between the two time instants. It can be also observed that some volatile products transported by molecular diffusion are present upstream of the sample.

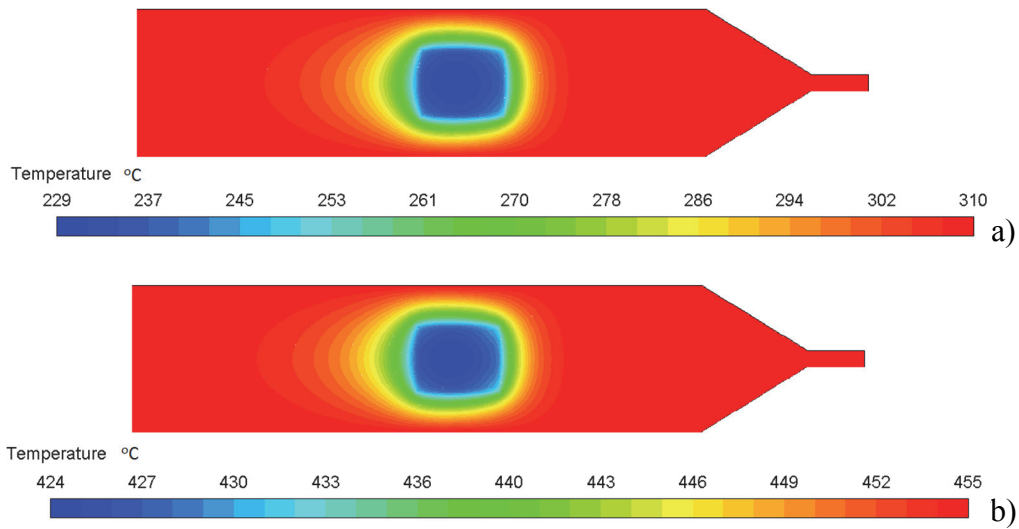


Fig. 3. Calculated contours of temperature ($^{\circ}\text{C}$) at times a) $t = 800$ s and b) $t = 1500$ s after process start-up (run #3)

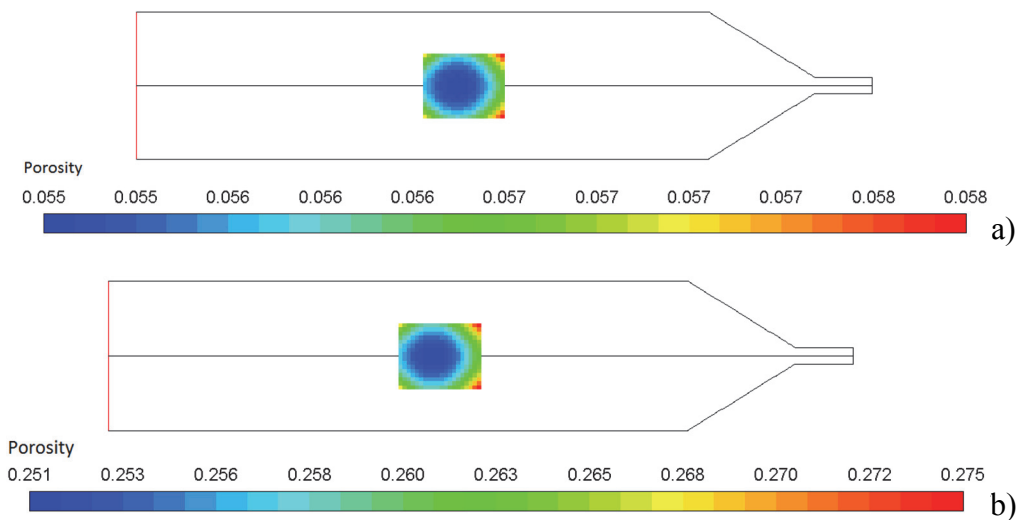


Fig. 4. Calculated contours of porosity (-) at times a) $t = 800$ s and b) $t = 1500$ s after process start-up (run #3)

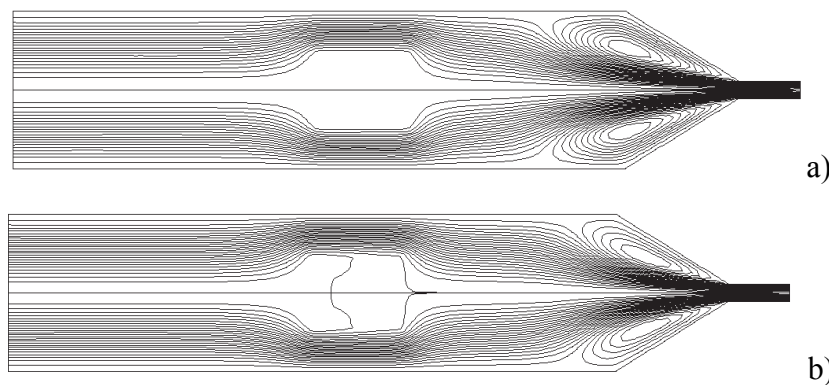


Fig. 5. Calculated gas streamlines at times a) $t = 800$ s and b) $t = 1500$ s after process start-up (run #3)

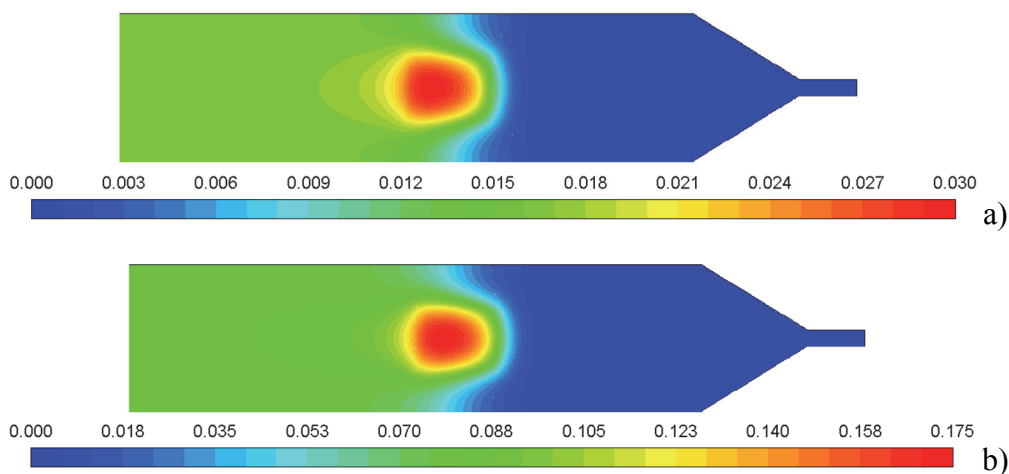


Fig. 6. Calculated contours of mass fraction of volatile pyrolysis products (-) at times a) $t = 800$ s and b) $t = 1500$ s after process start-up (run #3)

6. CONCLUSIONS

The results of numerical simulation of the pyrolysis process based on the simplified kinetic model of car tyre pyrolysis, implemented within CFD software (ANSYS Fluent), are in satisfactory agreement with the experimentally measured relative mass loss of the tyre sample during pyrolysis carried out in a laboratory reactor.

The obtained results indicate the importance of heat and mass transfer phenomena during the pyrolysis of the rubber material. The evident inhomogeneity of porosity, temperature and consequently the decomposition rate developed during the process impose the requirement of using dedicated numerical methods (e.g. CFD tools) for modelling of the pyrolysis process in industrial conditions.

This project is co-financed from the resources of the National Centre for Research and Development and the European Union under European Regional Development Fund in accordance with UOD-DEM-1-217/001.



The author would like to acknowledge one of the reviewers for very helpful comments and enlightening suggestions.

SYMBOLS

A	pre-exponential factor in Arrhenius equation, 1/min
C_p	specific heat, J/(kg·K)
D_i	mass diffusivity of component i , m^2/s
E	activation energy, J/mol
f_i	mass yield of component (product lump) i
g	gravity vector, m/s^2
k	thermal conductivity, W/(m·K)
P	pressure, Pa

R	universal gas constant = 8.314 J/(mol·K)
S_h	heat source, W/m ³
S_i	mass source of component I , kg/(m ³ ·s)
S_m	mass source, kg/(m ³ ·s)
S_p	momentum source, kg/(m ² ·s ²)
T	temperature, K
V	velocity vector, m/s
X_i	mass fraction of component i with respect to initial mass of tyre
Y_i	mass fraction of component I

Greek symbols

γ	porosity
μ	viscosity, Pa·s
ρ	density, kg/m ³

Subscripts

G	noncondensable gaseous products
L	condensable vapour (liquid) products
S	solid remainder
V	volatile products (compounds)
i	component index ($i = A, SBR$)
eff	effective (in porous medium)
pm	porous medium

REFERENCES

- ANSYS Fluent Theory Guide, 2017. Ansys Inc., rel. 18.0., January 2017. Available at: www.ansys.com.
- Antoniou N., Zabaniotou A., 2013. Features of an efficient and environmentally attractive used tyres pyrolysis with energy and material recovery. *Renewable Sustainable Energy Rev.*, 20, 539–558. DOI: 10.1016/j.rser.2012.12.005.
- Aylón E., Callén M. S., López J.M., Mastral A.M., Murillo R., Navarro M.V., Stelmach S., 2005. Assessment of tire devolatilization kinetics. *J. Anal. Appl. Pyrolysis*, 74, 259–264. DOI: 10.1016/j.jaap.2004.09.006.
- Aylón E., Fernández-Colino A., Murillo R., Grasa G., Navarro M.V., García T., Mastral A.M., 2010b. Waste tyre pyrolysis: Modelling of a moving bed reactor. *Waste Manage.*, 30, 2530–2536. DOI: 10.1016/j.wasman.2010.04.018.
- Aylón E., Fernández-Colino A., Murillo R., Navarro M.V., García T., Mastral A.M., 2010a. Valorisation of waste tyre by pyrolysis in a moving bed reactor. *Waste Manage.*, 30, 1220–1224. DOI: 10.1016/j.wasman.2009.10.001.
- Bianchi M., Bortolani G., Cavazzoni M., De Pascale A., Montanari I., Nobili M., Peretto A., Tosi C., Vecchi R., 2014. Preliminary design and numerical analysis of a scrap tires pyrolysis system. *Energy Procedia*, 45, 111–120. DOI: 10.1016/j.egypro.2014.01.013.
- Cherbański R., Wróblewski K., Molga E.J., 2016. Badanie procesu pirolizy zużytych opon samochodowych w reaktorze laboratoryjnym. *Inż. Ap. Chem.*, 55 (1), 16–17.
- Kaminsky W., Mennerich C., Zhang Z., 2009. Feedstock recycling of synthetic and natural rubber by pyrolysis in a fluidized bed. *J. Anal. Appl. Pyrolysis*, 85, 334–337. DOI: 10.1016/j.jaap.2008.11.012.
- Lam K.-L., Gebreegziabher T., Oyedun A. O., Lee H. K. M. Hui C.-W., 2012. CFD study on fluidized bed pyrolyzers. *Chem. Eng. Trans.*, 29, 661–666.
- Lopez G., Olazar M., Aguado R., Elordi G., Amutio M., Artetxe M., Bilbao J., 2010. Vacuum pyrolysis of waste tires by continuously feeding into a conical spouted bed reactor. *Ind. Eng. Chem. Res.*, 49, 8990–8997. DOI: 10.1021/ie1000604.
- Machniewski P., Rudniak L., Molga E., 2016. Modelowanie procesu pirolizy odpadów gumowych. *Inż. Ap. Chem.*, 55 (1), 28–29 (in Polish).

- Miranda M., Pinto F., Gulyurtlu I., Cabrita I., 2013. Pyrolysis of rubber tyre wastes: A kinetic study. *Fuel*, 103, 542–552. DOI: 10.1016/j.fuel.2012.06.114.
- Mtui P., 2013. CFD modeling of devolatilization and combustion of shredded tires and pine wood in rotary cement kilns. *Amer. J. Energy Engineering*, 1, 51-55. DOI: 10.11648/j.ajee.20130105.11.
- Niksiar A., Sohrabi M., 2014. Mathematical modeling of waste plastic pyrolysis in conical spouted beds: Heat, mass, and momentum transport. *J. Anal. Appl. Pyrolysis*, 110, 66–78. DOI: 10.1016/j.jaap.2014.08.005.
- Olazar M., Lopez G., Arabiourrutia M., Elordi G., Aguado R., Bilbao J., 2008. Kinetic modelling of tyre pyrolysis in a conical spouted bed reactor. *J. Anal. Appl. Pyrolysis*, 81, 127–132. DOI: 10.1016/j.jaap.2007.09.011.
- Queck A., Balasubramanian R., 2012. Mathematical modeling of rubber tire pyrolysis. *J. Anal. Appl. Pyrolysis*, 95, 1–13. DOI: 10.1016/j.jaap.2012.01.012.
- Yang J., Tanguy P.A., Roy C., 1995. Heat transfer, mass transfer and kinetics study of the vacuum pyrolysis of a large used tire particle. *Chem. Eng. Sci.*, 50, 1909–1922. DOI: 10.1016/0009-2509(95)00062-A.

Received 18 October 2016

Received in revised form 10 July 2017

Accepted 24 July 2017

LACCASE CONCENTRATION BY FOAM FRACTIONATION OF *CERRENA UNICOLOR* AND *PLEUROTUS SAPIDUS* CULTURE SUPERNATANTS

Michał Błatkiewicz^{*1}, Anna Antecką¹, Andrzej Górak^{1,2}, Stanisław Ledakowicz¹

¹Lodz University of Technology, Faculty of Process and Environmental Engineering, ul.
Wólczńska 213, 90-942, Łódź, Poland

²Dortmund University of Technology, The Department of Biochemical and Chemical Engineering,
Emil-Figge-Straße 70, D-44227 Dortmund, Germany

Foam fractionation process for concentration of laccases from two Basidiomycete strains under different process conditions was investigated. Culture supernatants of *Cerrena unicolor* and *Pleurotus sapidus* containing active laccase were used with and without surfactant additives. Two surfactants: cationic cetrimonium bromide (CTAB) and non-ionic Polysorbate 80 were applied in the range from 0.2 mM to 1.5 mM. The pH levels ranging from 3 to 10 were examined with particular attention to pH=4, which is close to the pI of the enzymes. Results show that the source of the enzyme is significant in terms of partitioning efficiency in a foam fractionation process. Laccase from *Cerrena unicolor* showed the best activity partitioning coefficients between foamate and retentate of almost 200 with yields reaching 50% for pH 7.5 and concentration of CTAB $c_{CTAB} = 0.5$ mM, whereas laccase from *Pleurotus sapidus* showed partitioning coefficients of up to 8 with 25% yield for pH 4 and $c_{CTAB} = 0.5$ mM.

Keywords: foam fractionation, Laccase, CTAB, Polysorbate 80

1. INTRODUCTION

Laccases (EC 1.10.3.2, p-diphenolic oxidases) are enzymes which belong to the group of oxidoreductases. They can be produced by various organisms, such as plants, insects, bacteria (Claus and Filip, 1997; Diamantidis et al., 2000; Harvey and Walker, 1999), but are most commonly found as extracellular products of fungi, especially the ones causing white rotting of wood (Songulashvili et al., 2007). Their purpose in nature is to decompose long lignocellulosic chains into molecules of lower mass, and therefore provide the host with a carbon source (Cohen et al., 2002; Reddy et al., 2003). However, they are also able of decomposing a variety of aromatic compounds, like aromatic amines, substituted phenols, or thiols (Xu, 1996).

Although biotechnology is currently one of the most advancing branches of science, downstream processing of biological products remains a time-consuming and expensive task (Raja et al, 2011). Therefore, a lot of research is focused on finding and developing novel, cost-effective, efficient methods of bioproduct separation and recovery with satisfying selectivity towards the desired product and granting its stability in the process. Various downstream processing methods of laccase have been investigated, including chromatographic methods (Scherer and Fischer, 1998) and aqueous two-phase extraction (Błatkiewicz et al., 2016; Prinz et al., 2014). One of the promising, currently investigated methods is foam fractionation (FF). It is a bubble separation technique which allows for separation of

*Corresponding authors, e-mail: michal.blatkiewicz@p.lodz.pl

amphiphilic molecules, such as proteins, from their aqueous solutions (Lemlich, 1968). The principle of the process is to generate liquid-gas interface in the form of foam by continuously feeding a batch of the desired bioproduct's aqueous solution with dispersed inert gas in a column. The emergent foam, enriched in the product, is then collapsed with the use of lowered pressure and collected as a foamate at the column outlet (Burghoff, 2012). As the bubbles migrate upwards, which is caused by the foam buildup within the column, their water content gets lower due to gravitational and capillary forces. This causes draining of the foam and coalescence of the constituent bubbles, and thus, further concentration of the product within the foam (Du et al., 2000; Merz et al., 2011a).

Foam fractionation has a number of advantages that makes it a feasible process. Not only is it carried out in mild conditions for biological molecules, but also it is suitable for diluted solutions (Uraizee and Narsimhan, 1990). Moreover, it is cost-effective and environment-friendly since it is not necessary to use chemical additives other than insignificant amounts of surfactant, while only inert gas is involved (Stowers et al., 2009). Additionally, since it is mostly amphiphilic compounds that concentrate on the liquid-gas interface, foam fractionation tends to be selective towards proteins.

Foam fractionation is used mostly as an early step in bioproduct recovery (Merz et al., 2011b). Therefore it is often applied to crude supernatants, in which the protein content is very low. This may cause high surface tensions and decrease the liquid's ability to foam. This is why surfactant supplementation is utilized for such processes to lower surface tensions and stabilize the structure of bubbles (Linke et al., 2007).

Although laccases produced by different hosts serve the same function, their structural differences often lead to different behaviors in downstream processes (Linke et al., 2007; Prinz et al., 2012). Foam fractionation of laccase has been reported in literature (Gerken et al., 2006; Linke et al., 2007), but the published research involved only commercially available pure laccase from *Trametes* spec., not from crude supernatants of fungal cultures. The purpose of this paper was to study differences in efficiency of foam fractionation of laccase-containing supernatants produced separately by two *Basidiomycete* strains: *Cerreña unicolor* and *Pleurotus sapidus* with the use of two surfactants: cationic cetyltrimethylammonium bromide (CTAB) and non-ionic polyoxyethylene (20) sorbitan monooleate (Polysorbate 80) under different pH values.

2. MATERIALS AND METHODS

The *C. unicolor* strain was initially grown on agar plates containing malt extract and mycological peptone. The *P. sapidus* strain was grown on agar plates containing malt extract and soybean peptone. After 7 days of growth the mycelium was homogenized with water with the use of IKA T25 Basic homogenizer at 8000 rpm and transferred into 200 ml flasks, containing Lindeberg-Holm growth medium for *C. unicolor* (Lindeberg and Holm, 1952) and standard culture medium suggested by Zorn for *P. sapidus* (Zorn et al., 2003). The medium was supplemented with Cu^{2+} source, without the use of inductors. The liquid fermentation was conducted in a Certomat BS-1 shaker at 110 rpm. The temperature of 28 °C for *C. unicolor* and 26 °C for *P. sapidus* was applied. The fermentation lasted 10 or 12 days respectively. Then, the supernatants were filtrated and frozen in 100ml containers at -20 °C. The defrosted supernatants showed initial activities of about 1500 U/l and 700 U/l respectively in relation to ABTS at pH = 4.5 in 25 °C.

Cetyltrimethylammonium bromide (CTAB) was purchased from Sigma-Aldrich. Polysorbate 80 was purchased from Fluka. 2,2'-azino-bis-(3-ethylbenzothiazoline-6-sulphonic acid) (ABTS) with the purity of 98% was purchased from Sigma-Aldrich.

The activity of laccase was measured using the ABTS assay according to Majcherczyk et al. (1998). The activity was defined as the amount of the enzyme catalyzing one μmol of ABTS per minute. It was

determined by the oxidation rate of ABTS molecules over time. The pH was adjusted to 4.5 using McIlvaine buffer. All the measurements were performed using a T80+ UV/Vis Spectrometer from PG Instruments Ltd. The measurements of absorbance increment were performed in 25 °C at 420 nm wavelength over 0.5 min. The extinction coefficient for ABTS at 420 nm wavelength is equal to $\varepsilon = 0.04321 \text{ l}/(\text{mmol cm})$. If the sample's activity was too high for the spectrometer's range, it was diluted accordingly. To calculate the enzymatic activity, the following equation was used:

$$\text{act} \left[\frac{U}{l} \right] = \frac{\Delta E \cdot D \cdot V_t}{\Delta t \cdot V_s \cdot d \cdot \varepsilon} \quad (1)$$

The experimental setup has been presented in Fig. 1. It consisted of a glass column of 62 cm in length and inner diameter of 3 cm, a foam collector, a Büchner flask connected to a pump producing low under-pressure, and a compressed air distributor equipped with a reducing valve set to 2 bar and an electronic valve for flux control. The column was equipped with a porous glass disperser at the bottom. Compressed air flowed to the disperser through an electronic valve which set the airflow to 2.4 l/h.

After fixing the airflow, 100 ml of the culture supernatant supplemented with surfactant was poured into the column and the foaming started. Then, a foam collector was installed at the top of the column which directed the foam into a Büchner flask equipped with a funnel to break down the foam. Each experiment was conducted until the foam was no longer able to reach the top of the column before collapsing. Then the experiment was terminated and volumes of the foamate (the collapsed foam) and the retentate (the liquid remaining in the column after the process) were measured. Samples of each phase were taken, and their enzymatic activities were measured. Every experiment was performed at room temperature.

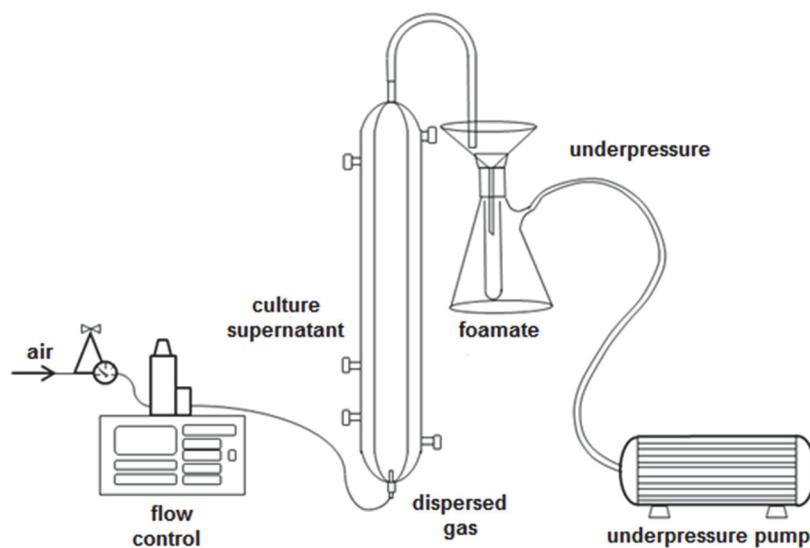


Fig. 1. Foam fractionation equipment setup

There are two major parameters which determine the efficiency of foam fractionation: the yield (recovery) in the foamate (Y), which informs about the recovery of the enzyme in a given phase and the activity partitioning coefficient (k_{act}), which informs about the ratio of enzymatic activities between the phases.

$$Y = \frac{V_{foam} \cdot \text{act}_{foam}}{V_{ini} \cdot \text{act}_{ini}} \quad (2)$$

$$k_{act} = \frac{\text{act}_{foam}}{\text{act}_{ret}} \quad (3)$$

3. RESULTS AND DISCUSSION

Preliminary experiments showed that the foaming properties of pure culture supernatants of both *Cerrena unicolor* and *Pleurotus sapidus* are not enough for the foam to reach the top of the column without breaking, so surfactant additives had to be used. Cetyltrimethylammonium bromide (CTAB) is a recommended surfactant for foam fractionation of laccase. However it may lower its recovery due to formation of stable complexes which deactivate laccase molecules (Linke et al., 2007; Walker and McCallion, 1980).

As stated by Shea et al. (2009), proteins are most hydrophobic at their isoelectric points (pI), which should lead to optimal conditions for foam fractionation, although it may also lead to their precipitation and aggregation. However, there have been reports of pH values varying significantly for the proteins' pI which proved to be more effective (Bacon et al., 1988; Chai et al., 1998; Linke et al., 2007). The isoelectric points of the laccases were determined by isoelectric focusing. The pI of laccases from both *C. unicolor* and *P. sapidus* were between 3 and 5. In general, throughout the experiments, the foaming time was between 40 and 60 minutes, and volumes of collected foamates were between 2.5 and 5.0 ml.

In order to choose the optimal pH for the process, a set of experiments with a constant CTAB concentration and varying pH values was conducted. Linke et al. (2007) chose the range of $c_{CTAB} = 0.4 - 1.2$ mM for their experiments with satisfying results. Therefore for the initial experiment of pH screening, the surfactant concentration was chosen to be 0.5 mM, which is about half of the surfactant's critical micelle concentration (0.9 - 1.0 mM). The results were presented in Figs. 2 and 3.

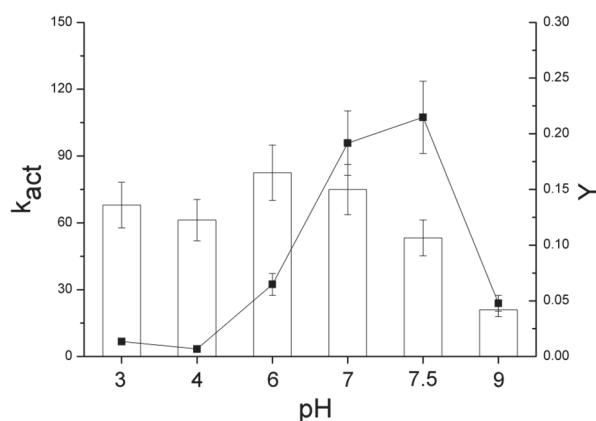


Fig. 2. Influence of pH on enzyme partitioning and foamate yield of laccase from *C. unicolor* at $c_{CTAB} = 0.5$ mM. (■) activity partitioning coefficient, (□) yield in the foamate

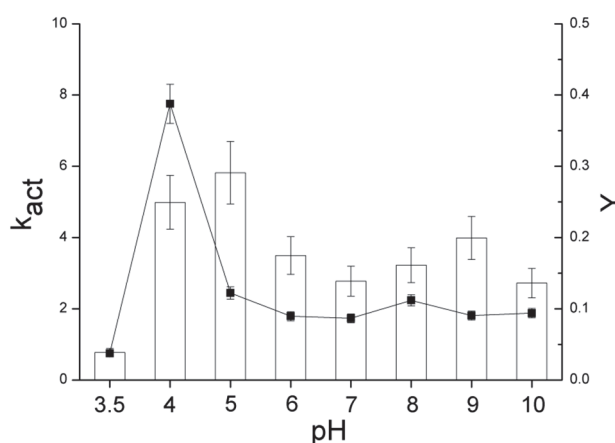


Fig. 3. Influence of pH on enzyme partitioning and foamate yield of laccase from *P. sapidus* at $c_{CTAB} = 0.5$ mM. (■) activity partitioning coefficient, (□) yield in the foamate

The pH had a significant influence on the effectiveness of the foam fractionating process for laccases from both hosts. As seen in Fig. 2., the highest activity partitioning coefficient (around 110) was achieved at pH = 7.5, whereas at pH = 4, which is close to the isoelectric point, the partitioning of the enzyme towards the foamate was very low. The differences in yields were less significant. In the case of *P. sapidus* laccase (Fig. 3), regardless of the pH value, the partitioning of laccase towards the foam was much less effective than in the case of *C. unicolor* laccase. The highest activity partitioning coefficient was no higher than 8. However, as opposed to *C. unicolor* laccase, foam fractionation of laccase from *P. sapidus* showed the best results for both activity partitioning and yield, at pH values close to the *pI* of the enzyme. It can be noticed that the highest yields do not line up with the highest partitioning coefficients. This is caused by the fact that at various pH conditions the foaming of the system can lead to carrying excess water with the foam and thus diluting the foamate. Since the volume of the foamate phase is usually very low (2 - 5 ml), even slight changes in volume can significantly decrease the partitioning coefficients. Thus a trade-off situation between high yield and high partitioning coefficient may occur.

The differences in partitioning between these two types of laccases in relation to their *pI* are very clear. While in the case of *P. sapidus* laccase, the pH in proximity to the molecule's *pI* resulted in highest k_{act} , for *C. unicolor* laccase it was quite the opposite: setting the pH away from the molecule's *pI* increased the partitioning towards the foam. Li et al. (2016) suggest that although at pH deviating from *pI* the repulsion between molecules increases due to increasing zeta potentials, it also reduces thickness of the foam. The thin foam may result in a low volume of foamate, and thus higher enrichment in the phase.

Although increased concentration of surfactants increases the foamability of the system, adsorption competition may occur at the gas-liquid interface (Shea et al., 2009). Therefore, even though at higher surfactant concentrations the recovery yields are increased (Linke et al., 2007), the enrichment within the foam may decrease, as more water is transported within the foam with lower concentration of the desired protein. To study this, a second set of experiments was conducted to investigate the surfactant concentration that can be treated as a compromise between partitioning coefficient and yield. Based on prior results, two pH values were chosen for the investigation of the CTAB concentration on the foam fractionation effectiveness: pH = 4, which is close to the protein's *pI*, and the neutral pH = 7, which was highly effective for fractionation of the *C. unicolor* laccase.

As expected, the yield in the foamate maintained the consecutive increase trend as the CTAB concentration was increased, both in the case of *C. unicolor* laccase (Figs. 4, 5) and *P. sapidus* laccase (Figs. 6, 7).

For the *C. unicolor* laccase at pH = 4 (Fig. 4.), even significantly increased concentrations did not cause the partitioning coefficients or recovery yields to increase satisfactorily. It can be noticed that one experimental point exceeded the surfactant's critical micelle concentration, which led to no increase in activity partitioning but with slightly higher recovery yield. However, as presented in Fig. 5, at pH = 7 the differences in foamate enrichment were significant. The process achieved its maximum partitioning coefficient at CTAB concentration of 0.5 mM, where k_{act} value reached almost 200. At higher CTAB concentrations the partitioning coefficient dropped significantly.

In the case of *P. sapidus* laccase, the results were analogous. At pH = 4 (Fig. 6.) there was a spike of higher foam enrichment at CTAB concentration of 0.5 mM, where the partitioning coefficient reached the value of 8. At neutral pH (Fig. 7.) the activity partitioning coefficient was unaffected by the surfactant concentration increase, while the foamate yields increased, but did not exceed 0.2 at $c_{CTAB} = 0.7$ mM.

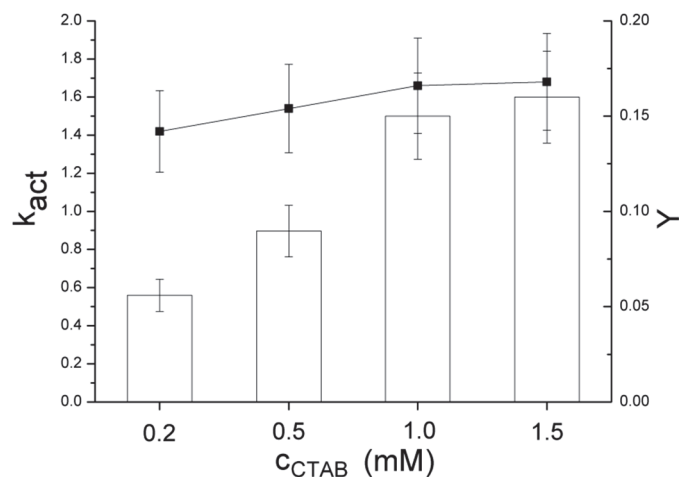


Fig. 4. Influence of CTAB concentration on enzyme partitioning and foamate yield of laccase from *C. unicolor* at pH = 4. (■) activity partitioning coefficient, (□) yield in the foamate

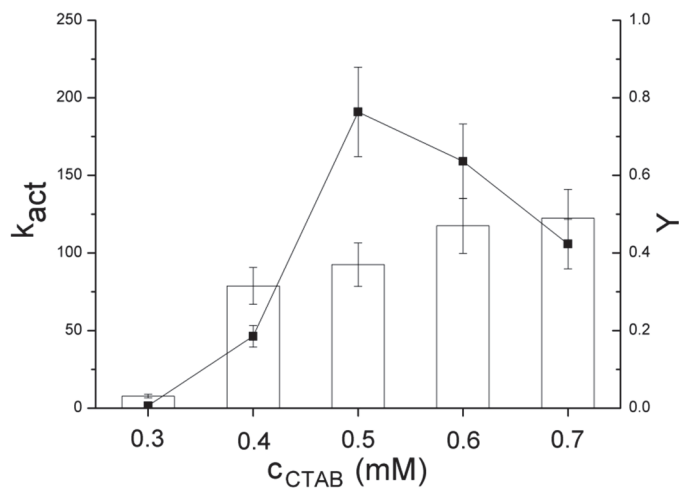


Fig. 5. Influence of CTAB concentration on enzyme partitioning and foamate yield of laccase from *C. unicolor* at pH = 7. (■) activity partitioning coefficient, (□) yield in the foamate

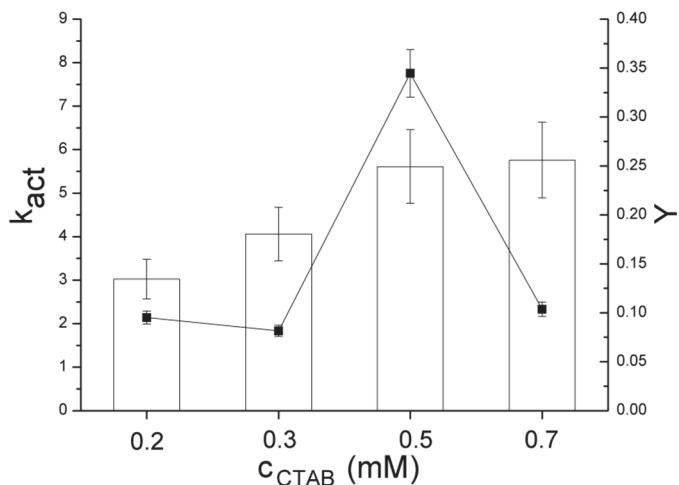


Fig. 6. Influence of CTAB concentration on enzyme partitioning and foamate yield of laccase from *P. sapidus* at pH = 4. (■) activity partitioning coefficient, (□) yield in the foamate

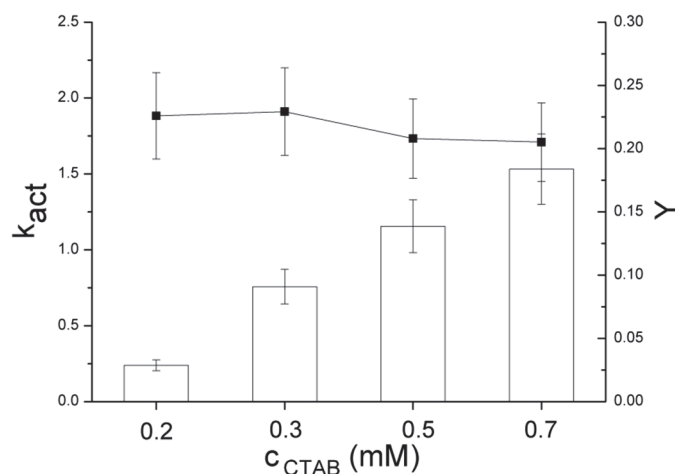


Fig. 7. Influence of CTAB concentration on enzyme partitioning and foamate yield of laccase from *P. sapidus* at pH = 7. (■) activity partitioning coefficient, (□) yield in the foamate

As a next step, another surfactant, Polysorbate 80, was investigated. Polysorbate 80 is a non-ionic surfactant, which does not foam as effectively as cationic surfactants such as CTAB. There are reports of using it as a foaming agent for foam fractionation (Linke et al, 2005; Bezelgues et al., 2008).

For the foam fractionation of laccase experiments, two different Polysorbate 80 concentrations were investigated: 0.5 mM and 1.0 mM. The surfactant has a very low critical micelle concentration of 0.012 mM, therefore the experiments were performed with maximum foamability. In the case of *C. unicolor* culture supernatant, the foam was stable enough to reach the top of the column only with the concentration of 1.0 mM. In the case of *P. sapidus* culture supernatant, the foam stability was insufficient at all examined concentrations.

Therefore, a set of experiments was conducted for *C. unicolor* laccase at $C_{Polysorbate80} = 1.0$ at different pH values, the data of which was presented in Fig. 8.

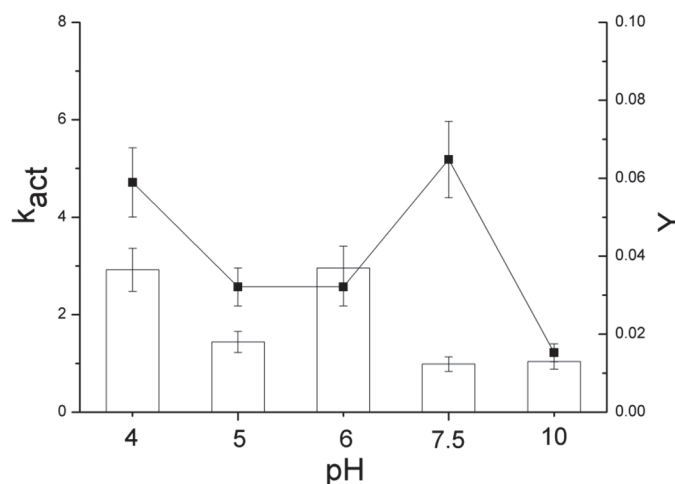


Fig. 8. Influence of pH on enzyme partitioning and foamate yield of laccase from *C. unicolor* at $C_{Polysorbate80} = 1.0$ mM. (■) activity partitioning coefficient, (□) yield in the foamate

In comparison to the results of foam fractionation with the use of CTAB, both the activity partitioning coefficients and the yields are significantly lower. At pH = 7.5 the k_{act} did not exceed 6, and the highest yield was lower than 0.04.

4. CONCLUSIONS

Foam fractionation of laccase from crude culture supernatants of *C. unicolor* and *P. sapidus* is a promising method of concentration of the enzyme, provided a proper surfactant supplement is used. Cetyltrimethylammonium bromide addition in the concentration of 0.5 mM significantly improves the foaming of the system without draining too much water towards the foamate, which results in higher enzyme partitioning coefficients at the cost of higher yield in the foamate. Polysorbate 80 as the foaming agent is not as effective as CTAB in terms of laccase enrichment in the foam fractionation process.

Although partitioning coefficients of almost 200 were obtained, recoveries of over 50% were not possible to achieve without diluting the foamate, which means that although it is possible to satisfactorily concentrate the enzyme, the majority of it remains within the retentate. Therefore, it is advised to employ other downstream processing methods along with foam fractionation. Also, it is important to note that foam fractionation is only a method for concentration of laccase from culture supernatants, not purification. Additional steps of separating the enzyme from other proteins and the surfactant must be taken in order to obtain a pure product.

In general, the foam fractionation process is more efficient for the culture supernatant of *C. unicolor* than that of *P. sapidus*. It may be caused by higher enzyme content within the supernatant of *C. unicolor* or differences in physicochemical properties of laccases from the two investigated strains.

The results are promising for further investigation of the process in the form of continuous foam fractionation.

The research was conducted as a part of a project number UMO-2013/11/B/ST8/00337 financed by the National Science Centre. The authors would like to thank Dr. Merz for providing the foam fractionation equipment.

SYMBOLS

<i>act</i>	enzymatic activity, U/l
<i>d</i>	thickness of the sample, mm
<i>D</i>	dilution coefficient
<i>E</i>	absorbance
<i>k_{act}</i>	activity partitioning coefficient
<i>t</i>	time, min
<i>V</i>	volume of the phase, ml
<i>V_s</i>	volume of the supernatant sample, μ l
<i>V_t</i>	total volume of the sample, μ l
<i>x</i>	mass fraction, wt-%
<i>Y</i>	yield

Greek symbols

ϵ	extinction coefficient at 420 nm wavelength, l/(mmol cm)
------------	--

Subscripts

<i>foam</i>	foamate
<i>ret</i>	retentate
<i>ini</i>	initial

REFERENCES

- Bacon J.R., Hemmant J.W., Lambert N., Moore R., Wright D.J., 1988. Characterization of the foaming properties of lysozymes and α -lactalbumins: A structural evaluation. *Food Hydrocolloid*, 2, 225-245. DOI: 10.1016/s0268-005x(88)80020-1.
- Bezelgues J.B., Serieye S., Crosset-Perrotin L., Leser M.E., 2008. Interfacial and foaming properties of some food grade low molecular weight surfactants. *Colloid Surfaces A*, 331, 56-62. DOI: 10.1016/j.colsurfa.2008.07.022.
- Blatkiewicz, M., Prinz, A., Górak, A., Ledakowicz, S., 2016. Partitioning of *Cerrena unicolor* laccase activity in an aqueous two-phase system. *Chem. Process Eng.*, 37, 269-280. DOI: 10.1515/cpe-2016-0022.
- Burghoff B., 2012. Foam fractionation applications. *J. Biotech.*, 161, 126-137. DOI: 10.1016/j.jbiotec.2012.03.008.
- Chai J., Loha V., Prokop A., Tanner R.D., 1998. Effect of bubble velocity and pH step changes on the foam fractionation of sporamin. *J. Agr. Food Chem.*, 46, 2868-2872. DOI: 10.1021/jf970929b.
- Claus H., Filip Z., 1997. The evidence of a laccase-like enzyme activity in a *Bacillus sphaericus* strain. *Microbiol. Res.*, 152, 209-216. DOI: 10.1016/s0944-5013(97)80014-6.
- Cohen R., Persky L., Hadar Y., 2002. Biotechnological applications and potential of wood-degrading mushrooms of the genus *Pleurotus*. *Appl. Microbiol. Biot.*, 58, 582-594. DOI: 10.1007/s00253-002-0930-y.
- Diamantidis G., Effosse A., Potier P., Bally R., 2000. Purification and characterization of the first bacterial laccase in the rhizospheric bacterium *Azospirillum lipoferum*. *Soil Biol. Biochem.*, 32, 919-927. DOI: 10.1016/s0038-0717(99)00221-7.
- Du L., Loha V., Tanner R.D., 2000. Modeling a protein foam fractionation process, In: Finkelstein M., Davison B.H. (Eds.), *Twenty-First Symposium on Biotechnology for Fuels and Chemicals*. Humana Press, 1087-1099. DOI: 10.1007/978-1-4612-1392-5_85.
- Gerken B.M., Nicolai A., Linke D., Zorn H., Berger R.G., Parlar H., 2006. Effective enrichment and recovery of laccase C using continuous foam fractionation. *Sep. Purif. Technol.*, 49, 291-294. DOI: 10.1016/j.seppur.2005.09.015.
- Harvey B.M., Walker J.R.K., 1999. Studies with plant laccases: I. Comparison of plant and fungal laccases. *J. Biochem. Mol. Biol. Biophys.*, 3, 45-51.
- Lemlich R., 1968. Adsorptive bubble separation methods—foam fractionation and allied techniques. *Ind. Eng. Chem.*, 60, 16-29. DOI: 10.1021/ie50706a005.
- Li R., Wu Z., Wang Y., Ding L., Wang Y., 2016. Role of pH-induced structural change in protein aggregation in foam fractionation of bovine serum albumin. *Biotech. Rep.*, 9, 46-52. DOI: 10.1016/j.btre.2016.01.002.
- Lindeberg G., Holm G., 1952. Occurrence of tyrosinase and laccase in fruit bodies and mycelia of some Hymenomycetes. *Physiol. Plantarum*, 5, 100-114. DOI: 10.1111/j.1399-3054.1952.tb08234.x.
- Linke D., Zorn H., Gerken B., Parlar H., Berger R. G., 2007. Laccase isolation by foam fractionation—new prospects of an old process. *Enzyme Microb. Tech.*, 40, 273-277. DOI: 10.1016/j.enzymictec.2006.04.010.
- Linke D., Zorn H., Gerken B., Parlar H., Berger R.G., 2005. Foam fractionation of exo-lipases from a growing fungus (*Pleurotus sapidus*). *Lipids*, 40, 323-327. DOI: 10.1007/s11745-005-1389-x.
- Majcherczyk A., Johannes C., Hüttermann A., 1998. Oxidation of polycyclic aromatic hydrocarbons (PAH) by laccase of *Trametes versicolor*. *Enzyme Microbial. Tech.*, 22, 335-341. DOI: 10.1016/s0141-0229(97)00199-3.
- Merz J., Burghoff B., Zorn H., Schembecker G., 2011a. Continuous foam fractionation: Performance as a function of operating variables. *Sep. Purif. Technol.*, 82, 10-18. DOI: 10.1016/j.seppur.2011.07.023.
- Merz J., Zorn H., Burghoff B., Schembecker G., 2011b. Purification of a fungal cutinase by adsorptive bubble separation: A statistical approach. *Col. Surfaces A*, 382, 81-87. DOI: 10.1016/j.seppur.2009.06.021.
- Prinz A., Zeiner T., Vössing T., Schüttmann I., Zorn H., Górak A., 2012. Experimental investigation of laccase purification using aqueous two-phase extraction. *Chem. Eng. Trans.*, 27, 349-354. DOI: 10.14233/ajchem.2014.17063.
- Prinz, A., Koch, K., Górak, A., Zeiner, T., 2014. Multi-stage laccase extraction and separation using aqueous two-phase systems: Experiment and model. *Process Biochem.*, 49, 1020-1031. DOI: 10.1016/j.procbio.2014.03.011.
- Raja S., Murty V. R., Thivaharan V., Rajasekar V., Ramesh V., 2011. Aqueous two phase systems for the recovery of biomolecules—a review. *Sci. Tech.*, 1, 7-16. DOI: 10.5923/j.scit.20110101.02.
- Reddy G.V., Babu P.R., Komaraiah P., Roy K.R.R. M., Kothari I.L., 2003. Utilization of banana waste for the production of lignolytic and cellulolytic enzymes by solid substrate fermentation using two *Pleurotus* species (*P. ostreatus* and *P. sajor-caju*). *Process Biochem.*, 38, 1457-1462. DOI: 10.1016/s0032-9592(03)00025-6.

- Scherer M., Fischer R., 1998. Purification and characterization of laccase II of *Aspergillus nidulans*. *Arch. Microb.*, 170, 78-84. DOI: 10.1007/s002030050617.
- Shea A.P., Crofcheck C.L., Payne F.A., Xiong Y.L., 2009. Foam fractionation of α -lactalbumin and β -lactoglobulin from a whey solution. *Asia Pac. J. Chem. Eng.*, 4, 191-203. DOI: 10.13031/2013.21982.
- Songulashvili G., Elisashvili V., Wasser S.P., Nevo E., Hadar Y., 2007. Basidiomycetes laccase and manganese peroxidase activity in submerged fermentation of food industry wastes. *Enzyme Microb. Tech.*, 41, 57-61. DOI: 10.1016/j.enzymitec.2006.11.024.
- Stowers C.C., Makarov V., Walker A., Edwards R.A., Tanner R.D., 2009. Effect of air flow rate on the foam fractionation of a mixture of egg white and egg yolk. *Asia Pac. J. Chem. Eng.*, 4, 180-183. DOI: 10.1002/apj.227.
- Uraizee F., Narsimhan G., 1990. Foam fractionation of proteins and enzymes: I. Applications. *Enzyme Microb. Tech.*, 12, 232-233. DOI: 10.1016/0141-0229(90)90045-r.
- Walker J.R., McCallion R.F., 1980. The selective inhibition of ortho- and para-diphenol oxidases. *Phytochemistry*, 19, 373-377. DOI: 10.1016/0031-9422(80)83184-0.
- Xu F., 1996. Oxidation of phenols, anilines, and benzenethiols by fungal laccases: correlation between activity and redox potentials as well as halide inhibition. *Biochem.*, 35, 7608-7614. DOI: 10.1021/bi952971a.
- Zorn H., Breithaupt D.E., Takenberg M., Schwack W., Berger R.G., 2003. Enzymatic hydrolysis of carotenoid esters of marigold flowers (*Tagetes erecta* L.) and red paprika (*Capsicum annuum* L.) by commercial lipases and *Pleurotus sapidus* extracellular lipase. *Enzyme Microb. Tech.*, 32, 623-628. DOI: 10.1016/s0141-0229(03)00020-6.

Received 12 December 2016

Received in revised form 21 July 2017

Accepted 24 July 2017

NUMERICAL ANALYSIS OF MOMENTUM TRANSFER PROCESSES IN A MECHANICALLY AGITATED AIR – BIOPHASE – LIQUID SYSTEM

Monika Musiał, Magdalena Cudak, Joanna Karcz*

West Pomeranian University of Technology, Szczecin, Department of Chemical Engineering,
al. Piastów 42, 71-065 Szczecin, Poland

The results of numerical computations concerning momentum transfer processes in an air – biophase – liquid system agitated in a bioreactor equipped with baffles and a Smith turbine (CD 6 impeller) are presented in this paper. The effect of sucrose concentration on the distributions of the velocity of the continuous phase, gas hold-up and the size of gas bubbles in the system was analysed. Simulation results were presented in the form of the contours of the analysed magnitudes. The effect of sucrose concentration on the averaged values (i.e. determined on the basis of local values) of gas hold-up and gas bubbles size was evaluated. The results of the numerical computations of gas hold-up were compared with our own experimental data.

Keywords: numerical modelling, momentum transfer, gas – solid – liquid system, bioreactor

1. INTRODUCTION

When straight blades of the Rushton turbine are curved with radius R , the modified high speed impeller can rotate in an agitated vessel in this way that blades push forward on the fluid with their concave or convex parts. The turbine disc impeller with six concave blades is known in literature as the Smith turbine (CD 6 impeller) and is recommended for gas dispersion in the liquid phase. Reduced cavities formed behind the blades compared to those for the Rushton turbine (Bakker, 2000) can be mentioned as the main advantages of the CD 6 impeller. Literature survey on different applications of the turbine impeller with curved blades shows that experimental studies concerning power consumption and mass and heat transfer were carried out mainly by Bielka et al. (2014); Frijlink (1987); Karcz and Kamińska-Borak (1997); Rielly et al. (1992); Sensel et al. (1993); Smith and Katsanevakis (1993); Van't Riet et al. (1976); Warmoeskerken and Smith (1989); Zhengming et al. (1991). Karcz and Kamińska-Brzoska (1994a,b) studied experimentally the influence of the geometrical parameters of the turbine with concave and convex blades on power consumption and heat transfer process in the liquid phase. Gas dispersion in the liquid phase in the agitated vessel equipped with a turbine disc impeller with curved blades was experimentally analysed by Cudak (2011, 2014); Musiał et al. (2015); Rielly et al. (1992); Sensel et al. (1993); Smith and Katsanevakis (1993); Van't Riet et al. (1976); Warmoeskerken and Smith (1989) and Zhengming et al. (1991).

Junker et al. (2000) experimentally examined dual impeller combinations of CD 6 impeller in fermentation vessels. They stated that the use of dual CD 6 impellers and hybrids containing the CD 6 impeller decreases power consumption and increases mass transfer rate in the gas – liquid system compared to results obtained for systems equipped with dual Rushton turbines.

*Corresponding authors, e-mail: Joanna.Karcz@zut.edu.pl

Using CFD simulation, Kharpe and Munshi (2014) carried out a numerical comparison of the Rushton turbine and CD 6 impellers operating in a non-Newtonian fluid agitated in a baffled vessel within the fully turbulent flow regime. Numerical results revealed that the flow field generated by the CD 6 impeller is smaller in magnitude than that for the Rushton turbine. Problems of simulation of gas – liquid hydrodynamics in a baffled agitated vessel with the Rushton turbine were analysed, in detail, by Scargiali et al. (Scargiali et al., 2007). An Eulerian – Eulerian approach was used with the $k - \varepsilon$ turbulence model. All bubbles were assumed to be of the same size. The effect of inter-phase forces on the results of simulation was considered. Numerical results were found to be in satisfactory agreement with experimental data.

Recently, a method of multiphase computational fluid dynamics coupled with the population balance method (CFD-PBM) has been successfully used to investigate hydrodynamics and mass transfer in gas-liquid agitated vessels (Gimbun et al., 2009; Musiał et al., 2014; Ranganathan and Sivaraman, 2011). Gimbun et al. (2009) used these methods to analyse scale-up problems for mechanically agitated gas-liquid systems in a vessel equipped with the Rushton turbine or CD 6 impeller. They conducted multiphase simulations using the Eulerian-Eulerian two-fluid model. The authors obtained the local bubble size distribution by solving the PBM using the quadrature methods of moments (QMOM). Devi and Kumar (2011, 2013) applied a CFD method to analyse flow patterns in an agitated vessel equipped with single or double CD 6 impellers. In the case of the single CD 6 impeller, multiple reference frames (MRF) impeller model and realizable $k - \varepsilon$ turbulence model were used (Devi and Kumar, 2011). For this case, CFD simulations predicted more turbulent kinetic energy dissipation near the vicinity of CD 6 impeller than for the Rushton turbine. Analysis of the numerical results obtained for the systems of the dual Rushton and CD 6 impellers showed that formation of the merging flow pattern is different in case of CD 6 impellers than in the case of Rushton turbines (Devi and Kumar, 2013).

Results of numerical simulation of hydrodynamics in an agitated vessel equipped with a turbine disc impeller with concave or convex blades make it possible to estimate local changes in the velocity of the fluid flow, therefore it is worth carrying out such computations in order to complete and extend experimental results.

The results of numerical computations concerning momentum transfer processes in an air – biophase – liquid system agitated in a bioreactor equipped with baffles and the Smith turbine (CD 6 impeller) are offered in this paper. The effect of sucrose concentration on velocity distributions in the continuous phase, gas hold-up and the size of gas bubbles in the system were analysed. The results of numerical calculations were compared with our previous experimental results.

2. THE RANGE OF SIMULATIONS

Computations were carried out for a baffled vessel of inner diameter $D = 0.288$ m. Liquid height in the bioreactor was equal to $H = D$ (Fig. 1a). Four flat baffles of width $B = 0.1D$ were symmetrically arranged on the inner wall of the vessel. A six-bladed CD 6 impeller of diameter $d = 0.33D$ was located on the height $h = 0.33D$ from the flat bottom of the vessel. Blades of the impeller had the following dimensions: length $a = 0.25d$, width $b = 0.2d$ and curvature radius $R = 0.5b$ (Fig. 2). Air was introduced into the bioreactor through a gas sparger in the shape of a ring, located under the impeller in the distance $e = 0.5h$ from the vessel bottom.

A three phase gas – biophase – liquid system was tested experimentally. An aqueous solution of sucrose with the concentration of 2.5, 5 or 10 % mass was used as the liquid phase. The aqueous suspension of yeasts with the concentration of 1 % was applied as the biophase. For the purposes of numerical calculations, the liquid pseudo-phase consisted of the aqueous solution of sucrose and 1% yeast (biophase) was assumed. Air was the dispersed phase. The air flow rate was equal to

$V_g = 3.89 \times 10^{-4} \text{ m}^3/\text{s}$ ($w_{og} = 5.97 \times 10^{-3} \text{ m/s}$; $v_{vm} = 1.245 \text{ (m}^3/\text{min)/m}^3$). Oxygen solubility in the broth was determined experimentally and amounted to 7 mg/dm^3 . Oxygen consumption was measured during experiments by means of an oxygen sensor.

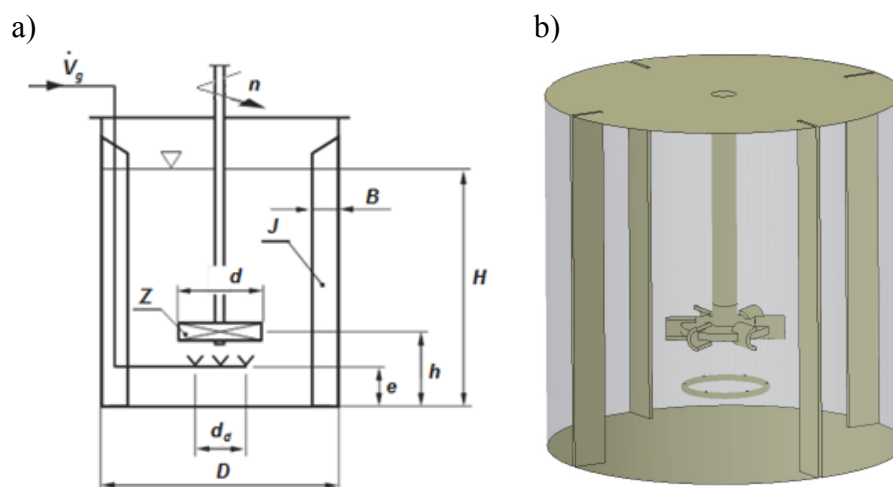


Fig. 1. Geometrical parameters of the agitated vessel

The system containing the aqueous solution of sucrose and yeast suspension showed the properties of a non-Newtonian fluid – shear thinning liquid. Viscosity was measured using a rheometer Haake RT 10. The physical properties of sucrose and yeast suspension were described in detail by Major-Godlewska et al. (Major-Godlewska et al, 2015).

Physical properties of the media, determined experimentally, depended on sucrose concentration and changed within the following ranges: density $\rho \text{ [kg/m}^3] \in <1009; 1041>$; interfacial tension $\sigma \text{ [N/m]} \in <0.076; 0.086>$; viscosity $\eta = k \cdot \gamma^{m-1}$ where $k \in <0.001183; 0.005241>$; $m \in <0.7129; 0.9699>$.

Computations were performed for the impeller speed equal to $n = 12 \text{ 1/s}$ (within the turbulent range of the fluid flow). Experimental studies performed for the physical system considered in this paper showed that below the agitator speed of 8 1/s poor dispersion of the gas in the liquid phase was observed, whereas surface aeration of the liquid was observed above 13 1/s .

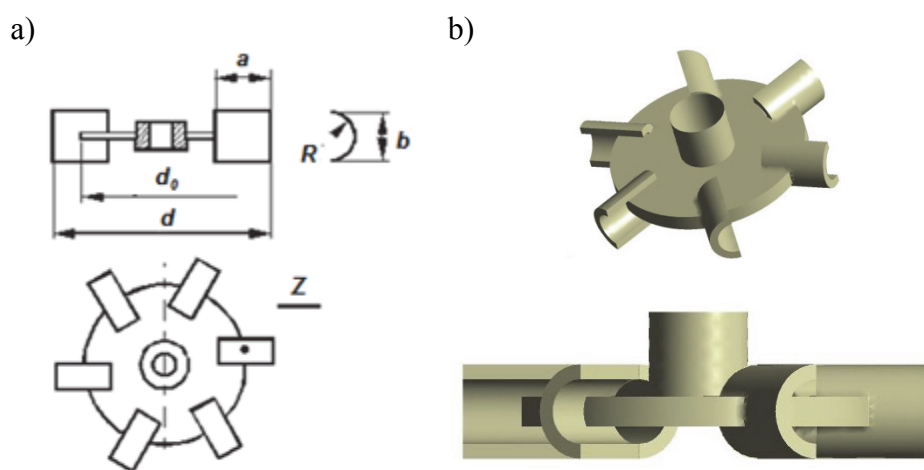


Fig. 2. Geometrical parameters of the CD 6 impeller

Numerical simulations were carried out using ANSYS Workbench and CFX solver version 16.1 (ANSYS, 2013). Geometry of the system was generated using ANSYS Design Modeler. Numerical

grids, created in ANSYS Mesh software, were made for two regions: the impeller-swept region and one for the rest of the bulk zone, in order to use the MRF (Multiple Reference Frames) method. For the geometry of the baffled agitated vessel with a turbine disc impeller with curved blades and the gas sparger, final numerical unstructured meshes consisted of over 920000 tetrahedral elements. Characteristic parameters of the mesh were as follows: a) aspect ratio 1.85; b) element quality 0.84; c) orthogonal quality 0.86. Such values correspond to acceptable quality of the used numerical mesh (ANSYS Inc., 2013).

The Euler-Euler numerical approach was used for simulations. Zero Equation model was used for the modelling of the dispersed phase. Shear Stress Transport (SST) model as the turbulence model and interactions between phases (resistance forces, coalescence and breakage models, turbulent transport) were taken into account in computations (Chung, 2002; Laudner and Spalding, 1974). The breakup model of Luo Svendsen and the coalescence model of Prince-Blanch were used to describe, respectively, breakage and coalescence of gas bubbles. Interphase transfer was determined using *Particle* model. The forces of interphase drag were defined using Schiller-Naumann equation of drag force. To model turbulence transfer between phases the Sato Enhanced Eddy Viscosity correlation was used. Turbulent dispersion force was determined using the Lopez de Bertodano model. The sizes of gas bubbles, divided into ten classes, were modelled by means of the Multiple Size Group Model (MUSIG).

In each simulation the boundary condition on the walls was set at “wall boundary condition”, while on the top of the vessel the boundary condition was set at the outlet with degassing condition in case of gas – liquid system. The gas distributor was modelled as an air inlet with a defined mass flow rate. On the shaft, the boundary condition was set at “rotating wall boundary condition” with the speed equal to $n = 12$ 1/s and with the direction consistent with the direction of impeller rotation. The MRF zone was set as the rotation region with the speed of 12 1/s. Computations were carried out until residuals reached the value of 10^{-4} .

3. RESULTS AND DISCUSSION

The results of numerical simulations are visualized in the form of contour maps. The distributions of liquid velocity, gas hold-up, gas bubble size and kinetic energy of turbulence were shown at three radial inter-sections of the bioreactor (under and above the impeller and at the impeller plane: $h/H = 0.26$; 0.33; 0.43) (Fig. 3a), as well as at two axial inter-sections (at the baffles plane (0°) and the plane located symmetrically between baffles (45°)) (Fig. 3b).

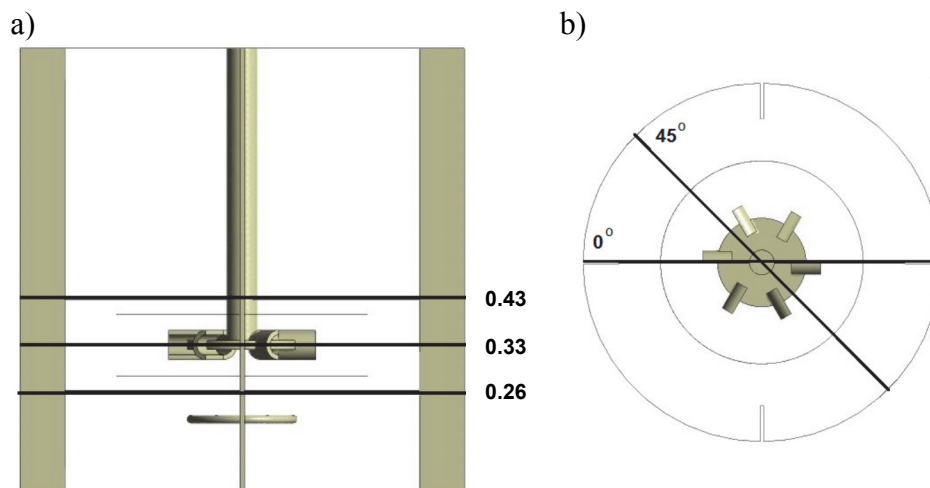


Fig. 3. Inter-sections of the bioreactor: a) axial, b) radial

Axial contours of liquid velocity in the bioreactor, obtained for different concentrations of the sucrose solutions in the liquid phase and two axial inter-sections (at the baffle plane (0°) and the plane located symmetrically between baffles (45°)), are presented in Figs. 4 - 5.

A comparison of the velocity contours in Figs. 4 - 5 shows that the most intensive agitation has taken place in the impeller zone. Liquid velocity behind impeller blades decreases with the increase of the yeast suspension concentration in the bioreactor. Axial contours of the gas hold-up φ , obtained for different sucrose solutions in the liquid phase and two axial inter-sections (at the baffle plane (0°) and the plane located symmetrically between baffles (45°)), are compared in Figs. 6 - 7. More asymmetry of the gas hold – up contours is observed for the axial plane located between baffles (Fig. 7). The highest values of the gas hold-up correspond to the regions located above the impeller. In the zone of the vessel located directly below the impeller gas bubbles are weakly dispersed. However, the dispersion of gas bubbles in the liquid improves when radial distance to the vessel wall in this zone decreases.

Examples of the axial distributions of gas bubble size in the bioreactor equipped with the Smith turbine (CD 6) are presented in Figs. 8 – 9. The smallest diameters of gas bubbles, equal to about 1 mm, correspond to the impeller zone ($z/H = 0.33$). Gas bubble diameter increases in the direction of the free surface of the liquid in the bioreactor. The most symmetrical distribution of gas bubble sizes was obtained for a physical system in which sucrose concentration in the liquid was equal to 5 % mass (Fig.8b, 9b).

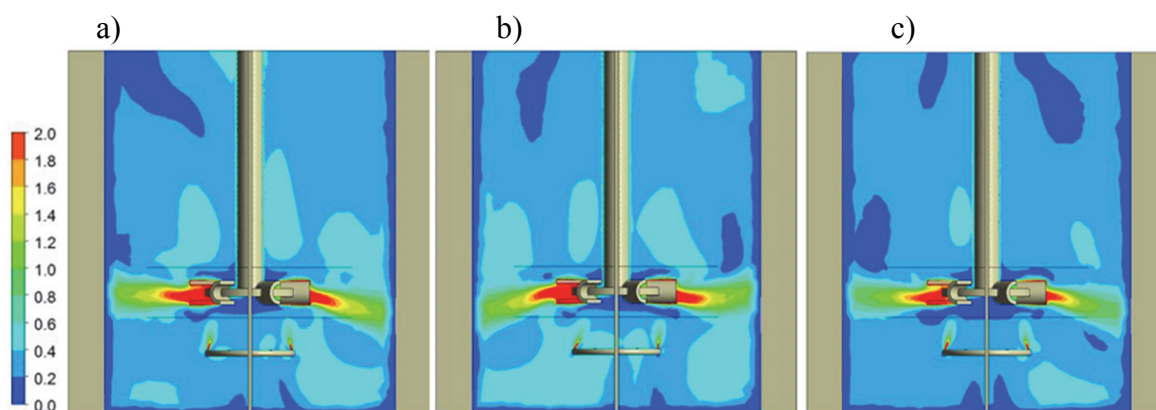


Fig. 4. Axial contours of liquid velocity at baffle plane (0°): a) air – 1% yeast suspension – 2.5% aqueous solution of sucrose, b) air – 1% yeast suspension – 5% aqueous solution of sucrose, c) air – 1% yeast suspension – 10% aqueous solution of sucrose

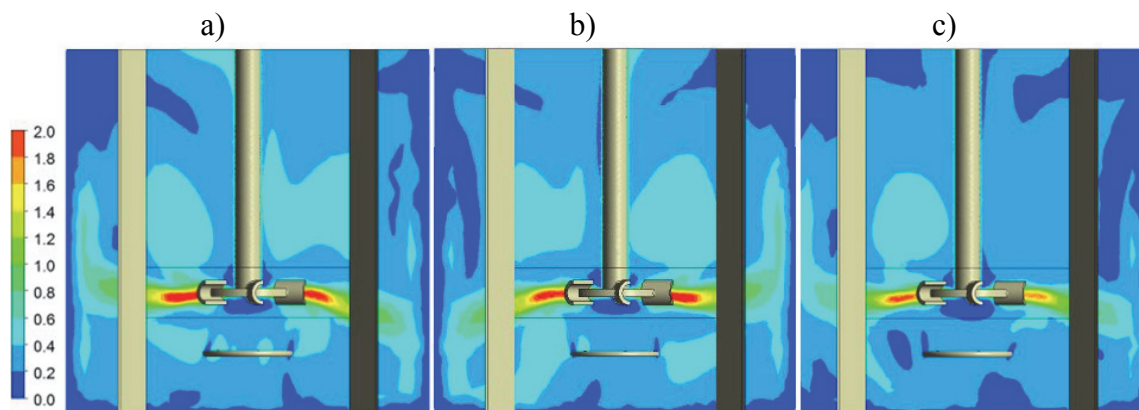


Fig. 5. Axial contours of liquid velocity at the plane located symmetrically between baffles (45°): a) air – 1% yeast suspension – 2.5% aqueous solution of sucrose, b) air – 1% yeast suspension – 5% aqueous solution of sucrose, c) air – 1% yeast suspension – 10% aqueous solution of sucrose

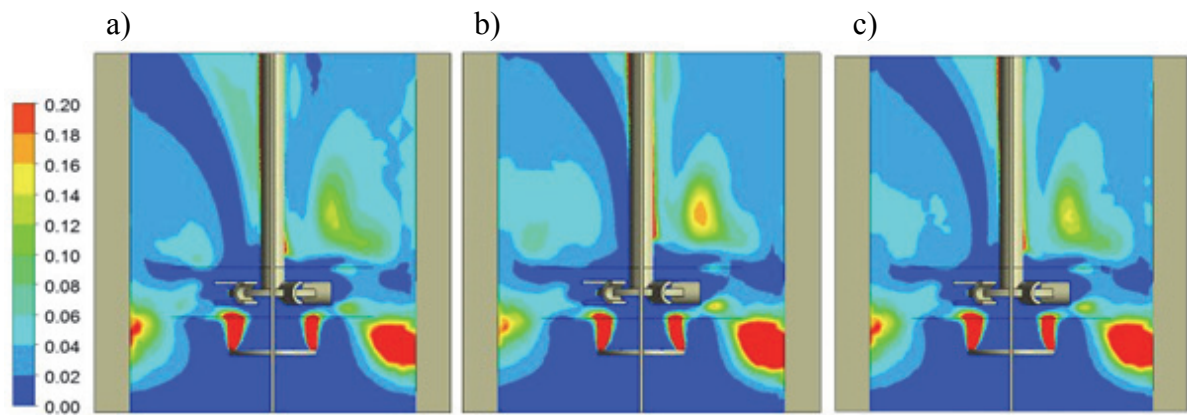


Fig. 6. Axial contours of the gas hold-up ϕ at baffle plane (0°): a) air – 1% yeast suspension – 2.5% aqueous solution of sucrose, b) air – 1% yeast suspension – 5% aqueous solution of sucrose, c) air – 1% yeast suspension – 10% aqueous solution of sucrose

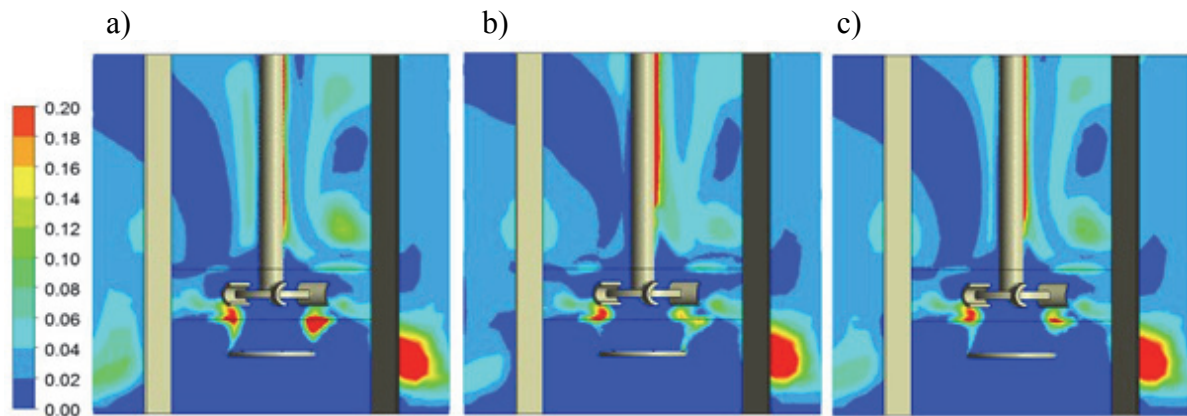


Fig. 7. Axial contours of the gas hold-up ϕ at the plane located symmetrically between baffles (45°): a) air – 1% yeast suspension – 2.5% aqueous solution of sucrose, b) air – 1% yeast suspension – 5% aqueous solution of sucrose, c) air – 1% yeast suspension – 10% aqueous solution of sucrose

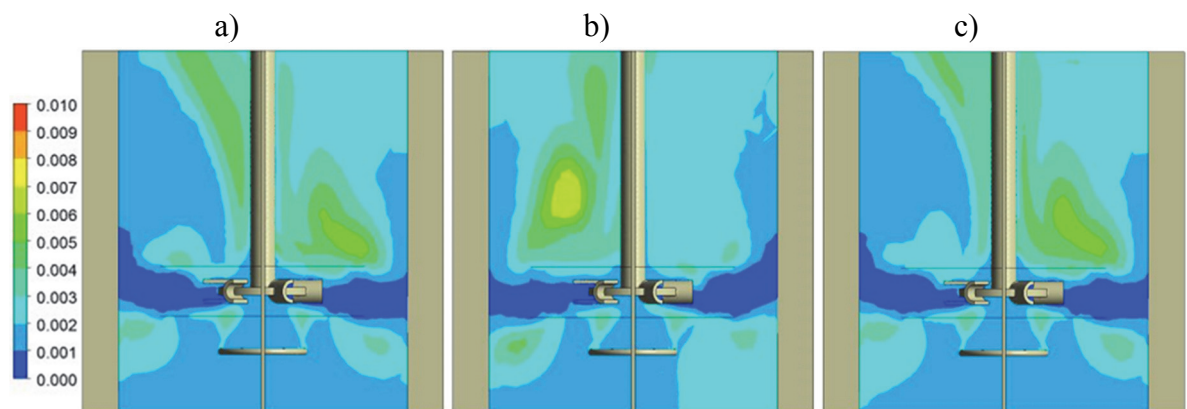


Fig. 8. Axial contours of the gas bubbles size at baffle plane (0°): a) air – 1% yeast suspension – 2.5% aqueous solution of sucrose, b) air – 1% yeast suspension – 5% aqueous solution of sucrose, c) air – 1% yeast suspension – 10% aqueous solution of sucrose

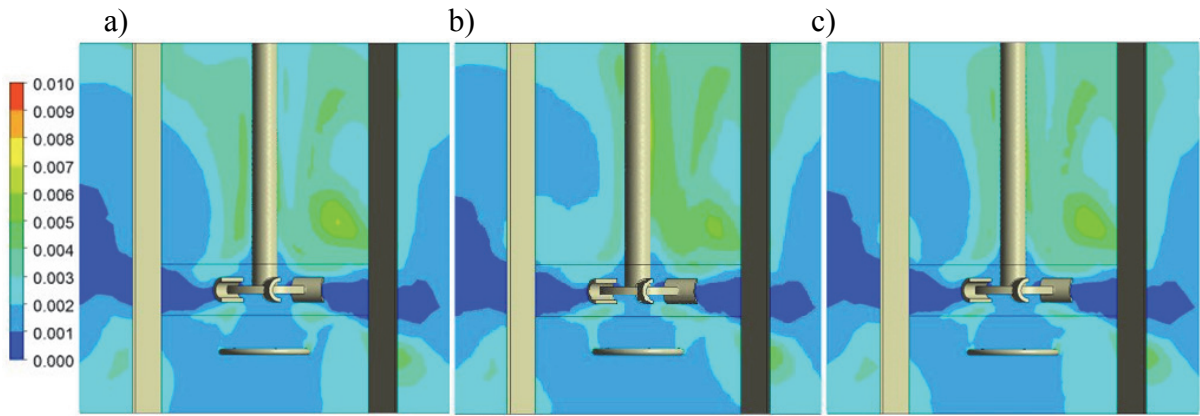


Fig. 9. Axial contours of the gas bubbles size at the plane located symmetrically between baffles (45°):
 a) air – 1% yeast suspension – 2.5% aqueous solution of sucrose, b) air – 1% yeast suspension – 5%
 aqueous solution of sucrose, c) air – 1% yeast suspension – 10% aqueous solution of sucrose

Distributions obtained in numerical calculations depend on the level of the agitator speed n , gas flow rate V_g and physical properties of the gas – liquid pseudo-phase (especially viscosity), as well as on the interaction between those parameters. Certain asymmetry of hydrodynamic distributions is observed in Figs. 4 - 9. These results can be explained as follows: the plane of the axial cross-section divides the vessel in this way that the position of both opposite curved blades of the impeller in this plane is not identical.

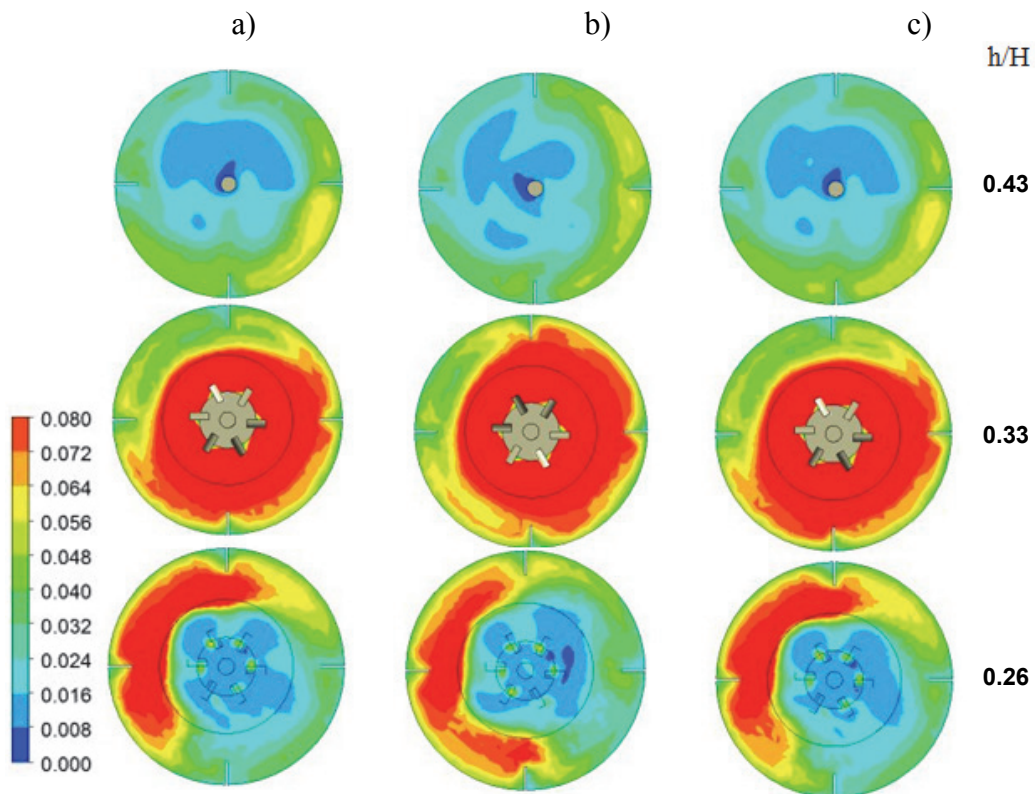


Fig. 10. Radial contours of turbulence kinetic energy k a) air – 1% yeast suspension – 2.5% aqueous solution
 of sucrose, b) air – 1% yeast suspension – 5% aqueous solution of sucrose, c) air – 1% yeast
 suspension – 10% aqueous solution of sucrose

At one axial half cross-section, rotation of the impeller makes the fluid flow round the convex side of the blade, whereas the concave side of the opposite blade in this plane is passed by the fluid at the

second axial half cross-section. Therefore, the local values of the analysed magnitudes on the right and left sides of the impeller shaft in this plane correspond to opposite points of the circulation loop, resulting from the convex or concave curvature of impeller blades. For this reason, certain asymmetry of hydrodynamic distributions can be justified. Strictly symmetrical distributions are characteristic only for flat blades of the impeller (Rushton turbine), where both opposite blades at the axial plane have an identical shape. The contours of the turbulence kinetic energy k and dissipation of turbulence kinetic energy ε for three levels of the dimensionless axial coordinate h/H equal to 0.26 (under impeller), 0.33 (level of the impeller disc) and 0.43 (above impeller) are shown in Figs. 10 - 11. On the basis of the performed simulations, an insignificant effect of sucrose concentration in the liquid phase was observed only in the values of turbulence kinetic energy k and dissipation of turbulence kinetic energy ε . The highest values of both k and ε corresponded to the level of the impeller height. In all the analysed cases, an asymmetry in the distributions of turbulence kinetic energy k was observed (Fig. 10).

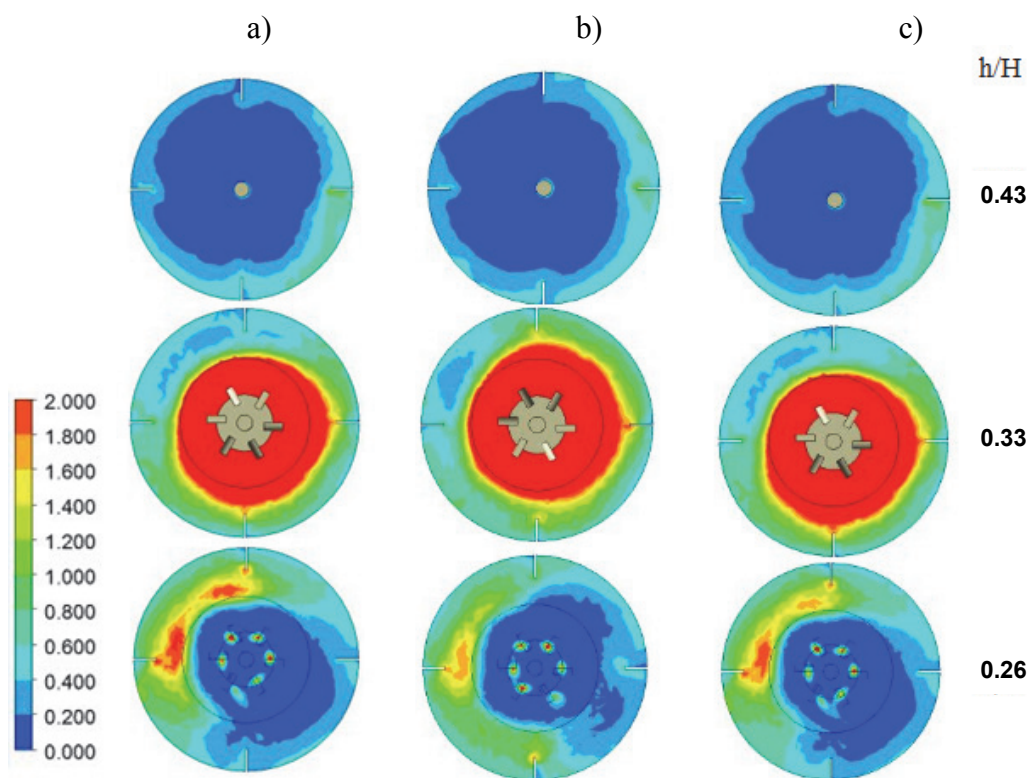


Fig. 11. Radial contours of dissipation of turbulence kinetic energy: a) air – 1% yeast suspension – 2.5% aqueous solution of sucrose, b) air – 1% yeast suspension – 5% aqueous solution of sucrose, c) air – 1% yeast suspension – 10% aqueous solution of sucrose

It is probably caused by disadvantageous hydrodynamic interaction between planar baffles and concave blades of the turbine impeller. The highest differences between values of the turbulence kinetic energy k exist in the region below the impeller in the bioreactor ($h/H = 0.26$, Fig. 10). The contours of energy dissipation ε obtained for both levels of the dimensionless axial coordinate h/H equal to 0.33 (level of the impeller disc) and 0.43 (above impeller) are more symmetrical than the contours for level $h/H = 0.26$ (Fig. 11).

Local values of the analysed parameters were numerically integrated for each plane of the bioreactor. Averaged values of the liquid velocity w , size of gas bubbles d_b , turbulence kinetic energy k and dissipation of turbulence kinetic energy ε are compared in Table 1 for different physical systems. A comparison between the averaged values of gas hold-up φ , determined numerically and our

experimental values (Musiał et al., 2015), is given in Table 2. Relative mean errors collected in Table 2 show sufficient agreement between both numerical and experimental values of the gas hold-up.

Table 1. Comparison of the averaged values of liquid velocity w , size d_b of gas bubbles, turbulence kinetic energy k and the dissipation of turbulence kinetic energy ε for different physical systems

	air – 1% yeast suspension – 2.5% aqueous solution of sucrose	air – 1% yeast suspension – 5% aqueous solution of sucrose	air – 1% yeast suspension – 10% aqueous solution of sucrose
w , m/s	0.629	0.625	0.624
d_b , m	1.975×10^{-3}	1.946×10^{-3}	2.057×10^{-3}
k , m^2/s^2	6.321×10^{-2}	6.301×10^{-2}	6.502×10^{-2}
ε , m^2/s^3	88.18	88.08	93.14

Table 2. Comparison of averaged values of gas hold-up φ

System	φ_{num}	φ_{exp}	$\pm\Delta$, %
air – 1% yeast suspension – 2.5% aqueous solution of sucrose	0.109	0.080	26.6
air – 1% yeast suspension – 5% aqueous solution of sucrose	0.101	0.083	17.8
air – 1% yeast suspension – 10% aqueous solution of sucrose	0.109	0.095	12.8

4. CONCLUSIONS

The results of the numerical simulations of hydrodynamics in the agitated vessel equipped with CD 6 impeller (Smith turbine) show that within the range of computations performed for a three phase gas – biophase – liquid system:

- The local values of liquid velocity decrease with the increase of biophase concentration in the fluid,
- The distributions of gas hold-up and gas bubble size slightly depend only on the concentration of sucrose in the liquid phase.

SYMBOLS

a	length of the impeller blade, m
B	width of baffle, m
b	width of the impeller blade, m
D	vessel diameter, m
d	impeller diameter, m
d_b	gas bubble size, m
d_d	sparger diameter, m
d_o	disc diameter, m
e	clearance between gas sparger and vessel bottom, m
H	liquid height in the agitated vessel, m
h	distance of the impeller from the vessel bottom, m
J	number of baffles
k	consistency index
k	turbulence kinetic energy, m^2/s^2
m	flow index

n	impeller speed, 1/s
R	radius of the blade curvature, m
vvm	volumetric gas flow rate, (m ³ /min)/m ³
V_g	gas flow rate, m ³ /s
w	averaged liquid velocity, m/s
w_{og}	superficial gas velocity, m/s
Z	number of impeller blades
z	axial coordinate, m

Greek symbols

ε	dissipation of turbulence kinetic energy, m ² /s ³
φ	gas hold-up
η	dynamic viscosity of the liquid, Pas
ρ	liquid density, kg/m ³
σ	interfacial tension, N/m

REFERENCES

- ANSYS CFX-Solver Theory Guide, Release 15.0, ANSYS, Inc, November 2013.
- Bakker A., *The Online CFM Book 2000*. Available at: www.bakker.org/cfm.
- Bielka I., Cudak M., Karcz J., 2014. Local heat transfer process for a gas-liquid system in a wall region of an agitated vessel equipped with the system of CD6-RT impellers. *Ind. Eng. Chem. Res.*, 53, 42, 16539-16549. DOI: 10.1021/ie503003t.
- Chung T.J., 2002. *Computational Fluid Dynamics*. Cambridge Univ. Press.
- Cudak M., 2011. Process characteristics for the mechanically agitated gas-liquid systems in the turbulent fluid flow. *Przem. Chem.*, 90, 9, 1000-1004 (in Polish).
- Cudak M., 2014. Hydrodynamic characteristics of mechanically agitated air – aqueous sucrose solutions. *Chem. Process Eng.*, 35, 1, 97-107. DOI: 10.2478/cpe-2014-0007.
- Devi T.T., Kumar B., 2013. Comparison of flow patterns of dual Rushton and CD-6 impellers. *Theor. Found. Chem. Eng.*, 47, 4, 344-355. DOI: 10.1134/S0040570513040210.
- Devi T.T., Kumar B., 2011. Analyzing flow hydrodynamics in stirred tank with CD-6 and Rushton impeller. *Int. Rev. Chem. Eng.*, 3, 1, 440-448.
- Frijlink J.J., 1987. Roerders in begaste Suspensions. *i² – Prozesstechnologie*, 9, 47-51.
- Gimbun J., Rielly C.D., Nagy Z.K., 2009. Modelling of mass transfer in gas-liquid stirred tanks agitated by Rushton turbine and CD 6 impeller: A scale-up study. *Chem. Eng. Res. Des.*, 87, 437-451. DOI: 10.1016/j.cherd.2008.12.017.
- Junker H.J., Mann Z., Hunt G., 2000. Retrofit of CD-6 (Smith) impeller in fermentation vessels. *Appl. Biochem. Biotechnol.*, 89, 1, 67-83. DOI: 10.1385/ABAB:89:1:6.
- Karcz J., Kamińska-Brzoska J., 1994. Experimental studies of the influence of the blade curvature of a disc turbine on power consumption. *Inż. Chem. Proc.*, 15, 3, 371-378.
- Karcz J., Kamińska-Brzoska J., 1994. Heat transfer in a jacketed stirred tank equipped with baffles and concave disc impeller. *8th European Conference on Mixing, ICHIME Symposium Series*, 136, 449-456. Cambridge, 21-23.09.1994.
- Karcz J., Kamińska-Borak J., 1997. An effect of stirred tank geometry on heat transfer efficiency – Studies for concave disc turbine. *9th European Conference on Mixing, Recent Progres en Genie des Procedes*, 11, 51, 265-272. Paris 18-21.03. 1997.
- Khapre A., Munshi B., 2014. Numerical comparison of Rushton turbine and CD-6 impeller in non-Newtonian fluid stirred tank. *International Scholarly Scientific Research Innovation*, 8, 11, 1260-1267. Available at: scholar.waset.org/1999.2/5555526.
- Laudner B.E., Spalding J.L., 1974. The numerical computation of turbulent flows. *Comput. Methods Appl. Mech. Eng.*, 3, 269-289. DOI: 10.1016/0045-7825(74)90029-2.

- Major-Godlewska M., Bitenc M., Karcz J., 2015. Experimental analysis of an effect of the nutrient type and its concentration on the rheological properties of the baker's yeast suspensions. *Polish J. Chem. Technol.*, 17, 3, 110-117. DOI: 10.515/pjct-2015-0058.
- Musiał M., Karcz J., Cudak M., 2014. Use of CFD metod for analysis of hydrodynamics in a baffled agitated vessel with CD 6 impeller. *Przem. Chem.*, 93, 9, 1599-1603 (in Polish).
- Musiał M., Cudak M., Karcz J., 2015. Gas hold-up for gas-liquid-biophase systems in the bioreactor with CD 6 impeller. *Inż. i Ap. Chem.*, 54, 4, 182-183 (in Polish).
- Ranganathan P., Sivaraman S., 2011. Investigations on hydrodynamics and mass transfer in gas-liquid stirred reactor using computational fluid dynamics. *Chem. Eng. Sci.*, 66, 3108-3124. DOI: 10.1016/j.ces.2011.03.007.
- Rielly C.D., Evans G. M., Davidson J.F., Carpenter K.J., 1992. Effect vessel scale-up on the hydrodynamics of a self-aerating concave blade impeller. *Chem. Eng. Sci.*, 47, 13/14, 3395-3402. DOI: 10.1016/0009-2509(92)85050-L.
- Scargiali F., D'Orazio A., Grisafi F., Brucato A., 2007. Modelling and simulation of gas-liquid hydrodynamics in mechanically stirred tanks. *Chem. Eng. Res. Des.*, 85(A5), 637-646. DOI: 10.1205/cherd06243.
- Sensel M.E., Meyers K.J., Fasano J.B., 1993. Gas dispersion at high aeration rates in low to moderately viscous Newtonian liquids. *Process Mixing: Chem. Biochem. App., Part II, AIChE Symp. Ser.*, 89, 293, 76-81.
- Singh H., Fletcher D. F., Nijdam J. J., 2011. An assessment of different turbulence models for predicting flow in a baffled tank stirred with a Rushton turbine. *Chem. Eng. Sci.*, 66, 5976-5988. DOI: 10.1016/j.ces.2011.08.018.
- Smith J.M., Katsanevakis A.N., 1993. Impeller power demand in mechanically agitated boiling systems. *Chem. Eng. Res. Des.*, 71, Part A, 145-152.
- Van't Riet K., Boom J.M., Smith J.M., 1976. Power consumption impeller coalescence and recirculation in aerated vessels. *Trans. Inst. Chem. Eng.*, 54, 124-131.
- Warmoeskerken M.M.C.G., Smith J.M., 1989. The hollow blade agitator for dispersion and mass transfer. *Chem. Eng. Res. Des.*, 67, 193-198.
- Zhengming G., Yingchen W., Yanmin Z., Litian S., 1991. Study on gas-liquid mass transfer characteristics in an agitated vessel. Part II. The effects of geometric parameters of an agitated tank on the volumetric mass transfer coefficient. *7th European Conference on Mixing, Part II, Brugge, Belgium, 18-20.09.1991*, 315-320.

Received 10 October 2016

Received in revised form 28 June 2017

Accepted 29 July 2017

APPLICATION OF NEW CHEMICAL TEST REACTIONS TO STUDY MASS TRANSFER FROM SHRINKING DROPLETS AND MICROMIXING IN THE ROTOR-STATOR MIXER

Jerzy Bałdyga, Michał Kotowicz*

Warsaw University of Technology, Faculty of Chemical and Process Engineering, ul. Waryńskiego 1, Warsaw, Poland

A pair of fast competitive reactions, neutralization and 2,2-dimethoxypropane (DMP) hydrolysis, has been applied to study mass transfer and micromixing in a T 50 Ultra-Turrax® - IKA rotor-stator device. In experiments the dispersed organic phase containing p-Toluenesulfonic acid (pTsOH) dissolved in diisopropyl ether, whereas the continuous phase was represented by the aqueous solution of sodium hydroxide, 2,2-dimethoxypropane (DMP) and ethanol. During mixing a fast mass transfer of a solute (pTsOH) from organic phase droplets, which were shrinking due to fast dissolution of the organic solvent, was followed by micromixing and chemical reactions in the continuous phase. Measured hydrolysis yields were applied to express effects of mixing on the course of chemical reactions. Modeling was based on application of models describing drop breakup, mass transfer in the liquid-liquid system and micromixing. Combined effects of mass transfer and drop breakage on drop population were expressed using the population balance equations. The model has been used to interpret experimental results, in particular to identify the efficiency of mixing.

Keywords: efficiency of mixing, mass transfer, micromixing, rotor-stator mixer, test reactions

1. INTRODUCTION

Many chemical reactions leading to desirable intermediate and end-products (such as pharmaceutical intermediates and other fine chemicals) are accompanied by side reactions producing undesired byproducts. The creation of byproducts decreases the yield of desired reactions and requires costly product separation. Even when the desired reaction is very fast compared to undesired ones, its rate can be controlled by mass transfer and micro-mixing, and the final yield and selectivity can result then from competition between the desired, mass transfer and micro-mixing controlled chemical reaction and other, slower reactions. Hence, to control product distribution of complex chemical reactions one needs not only to have detailed information on their kinetics and thermodynamics but also understand and interpret the effects of flow, mass transfer and following it micro-mixing on their course.

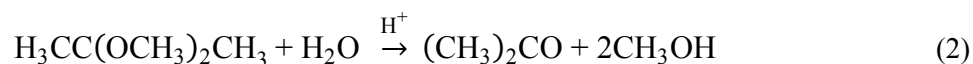
Test chemical reactions are commonly used as molecular probes to investigate mixing processes in both homogeneous and heterogeneous liquid-liquid systems. To employ the set of chemical reactions as test reactions one needs to know reaction schemes, reaction kinetics (at least one reaction must be faster than the mixing rate) and analytic methods to determine product distribution. Reagents and products should be stable and not toxic. Many different systems were proposed either to study micromixing in single-phase systems (Bałdyga and Bourne, 1990; Bałdyga and Bourne, 1999; Bałdyga et al., 1998; Fournier et al., 1996) or to study mass transfer in two-phase liquid-liquid systems (Jasińska et al.,

*Corresponding authors, e-mail: m.kotowicz@ichip.pw.edu.pl

2013b; Jasińska et al., 2016). By choosing a proper one and treating product distribution as the segregation index, one can compare mixing intensity in different systems. One can identify as well the time constant for mixing and mass transfer. Moreover, it is possible to relate the product distribution to such a parameter as the rate of energy dissipation, and obtain as well relations necessary to identify the minimum rate of energy dissipation required for measured product distribution and related mixing efficiency. It has been shown (Jasińska et al., 2013a) that mixing efficiency of rotor-stator mixers for homogeneous systems decreases with increasing rotational speed due to shrinking of reaction zone to the feed inlet and increasing effects of inertial-convective mixing. One can as well compare energetic efficiencies of mass transfer in rotor-stator mixers differing in geometry (Jasińska et al., 2013b). Having experimental data one can validate the phenomenological micromixing and mass transfer models including modeling employing CFD. Validated models can be used to optimize system geometry and process parameters (such as feeding rate and power input). Modeling can be used to increase desired product yield and decrease operational costs. Comprehensive reviews on the application of chemical test reactions to study micromixing and mass transfer in single-phase and two-phase systems can be found in the papers by (Bourne, 2003) and (Jasińska, 2015). In the case of two-phase test systems, different reacting species were dissolved both in the continuous phase and a solvent forming the dispersed phase. The solvent was not soluble in the continuous phase, so the volume fraction of the dispersed phase was constant during the process. However, there are industrial applications where the dispersed phase shrinks during the process. In next section of this paper a new system of test reactions for mixing in liquid-liquid systems is proposed. Contrary to other studies on two-phase systems, the proposed system features fast dissolution of the dispersed phase in the reaction environment.

2. MATERIALS AND METHODS

In this work we consider the case of fast mass transfer of solute from droplets that are shrinking due to fast dissolution of the organic phase, dispersed in the continuous aqueous phase. The dispersed organic phase consisted of a solvent (mixture of diisopropyl ether and ethanol) and *p*-toluenesulfonic acid (pTsOH) being an acidic reactant in the system of test reactions. The continuous phase was represented by the aqueous solution of sodium hydroxide (alkaline reactant), 2,2-dimethoxypropane (DMP) and ethanol.



The first reaction can be treated as instantaneous, the second reaction is catalyzed by hydrogen ions H^+ and can be treated as fast. Equations (1) and (2) represent modification of the set of test reactions proposed earlier (Bałdyga et al., 1998) for homogeneous systems. In the present case ethanol was used to increase solubility of pTsOH in the ether and its volume fraction in the organic phase was equal to 0.25. The continuous, aqueous phase contained 2,2-dimethoxypropane (DMP), NaOH and ethanol. Ethanol was used as well as an internal standard for chromatographic analysis (GC). The volume fraction of organic phase was 0.014 and the molar ratios of base, acid and DMP were respectively 1.05:1.0:1.05. The excess of base was required to maintain stability of DMP before determining the concentrations after performing reactions. In Table 1, initial concentrations of applied species are presented.

Experiments were carried out in the semibatch manner in a T 50 Ultra-Turrax® - IKA rotor-stator mixer placed in a rig shown in Figure 1. The rig was placed under fume hood. The diameters of the stator and the rotor were equal to 45 mm and 36 mm respectively; the gap size was equal to 0.5 mm. The rotor-stator mixers are characterized by high energetic efficiency of dispersion processes due to

focused delivery of energy to the active high-shear regions that occupy a very small fraction of internal mixer space (Jasińska et al., 2013b; Jasińska et al., 2016). Due to pumping capabilities of the rotor-stator mixer, no additional pump was required in the experimental setup. The initial temperature for each experiment was 25°C and the increase of temperature during 2 minute experiment was less than 5 degrees for maximum rotational velocity. The inlet of organic phase was situated before the main inlet to the rotor stator vessel. After an addition of organic phase, the mixer was working for 20 seconds at a chosen rotational speed and during that time the inlet of organic phase was flushed with the reaction mixture. Then samples for chromatographic analysis were collected at the slowest rotational speed to prevent further heating of the mixture. Three or four samples were collected at 10 second intervals to check the mixture uniformity and put into cool (5°C) store. Uniformity was achieved for all samples; the difference in ether concentration in different samples was lower than 5% and increased with the time after which the given sample was collected. Samples were analysed on a HP 6890 gas chromatograph with a 30m column model RTX 1701. The chromatograph was set with the initial oven temperature of 40°C, whereas the speed of temperature growth was 7°C/min and time of analysis was equal to 10.5 min. Injection volume was 0.5 μL and samples during collection were diluted 10 times so the salt concentration was less than 0.4 mmol/dm^3 . The generation of methanol was quantified and experiments were considered as valid only when proper molar balances for DMP and its products were obtained. In Table 2 below, results for cases 1 and 2 (Table 1) are shown.

Table 1. Composition of reaction mixtures and initial concentrations. Two variants of composition were investigated, Case 1 and Case 2

Phase	Substance	Case 1 $c_1, \text{mol}/\text{m}^3$	Case 2 $c_2, \text{mol}/\text{m}^3$
continuous	ethanol	39.5	39.5
	NaOH	4	3.5
	DMP	4	3.5
dispersed	pTsOH	268	234
	ethanol	4120	4120

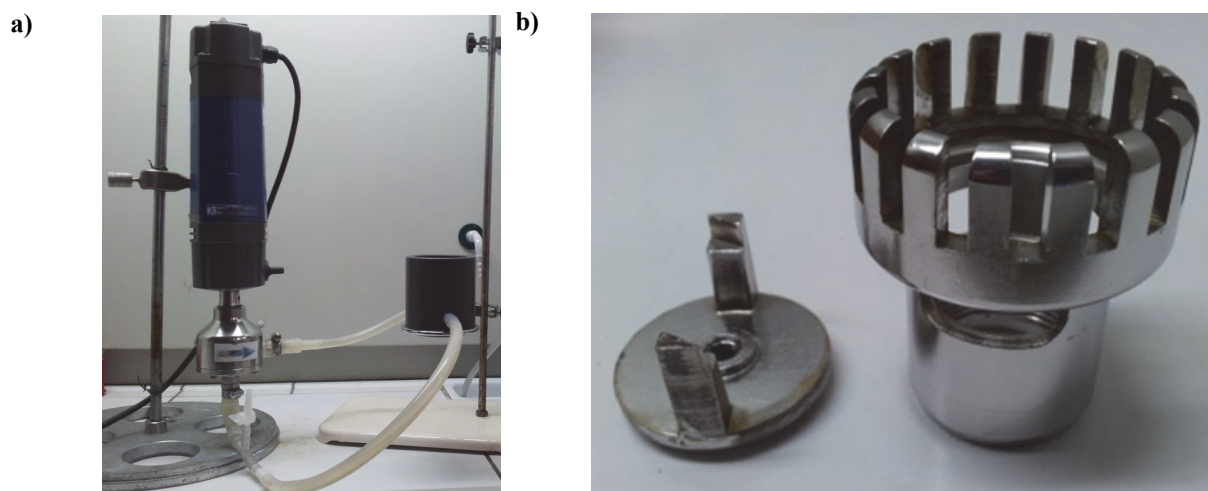


Fig. 1. Experimental setup: (a) experimental rig, (b) rotor and stator

Table 2. Conversion of DMP as a function of rotational speed. The first index denotes the case variant (1 or 2), the second shows values before and after the reaction. For the first case, the estimated error for the value of pH before and after reaction is 0.07 and 0.45, for second corresponding values are 0.11 and 0.25. The value of Δn_{err} is deviation from theoretical ratio of change of moles of methanol to DMP, which equals 2

N [1/min]	Q [ml/s]	t_{in} [s]	$\varepsilon_{N,Q}$ [m ² /s ³]	pH _{1,0}	pH _{1,1}	$\Delta n_{DMP,1}$ [%]	Δn_{err} [%]	pH _{2,0}	pH _{2,1}	$\Delta n_{DMP,2}$ [%]	Δn_{err} [%]
4000	41	4.4	579	10.97	8.68	-41.9	-7.5	10.98	8.33	-42.44	-2.0
5200	65	3.4	1417	10.97	8.86	-41.02	-1.3	10.99	8.47	-41.68	-1.5
6400	94	2.6	2907	10.95	8.52	-40.83	-2.0	11.0	8.43	-40.26	-3.0
7600	108	2.1	4772	10.98	8.75	-36.63	-4.5	11.0	8.28	-35.38	+4.0
8800	119	1.9	7191	11.02	8.73	-34.48	-0.5	10.9	8.47	-33.58	-0.5
10000	132	1.7	10404	11.0	8.37	-29.15	-5.0	10.93	8.49	-20.53	+2.0

The feeding time of organic phase t_{in} was roughly proportional to volumetric flow rate of the main stream Q and is shown in Table 2 below. The rate of energy dissipation was calculated according to Eq. (3). This equation is based on the two-term expression for the power number as suggested by (Baldyga et al. 2007). It includes the effects of the rotor speed and the pumping rate, with constants P_{oz} and K equal to 0.147 and 14.49, respectively (Cheng et al., 2013). The constants are characteristic to dual ultrafine teathed rotor stator mixers.

$$\varepsilon_{N,Q} = \frac{P}{\dot{M}\tau} = \frac{1}{\tau} \left(\frac{P_{oz} N^3 D^5}{Q} + KN^2 D^2 \right) \quad (3)$$

To model the interphase mass transfer from shrinking droplet, two interface concentrations are assumed to be in equilibrium. It is further assumed that the composition of the acid dissolved in the organic phase is constant, at least in large droplets, due to fast droplets shrinking that is faster than molecular diffusion. It is also assumed that the partition coefficient for the system aqueous solution - diisopropyl ether does not depend on concentration, so there exists linear equilibrium relationship between compositions of the solvent within the droplet and at interface, which is represented by constant κ , $\kappa = c'_i / \rho_{org}$. The rate of dissolution of a spherical droplet of diameter d is thus given by (Eq. 4):

$$\frac{d(V_d \rho_{org})}{dt} = -k_L (c'_{si} - c') \pi d^2 \cong -k_L \kappa \rho_{org} \pi d^2 \quad (4)$$

To determine the value of the partition coefficient, solutions of diisopropyl ether, pTsOH and ethanol were prepared with varying concentrations of acid (216 - 267 mol/m³) and volume fraction of ethanol equal to 0.25. Then portions of the organic phase were added drop by drop with a burette to the aqueous solution. The visible two phase system was homogenized with shaking of the flask. The measurement was terminated when no more organic phase could be dissolved in the aqueous phase. Considering that water solubility in ether is negligible, the volume fraction of the organic phase in water was calculated and the constant κ was determined. No significant effect of the concentration of acid in the organic phase on the equilibrium constant was observed and the obtained value of κ was equal to 0.017 ± 0.001 . Experiments were performed in the temperature of 25 °C, both for distilled water and solution of reactants as in the test reaction system. No influence of the composition of continuous phase on the partition coefficient was observed.

2. PROPOSED MODEL

To interpret experimental data, a method combining the model of mass transfer with the micromixing engulfment model is proposed. Firstly, Lagrangian model which governs evolution of single droplet is derived. The dispersed phase is denoted by index d and the continuous phase by index c . $D_{s,c}$ denotes the coefficient of molecular diffusion of the solvent in the continuous phase. Assuming constant density of droplets, the rate of change of its volume is given by Eq. (4). The mass transfer coefficient was calculated according to the model proposed by (Polyanin, 1984):

$$k_L = \frac{D_{s,c}}{d_p} 0.620 \left(\frac{\mu_d}{\mu_c} + 1 \right)^{-0.5} Pe_M^{0.5} \quad (5)$$

where $Pe_M = \frac{d_p^2}{D_{s,c}} \left(\frac{\varepsilon}{\nu} \right)^{0.5}$

Each portion of a droplet containing pTsoH (A) that dissolves in the continuous phase starts to engulf NaOH (B) and DMP (D) rich solution. The growth of A-rich reaction zone for fluid element denoted by i is given by the relation resulting from the self-engulfment model of micromixing (Bałdyga and Bourne, 1989):

$$x_{A,i} = x_{A,i}^0 \frac{e^{Et}}{1 - x_{A,i}^0 (1 - e^{Et})} \quad (6)$$

$$x_{A,i}^0 = \frac{\int_0^{t_i} \frac{dV_d}{dt} dt}{V_B \phi + \int_0^{t_i} \frac{dV_d}{dt} dt} \quad (7)$$

where x_A is the volume fraction of A-rich fluid in the engulfed volume, ϕ is the volume fraction of the organic phase represented by traced droplet at initial state. As the reaction of neutralization is instantaneous, it is controlled by micromixing and the mass balance of acid in the engulfed volume is given by (Eq. 8):

$$\frac{d(V_A c_A)}{dt} = EV_A (1 - x_A) \langle c_A \rangle - V_A E (1 - x_A) \langle c_B \rangle \quad (8)$$

$$\frac{d(V_A c_D)}{dt} = EV_A (1 - x_A) (\langle c_D \rangle - c_D) - V_A k_2 c_D c_A \quad (9)$$

$$\frac{d(V_A c_T)}{dt} = -EV_A (1 - x_A) c_T + V_A k_2 c_D c_A \quad (10)$$

$$\frac{d(V_A c_R)}{dt} = -EV_A (1 - x_A) c_R + V_A E (1 - x_A) \langle c_B \rangle \quad (11)$$

The next three equations (Eqs. 9, 10, 11) represent the balance of DMP, acetone and salt in the engulfed volume. Initial droplet diameter for just dispersed droplets can be calculated from Eq. 12 proposed by (Kolmogorov, 1949):

$$d = \frac{C_x \sigma^{0.6}}{\varepsilon^{0.4} \rho_c^{0.6}} \quad (12)$$

Earlier experiments employing test reactions to study micromixing in rotor stator devices indicated that efficiency of mixing decreases with increasing rotor speed (Jasińska et al., 2013a; Jasińska et al., 2013b) to some asymptotic value. Mixing efficiency was originally defined by (Ottino and Macosko, 1980) to estimate energetic effectiveness of the process of mixing between elongated slabs in laminar flow or in the viscous-convective and viscous-diffusive subranges of turbulence. It characterises the ratio of energy really applied to increase the intermaterial area to the whole energy dissipated during the flow. This definition determines the form of the expression for mixing efficiency. (Jasińska et al., 2013a) extended this definition to account for mixing on the molecular scale. They introduce the ideal, reference process of mixing that was described with the reference model, the engulfment model of micromixing. Prediction of the E-model can be used as a calibration curve, which based on experimentally determined X_S values gives the smallest, “theoretical” values of the rate of energy dissipation necessary to obtain experimental X_S , that can be later compared with the energy really used in experiments. Determination of mixing efficiency enables to correct the mixing ($E = 0.058(\varepsilon/\nu)^{0.5}$) and mass transfer (Eq. 5) parameters.

The influence of efficiency factors on the predicted reaction yield $X_{S,eff}$. $X_S = (N_{D0} - N_D)/N_{D0}$, is fundamental. If they were neglected then conversion would be strongly underestimated and the model would yield conversion of dimetoxyp propane, expressed by the product distribution X_S , of less than 1% in the considered energy dissipation range. The model predictions and the experimental data are presented in Fig. 2.

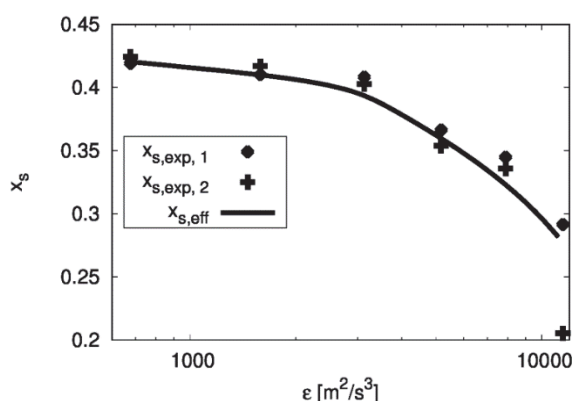


Fig. 2. Predicted $X_{s,eff}$ and observed $X_{s,exp}$ values of the product distribution vs. rate of energy dissipation

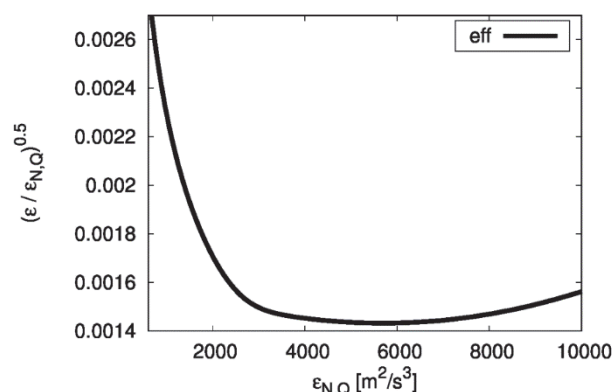


Fig. 3. Mixing efficiency as a function of the rate of energy dissipation

In Fig. 3 the efficiency of mixing is plotted. Figures 2 and 3 show that within the range of energy dissipation between 500–3000 m^2/s^3 , the decomposition yield decreases only slightly, whereas the energetic efficiency of mixing decreases significantly. On the other hand it is interesting that efficiency starts to increase when the rotational speed higher than 6400 rpm is applied. In this range sensitivity of the product distribution to the rotor rotation speed increases. From the viewpoint of energetic efficiency and primary product yield it can be beneficial to carry out a reaction in the rotor stator mixer at full rotor speed.

The Hatta number for the slower reaction, (Eq. 2), is in the range between 0.092 – 0.009 in the considered range of energy dissipation, which indicates that the reaction is running in the regime of slow reaction from viewpoint of diffusional mass transfer. The Damköhler number based on the engulfment time constant (Eq. 13), takes values from the range of 0.123 – 12.288. Characteristic times of micromixing (Eq. 13) (Bałdyga and Bourne, 1999), mass transfer (Eq. 14) and internal mass transfer of acid (Eqs. 15 and 16) indicate that a reaction is controlled by mass transfer of the solvent that determines the rate of drop shrinking. This mechanism persists up to the energy of dissipation of 3000 m^2/s^3 , where the orders of magnitude of micromixing and solvent mass transfer time scales

become equal (Fig. 4). Note that $D_{A,d}$ denotes the coefficient of molecular diffusion of pTsoH in the dispersed phase.

$$\tau_E = 12 \left(\frac{V}{\varepsilon} \right)^{0.5} \quad (13)$$

$$\tau_D = \frac{d}{6k_L} \quad (14)$$

$$\tau_{D,in} = \frac{d}{6k_{L,in}} \quad (15)$$

$$k_{L,in} = \frac{Sh D_{A,d}}{d}, \quad Sh = \frac{2}{3} \pi^2 \quad (16)$$

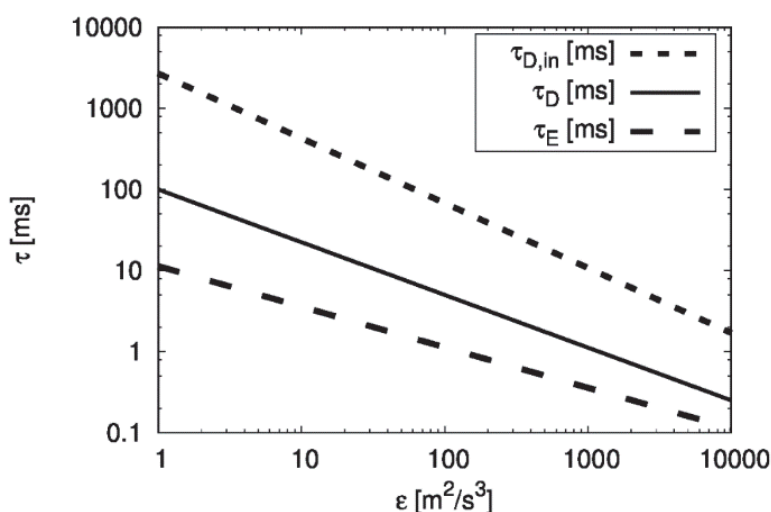


Fig. 4. Time scales for the investigated system as a function of the rate of energy dissipation. The mean residence time for $N = 10000$ rpm is 96 ms and for $N = 4000$ rpm is 310 ms. Time scale for slower reaction is 400 ms

As experiments have shown, the organic phase disappears after the first pass through the mixer. The residence time in the mixing vessel is less than second for all experiments. The model will only predict droplet dissolution correctly if the size of considered droplets will be of the order of micrometers. As shown in the caption of Fig. 5, the multifractal model of drop breakage (Bałdyga and Podgórska, 1998) is applied, as given by Eq. 17, which includes intermittency of turbulence and predicts smaller droplets than Kolmogorov theory of drop breakage (Eq. 12). In fact, Eq. 12 predicts the most probable, not the maximum stable drop size. To calculate the total duration time of the breakage event sequence, a series of droplet breakage events into daughter droplets of equal volume was considered. The initial drop size was assumed to be slightly below the size of the integral length scale for the mixer and the final drop size was defined by the size predicted by multifractal model of turbulence as applied to droplet breakage (Bałdyga and Podgórska, 1998). The equation for maximum stable drop size takes the form:

$$d = C_x^{1.54} L \left(\frac{\sigma}{\rho_c \varepsilon^{2/3} L^{5/3}} \right)^{0.93} \quad (17)$$

The duration of droplet breakage sequence was estimated using the inverse of the breakage frequency for the multifractal model (Eq. 18). Constants required to calculate the upper bound of multifractal exponent and breakage frequency were equal to $C_x = 0.23$, $C_g = 0.0035$. The integral length scale was taken as 0.4 mm based on results of (Jasińska et. al, 2014).

$$\tau_b(d) = \left(C_g \sqrt{\ln\left(\frac{L}{d}\right)} \langle \varepsilon \rangle^{1/3} \int_{\alpha_{min}}^{\alpha_x} \frac{d^{\frac{\alpha+2-3f(\alpha)}{3}}}{L} \right)^{-1} \quad (18)$$

The time of droplet breakage $\tau_c = \sum \tau_b$ (Fig. 5), calculated using the multifractal model of turbulence, is small or comparable to time scales of other phenomena depending on final droplet diameter and shows that residence time of few microseconds in high shear stress region suffices to develop high specific surface for the studied liquid-liquid system. The rates of final breakage events leading to the considered drop size, control in fact the overall breakage time (Fig. 5). As breakage takes place in the high shear region of the mixer, following it shrinking of droplets and micromixing are present in the zone of a smaller rate of energy dissipation behind the screen. This explains why efficiency of micromixing is so small as shown in Fig. 3.

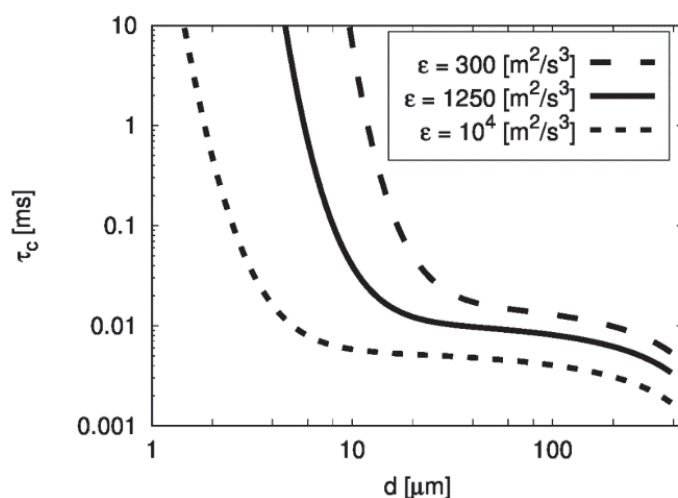


Fig. 5. Time of breakage sequence, $\tau_c = \sum \tau_b$ for a droplet of the initial size equal to 0.39 mm for 3 values of the rate of energy dissipation. Maximum stable droplet sizes d are 8.4, 3.5, 1 μm respectively. This can be compared to droplet size calculated with Kolmogorov theory: 33, 19, 8.2 μm

Having analysed time scales of phenomena identified in the performed experiment, an attempt to simulate evolution of dispersed phase with the population balance model was undertaken. The main reason was to check assumptions on the controlling mechanism for pTsOH transfer to continuous phase at this stage of the process when the droplets are small. Firstly one dimensional model (Eq. 19) including dissolution (Eq. 4) and breakage process kinetics (inverse of Eq. 18) was solved with the direct numerical method. Gauss-Lobatto-Legendre collocation points were used as a type of numerical grid. Advection terms were discretized with differential quadrature rule (Bellman et. al., 1972) derived for 50 GLL points. Integral terms were calculated with Gaussian quadrature rule. Neumann boundary conditions were applied to both ends of the domain (equal to flux at left boundary and zero at right boundary). To cover a broad range of droplet diameters, logarithmic mapping was used for size coordinate. Such nonlinear mapping introduces an error into the numerical method but after analyzing results for the considered cases, the (overestimating) error in conservation of volume of tracked dispersed phase was not higher than 5% of the initial volume. Forward Euler numerical scheme was employed for time discretization and U-shaped parabolic distribution was used as daughter distribution function (Bałdyga and Podgórska, 1998). The evolution of density and moments for various values of the energy dissipation rate can be seen below in Fig. 6. As the solution method calculates density function directly, corresponding moments were calculated from their definitions.

$$\frac{\partial n}{\partial t} + \frac{\partial(nG)}{\partial d_p} = \int_{d_p}^{\infty} g(d') b(d_p / d') n(d') d(d') - g(d_p) n(d_p) \quad (19)$$

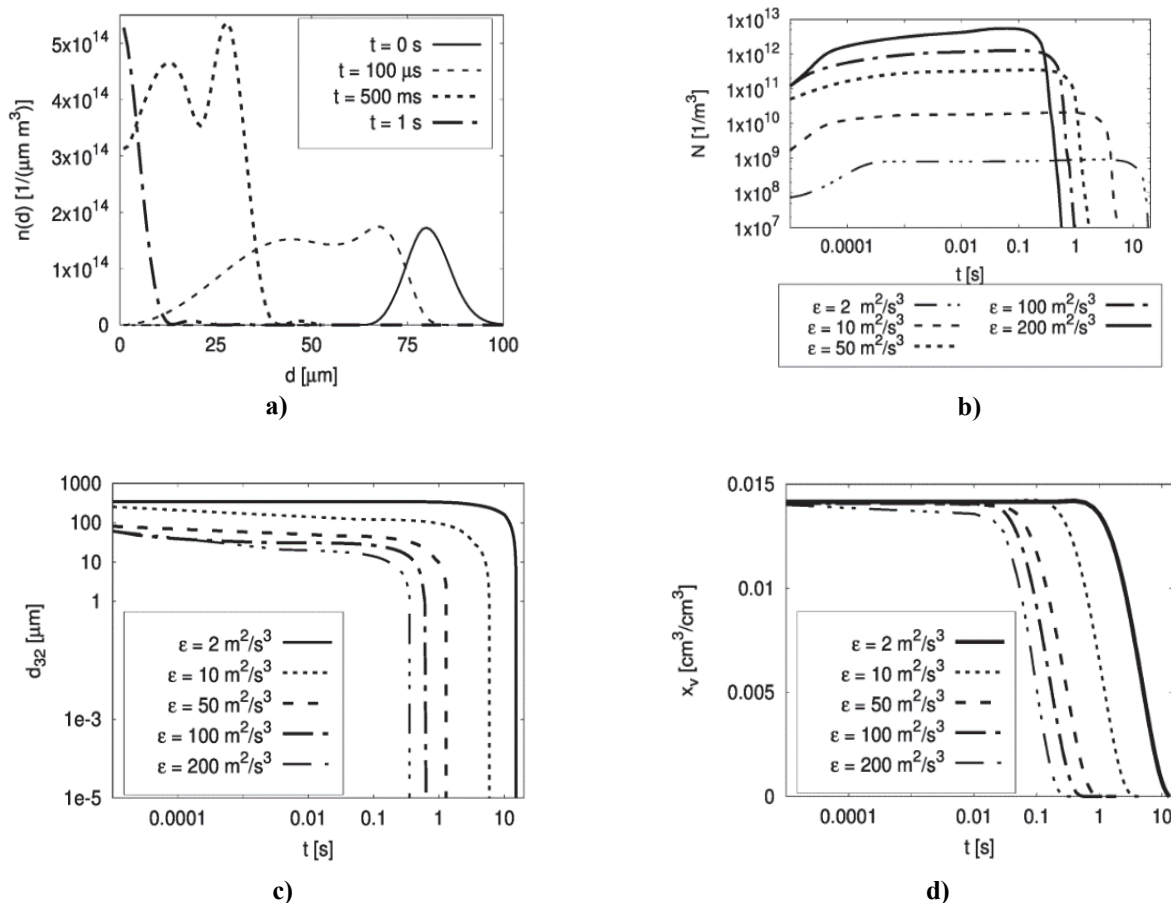


Fig. 6. Prediction of evolution of population of droplets. As initial 1D distribution, the lognormal distribution was assumed with mean 700, 250, 80, 60, 60 μm for subsequent increasing values of rate of energy dissipation and standard deviation equal to 5 μm for each case. (a) number density function $n(d)$ for the rate of energy dissipation of $50 \text{ m}^2/\text{s}^3$, (b) number concentration of droplets N , (c) mean Sauter diameter d_{32} and (d) volume fraction of dispersed phase, x_v

The predictions from simulations are consistent with time scale analysis. During the initial period of the experiment the breakage process dominates, the number of droplets increases rapidly and the amount of dissolved organic phase is negligible. Then drop dissolution process is mostly present and depending on energy dissipation rate it can take from 0.1 to 10 seconds. Figure 6a, where the number density function $n(d)$ is presented, shows that bimodal distribution is formed. This is direct consequence of using the U-shaped daughter distribution function.

To check how the composition of droplets changes during the process, the population balance model was extended by introducing acid concentration as the second state space coordinate. Because the solubility of *p*-toluenesulfonic acid in the organic phase is much lower than in water it can be assumed that except shrinking, only internal mass transfer will be meaningful for overall transfer of acid into the aqueous solution. Using the correlation for Sherwood number presented above (Eq. 16) the expression for acid transfer is given by (Eq. 20):

$$C_R = \frac{dC_A}{dt} = -k_{L,in}c_A \frac{A}{V} = -k_{L,in}c_A \frac{6}{d_p} \quad (20)$$

$$\frac{\partial n}{\partial t} + \frac{\partial(nG)}{\partial d_p} + \frac{\partial(nC_R)}{\partial c_A} = \int_{d_p}^{\infty} g(d')b(d_p/d')n(d',c_A)d(d') - g(d_p)n(d_p,c_A) \quad (21)$$

The two dimensional population balance (Eq. 21), was solved with a similar method as applied for 1D case and following results were obtained (Figs. 7 and 8). For an additional dimension, Neuman boundary conditions were applied in an analogous manner as for 1D problem.

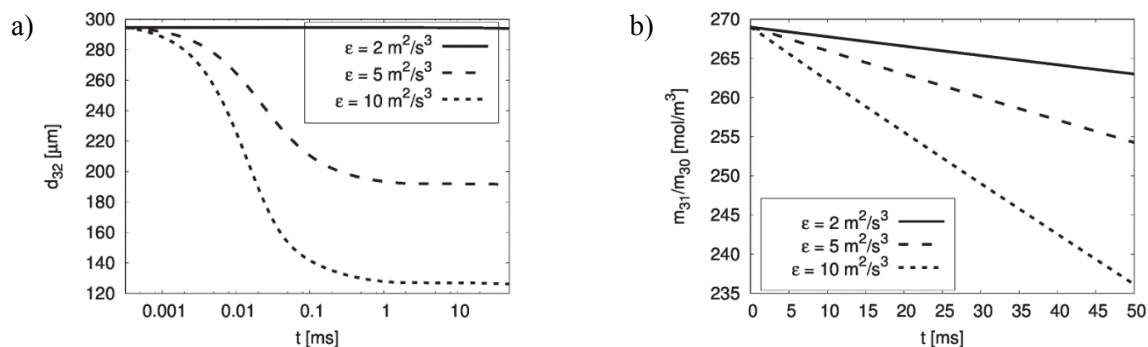


Fig. 7. Results of simulation of 2D population: (a) evolution of the mean Sauter diameter d_{32} and (b) mean concentration of a solute A in population of droplets m_{31}/m_3 . Duration of simulation was 50ms

For the energy dissipation rate equal to $2 \text{ m}^2/\text{s}^3$ the starting drop diameter is nearly equal to that predicted by the breakage model and no further breakage is observed (Fig. 7a). For higher values of the rate of energy dissipation the maximum stable drop size is observed after about $100 \mu\text{s}$ and this time decreases with increasing the rate of energy dissipation. Figure 7b shows some decrease in time of the average solute concentration. Figure 8 explains this effect; it illustrates the evolution in time of the 2D distribution. Clearly, initially there is just a drift of the distribution in the direction of smaller droplets due to breakage without observable effects of pTsoH diffusion. When much smaller droplets are created due to shrinking and breakage, the effects of molecular diffusion become significant. This means that at final stages of droplet life, the assumption that the controlling mechanism for pTsoH transfer to the continuous phase is droplet shrinking, is not fulfilled and both mechanisms of drop shrinking and molecular diffusion are influential.

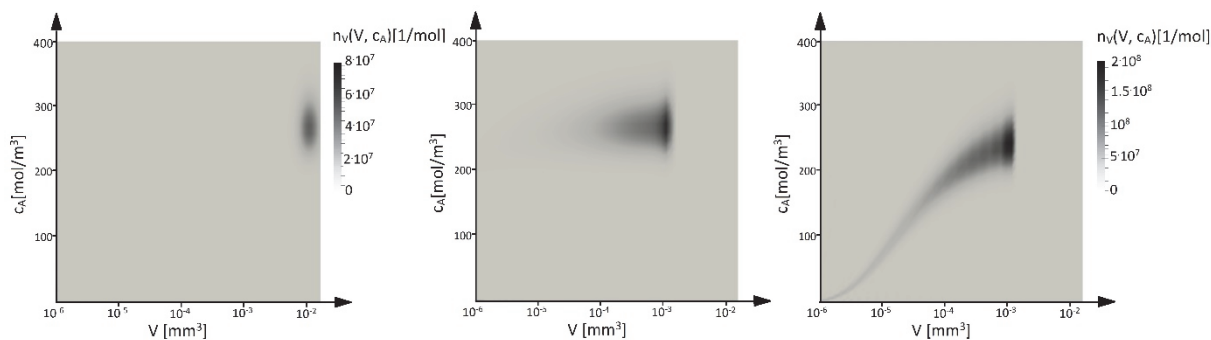


Fig. 8. Evolution of two dimensional volume density function $n_v(V, c_A)$ [1/mol] during simulation for rate of energy dissipation equal to $10 \text{ m}^2/\text{s}^3$. The following pictures present results at the initial moment, after 2ms and 50ms of simulation. Note that the middle and right figures have the same scale. As in 1D case, 2D lognormal distribution with means equal to $300 \mu\text{m}$, $265 \text{ mol}/\text{m}^3$ and standard deviations for size and concentration equal to $5 \mu\text{m}$, $1 \text{ mol}/\text{m}^3$ respectively was used to describe population at the initial period of the process

4. CONCLUSIONS

A new set of competitive test reactions to be applied in a liquid-liquid system was proposed. Simplicity of the reaction scheme as well as a simple and direct method of determination of product distribution makes this new set of test reactions a decent tool for investigation of product yields in mixers of any

type and for any mode of operation. It was proved that this system is suitable for investigating mixing processes in rotor stator devices. The conclusions presented by earlier investigators (Jasińska et al., 2013a; Jasińska et al., 2013b), that mixing efficiency in rotor stator devices for both homogeneous and heterogeneous systems decreases with increasing the rotational rotor speed, were confirmed and mixing efficiency factors were obtained based on experimental data. It has been shown that the engulfment model of micromixing, commonly used to describe homogeneous systems, can be combined with the mass transfer model for liquid-liquid systems and applied to model the evolution of mass transfer in a system with droplet shrinking in the continuous phase.

It should be pointed out that the identified values of the efficiency of mixing (mass transfer and micromixing) depend on the applied reference models, i.e. the engulfment model of micromixing, the mass transfer model by (Polyanin, 1984) and the model for the maximum stable drop size by (Kolmogorov, 1949). These models were chosen because they were verified experimentally by many researchers and can be treated as reliable, at least regarding their form. Although the application of other models is possible, one should always inform which model was used.

Finally, 1D and 2D population balance models were used to simulate the evolution of dispersed phase. Results showed that the assumption about constant acid concentration during droplet dissolution can be too coarse approximation for very small droplets and future work should address that issue.

The authors acknowledge the financial support from Polish National Science Centre (Grant agreement number: DEC-2013/11/B/ST8/00258).

SYMBOLS

b	daughter distribution function
c	concentration, mol/m ³
c'	concentration, kg/m ³
c'_i	interfacial concentration, kg/m ³
$\langle c \rangle$	mean concentration, mol/m ³
C_x	proportionality constant for expression for maximum stable drop size
C_g	proportionality constant for multifractal model
C_R	rate of change of acid concentration, mol/(m ³ · s)
d, d_p	droplet diameter, m
D	rotor diameter, m
$D_{S,C}$	diffusion coefficient of solvent in continuous phase, m ² /s
$D_{A,d}$	diffusion coefficient of pTsoH in dispersed phase, m ² /s
eff	mixing efficiency factor
E	engulfment parameter, 1/s
$f(\alpha)$	multifractal spectrum, according to (Bałdyga and Podgórska, 1998)
g	breakage frequency, 1/s
k_2	kinetic constant of slower reaction, m ³ /(mol · s)
k_L	external mass transfer coefficient, m/s
$k_{L,in}$	internal mass transfer coefficient, m/s
K	constant related to flow term in power expression
L	integral length scale of turbulence, m
m	moment calculated from number density function
\dot{M}	mass flow rate, kg/s
$n(d)$	1D number density function, 1/(μm · m ³)
$n_v(V, c_A)$	2D volume density function, 1/mol

N	rotational rotor speed, s^{-1}
P	power input, W
P_{oz}	power number at zero flow rate
t_{in}	feeding time, s
Q	flow rate, m^3/s
V_A	total volume of organic phase, m^3
V_B	total volume of continuous phase, m^3
V_d	droplet volume, m^3
$X_{s,eff}$	predicted reaction yield
$X_{s,exp}$	experimental reaction yield
x_A	volume fraction of A-rich fluid in micromixing model
α	multifractal exponent
ε	energy dissipation rate, m^2/s^3
$\varepsilon_{N,Q}$	overall energy dissipation rate in rotor-stator device, m^2/s^3
κ	solubility constant of diisopropyl ether in water, partition coefficient
μ_c	dynamic viscosity of continuous phase, $kg/(m \cdot s)$
μ_d	dynamic viscosity of dispersed phase, $kg/(m \cdot s)$
ν	kinematic viscosity of continuous phase, m^2/s
ρ_c	density of continuous phase, kg/m^3
ρ_{org}	density of organic phase, kg/m^3
σ	interfacial tension, N/m
τ	mean residence time in rotor stator, s
τ_b	time scale of drop breakage, s
τ_c	time necessary to break a droplet to its final size, ms
τ_E	micromixing time scale, s
τ_D	mass transfer time scale, s
$\tau_{D,in}$	internal mass transfer time scale, s
ϕ	volume fraction of organic phase represented by single droplet

Subscripts

A	pTsOH
B	NaOH
D	DMP
R	salt
s	solvent
T	acetone

REFERENCES

- Baldyga J., Bourne J.R., 1989. Simplification of micromixing calculations. II. New applications. *The Chem. Eng. J.*, 42, 93-101. DOI: 10.1016/0300-9467(89)85003-8.
- Baldyga J., Bourne J.R., 1990. The effect of mixing on parallel reactions. *Chem. Eng. Sci.*, 45, 907-916. DOI: 10.1016/0009-2509(90)85013-4.
- Baldyga J., Bourne J.R., 1999. *Turbulent mixing and chemical reactions*. Willey, Chichester.
- Baldyga J., Bourne J.B., Walker B., 1998. Non-isothermal micromixing in turbulent liquids: Theory and experiment. *Canadian J. Chem. Eng.*, 76, 641-649. DOI: 10.1002/cjce.5450760336.
- Baldyga J., Kowalski A., Cooke M., Jasińska M., 2007. Investigations of micromixing in a rotor-stator mixer. *Chem. Process Eng.*, 28, 867-877.
- Baldyga J., Podgórska W., 1998. Drop break-up in intermittent turbulence: Maximum stable and transient sizes of drops. *Canadian J. Chem. Eng.*, 76(3), 456-470. DOI: 10.1002/cjce.5450760316.

- Bellman R., Kashef B.G., Casti J., 1972. Differential quadrature: A technique for the rapid solution of nonlinear partial differential equations. *J. Comput. Phys.*, 10, 40-52. DOI: 10.1016/0021-9991(72)90089-7.
- Bourne J.R., 2003. Mixing and the selectivity of chemical reactions. *Org. Proc. Res. Dev.*, 7, 471-508. DOI: 10.1021/op020074q.
- Cheng Q., Xu S., Shi J., Li W., Zhang J., 2013. Pump capacity and power consumption of two commercial in-line high shear mixers. *Ind. Eng. Chem. Res.*, 52, 525-537. DOI: 10.1021/ie3023274.
- Fournier M.C., Falk L., Villermaux J., 1996. A new parallel competing reaction system for assessing micromixing efficiency - Experimental approach. *Chem. Eng. Sci.*, 51, 5053-5064. DOI: 10.1016/0009-2509(96)00270-9.
- Jasińska M., Bałdyga J., Cooke M., Kowalski A., 2013a. Application of test reactions to study micromixing in the rotor-stator mixer (test reactions for rotor-stator mixer). *Appl. Therm. Eng.*, 57, 172-179. DOI: 10.1016/j.applthermaleng.2012.06.036.
- Jasińska M., Bałdyga J., Cooke M., Kowalski A., 2013b. Investigations of mass transfer with chemical reactions in two-phase liquid-liquid systems. *Chem. Eng. Res. Des.*, 91, 2169-2178. DOI: 10.1016/j.cherd.2013.05.010.
- Jasińska M., Bałdyga J., Cooke M., Kowalski A., 2016. Mass transfer and chemical test reactions in the continuous-flow rotor-stator mixer. *Theor. Found. Chem. Eng.*, 50, 901-906. DOI: 10.1134/S0040579516060075.
- Jasińska M., Bałdyga J., Hall S., Pacek A.W., 2014. Dispersion of oil droplets in rotor-stator mixers: Experimental investigations and modeling. *Chem. Eng. Process. Process Intensif.*, 84, 45-53. DOI: 10.1016/j.cep.2014.02.008.
- Jasińska M., 2015. Test reactions to study efficiency of mixing. *Chem. Process Eng.*, 36, 171-208. DOI: 10.1515/cpe-2015-0013.
- Kolmogorov A.N., 1949. Disintegration of drops in turbulent flows. *Dokl. Akad. Nauk SSSR*, 66, 825-828.
- Ottino J.M., Macosko C.W., 1980. An efficiency for batch mixing of viscous fluids. *Chem. Eng. Sci.*, 35, 1454-1457. DOI: 10.1016/0009-2509(80)85142-6.
- Polyanin A.D., 1984. Three-dimensional diffusive boundary-layer problems. *Zhurnal Prikladnoi Mekhaniki i Tekhnicheskoi Fiziki*, 4, 71-81.

Received 12 November 2016

Received in revised form 21 August 2017

Accepted 04 September 2017

OPTIMIZATION OF GEOMETRIC PARAMETERS OF A RIBBON IMPELLER

Czesław Kuncewicz*, Jacek Stelmach

Łódź University of Technology, Faculty of Process and Environmental Engineering, ul. Wólczańska 213, 90-924 Łódź, Poland

Geometric parameters of a ribbon impeller were optimized on the basis of numerical calculations obtained from the solution of our own 3D/2D hybrid model. The optimization was made taking into account mixing power and homogenization time for ribbon impellers with a different number of ribbons and width operating in a laminar motion for Newtonian fluid. Due to minimum mixing energy required to stir a unit volume of liquid the most efficient impeller appeared to be that with one ribbon of width equal to 0.1 to 0.15 of the mixing vessel diameter. Impellers with more than one ribbon needed much higher mixing power but did not increase significantly secondary circulation in the vessel. These impellers increased first of all primary circulation, i.e. they increased only circular motion of liquid in the vessel.

Keywords: mixing, laminar motion, ribbon impellers, optimization

1. INTRODUCTION

Mixing in the liquid phase is very often used in various technological processes, and in many cases efficiency of the whole process depends on mixing intensity. This refers, for example, to fast chemical reactions controlled in the reactor by the rate of mixing in a micro scale. A similar problem arises in the mixing of highly viscous liquids, e.g. during polymerization. In general, for mixing highly viscous liquids: anchor, ribbon or screw impellers are used. The first of these works well in the case when there is a need of a jacketed heat exchange on the mixing reactor wall. The paddle of an anchor operating near the tank wall disrupts thermal boundary layer thus increasing the intensity of heat exchange on its wall. However, this type of impeller produces a very weak radial-axial circulation which usually results in poor mixing of the liquid in the whole volume of the vessel. Ribbon impellers do not have this disadvantage. Structurally they are more difficult to manufacture but due to relative inclination of the rotating ribbon the impeller pumps liquid up or down thereby increasing significantly the radial-axial circulation and as a result decreasing the mixing time. Therefore, this type of impellers is widely applied when you need to mix highly viscous liquids (Delaplace et. al., 2000; Dalaplace et. al., 2006; Kuncewicz, 2012; Robinson and Cleary, 2012).

Due to the extensive use of ribbon impellers in industrial practice they have been the subject of frequent research. Curran (Curran et. al., 2000) studied experimentally the hydrodynamics and circulation time in a reactor with a simple and double helical ribbon impeller in case of yield stress fluids. They revealed the independency of the dimensionless circulation time of the fluid rheology and pumping direction in case of the double helical ribbon. In contrast, the simple ribbon presented high values of dimensionless circulation time for the highest viscosity fluid. Robinson and Cleary (Robinson and Cleary, 2012) have studied the mixing flow within three variants of the helical ribbon impellers,

*Corresponding authors, e-mail: czeslaw.kuncewicz@p.lodz.pl

a single helical ribbon impeller, a double helical ribbon and a single helical ribbon combined with a central screw. They proved that the mixing rate is better while adding an extra ribbon compared to the single ribbon results, while, the addition of a central screw leads to a creation of a low mixing zone surrounding the screw. However, this work did not specify the mixing efficiency for this type of stirrer.

Many similar papers have been written since and they concern the hydrodynamics of the mixer or mixing times or both parameters simultaneously. However, they do not include studies on the circulation times inside the mixer and the relationship between mixing time and circulation time. The presented work complements this gap.

Over the last two decades there has been a growing number of works based on numerical calculations using CFD techniques (Ameur et.al., 2015; Ameur, 2017; Anne-Archard et. al., 2006) or experimental work using modern measurement techniques (Takahashi et al., 2015; Wang et al., 2012).

Another area of interest of ribbon impellers is the food industry. Especially when you should reach concentration of solid phase of more than 50% (Hou, 2016; Zhang, 2014). A high value of secondary circulation in the r-z plane in the mixer even at low rotational speeds of the stirrer effectively mixes the two phases without destroying the solid. So, the helical ribbon impeller was successfully introduced into pretreatment reactors for the purpose of intensified mixing of corn stover with liquid dilute acid solution and hot steam (He et.al., 2014a; He et.al., 2014b) or into bioreactors for enzymatic hydrolysis and fermentation (Liu et al., 2012; Zhang et al., 2010; Zhao et al., 2013). The results showed that the bioconversion yield and pretreatment efficiency was significantly improved. Wu (2012) made a comparison of six types of impellers for mixing high-solids anaerobic digestion systems and found the helical ribbon impeller was the most effective solution.

From the viewpoint of obtaining a homogeneous mixture in the entire volume of the vessel, we often employ two basic concepts: the homogenization time τ_m and circulation time τ_c . Both concepts refer to mixing in the entire tank volume and despite not very precise definition they have been used for a long time. By definition (Stręk, 1981) the time of homogenization τ_m (or mixing time) is the time needed by the system to reach high enough homogeneity required by process conditions. The time of circulation τ_c is the average time which every element of the liquid requires for making one full circulation loop in the radial-axial plane in the vessel. As has been mentioned, both definitions are unclear. Hence, results obtained by different authors who additionally use different measuring techniques can differ appreciably. The values of τ_m and τ_c are directly related to secondary circulation in the tank, i.e. to the volumetric flow rate of liquid V_s [m^3/s] in the r-z plane. The higher the value of V_s , the shorter the time of homogenization τ_m . To practically determine the time of homogenization various measuring techniques are used (see legend to Table 1).

Table 1 shows experimental data available in the literature regarding the time of homogenization τ_m , circulation τ_c and power of mixing in the form of product $\text{Po} \cdot \text{Re} = A$. The values of τ_m and τ_c are given in the form of dimensionless products $N\tau_m$ and $N\tau_c$. Table 1 gives also geometry of the ribbon impeller-vessel system and measuring method which was used to determine the time of homogenization.

Data in Table 1 refer only to ribbon impellers because according to many authors (Bakker and Gates, 1995; Coyle et al., 1970; Rieger et al., 1986; Shiue and Wong, 1984) this type of impeller is most suitable for mixing liquids with high viscosity.

It can be easily seen from Table 1 that mixing times are always several times greater than the circulation times (Carreau et al., 1976; Guerin et al., 1984; Takahashi et al., 1989; Takahashi et al., 1994). Therefore, an attempt can be made to find a relationship between the values of τ_m and τ_c for the same type of impeller irrespective of its geometric parameters. In other words, it is possible to determine the number of full circulation loops which should be made by every element of liquid in the vessel to make the liquid obtain an appropriate degree of homogeneity. Figure 1 shows selected data

from Table 1 concerning the values of τ_m and τ_c for ribbon impellers with different geometric parameters.

Table 1. The time of homogenization and circulation for ribbon impellers available in the literature

Authors	$d(m)$	D/d	w/d	p/d	H/d	N_R	A	$N\tau_m$	$N\tau_c$
Carreau et al. (1976)	0.130	1.110	0.097	0.719	1.11	2	355.0	45 ¹⁾	13.2 ^{a)}
	0.130	1.110	0.097	1.048	1.11	2	234.0	51 ¹⁾	13.1 ^{a)}
	0.130	1.110	0.195	0.707	1.11	2	314.0	25 ¹⁾	7.1 ^{a)}
Ulbrecht and Carreau (1985)	0.105	1.370	0.121	0.848	1.37	2	199.0	55 ¹⁾	15 ^{a)}
	0.130	1.110	0.097	0.695	1.11	1	160.0	61.0 ¹⁾	21.8 ^{a)}
	0.222	1.110	0.099	0.690	1.12	2	-	-	-
Coyle et al. (1970)	0.432	1.059	0.083	0.500	1.06	1	-	63.0 ^{a)}	20.0 ^{a)}
Gelus (1979)	-	1.111	0.111	1.000	1.00	2	265	100 ⁸⁾	9.5 ^{b)}
	-	1.111	0.111	1.000	1.00	2	265	1301 ^{a)}	12 ^{a)}
Guerin et al. (1984)	0.130	1.108	0.100	0.720	1.11	2	-	45.0 ¹⁾	12.9 ^{a)}
	0.130	1.108	0.100	1.050	1.11	2	-	49.0 ¹⁾	12.3 ^{a)}
	0.130	1.108	0.200	0.710	1.11	2	-	22.0 ¹⁾	11.0 ^{a)}
	0.130	1.108	0.100	0.700	1.11	1	-	53.0 ¹⁾	17.7 ^{a)}
	0.220	1.127	0.100	0.700	1.11	2	-	45.0 ¹⁾	17.3 ^{a)}
Nagata et al. (1956)	0.094	1.064	0.117	0.745	1.06	1	250.0	33.0 ¹⁾	11.0 ^{a)}
	0.094	1.064	0.117	1.112	1.06	1	192.0	33.0 ¹⁾	11.7 ^{a)}
	0.191	1.053	0.105	1.000	1.05	2	330.0	33.0 ¹⁾	-
	0.285	1.053	0.105	1.000	1.01	2	302.0	33.0 ¹⁾	12.7 ^{a)}
Soliman (1985)	0.602	1.053	0.100	1.000	1.01	2	315	49.0 ¹⁾	12.8 ^{c)}
Takahashi et al. (1982, 1988)	0.096	1.040	0.104	0.937	1.04	1	-	∞ ⁶⁾	-
	0.088	1.138	0.114	1.025	1.14	1	-	∞ ⁶⁾	-
	0.082	1.222	0.122	1.101	1.22	1	-	∞ ⁶⁾	-
	0.096	1.040	0.104	0.937	1.04	2	-	239.0 ⁶⁾	8.2 ^{a)}
	0.089	1.126	0.113	1.015	1.13	2	-	53.8 ⁶⁾	10.0 ^{a)}
	0.083	1.209	0.121	1.089	1.21	2	-	∞ ⁶⁾	11.3 ^{a)}
	0.090	1.110	0.111	0.665	1.11	2	-	56.4 ⁶⁾	14.7 ^{a)}
	0.090	1.115	0.111	0.502	1.11	2	-	68.5 ⁶⁾	15.4 ^{a)}
	0.089	1.126	0.113	1.351	1.13	2	-	245 ⁶⁾	9.9 ^{a)}
	0.088	1.136	0.114	2.045	1.14	2	-	∞ ⁶⁾	9.6 ^{a)}
	0.090	1.115	0.084	1.004	1.11	2	-	106.0 ⁶⁾	10.5 ^{a)}
	0.090	1.114	0.140	1.003	1.11	2	-	42.3 ⁶⁾	7.2 ^{a)}
	0.090	1.109	0.169	0.999	1.11	2	-	33.0 ⁶⁾	5.8 ^{a)}
0.091	1.098	0.220	0.989	1.10	2	-	56.2 ⁶⁾	7.6 ^{a)}	
Takahashi et al., (1988, 1989)	0.122	1.049	0.106	0.959	1.05	2	351.1	239.0 ⁶⁾	8.7 ^{a)}
	0.112	1.143	0.117	1.104	1.14	2	290.6	53.8 ⁶⁾	9.2 ^{a)}
	0.103	1.243	0.127	1.188	1.24	2	275.3	∞ ⁶⁾	12.0 ^{a)}
	0.113	1.133	0.116	0.728	1.13	2	356.6	56.4 ⁶⁾	12.0 ^{a)}
	0.115	1.113	0.114	0.503	1.11	2	425.1	68.5 ⁶⁾	18.2 ^{a)}
	0.117	1.094	0.167	1.020	1.09	2	339.4	33.0 ⁶⁾	9.5 ^{a)}
	0.116	1.103	0.224	1.009	1.10	2	372.4	56.2 ⁶⁾	8.8 ^{a)}
Takahashi et al. (1994)	0.117	1.094	1.167	1.020	1.09	2	339.4	38.4 ¹⁾	8.4 ^{a)}

Measuring method of homogenization time - 1) colorimetric method combined with visual observation, 2) colorimetric method combined with photoelectric measurements, 3) colorimetric method with video recording, 4) addition of a colored tracer with visual observation, 5) chemical method, 6) method with the use of liquid crystals (dependence of the color of liquid crystals on temperature), 7) method with the use of fluorescence tracers, 8) conductometric method

Measurement of circulation time - a) visualization of the trajectory of suspended particles, b) conductometric method, c) calculated on the basis of measured axial velocities, d) thermal method

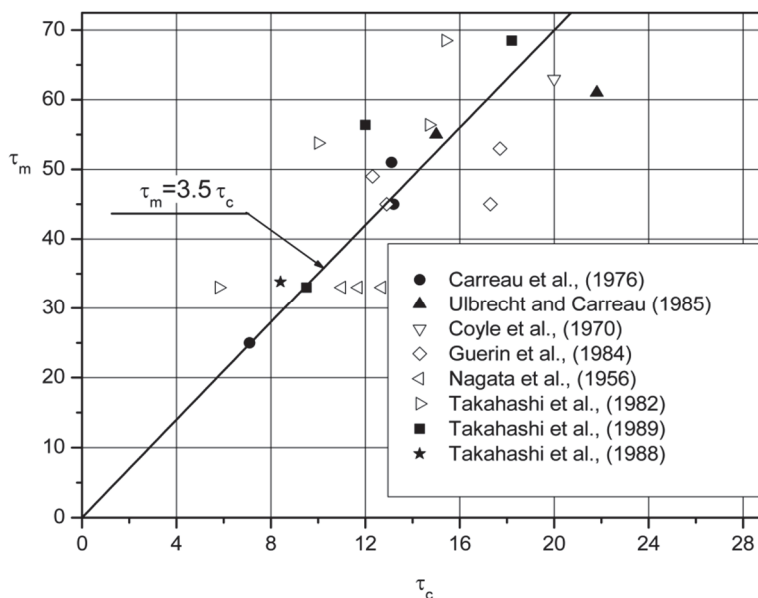


Fig. 1. Dependence of homogenization time on circulation time for ribbon impellers

The scattering of experimental points observed in Fig. 1 is relatively large and is mainly due to different measuring techniques used to determine times τ_m and τ_c and different geometries of the impeller-vessel system. As follows from Fig. 1, the values of τ_m and τ_c are interrelated, but it is difficult to find a precise functional relation between the two variables. It was therefore decided to apply the simplest linear relation (1) which indicates that the liquid contained in the tank can be considered well mixed if each element of the liquid performs 3 or 4 circulation loops in the vessel on average.

$$\tau_m = 3.5 \cdot \tau_c \pm 16.2\% \quad (1)$$

The time average of circulation τ_c can be determined from the secondary circulation V_s and volume of the stirred liquid V .

$$\tau_c = \frac{V_s}{V} \quad (2)$$

As follows from Table 1, in some studies (Takahashi et al., 1982; Takahashi et al., 1989) the values of τ_m are several times higher than similar values quoted by other authors. In certain cases $\tau_m \rightarrow \infty$ which means that in the tank small zones with poorer mixing were observed and in this case only a subjective assessment of the experimenter decided the value of τ_m . Therefore, not all data contained in Table 1 have been taken into account in Fig. 1.

In addition to experimental methods used in studies on the hydrodynamics of mixing vessels in a laminar motion, for decades CFD methods have been increasingly applied. They are used to determine the distribution of all hydrodynamic values in the entire volume of the mixing vessel. Noteworthy are the early studies of Thiele (1972) and Ohta et al. (1985) regarding solutions in the 2D space, first solutions of full models in the 3D space proposed by Harvey et al. (1995) and Kaminoyama et al. (1999) and others, or the 3D/2D hybrid model developed by Kuncewicz and Pietrzykowski (2010). The idea of the last model was that a full 3D model was solved in the impeller region and its vicinity, while in the other parts of the vessel a much simpler 2D model was solved. In this way the time needed for model solution was shortened from 7 to 10 times without compromising accuracy of the results.

In our previous work (Kuncewicz et al., 2013) using solutions of a 3D/2D hybrid model we found that for a ribbon impeller with one ribbon its optimal parameters referring to mixing time and mixing power are geometric invariants $d/D = 0.92$ and $p/d = 1$.

In this study, using the same 3D/2D model we decided to investigate the effect of two other parameters of the ribbon impeller, i.e. the number of ribbons N_R and their widths on the time of homogenization and mixing power and to determine two other optimal parameters of ribbon impellers.

2. EXPERIMENTAL

In the experimental part the correctness of the solution of a 3D/2D hybrid model for ribbon impellers equipped with more than one ribbon (Fig. 2) or impellers with reduced ribbon width (Fig. 3) was verified. Figures 2a and 3a show a comparison of model distributions of peripheral velocities u_ϕ^* (solid lines) and axial velocities u_z^* with their experimental values (points). The experimental values were obtained using a Dantec Laser Doppler Anemometer (LDA). The method of calculating mean velocity values u_z , u_ϕ is given in our previous work (Kuncewicz and Pietrzykowski, 2010).

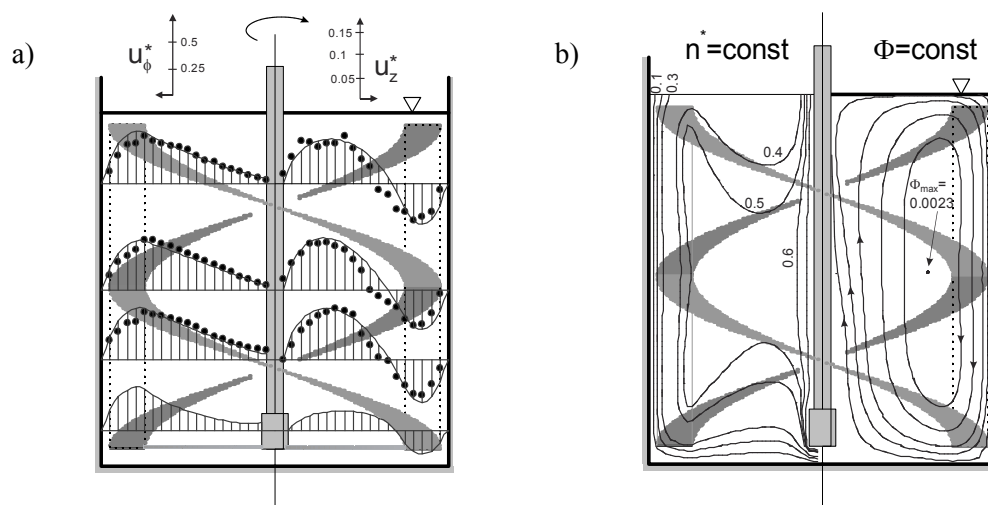


Fig. 2. Model verification (a) and liquid circulation in the tank (b) for $Re = 10$, $d/D = 0.92$, $w/D = 0.1$, $N_R = 2$

As follows from the analysis of Figs. 2a and b figures, good agreement of both compared values was obtained which indirectly proves the correctness of the model solutions. The highest peripheral velocities were always observed in the case of impeller region, while the greatest axial components occurred not only in the region where liquid was pumped to the bottom of the tank but also in the middle of the tank where the same stream was returning to the liquid level. Comparing results shown in Figs. 2 and 3 it should be noted that for the impeller with two ribbons there was a more than a twofold increase of peripheral circulation V_p associated with the impeller rotation. Secondary circulation V_s , i.e. circulation in the r-z plane also increased. However, that increase was much smaller and amounted to only about 30%. This is due to a maximum value of stream function Φ_{max} for both compared impellers. Hence, in this case there was an uneven growth of primary and secondary circulation in the tank and it could be concluded that the increase of the total active surface of the impeller caused first of all an increase of peripheral velocities in the tank. It should also be taken into account that the comparison referred to the impellers with different ribbon widths and their numbers.

Liquid circulation inside the tank is shown in Figs. 2b and 3b. In the middle part of the tank liquid circulates at approximately constant relative peripheral frequency $n = (0.5 - 0.6) \cdot N$ in the case of a double-ribbon impeller and at frequency $n = (0.35 - 0.45) \cdot N$ in the impeller with one ribbon. In both cases peripheral velocities were always two or three times higher than axial velocities. In the impeller region, due to the proximity of the tank wall, relative peripheral frequencies n^* decrease, although

taking into account large radius along which the liquid moves in this region its absolute peripheral velocity is the highest.

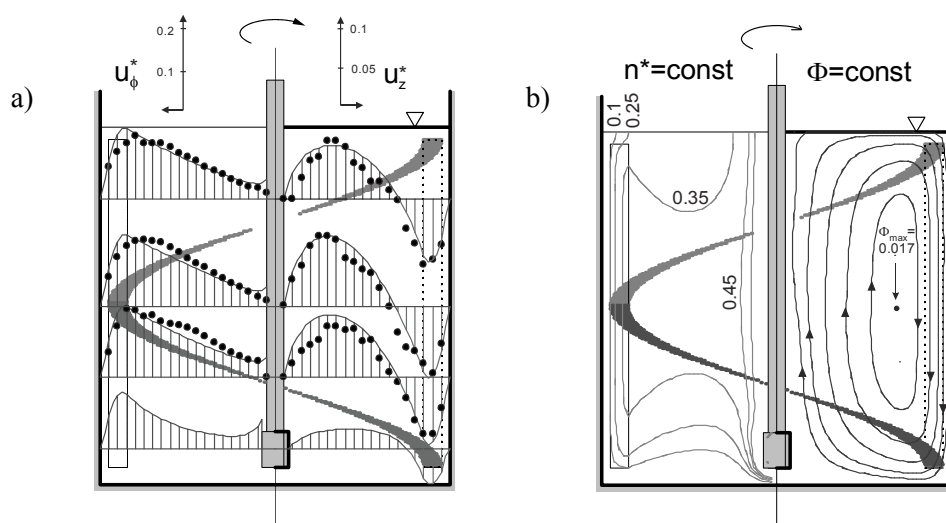


Fig. 3. Model verification (a) and liquid circulation in the tank (b) for $Re = 10$, $d/D = 0.92$, $p/d = 1$, $w/D = 0.075$, $N_R = 1$

3. MODEL CALCULATIONS

In laminar motion the flow of liquid in the whole tank depends largely on flow in the impeller region. Figure 4 shows model distributions of dimensionless velocity u_ϕ^* for impellers with variable ribbon widths w and their number N_R , while Fig. 5 presents similar distributions for dimensionless axial velocity u_z^* . As follows from Fig. 4 an increase in the ribbon width and their number causes always an increased peripheral circulation in the impeller region. A fourfold increase in the ribbon width ($w/D = 0.05 - 0.2$) increases almost twice the maximum liquid velocity u_ϕ^* in the impeller region. Similarly, the number of ribbons has also great impact. A three-ribbon impeller produces primary circulation which is 60% higher than that of a single-ribbon impeller. In general, it can be concluded that the greater the impeller surface the bigger the liquid stream flowing in the impeller region in the peripheral direction.

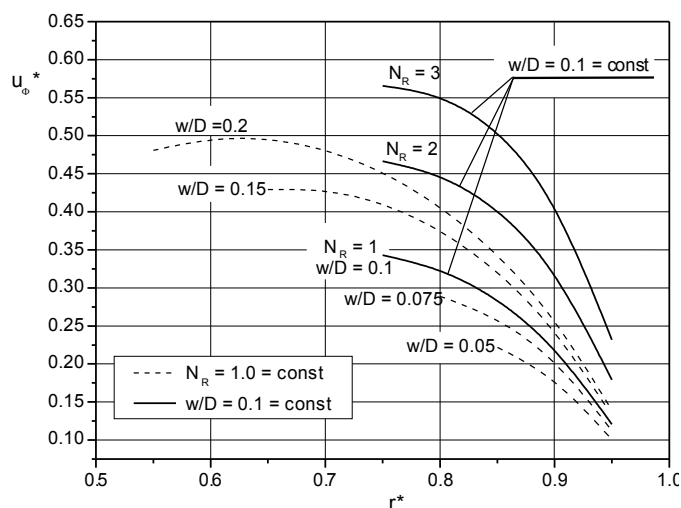


Fig. 4. Liquid flow in the impeller region in peripheral direction for $Re = 10$, $d/D = 0.92$, $p/d = 1$

On the other hand, an ambiguous impact of the width and number of ribbons on dimensionless axial velocities u_z^* in the impeller region can be observed when analysing the distributions $u_z^* = f(r^*)$ in Fig. 5. Axial velocities u_z^* increase with an increase of the ribbon width only to the value of $w/D \cong 0.15$. The ribbon of width $w/D = 0.2$ has significantly lower axial velocity (the assumed direction of impeller rotations forced liquid flow down the tank, so axial velocities had sign “-”). Thus, excessive increase of the ribbon surface area is not advisable in this case. A similar conclusion can be drawn when analysing distributions $u_z^* = f(r^*)$ for impellers with different number of ribbons N_R . In this case the increase of impeller area by adding a second and third ribbon, for the same ribbon width $w/D = 0.1$, causes even a decrease of axial velocities in the impeller region. This effect is similar to that observed in the case of the impact of ribbon width on distributions $u_z^* = f(r^*)$ for $w/D > 0.15$. Probably too large active surface area of the ribbons in the mixer causes disturbances in the creation of regular loops inside the vessel.

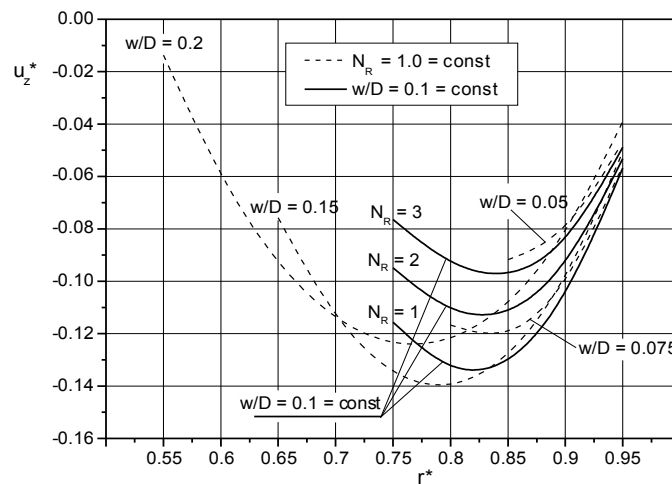


Fig. 5. Liquid flow in the impeller region in axial direction for $Re = 10$, $d/D = 0.92$, $p/d = 1$

Peripheral and axial velocities in the impeller region are only part of the whole peripheral and axial circulation in the tank. Therefore having the distributions of all three velocity components in the entire tank (Figs. 2 and 3) one can determine the value of primary circulation V_p and secondary circulation V_s i.e. the volumetric flow rate of liquid towards the peripheral and radial-axial direction in the whole tank. The values of V_p and V_s are usually given in the form of dimensionless numbers of primary and secondary circulation K_p and K_s , respectively, defined by Eq. (3).

$$K_p = \frac{V_p}{nd^3}; \quad K_s = \frac{V_s}{Nd^3} \quad (3)$$

On the basis of peripheral velocity distributions near the wall and bottom of the vessel obtained from 3D/2D model solutions it was also possible to determine the mixing power P and then to calculate the dimensionless power number Po and product $Po \cdot Re = A$. The value of this product for laminar mixing and for a specified impeller is a constant value independent of the Reynolds number. Functional relations $K_p, K_s, A = f(N_R, w/D)$ obtained from model solutions are shown in Fig. 6.

The width of ribbons in a moderate way affects the power of mixing. A fourfold increase of the ribbon width caused only about 25% increase in the mixing power (Fig. 6b). In contrast, the mixing power depended strongly on the number of ribbons. Addition of the second and third ribbon to the single-ribbon impeller resulted in an increase of the mixing power by 58% and 102%, respectively. In both cases the growth of mixing power can be explained by increase in friction resistance that is dominant resistance in the laminar motion. Figure 6a illustrates the influence of the two analysed parameters on

the total primary and secondary circulation in the mixer in form of the dimensionless value of K_p and K_s .

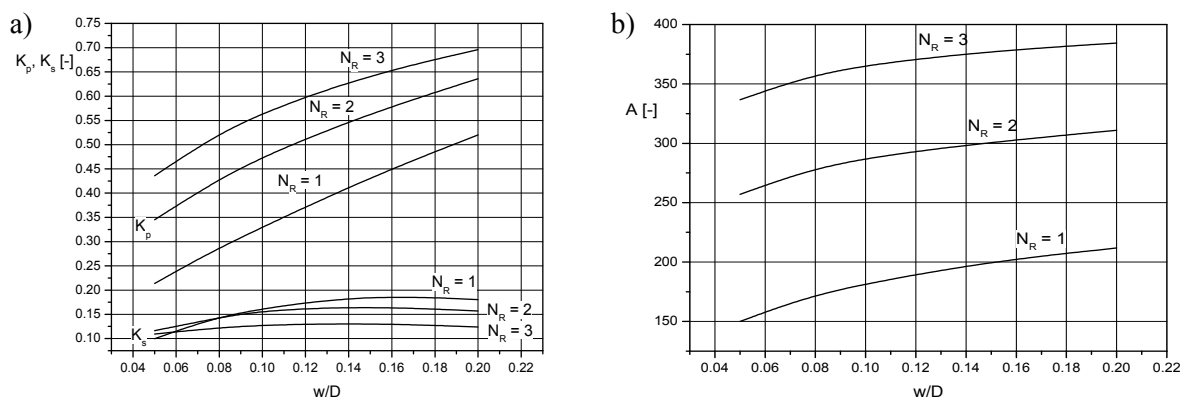


Fig. 6. Primary and secondary circulation in the vessel (a) and the mixing power (b) for $Re = 10, d/D = 0.92, p/d = 1.0$

As follows from analysis of Fig. 6a for ribbon width $w/D = 0.1$, addition of the second and third ribbon caused an increase of the primary circulation K_p by 44% and 71%, respectively, while the secondary circulation K_s remained virtually unchanged and for $N_R = 3$ it was even decreased. Hence, the addition of second and third ribbon resulted only in an increase of peripheral circulation which has no effect on circulation time τ_c , and consequently on mixing time τ_m . The above presented results of mathematical modelling show that additional energy demand needed to drive the second and third ribbon is completely ineffective.

To demonstrate more clearly that addition of the second and third ribbon is pointless one should analyse Table 2 which presents changes in the K_p/K_s ratio for a different number of ribbons.

Table 2. The effect of the number of ribbons N_R on primary and secondary circulation in the vessel for $w/d = 0.1$

N_R	K_p	K_s	A	K_p/K_s
1	0.330	0.162	182.0	2.03
2	0.476	0.159	288.2	2.99
3	0.567	0.128	366.0	4.42

To fully optimize the ribbon impellers the assumed optimization criterion was the value of U_E defined as the amount of energy needed to attain an appropriate mixing degree of liquid unit volume, i.e.

$$U_E = \frac{E}{V} = \frac{P \cdot \tau_m}{V} \quad \left[\frac{\text{J}}{\text{m}^3} \right] \quad (4)$$

This method is applied universally and can also be observed in other unit operations of chemical engineering (Obraniak and Gluba, 2012). The value of U_E can be determined as a unit mixing energy. Taking into account Eqs. (1) to (3) and Eq. (5) which determine mixing power in the laminar regime

$$P = A \cdot N^2 d^3 \eta \quad [\text{W}] \quad (5)$$

after simple transformations Eq. (4) will assume the following form

$$U_E = \frac{3.5 \cdot AN\eta}{K_s} \quad \left[\frac{\text{J}}{\text{m}^3} \right] \quad (6)$$

The smaller U_E the more efficient the impeller. It follows from Eq. (6) that with an increase of the mixing power (constant A from Fig. 6b) and decrease of secondary circulation (K_s), the value of unit mixing energy U_E will increase, i.e. mixing efficiency is lower. Such a tendency of changes is largely self-evident. Equation (6) also indicates that the viscosity of the liquid and the impeller rotation have negative impact on the efficiency of the mixing. From the phenomenological point of view the tendency of changes is most understandable. It should be noted that, as follows from Eqs. (3) and (5), rotation frequency of the impeller causes a faster increase of mixing power P than the increase of secondary circulation V_s in the vessel ($P \propto N^2$ and $V_s \propto N$). Therefore the value of N is in the numerator and not in the denominator of Eq. (6). A dimensional form of Eq. (6) can be transformed to its dimensionless form U_E^*

$$U_E^* = \frac{U_E}{n\eta} = \frac{3.5 \cdot A}{K_s} \quad [-] \quad (7)$$

Owing to this the values of U_E^* can be directly compared for ribbon impellers with different geometric parameters. A comparison is presented in Fig. 7.

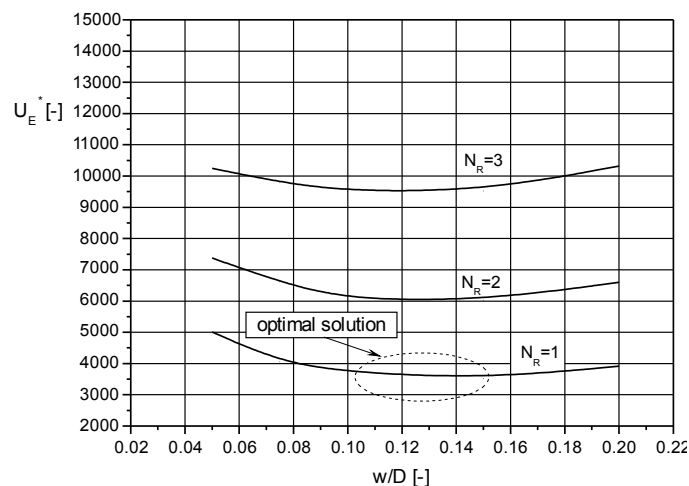


Fig. 7. Dimensionless unit mixing energy for ribbon impellers at $Re = 10$, $p/d = 1.0$ and $d/D = 0.92$

As can be seen from Fig. 7 the smallest U_E^* occurs for a single-ribbon impeller with ribbon width $w/D = 0.10$ to 0.15 . Hence, from solutions of the 3D/2D model it follows that if the main purpose of mixing is to obtain a homogeneous mixture, from the economic point of view the most optimal ribbon impeller is that with the geometric parameters: $d/D = 0.92$, $p/d = 1.0$, $N_R = 1$ and $w/D = 0.10$ to 0.15 . For other purposes than homogenization (e.g. jacketed heat exchange) ribbon impellers with different geometric parameters should be used.

4. CONCLUSIONS

- The hybrid 3D/2D model developed in earlier work is also valid for ribbon impellers which have more than one ribbon.
- An increase of the ribbon width has a moderate effect on the growth of mixing power and secondary circulation in the tank, and for $w/D > 0.15$ even a decrease in the value of V_s occurs.
- A bigger number of ribbons in the tank results only in a significant increase of mixing power and growth of peripheral circulation in the tank. This means that the addition of the second and third ribbon is unprofitable.

- If the primary purpose of mixing is to achieve short mixing times τ_m , from the economic point of view an optimal ribbon impeller operating in laminar regime is the impeller with the following parameters: $d/D = 0.92$, $p/d = 1.0$, $N_R = 1$ and $w/D = 0.10 - 0.15$.

The research was carried out within grant no. 501/10-34-1-7015

SYMBOLS

A	constant = $Po \cdot Re$, [-]
d, D	ribbon and tank diameter, respectively [m]
E	unit mixing energy, [W/m^3]
H	liquid height in the tank, [m]
K_p, K_s	dimensionless number of primary and secondary circulation, respectively, [-]
N, n	frequency rotation of impeller and liquid, respectively, [rev/s]
N_R	number of ribbons, [-]
n^*	dimensionless frequency rotation of liquid = n/N , [-]
P	mixing power, [W]
p	ribbon pitch, [m]
R	tank radius, [m]
r^*	dimensionless radius = r/R
U_E	energy needed to achieve the appropriate mixing degree of 1 m^3 of liquid, [J/m^3]
U_E^*	dimensionless form of U_E according of Eq. (7), [-]
u_ϕ, u_z	tangential and axial velocity, respectively, [m/s]
u_ϕ^*, u_z^*	dimensionless tangential and axial velocity, respectively, $u_\phi (u_z)/(\pi DN)$, [-]
w	ribbon width, [m]
V	volume of liquid, [m^3]
V_p, V_s	primary and secondary volumetric flow rate, [m^3/s]
τ_m, τ_c	mixing and circulation time, respectively, [s]
Φ	stream function, [-]
Po	power number = $P/(N^3 d^5 \rho)$
Re	Reynolds number = $Nd^2 \rho/\eta$

REFERENCES

- Ameur, H., Kamla, Y., Sahel, D., 2017. Performance of helical screw impellers for mixing of viscous liquids in cylindrical reactors. *Chemistry Select*, 2, 1891-1894. DOI: 10.1002/slct.201602072.
- Ameur, H., 2015. Energy efficiency of different impellers in stirred tank reactors. *Energy*, 93, 1980-1988. DOI: 10.1016/j.energy.2015.10.084.
- Anne-Archard D., Marouche M., Boisson H.C., 2006. Hydrodynamics and Metzner–Otto correlation in stirred vessels for yield stress fluids. *Chem. Eng. J.*, 125, 15–24. DOI: 10.1016/j.cej.2006.08.002.
- Bakker A., Gates L.E., 1995. Properly choose mechanical agitators for viscous liquids. *Chem. Eng. Progress*, 91, 25-34.
- Carreau P.J., Patterson I., Yap C.Y., 1976. Mixing of viscoelastic fluids with helical-ribbon agitators - I. Mixing time and flow patterns. *Can. J. Chem. Eng.*, 54, 135-142. DOI: 10.1002/cjce.5450540303.
- Coyle C.K., Hirschland H.E., Michel B.J., Oldshue J.Y., 1970. Mixing in viscous liquids. *AIChE J.*, 16, 903-906. DOI: 10.1002/aic.690160608.
- Curran S.J., Hayes R.E., Afacan A., Williams M., Tanguy P., 2000. Experimental mixing of a yield stress fluid in a laminar stirred tank. *Ind. Eng. Chem. Research*, 39, 195–202. DOI: 10.1021/ie990468e.

- Delaplace G., Leuliet J.C., Relandeau V., 2000. Circulation and mixing times for helical ribbon impellers. Review and experiments. *Exp. Fluids*, 28, 170-182. DOI: 10.1007/s003480050.
- Delaplace G., Guerin R., Leuliet J.C., Chhabra R.P., 2006. An analytical model for the prediction of power consumption for shear-thinning fluids with helical ribbon and helical screw ribbon impellers. *Chem. Eng. Sci.*, 61, 3250–3259. DOI: 10.1016/j.ces.2005.11.069.
- Gelus M., Le Cardinal G., Germain E., 1979. Choix d'un agitateur lorsque la viscosité varie de 1 centipoise à 2000. *Entropie*, 88, 54-59.
- Guerin P., Carreau P.J., Patterson W.I., Paris J., 1984. Characterization of helical impellers by circulation times. *Can. J. Chem. Eng.*, 62, 301-309. DOI: 10.1002/cjce.5450620302.
- Harvey A.D., Lee C.K., Rogers S.E., 1995. Steady-state modeling and experimental measurements of a baffled impeller stirred tank. *AIChE J.*, 41, 2177-2186. DOI: 10.1002/aic.690411002.
- He Y., Zhang L., Zhang J., Bao J., 2014a. Helically agitated mixing in dry dilute acid pretreatment enhances the bioconversion of corn stover into ethanol. *Biotechnol. Biofuels*, 7, 1. DOI: 10.1186/1754-6834-7-1.
- He Y., Zhang J. J., Bao J., 2014b. Dry dilute acid pretreatment by co-currently feeding of corn stover feedstock and dilute acid solution without impregnation. *Bioresour. Technol.*, 1, 360–364. DOI: 10.1016/j.biortech.2014.02.074.
- Hou W., Zhang L., Zhang, J. Bao J., 2016. Rheology evolution and CFD modeling of lignocellulose biomass during extremely high solids content pretreatment. *Biochem. Eng. J.*, 105, 412–419. DOI: 10.1016/j.bej.2015.10.021.
- Kaminoyama M., Watanabe M., Nishi K. and Kamiwano M., 1999. Numerical simulation of local heat transfer coefficient in stirred vessel with impeller for highly viscous fluids. *J. Chem. Eng. Japan*, 32, 23-30. DOI: 10.1252/jcej.32.23.
- Nagata S., Yanagimoto M., Yokoyama T., 1956. Studies on the mixing of high viscous liquids. *Memoirs of the Faculty of Engineering, Kyoto University*, 18, 444-460.
- Kunczewicz Cz., Pietrzykowski M., 2010. A 3D/2D hybrid model for flat blade impellers operating in the laminar flow. *Chem. Proc. Eng.*, 31, 289-302.
- Kunczewicz C. 2012. *Mieszanie cieczy wysokolepkich. Podstawy procesowe*. Wydawnictwo Politechniki Łódzkiej (in Polish).
- Kunczewicz Cz. Rieger F., M. Pietrzykowski, J. Stelmach, 2013. 3D/2D hybrid model for ribbon impellers operating in laminar regime. *Chem. Eng. Process. Process Intensif.*, 73, 50-58. DOI: 10.1016/j.cep.2013.08.003.
- Liu W., Wang Y.M., Yu Z.C., Bao J., 2012. Simultaneous saccharification and microbial lipid fermentation of corn stover by oleaginous yeast *Trichosporon cutaneum*. *Bioresour. Technol.*, 118, 13–18. DOI: 10.1016/j.biortech.2012.05.038.
- Obraniak A., Gluba T., 2012. Model of energy consumption in the range of nucleation and granule growth in drum granulation bentonite. *Physicochemical Problems of Mineral Processing*, 48,1, 121-128.
- Ohta M., Kuriyama M., Arai K., Saito S., 1985. A two-dimensional model for the secondary flow in an agitated vessel with anchor impeller. *J. Chem. Eng. Japan*, 18, 81-84. DOI: 10.1252/jcej.18.81.
- Rieger F., Novak V., Havelkova D., 1986. Homogenization efficiency of helical ribbon agitators. *Chem. Eng. J.*, 33, 143-150. DOI: 10.1016/0300-9467(86)80013-2.
- Robinson M., Cleary P.W., 2012. Flow and mixing performance in helical ribbon mixers. *Chem. Eng. Sci.*, 84, 382–398. DOI: 10.1016/j.ces.2012.08.044.
- Shiue S.J., Wong C.W., 1984. Studies on homogenization efficiency of various agitators in liquid blending. *Can. J. Chem. Eng.*, 62, 602-609. DOI: 10.1002/cjce.5450620505.
- Soliman M.G., 1985. *Agitation de fluides visqueux pseudoplastiques par un double ruban hélicoïdal*. Thesis, I.N.P. Toulouse, France.
- Stręk F., 1981. *Mieszanie i mieszalniki*. WNT Warszawa.
- Takahashi K., Sasaki M., Arai K., 1982. Effects of geometrical variables of helical ribbon impellers on mixing of highly viscous Newtonian liquids. *J. Chem. Eng. Japan*, 15, 217-224. DOI: 10.1252/jcej.15.217.
- Takahashi K., Yokota T., Konno H., 1988. Mixing of pseudoplastic liquid in a equipped with a variety of helical ribbon impellers. *J. Chem. Eng. Japan*, 21, 63-68. DOI: 10.1252/jcej.21.63.
- Takahashi K., Iwaki M., Yokota T., Konno H., 1989. Circulation time for pseudoplastic liquids in a vessel equipped with a variety of helical ribbon impellers. *J. Chem. Eng. Japan*, 22, 413-418. DOI: 10.1252/jcej.22.413.
- Takahashi K., Yokota T., Furukawa T., Harada K., 1994. Mixing of highly viscous newtonian liquid in a helical ribbon agitated vessel at various liquid depths. *J. Chem. Eng. Japan*, 27, 244-247. DOI: 10.1252/jcej.27.244.

- Takahashi K., Sugawara N., Takahata Y., 2015. Mixing time in an agitated vessel equipped with large impeller. *J. Chem. Eng. Japan*, 48, 513-517. DOI: 10.1252/jcej.14we192.
- Thiele H., 1972. *Strömung und Leistungsbedarf beim Rühren Newtonscher Flüssigkeiten mit Anker, Blatt- und Turbinenrühren in laminar Bereich*. Dissertation, Technische Universität Berlin.
- Ulbrecht J., Carreau P., 1985. *Mixing of Liquids by Mechanical Agitation*, Chapter 4. Gordon and Breach, New York.
- Wang Xiao, Fradette L., Takenaka K., Tanguy Ph., 2012. Effect of operating parameters on the mixing performance of the superblend coaxial mixer. *Ind. Eng. Chem. Research*, 51, 1826-1833. DOI: 10.1021/ie200707n.
- Wu B.X., 2012. CFD simulation of mixing for high-solids anaerobic digestion. *Biotechnol. Bioeng.*, 109, 2116-2126. DOI: 10.1002/bit.24482.
- Zhang J., Chu D.Q., Huang J., Yu Z.C., Dai G.C., Bao J., 2010. Simultaneous saccharification and ethanol fermentation at high corn stover solids loading in a helical stirring bioreactor. *Biotechnol. Bioeng.*, 105, 718-728. DOI: 10.1002/bit.2259.
- Zhang L., Zhang J., Li C., Bao J., 2014. Rheological characterization and CFD modelling of corn stover-water mixing system at high solids loading for dilute acid pretreatment. *Biochem. Eng. J.*, 90, 324-332. DOI: 10.1016/j.bej.2014.06.018.
- Zhao K., Qiao Q.A., Chu D.Q., Gu H.Q., Dao T.H., Zhang J., Bao J., 2013. Simultaneous saccharification and high titer lactic acid fermentation of corn stover using a newly isolated lactic acid bacterium *Pediococcus acidilactici* DQ2. *Bioresour. Technol.*, 135, 481-489. DOI: 10.1016/j.biortech.2012.09.063.

Received 27 October 2016

Received in revised form 21 August 2017

Accepted 04 September 2017

Instructions for Authors

All manuscripts submitted for publication in Chemical and Process Engineering must comprise a description of original research that has neither been published nor submitted for publication elsewhere.

The content, aim and scope of the proposals should comply with the main subject of the journal, i.e. they should deal with mathematical modelling and/or experimental investigations on momentum, heat and mass transfer, unit processes and operations, integrated processes, biochemical engineering, statics and kinetics of chemical reactions. The experiments and modelling may cover different scales and processes ranging from the molecular phenomena up to production systems. The journal language is grammatically correct British English.

Chemical and Process Engineering publishes: i) full text research articles, ii) invited reviews, iii) letters to the editor and iv) short communications, aiming at important new results and/or applications. Each of the publication form is peer-reviewed by at least two independent referees.

Submission of materials for publication

The manuscripts are submitted for publication via email address *A.Bin@ichip.pw.edu.pl*. When writing the manuscript, authors should preferably use the template for articles, which is available on the *www.degruyter.com/view/j/cpe*.

Proposals of a paper should be uploaded using the Internet site of the journal and should contain:

- a manuscript file in Word format (*.doc, *.docx),
- the manuscript mirror in PDF format,
- all graphical figures in separate graphics files.

In the following paragraph the general guidelines for the manuscript preparation are presented.

Manuscript outline

1. Header details

- a. Title of paper
- b. Names (first name and further initials) and surnames of authors
- c. Institution(s) (affiliation)
- d. Address(es) of authors
- e. Information about the corresponding author; academic title, name and surname, email address, address for correspondence

2. Abstract – should contain a short summary of the proposed paper. In the maximum of 200 words the authors should present the main assumptions, results and conclusions drawn from the presented study.

3. Keywords – Up to 5 characteristic keyword items should be provided.

4. Text

- a. Introduction. In this part, description of motivation for the study and formulation of the scientific problem should be included and supported by a concise review of recent literature.
- b. Main text. It should contain all important elements of the scientific investigations, such as presentation of experimental rigs, mathematical models, results and their discussion. This part may be divided into subchapters.
- c. Conclusions. The major conclusions can be put forward in concise style in a separate chapter. Presentation of conclusions from the reported research work accompanied by a short commentary is also acceptable.

Figures: drawings, diagrams and photographs should be located in appropriate places in the manuscript text according to the template. Their graphical form should be of vector or raster type with the minimum resolution of 900 dpi. In addition, separate files containing each of the drawings, graphs and photos should be uploaded onto the journal Web site in one of the following formats: bmp, gif, tiff, jpg, eps. Due to rigid editorial reasons, graphical elements created within MS Word and Excel are not acceptable. The final length of figures should be intended typically for 8 cm (single column) or 16 cm in special cases of rich-detail figures. The basic font size of letters in figures should be at least 10 pts after adjusting graphs to the final length.

Figures: drawings, diagrams and photographs should be in gray scale. In case of coloured graphs or photo an additional payment of 300 PLN (72 €) per 1 page containing coloured figures on both sides, or 150 PLN (36 €) per page containing coloured figures on one side will be required.

Tables should be made according to the format shown in the template.

All figures and tables should be numbered and provided with appropriate title and legend, if necessary. They have to be properly referenced to and commented in the text of the manuscript.

5. List of symbols should be accompanied by their units

6. Acknowledgements may be included before the list of literature references

7. Literature citations

The method of quoting literature source in the manuscript depends on the number of its authors:

- single author – their surname and year of publication should be given, e.g. Marquardt (1996) or (Marquardt, 1996),
- two authors – the two surnames separated by the conjunction “and” with the publication year should be given, e.g. Charpentier and McKenna (2004) or (Charpentier and McKenna, 2004),
- three and more authors – the surname of the first author followed by the abbreviation “et al.” and year of publication should be given, e.g. Bird et al. (1960) or (Bird et al., 1960).

In the case of citing more sources in one bracket, they should be listed in alphabetical order using semicolon for separation, e.g. (Bird et al., 1960; Charpentier and McKenna, 2004; Marquardt, 1996). Should more citations of the same author(s) and year appear in the manuscript then letters “a, b, c, ...” should be successively applied after the publication year.

Bibliographic data of the quoted literature should be arranged at the end of the manuscript text in alphabetic order of surnames of the first author. It is obligatory to indicate the DOI number of those literature items, which have the numbers already assigned. Journal titles should be specified by typing their right abbreviations or, in case of doubts, according to the List of Title Word Abbreviations available at <http://www.issn.org/2-22661-LTWA-online.php>.

Examples of citation for:

Articles

Charpentier J. C., McKenna T. F., 2004. Managing complex systems: some trends for the future of chemical and process engineering. *Chem. Eng. Sci.*, 59, 1617-1640. DOI: 10.1016/j.ces.2004.01.044.

Information from books (we suggest adding the page numbers where the quoted information can be found)

Bird R. B., Stewart W.E., Lightfoot E.N., 2002. *Transport Phenomena*. 2nd edition, Wiley, New York, 415-421.

Chapters in books

Hanjalić K., Jakirlić S., 2002. Second-moment turbulence closure modelling, In: Launder B.E., Sandham N.D. (Eds.), *Closure strategies for turbulent and transitional flows*. Cambridge University Press, Cambridge, 47-101.

Conferences

ten Cate A., Bermingham S.K., Derksen J.J., Kramer H.M.J., 2000. Compartmental modeling of an 1100L DTB crystallizer based on Large Eddy flow simulation. *10th European Conference on Mixing*. Delft, the Netherlands, 2-5 July 2000, 255-264.

8. Payments

Starting from 2014 a principle of publishing articles against payment is introduced, assuming non-profit making editorial office. According to the principle authors or institutions employing them, will have to cover the expenses amounting to 40 PLN (or 10 €) per printed page. The above amount will be used to supplement the limited financial means received from the Polish Academy of Sciences for the editorial and publishing; and in particular to increase the capacity of the next CPE volumes and to proofread the linguistic correctness of the articles. The method of payment will be indicated in an invoice sent to the authors or institutions after acceptance of their manuscripts to be published. In justifiable cases presented in writing, the editorial staff may decide to relieve authors from basic payment, either partially or fully.

All correspondence should be sent to Editor-in-Chief, Prof. Andrzej K. Biń, email address A.Bin@ichip.pw.edu.pl.



The Azoty Group is a future-oriented project. But this has always been the case. When in 1927 President Ignacy Mościcki decided to build the State-owned Nitrogenous Compounds Factory it was a vision of the future. A vision of Poland's grand chemical industry.

This vision, and the history of all the companies the Group put together give us the picture of one of the key capital groups in the European fertiliser-chemical sector.



GRUPA
AZOTY



grupaazoty.com

